

Copyright  
by  
Jérôme Sicard  
2014

The Dissertation Committee for Jérôme Sicard  
certifies that this is the approved version of the following dissertation:

**Development of an Extremely Flexible,  
Variable-Diameter Rotor for a Micro-Helicopter**

Committee:

---

Jayant Sirohi, Supervisor

---

Jeffrey K. Bennighof

---

Wallace T. Fowler

---

Chad M. Landis

---

Lance Manuel

---

Hans M. Mark

**Development of an Extremely Flexible,  
Variable-Diameter Rotor for a Micro-Helicopter**

by

**Jérôme Sicard, B.S., M.S.E.**

**DISSERTATION**

Presented to the Faculty of the Graduate School of  
The University of Texas at Austin  
in Partial Fulfillment  
of the Requirements  
for the Degree of

**DOCTOR OF PHILOSOPHY**

THE UNIVERSITY OF TEXAS AT AUSTIN

May 2014

Dedicated to the bride and groom-to-be Véronique and Sébastien.

## Acknowledgments

I would like to acknowledge here some of those, who, directly or indirectly have contributed to the successful completion of this work.

Foremost, I would like to express my deepest gratitude and appreciation to Dr. Jayant Sirohi for his inspiring guidance over the course of my graduate study. He has been a tremendous mentor to me. By directing the path of my research at time, while giving me enormous intellectual freedom and space, he enabled me to grow as a research scientist. I am profoundly thankful for his effort in supporting our research and giving me the opportunity to attend technical international symposiums, as well as for his undertaking to introduce me to the leading scientists in the field. Our formal and informal conversations were always enriching and will have a profound impact on the remaining of my professional career. I am enthusiastic about pursuing our route together and collaborating on future research initiatives.

I would like to extend my appreciation to the members of my dissertation committee: Dr. Jeffrey Bennighof, Dr. Wallace Fowler, Dr. Chad Landis, Dr. Lance Manuel and Dr. Hans Mark. Their insightful comments and encouragements have been instrumental to the completion of this work. The broad vision they held on this research provided critical guidance during the times when I was entrenched with a narrower perspective.

I would like to thank Joseph Pokluda for his assistance in the machine shop and for his contagious cheerful disposition. In addition, the administrative support of Donna Soward and Geetha Rajagopal was always very efficient and much appreciated.

I am indebted to my colleagues and friends in the aeroelasticity and rotorcraft research group at the University of Texas at Austin. Brent, Anand, George and Chris provided valuable criticisms and recommendations during research reviews. I was always fortunate to find them by my side to celebrate various academic achievements.

Throughout my time in Texas, I had the privilege to study alongside great fellow graduate students, many of whom became true friends. Among them, I would like to thank particularly Woutijn, Santiago, Colin, Dominik, Alan, Scott, Zach and Sundeep for both work-related and also refreshingly non-work-related conversations during lunch breaks, coffee breaks and bike rides. They shared with me moments of joy and helped me overcome the stressful times.

France has been and will always be the place I call home. After living in the United-States for five years, I always found heart-warming to meet and converse with my French companions, in the language of Molière. I am particularly grateful to Etienne, Mathieu and Philippe for providing me with the unique savor of France that I occasionally missed. In addition, each of my trips back to France was warmly celebrated by my closest friends. In particular, I wish to acknowledge Antoine, Yohan, Pierre, Nicolas, Mathieu,

Frédéric, Lucien and Franck whose welcome always made me feel like we had said goodbye the previous day. In spite of the long distances separating us, I could always feel their presence which gave me the energy I needed to be successful in my graduate studies. Merci!

I fondly wish to acknowledge my best friend Miao and the woman I love Alexis for their perennial supply of encouragement, support and for enlightening me when I did not see my way clearly. The journey of a doctoral student is sprinkled with times of doubt and despondency. With Miao and Alexis, I knew I would always find the attentive ear I needed, or a shoulder to rest on. Both of them know that I will always be there for them.

My brother, Frédéric, has become my greatest source of motivation and dedication. He is the reason why I was able to spend late nights working on this research, and to carry on the following days. His perseverance is boldly inspiring and humbling; I owe him immeasurably for showing to me how fortunate I am to pursue my dreams.

Last but not least, words cannot capture my deepest gratitude and acknowledgment of my parents. They are my confidants, my most trusted advisors, and most importantly, my model. They assisted me in always making the right decisions throughout my entire education. They were by my side the day when I decided to leave France and enter graduate school. It was with them that I decided to carry on after the Master's degree and embark on the Ph.D. program. And they will once again be with me at the commencement. It is adequate to say that they are the reason for the existence of this work.

# Development of an Extremely Flexible, Variable-Diameter Rotor for a Micro-Helicopter

Jérôme Sicard, Ph.D.

The University of Texas at Austin, 2014

Supervisor: Jayant Sirohi

This dissertation describes the design, analysis and testing of an unconventional rotor featuring extremely flexible, retractable blades. These rotor blades are composed of a flexible matrix composite material; they are so flexible that they can be rolled up and stowed in the rotor hub. The motivation for this study is to equip the next generation of unmanned rotary-wing vehicles with morphing rotors that can change their diameter in flight, based on mission requirements. Due to their negligible structural stiffness, the static and dynamic behavior of these blades is dominated by centrifugal effects. Passive stabilization of the flexible blades is achieved by centrifugal stiffening in conjunction with an appropriate spanwise and chordwise mass distribution. In particular, such blades are susceptible to large deformations. For example, a combination of the trapeze effect and the tennis racquet effect induces a large negative twist that results in decreased efficiency. Additionally, the rotor blades are prone to aeroelastic instabilities due to their low rotating torsional frequency, and it is seen that without careful design the blades experience coupled pitch-flap limit cycle oscillations.

The primary focus of this research is to develop analytical and experimental tools to predict and measure the deformations of an extremely flexible rotor blade with non-uniform mass distribution. A novel aeroelastic analysis tailored towards unconventional blades with negligible structural stiffness is developed. In contrast to conventional analyses developed for rigid rotor blades, the present analysis assumes very large elastic twist. The nonlinear coupled equations of motion for the flap bending, lead-lag bending and torsion of an elastic rotating blade are derived using Hamilton's principle. The virtual work associated with unsteady aerodynamic forces in hover is included in the analysis. An ordering scheme consistent with the relevant physical quantities is defined and terms up to second order are retained in the Hamiltonian. The equations of motion are solved using a nonlinear finite element analysis. The steady-state deformation of the rotor blade is obtained from the time invariant part of the solution. The rotating flap, lag and torsional frequencies are found by solving the eigenvalue problem associated with the homogeneous system of equations. Finally, stability boundaries are computed for various operating conditions and the influence of parameters such as rotational velocity and collective pitch angle is discussed.

The analytical predictions are validated by experimental measurements of the blade deformation in hover. These measurements are obtained by a novel, non-contact optical technique called three-dimensional Digital Image Correlation (3D DIC). The use of this technique is demonstrated for the first time to obtain full-field deformation measurements of a rotating blade. In

addition, stability boundaries are extracted from experimental observations and correlated with predictions.

# Table of Contents

<b>Acknowledgments</b>	<b>v</b>
<b>Abstract</b>	<b>viii</b>
<b>Nomenclature</b>	<b>xvii</b>
<b>List of Tables</b>	<b>xxii</b>
<b>List of Figures</b>	<b>xxiii</b>
<b>Chapter 1. Introduction</b>	<b>1</b>
1.1 Problem Statement . . . . .	1
1.2 State of the Art . . . . .	4
1.2.1 Aeroelastic analysis of rotor blades . . . . .	4
1.2.1.1 Rotor blade structural model . . . . .	5
1.2.1.2 Rotor aerodynamic model . . . . .	8
1.2.1.3 Aeroelastic analyses for rotor blades with negli- gible structural stiffness . . . . .	11
1.2.2 Measurement of blade deformation . . . . .	13
1.3 Present Approach . . . . .	15
1.4 Contribution of the Present Research . . . . .	16
1.5 Organization of the Dissertation . . . . .	19
<b>Chapter 2. Analytical Study</b>	<b>21</b>
2.1 General Procedure . . . . .	22
2.1.1 Trim solution . . . . .	22
2.1.2 Perturbed equations of motion . . . . .	23
2.1.3 Stability analysis . . . . .	25
2.2 Blade Coordinate Systems . . . . .	26

2.3	Blade Displacement Variables . . . . .	29
2.4	Ordering Scheme . . . . .	35
2.5	Structural Model . . . . .	38
2.5.1	Modeling of the trapeze effect . . . . .	39
2.5.1.1	Kinematics relationships . . . . .	40
2.5.1.2	Restoring moment relationships . . . . .	48
2.5.1.3	Torsional frequency . . . . .	52
2.5.2	Modeling of other extension-torsion coupling effects . . . . .	62
2.5.2.1	Vlasov effect . . . . .	62
2.5.2.2	Composite material coupling . . . . .	65
2.5.3	Modeling of the kinematic foreshortening due to bending . . . . .	67
2.5.4	Definition of the reference axis . . . . .	68
2.5.5	Choice of coordinates . . . . .	77
2.5.5.1	Elastic pitch angle $\theta$ vs. twist angle $\phi$ . . . . .	78
2.5.5.2	Implicit vs. explicit kinematic foreshortening . . . . .	79
2.5.5.3	True vs. quasi coordinates . . . . .	80
2.5.5.4	Example: Elastic rotor blade undergoing coupled extension-flap motion . . . . .	81
2.5.6	Inextensible blade assumption . . . . .	85
2.5.7	Blade strain energy . . . . .	86
2.5.7.1	Strain tensor . . . . .	86
2.5.7.2	Structural cross-sectional constants . . . . .	91
2.5.7.3	Variation in the strain energy . . . . .	92
2.5.7.4	Linearized strain energy . . . . .	96
2.5.8	Blade kinetic energy . . . . .	96
2.5.8.1	Inertial cross-sectional constants . . . . .	97
2.5.8.2	Variation in the kinetic energy . . . . .	99
2.5.8.3	Time-invariant kinetic energy . . . . .	102
2.5.8.4	Linearized kinetic energy . . . . .	103
2.5.9	Blade gravitational potential energy . . . . .	104
2.5.10	Potential energy stored in the root springs . . . . .	104
2.5.11	Modeling of the tip mass . . . . .	105

2.5.11.1	Configuration BP . . . . .	106
2.5.11.2	Configuration C . . . . .	112
2.6	Aerodynamic Model . . . . .	114
2.6.1	Unsteady aerodynamic model . . . . .	115
2.6.1.1	Theodorsen's theory for a flat plate . . . . .	116
2.6.1.2	Unsteady aerodynamics theory for a rotor blade in hover . . . . .	120
2.6.2	Quasi-steady aerodynamic model . . . . .	129
<b>Chapter 3. Numerical Models</b>		<b>132</b>
3.1	Solution by Assumed-Modes Method . . . . .	132
3.2	Solution by Finite Element Method . . . . .	135
3.2.1	Beam finite elements . . . . .	136
3.2.2	Shape functions . . . . .	138
3.2.3	Computation of the trim solution . . . . .	140
3.2.3.1	Newton-Raphson method . . . . .	141
3.2.3.2	Line search and backtracking algorithm . . . . .	143
3.2.3.3	Gaussian quadrature rule . . . . .	145
3.2.3.4	Computation of the cross-sectional constants . . . . .	145
3.2.3.5	Assembly of the global stiffness matrix . . . . .	148
3.2.3.6	Boundary conditions . . . . .	149
3.2.4	Computation of the stability boundaries . . . . .	151
3.2.4.1	Determination of divergence . . . . .	152
3.2.4.2	Determination of flutter . . . . .	153
3.3	Algorithm Flow Chart . . . . .	156
<b>Chapter 4. Experimental Procedures</b>		<b>158</b>
4.1	Rotor Blades Design and Fabrication . . . . .	158
4.1.1	Flexible blade C . . . . .	159
4.1.2	Flexible blade BP . . . . .	160
4.1.3	Stiff blade R . . . . .	162
4.1.4	Stiff blade M . . . . .	163
4.1.5	Blade design matrix . . . . .	163

4.2	Blade Material Properties . . . . .	166
4.3	Aerodynamic Coefficients . . . . .	169
4.4	Test Matrix . . . . .	172
4.5	Test Bench . . . . .	174
4.5.1	Hover test stands . . . . .	174
4.5.2	Laser distance sensor . . . . .	177
4.5.3	Laser inclinometer . . . . .	178
4.6	Digital Image Correlation Technique . . . . .	178
4.6.1	Blade preparation . . . . .	179
4.6.2	Digital cameras . . . . .	180
4.6.3	Calibration . . . . .	180
4.6.4	Image acquisition . . . . .	182
4.6.5	Computation of deformation . . . . .	183
4.6.6	Spatial resolution . . . . .	185
<b>Chapter 5. Results and Discussion</b>		<b>186</b>
5.1	Flexible Rotor Blade Performance in Hover . . . . .	187
5.2	Validation of the DIC Technique . . . . .	189
5.3	Validation of the Numerical Analysis . . . . .	193
5.3.1	Static elasticity test cases . . . . .	194
5.3.1.1	Euler-Bernoulli cantilever beam under its own weight . . . . .	194
5.3.1.2	Euler-Bernoulli cantilever beam under distributed torsion . . . . .	195
5.3.1.3	Euler-Bernoulli cantilever beam under its own weight with a torsional spring at the root . . . . .	196
5.3.1.4	Euler-Bernoulli cantilever beam subjected to a concentrated shear force . . . . .	197
5.3.1.5	Euler-Bernoulli cantilever beam subjected to a concentrated torque . . . . .	198
5.3.2	Princeton beam test case . . . . .	198
5.3.2.1	Static deflections . . . . .	199
5.3.2.2	Natural frequencies . . . . .	201
5.3.3	Dynamics test cases . . . . .	202

5.3.3.1	Bending frequencies of a rotating beam . . . . .	203
5.3.3.2	Torsional frequencies of a rotating beam . . . . .	207
5.4	Aeroelastic Behavior of the Flexible Rotor BP . . . . .	212
5.4.1	Trim state in hover . . . . .	212
5.4.2	Stability Analysis . . . . .	216
5.4.2.1	Flutter boundaries of the flexible blades BP . . . . .	216
5.4.2.2	Influence of the chordwise position of the tip mass on the flutter boundaries . . . . .	219
5.4.2.3	Effect of a change in rotor diameter on the flutter boundaries . . . . .	220
<b>Chapter 6.</b>	<b>Summary and Future Work</b>	<b>251</b>
<b>Appendices</b>		<b>257</b>
<b>Appendix A.</b>	<b>An alternative derivation of the torsional frequency     associated with the trapeze effect</b>	<b>258</b>
<b>Appendix B.</b>	<b>Use of quasi-coordinates in Hamilton's Principle</b>	<b>260</b>
<b>Appendix C.</b>	<b>Additional analytical results</b>	<b>265</b>
<b>Appendix D.</b>	<b>First-order Taylor approximation of energy ex-     pressions</b>	<b>273</b>
D.1	Linearized strain energy . . . . .	273
D.2	Linearized kinetic energy . . . . .	277
D.3	Linearized gravitational potential energy . . . . .	280
D.4	Linearized tip mass kinetic energy . . . . .	280
D.5	Linearized tip mass gravitational potential energy . . . . .	283
D.6	Linearized virtual work done by unsteady aerodynamic loads . . . . .	283
D.7	Linearized virtual work done by steady aerodynamic loads . . . . .	286
<b>Appendix E.</b>	<b>Numerical computation of the Jacobian matrix     using the complex-step derivative approximation</b>	<b>288</b>
<b>Appendix F.</b>	<b>Response of a mass-spring system subject to gy-     roscopic effects</b>	<b>290</b>

Appendix G. Front panel of custom NI LabView virtual instrument	292
Appendix H. Circuit diagram of DAQ and transducers	294
Bibliography	295
Vita	311

# Nomenclature

## Acronyms

<i>AHS</i>	American Helicopter Society
<i>BEMT</i>	Blade Element Momentum Theory
<i>DIC</i>	Digital Image Correlation
<i>DOF</i>	Degree of Freedom
<i>EHP</i>	Extended Hamilton's Principle
<i>FEM</i>	Finite Element Method
<i>FM</i>	Figure of Merit
<i>IMU</i>	Inertial Measurement Unit
<i>ISR</i>	Intelligence, Surveillance and Reconnaissance
<i>LDS</i>	Laser Distance Sensor
<i>MAV</i>	Micro Aerial Vehicle
<i>PMI</i>	Projection Moiré Interferometry
<i>RPM</i>	Revolution Per Minute
<i>UAV</i>	Unmanned Air Vehicle
/rev	per revolution

## Roman symbols

$A$	Blade cross-sectional area, [m <sup>2</sup> ]
$A_m$	Tip mass cross-sectional area, [m <sup>2</sup> ]
$B_1$	Cross-sectional constants, [m <sup>6</sup> ]
$B_2, B_3$	Cross-sectional constants, [m <sup>5</sup> ]
$C_1$	Warping rigidity [m <sup>6</sup> ]
$C_{ij}$	Damping matrix
$C_{d0}$	Profile drag coefficient, [-]
$C_l$	Lift coefficient, [-]
$C_{l\alpha}$	Lift curve slope coefficient, [/rad]
$C_{l0}$	Lift coefficient at zero angle of attack, [-]
$C_{m0}$	Pitching moment coefficient at zero angle of attack, about the aerodynamic center, [-]

$C_T$	Thrust coefficient, [-]
$C(k)$	Theodorsen lift deficiency function
$C'(k)$	Loewy lift deficiency function
$c$	Airfoil chord, [m]
$D$	Drag, [N]
$d_\eta, d_\xi$	Chordwise and flatwise offsets of mass centroid of blade cross-section from elastic axis, [m]
$E$	Young's modulus, [Pa]
$e_\eta, e_\xi$	Chordwise and flatwise offsets of area centroid of blade cross-section from elastic axis, [m]
$G$	Shear modulus, [Pa]
$G_{ij}$	Gyroscopic matrix
$g$	Gravitational acceleration, [m/s <sup>-2</sup> ]
$H$	Hamiltonian
$h$	Vertical separation between vortex sheets below the airfoil, [m]
$I_{ij}$	Identity matrix
$I_\xi, I_\eta$	Blade area moments of inertia about $\eta$ and $\xi$ axes, [m <sup>4</sup> ]
$I_{\eta\xi}$	Blade area product of inertia, [m <sup>4</sup> ]
$J$	Polar moment of inertia about elastic axis, [m <sup>4</sup> ]
$K_{ij}$	Stiffness matrix
$k$	Reduced frequency, [-]
$k_A$	Polar radius of gyration about elastic axis, [m <sup>2</sup> ]
$k_m$	Polar radius of gyration of blade cross-sectional mass about elastic axis, [m <sup>2</sup> ]
$k_{m\xi}, k_{m\eta}$	Mass radii of gyration about $\eta$ and $\xi$ axes, [m <sup>2</sup> ]
$k_\zeta, k_\beta, k_\theta$	Torsional stiffness of root springs, [N.m/rad]
$L$	lift, [N]
$L_m$	Length of the tip mass, [m]
$L_1, L_2$	Distances between tip mass ends and tip mass attachment point, [m]
$M$	Aerodynamic pitching moment, [N.m]
$M_{ij}$	Mass matrix
$m$	$\omega/\Omega$ , [-]
$m_0$	Mass per unit length, [kg/m]
$m_m$	Tip mass per unit length, [kg/m]
$N$	Number of finite elements, [-]
$N_{DOF}$	Number of degrees of freedom, [-]

$N_l$	Order of Gaussian quadrature formula, [-]
$N_n$	Number of nodes, [-]
$q_i$	Generalized coordinate
$R$	Rotor radius, [m]
$Re$	Reynolds number, [-]
$\mathbf{r}$	Position vector, [m]
$r$	Curvilinear coordinate, along the deformed elastic axis, [m]
$T$	Kinetic energy, [N.m]
$T_{ij}$	Transformation matrix
$T_0$	Time invariant kinetic energy, [N.m]
$T_{SV}$	Torque predicted by Saint-Venant's theory, [N.m]
$t$	Airfoil thickness, [m]
$\mathbf{U}$	Resultant velocity of flow around the airfoil, [m/s]
$U$	Strain energy, [N.m]
$u$	Displacement in the $X$ -direction, [m]
$u_e$	Elongation, [m]
$u_F$	Kinematic foreshortening, [m]
$U_P$	Axial velocity, [m/s]
$U_T$	Tangential velocity, [m/s]
$V$	Potential energy, [N.m]
$V_g$	Gravitational potential energy, [N.m]
$V_i$	Induced velocity, [m/s]
$V_{sp}$	Restoring potential energy contained in root springs, [N.m]
$V_\infty$	Free stream velocity, [m/s]
$v$	Lead-lag bending deflection, along the $Y$ -axis, [m]
$v^*$	Chordwise bending deflection, along the $\eta$ -axis, [m]
$W_a$	Work done by aerodynamic forces, [N.m]
$W_{aQS}$	Work done by quasi-steady aerodynamic forces, [N.m]
$W_{nc}$	Work done by non-conservative forces, [N.m]
$w$	Flap bending deflection, along the $Z$ -axis, [m]
$w^*$	Flatwise bending deflection, along the $\xi$ -axis, [m]
$w_l$	Gaussian integration weight, [-]
$x$	Spanwise coordinate, along $X$ -axis, [m]
$x_0$	Root cutout, [m]
$x_A$	Aerodynamic center offset from the elastic axis, [m] (positive when ahead of the elastic axis)
$x_l$	Gaussian integration coordinate, [m]

$x_m$	Spanwise coordinate of the tip mass attachment point, [m]
$\{X, Y, Z\}$	Hub-fixed reference frame
$\{X_I, Y_I, Z_I\}$	Newtonian reference frame
$\{X_m, Y_m, Z_m\}$	Tip mass-fixed reference frame
$\{\zeta, \eta, \xi\}$	Blade-fixed reference frame

### Greek symbols

$\gamma$	Engineering shear strain, [m/m]
$\delta( )$	indicates the variations of
$\eta_m, \xi_m$	Offsets between the point of attachment of the tip mass and the elastic axis, [m]
$\bar{\theta}$	Local pitch angle, [rad]
$\theta$	Local elastic pitch angle, [rad]
$\theta_0$	Collective pitch angle, [rad]
$\theta_{ind}$	Index angle between the tip mass longitudinal axis and the blade chord, [rad]
$\theta_D$	Local pitch angle measured by DIC, [rad]
$\kappa$	Induced power correction factor, [-]
$\kappa_i$ 's	Curvatures, [1/m]
$\lambda_i$	Inflow ratio, [-]
$\rho$	Blade mass density, [kg/m <sup>3</sup> ]
$\rho_m$	Tip mass density, [kg/m <sup>3</sup> ]
$\rho_\infty$	Air mass density, [kg/m <sup>3</sup> ]
$\sigma$	Rotor solidity, [-]
$\sigma_{ij}$	Normal stress, [Pa]
$\tau_{ij}$	Shear stress, [Pa]
$\phi$	Elastic twist angle, [rad]
$\chi, \lambda$	Bound variables
$\Omega$	Rotor angular velocity, [rad/s]
$(\bar{\zeta}, \bar{\beta}, \bar{\theta})$	Euler angles, [rad]

### Superscripts

$( )^+$	$\partial/\partial r$
$( )$	time derivative
$( )'$	spatial derivative

<sup>**</sup> ( )	$(1/\Omega) \partial/\partial t$
( ) <sup>a</sup>	indicates quantity related to aerodynamic force
( ) <sup>CF</sup>	indicates quantity related to centrifugal force
( ) <sup>i</sup>	indicates the $i^{th}$ iteration

### Subscripts

( ) <sub>0</sub>	indicates value at trim condition
( ) <sub>75</sub>	indicates value at 75% radius location
( ) <sub>b</sub>	indicates quantity related to the blade airfoil
( ) <sub>m</sub>	indicates quantity related to the tip mass

## List of Tables

2.1	Ordering scheme . . . . .	36
2.2	Order of terms retained for each equation of motion in Kaza and Kvaternik, 1977 . . . . .	37
2.3	Truncation strategy . . . . .	38
3.1	Nature of the free response for various values of $\delta$ and $k$ . . . . .	152
4.1	Blade design matrix . . . . .	164
4.2	Material properties of carbon fibers and resins . . . . .	167
4.3	Material properties of flexible blades . . . . .	168
5.1	Theoretical precision of displacement vectors computed by DIC . . . . .	191
5.2	Princeton beam parameters . . . . .	199
5.3	Torsional frequencies of Princeton beam ( $\theta_0 = 0$ and $P = 0$ lb) . . . . .	203
5.4	Simplified UH-60 blade parameters . . . . .	204
5.5	Bending frequencies of hinged rotating model blade . . . . .	205
5.6	Bending frequencies of clamped rotating model blade . . . . .	206
5.7	Bending frequencies of rotating blade with root offset . . . . .	206
5.8	Bending frequencies of rotating blade with tip mass . . . . .	207
5.9	Torsional frequencies of clamped-free rotating blade . . . . .	208
5.10	Torsional frequencies of hinged-free rotating blade . . . . .	209
5.11	Torsional frequencies of cantilever rotating pipe . . . . .	212

## List of Figures

1.1 Stowable flexible rotor concept . . . . .	2
1.2 Micro-helicopter with 18 inch diameter flexible rotors . . . . .	3
2.1 Coordinate systems . . . . .	27
2.2 Euler angles for a lag-flap-pitch sequence . . . . .	28
2.3 Undeformed and deformed shape of a trapeze in torsion . . . . .	40
2.4 Kinematic foreshortening induced in a twisted trapeze, for various chord over length ratios . . . . .	42
2.5 Undeformed and deformed shape of a thin ribbon in torsion . . . . .	44
2.6 Parametrization of a helix . . . . .	45
2.7 Restoring torque induced by longitudinal stresses in the fibers . . . . .	50
2.8 Schematic of propeller moment acting on a rotating blade . . . . .	53
2.9 Cable rotor with disk at the tip . . . . .	55
2.10 Cable rotor with solid rod at the tip . . . . .	57
2.11 Variation of the steady-state twist angle with the root pitch . . . . .	58
2.12 Variation of the torsional frequency with the root pitch ( $y_m/c = 0.25$ ) . . . . .	59
2.13 Variation of the torsional frequency and twist of a cable rotor, as a function of the tip mass chordwise position ( $\theta_0 = 20^\circ$ ) . . . . .	61
2.14 Laminated element with force and moment resultants . . . . .	66
2.15 Foreshortening associated with out-of-plane bending . . . . .	67
2.16 Infinitely soft beam under combined axial loading ( $P$ ) and shear loading ( $V$ ) . . . . .	70
2.17 Bending/twist deformation due to a shear force ( $P = 0$ ) . . . . .	71
2.18 Bending/twist deformation due to a shear force ( $P \neq 0$ ) . . . . .	72
2.19 Free-body-diagram of the forces and moments applied to a rotor blade with tip mass . . . . .	74
2.20 Spanwise locus of centroid of the axial stress field . . . . .	76
2.21 Elastic string undergoing pure flap . . . . .	81

2.22	Components of the longitudinal strain . . . . .	90
2.23	Flap torsional spring . . . . .	105
2.24	Position and orientation of the tip mass in the blade configuration BP . . . . .	106
2.25	Position and orientation of the tip mass for the blade configuration C . . . . .	112
2.26	Thin airfoil section undergoing pitching and heaving motion . . . . .	117
2.27	Theodorsen lift deficiency function . . . . .	119
2.28	Aerodynamic forces on a blade cross-section . . . . .	123
3.1	Beam finite element . . . . .	137
3.2	Newton-Raphson algorithm for 1-D case . . . . .	142
3.3	Polar coordinate system for calculation of cross-sectional constants . . . . .	146
3.4	Assembly of the global stiffness matrix for $N = 2$ elements. The dashed-line and solid-line boxes correspond to the local matrices of elements numbered 1 and 2 respectively. . . . .	148
3.5	Regula Falsi method for $p \in \mathbb{R}$ . . . . .	155
3.6	Algorithm flow chart . . . . .	157
4.1	Schematic of flexible rotor blade C . . . . .	159
4.2	Mold for wet lay-up of blades C . . . . .	160
4.3	Sketch of flexible blade BP . . . . .	161
4.4	Planform of flexible blade BP . . . . .	162
4.5	Extremely flexible rotors and stiff rotors at rest . . . . .	165
4.6	Coordinate system of a generally orthotropic material . . . . .	168
4.7	2-D mesh of the flow surrounding a circular arc airfoil . . . . .	170
4.8	Contours of static pressure for various angles of attack ( $Re = 16, 160$ ) . . . . .	170
4.9	Simulated lift and drag coefficients compared to experimental measurements . . . . .	171
4.10	Stiff rotor blade M mounted on hover test stand . . . . .	175
4.11	Extremely flexible rotor blades C mounted on hover test stand . . . . .	176
4.12	High-contrast random pattern on the bottom surface of rotor blades . . . . .	179

4.13	Reference system of axes defined during calibration . . . . .	181
4.14	Raw images acquired with DIC system . . . . .	182
4.15	Computation of local pitch angle $\theta_D$ using surface heights of leading-edge and trailing-edge ( $z_{LE}$ and $z_{TE}$ ) measured by DIC . . . . .	184
4.16	Blade cross-section in the deformed configuration, projected in the vertical plane (note: $\eta$ and $\xi$ are not in the same plane as $Y$ and $Z$ ) . . . . .	184
5.1	Thrust coefficients ( $\Omega = 1500 \text{ RPM}$ ) . . . . .	222
5.2	High twist induced over the inboard section of flexible blades C ( $\Omega = 1500 \text{ RPM}$ , $\theta_0 = 16^\circ$ ) . . . . .	223
5.3	Tip pitch angle controlled by use of the propeller moment acting on the tip mass ( $\Omega = 1500 \text{ RPM}$ , $\theta_0 = 22^\circ$ ) . . . . .	223
5.4	Figures of merit ( $\Omega = 1500 \text{ RPM}$ ) . . . . .	224
5.5	Power coefficient vs. thrust coefficient ( $\Omega = 1500 \text{ RPM}$ ) . . . . .	224
5.6	Pitch-flap flutter observed on flexible rotor blades C ( $\Omega = 1500 \text{ RPM}$ , $\theta_0 = 0^\circ$ ) . . . . .	225
5.7	Blade section position and shape measured by DIC and LDS at 3/4 span of rigid blade M ( $\theta_0 = 11^\circ$ , $\Omega=500, 700, 900 \text{ RPM}$ ) . . . . .	226
5.8	Spanwise variation of pitch measured by DIC, compared to design parameters (rigid blade M, washout twist, $-0.7 \text{ deg/cm}$ ), at various root pitch angles ( $\Omega = 300 \text{ RPM}$ ) . . . . .	227
5.9	Root pitch angle of flexible blade BP measured by DIC, and compared to measurement of root pitch angles by laser inclinometer ( $\Omega = 1200 \text{ RPM}$ ) . . . . .	228
5.10	Euler-Bernoulli cantilever beam of rectangular cross-section, loaded by its own weight ( $\rho = 2700 \text{ kg/m}^3$ , $EI_\eta = 0.0073 \text{ N.m}^2$ ) . . . . .	229
5.11	Euler-Bernoulli cantilever beam of rectangular cross-section, loaded by uniformly distributed torsion ( $t = 1 \text{ N.m/m}$ , $GJ = 0.4489 \text{ N.m}^2$ ) . . . . .	230
5.12	Axial foreshortening in beam under distributed torsion ( $t = 1 \text{ N.m/m}$ , $GJ = 0.4489 \text{ N.m}^2$ ) . . . . .	231
5.13	Euler-Bernoulli beam of rectangular cross-section, with spring at the root, loaded by its own weight ( $\rho = 2700 \text{ kg/m}^3$ , $EI_\eta = 0.0073 \text{ N.m}^2$ , $k_\beta = 1 \text{ N.m/rad}$ ) . . . . .	232
5.14	Euler-Bernoulli cantilever beam of rectangular cross-section, subjected to a concentrated load ( $a = 2R/3$ , $F_z = 1 \text{ mN}$ , $EI_\eta = 0.0073 \text{ N.m}^2$ ) . . . . .	233

5.15	Cantilever beam of rectangular cross-section, subjected to a concentrated torque ( $M_x = 1$ N.m, $GJ = 1.0860$ N.m <sup>2</sup> ) . . . .	234
5.16	Apparatus and experimental set-up for the Princeton beam static deflection experiments, from Dowell & Traybar, 1975 . .	235
5.17	Bending deflections of Princeton beam for tip load $P = 1$ lb .	236
5.18	Twist of Princeton beam for tip load $P = 1$ lb . . . . .	237
5.19	Natural frequencies of Princeton beam for tip load $P = 1$ lb .	238
5.20	Measured deformation of rotor blade BP compared to numerical predictions ( $\Omega = 1200$ RPM) . . . . .	239
5.21	Measured axial displacement and lead-lag bending of rotor blade BP ( $\Omega = 1200$ RPM) . . . . .	240
5.22	Variation of thrust of rotor blade BP as a function of the collective pitch . . . . .	241
5.23	Natural frequencies of rotor blade BP . . . . .	242
5.24	Natural frequencies in vacuum of UH-60A rotor blade; F: Flap, C:Lag, T:Torsion; pitch link stiffness 1090 ft-lb/deg, from Datta & Chopra, 2004 . . . . .	243
5.25	Mode shapes ( $\theta_0 = 0^\circ$ , $\Omega = 1000$ RPM) . . . . .	244
5.26	Damping coefficient of flap-lag-torsion mode . . . . .	244
5.27	Damping coefficient of torsional modes . . . . .	245
5.28	Damping coefficient of coupled lag-torsion and third torsional mode . . . . .	246
5.29	Influence of the tip mass chordwise position on the natural frequencies . . . . .	247
5.30	Influence of the tip mass chordwise position on the damping of the coupled flap-lag-torsion mode and the first torsional mode	248
5.31	Influence of the tip mass chordwise position on the damping of the second torsional mode and the coupled lag-torsion mode .	249
5.32	Influence of the rotor diameter on the stability boundaries . .	250
A.1	Cable rotor with cross bars at the tip . . . . .	258
G.1	Control & Time Analysis . . . . .	292
G.2	Frequency Analysis . . . . .	293
G.3	Post Processing . . . . .	293
H.1	Circuit diagram of DAQ equipment and transducers . . . . .	294

# Chapter 1

## Introduction

### 1.1 Problem Statement

Micro aerial vehicles (MAVs) have become increasingly popular over the past decade as they are capable of performing missions that conventional manned vehicles or larger unmanned aerial vehicles cannot [1]. MAVs, as originally defined by DARPA [2], include any Unmanned Air Vehicle (UAV) whose length dimensions are less than 6 inches (15.2 cm) and whose gross takeoff weight is approximately 7 ounces (200 gm) or less. Their small size allows them to be undetected, and to penetrate confined areas, which makes them well suited to operate in caves or other indoor locations. Among the types of MAVs in development, rotary-wing MAVs offer unique strengths related to their ability to take off and land vertically, hover, and fly at very low advance ratios [3, 4]. These capabilities make micro-helicopters very well suited for military intelligence, surveillance and reconnaissance (ISR) missions. However, several challenges inherent to the complexity of these missions must be addressed, before fully taking advantage of the benefits offered by a versatile micro-helicopter. Flying in congested terrain increases the likelihood of blade impact with obstacles. Additionally, the size of the rotor limits its ability to access confined spaces.

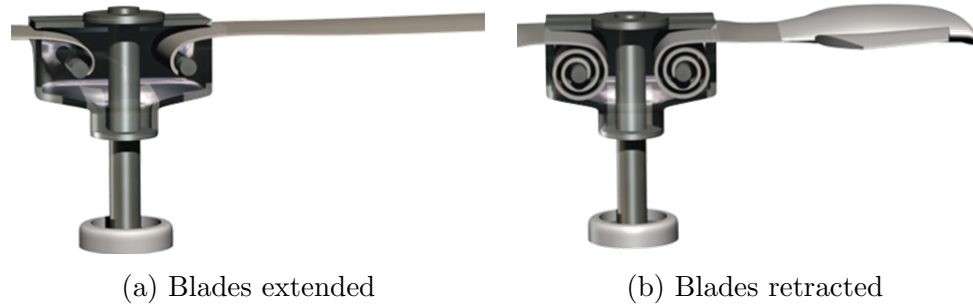


Figure 1.1: Stowable flexible rotor concept

An extremely flexible, variable-diameter rotor is proposed as a solution to some of these issues. This rotor features blades that are so flexible that they can be rolled up in a compact cylinder, and stowed in the rotor hub, as shown in Fig. 1.1. In this way, the rotor diameter can be changed in flight; a large rotor diameter increases the hover endurance while a smaller rotor diameter is beneficial to access confined spaces. Similarly, reducing the rotor diameter during outdoor flight decreases the sensitivity of a micro-helicopter to gusts by increasing its disk loading. The full retraction of the blades is also advantageous for storage and ground transportation of the MAV. Finally, the probability of survival of the vehicle upon collision with an object is increased by the high compliance of the rotor blades. In such an event, the rotor blade can deform elastically before recovering its original shape.

The flexible rotor concept has been explored in several patents [5, 6, 7, 8] and studies [9, 10, 11, 12, 13] in the past. Previous studies have typically involved a rotor blade consisting of a thin sheet passively stabilized by centrifugal forces acting on a tip mass. Flexible structural members such as cables or rods



Figure 1.2: Micro-helicopter with 18 inch diameter flexible rotors

were incorporated in the spanwise direction to react the centrifugal loads. This type of rotor blade has negligible structural stiffness in the bending or torsion degrees of freedom, and relies solely on centrifugal forces for stability.

The flexible rotor blade design explored in this dissertation consists of a thin carbon-fiber composite sheet in conjunction with a tip body. They are incorporated in two coaxial counter-rotating two-bladed rotor systems, as shown in Fig. 1.2. To minimize the total weight of the system, the tip mass is of the same order of magnitude as the blade mass. The composite sheet is designed to sustain the centrifugal loads on the blade, eliminating the need for cables at the leading and trailing edges. The blades are untwisted and have a constant chord. Their airfoil is a circular arc, which is very efficient at the low Reynolds number regime in which micro-helicopters operate [14].

This dissertation documents the design, analysis, fabrication and test-

ing of an extremely flexible, variable-diameter rotor. An aeroelastic analysis tailored to rotor blades with negligible structural stiffness is developed. The fabrication of prototype blades is described and their testing is reported. The predictions obtained by the aeroelastic analysis are validated by experimental measurements of the rotor blade deformation in hover. In addition, the analysis is used to explore the effect of design parameters on the performance and stability boundary of extremely flexible rotor blades.

## **1.2 State of the Art**

The literature on aeroelastic analyses of rotor blades is reviewed in § 1.2.1. Particular attention is given to analyses of blades with negligible structural stiffness. In addition, the state of the art of experimental measurement of blade deformation is presented in § 1.2.2.

### **1.2.1 Aeroelastic analysis of rotor blades**

The analytical study of rotating blades sparked a lot of interest throughout the second half of the 20th century, particularly to support the development of rotorcraft aeromechanics analyses. A detailed review of these comprehensive analyses, which embrace the evaluation of the performance, loads, vibration, stability, flight dynamics and noise of a helicopter, was presented by Johnson in his AHS Nikolsky Honorary Lecture [15]. The analysis described in this dissertation focuses on the prediction of blade deformation, stability boundaries and performance of an isolated rotor, operating in hover. Such an

analysis requires the accurate modeling of the structural dynamics as well as the aerodynamics of the rotor. The publications that served as a basis for the analysis developed in this dissertation are presented below.

### 1.2.1.1 Rotor blade structural model

Rotor blades are typically slender structures with their spanwise dimension being much larger than the flatwise and chordwise dimensions. They are subjected to the combined effects of inertial loads, aerodynamic forces and moments, and, to a lesser extent, gravitational loads. Their boundary conditions vary from a cantilever to hinged-free configuration, depending on the hub design. Consequently, rotor blades have been classically modeled as beam structures. In the 1950s, beam theories were first applied to the problem of rotor blade structural dynamics. Then, the theories were refined, motivated by the need for general purpose analyses capable of predicting the behavior of a wide variety of rotors. The engineering beam theories developed over the years for rotorcraft application can be classified in three categories [16]:

1. Linear theories
2. Nonlinear theories based on truncation schemes
3. Nonlinear theories based on a small-strain approximation

**Linear theories** Rotating beam analyses were first derived in a linear form for the uncoupled cases of pure bending by Yntema [17], and pure torsion by

Wood and Perring [18]. The case of combined bending in two directions was treated by Mendelson [19]. A few factors were neglected in those studies, such as the variable stiffness and mass distribution along the blade, the coupling due to centrifugal loads, or the non-coincidence of the elastic axis and tensile axis. The elastic axis is classically defined as the spanwise locus of points where a transverse load produces only bending (no torsion) of the rotor blade. The tensile axis is defined as the spanwise locus of the centroids of the cross-sectional areas effective in carrying tension. Houbolt and Brooks [20] extended the previous studies to derive the partial differential equations of motion for the coupled bending and torsion of twisted, nonuniform beams. No assumption regarding the coincidence of elastic axis and tensile axis was made. In addition, only linear terms were retained. This work formed the initial basis of helicopter rotor blade analysis.

**Nonlinear theories based on truncation schemes** As the significance of nonlinear effects in the aeroelasticity of rotary-wings was discovered, nonlinear equations of motion for combined flap bending, lead-lag bending, torsion, and extension of twisted, nonuniform rotor blades were derived independently by several researchers. Some well-known examples are the work by Hodges and Dowell [21], Kaza and Kvaternik [22], and Rosen and Friedmann [23]. These theories relied on the restriction that bending deflections normalized by the rotor radius and angles of twist were small with respect to unity. The equations of motion were derived assuming a displacement field and the rotor blades

were discretized into beam elements for which the cross-sectional constants were calculated at the elastic axis. Ordering schemes were defined in which each dimensionless quantity was related to powers of a small parameter  $\epsilon$ , representative of the normalized flap bending deflection. Subsequently, the equations were truncated to retain terms up to second or third order. Due to the choice of ordering scheme, these analyses were only valid for rotor blades experiencing moderate bending displacements, on the order of 15% of the rotor radius, and small angles of twist up to 10 degrees.

**Nonlinear theories based on a small-strain approximation** In the mid 1980s, studies addressing the arbitrarily large displacements and rotations of rotor blades were derived. These theories relied on a geometrically exact beam theory, initially developed by Hodges [24]. They invoked a small strain assumption but had no limitation regarding the rotations caused by deformation. They were also generally more compact than the analyses relying on truncation schemes, because it was not necessary to expand the transcendental functions inherent to nonlinear beam analyses [16].

After 1985, research efforts were focused on modeling rotor blades with anisotropic material properties [25], as well as deriving analyses that did not rely on an assumed displacement field or warping functions [26, 27]. An extensive review of modern beam analyses for rotorcraft applications was presented by Hodges [16].

### 1.2.1.2 Rotor aerodynamic model

The role of the rotor aerodynamic model is to compute the airloads. The airloads (aerodynamic forces and moments) are caused by the relative motion of the blades with respect to air, and depend upon the blade airfoil shape and angle of attack, the incident air velocities, and the rate of blade elastic deformation. In addition, the magnitude of the airloads depends strongly on the location along the blade span, typically increasing parabolically from the blade root to the tip. As a result, airloads are classically computed for a given blade section, following a two-dimensional aerodynamics approach, and then integrated over the blade span. In addition, correction factors are included to take into account three-dimensional effects. This method is referred to as *2-D section theory* or *strip theory*.

When computing the angle of attack at a particular blade station, the air velocity induced by the generation of lift must be known. Several theories aimed at estimating this induced velocity, called inflow, have been proposed. The simplest approach, attributed to Rankine [28], and further developed by Froude [29] and Glauert [30], is known as the Rankine-Froude momentum theory. This method assumes that the rotor can be idealized as an infinitesimally thin actuator disk, imparting a uniform velocity to the mass of air passing through a control volume surrounding the rotor. While this method is useful for a global analysis of the rotor, it does not distinguish between rotor configurations. In particular, the total number of blades or the blade geometry are not taken into account. In addition, this method does not predict

a variation of inflow along the blade spanwise direction. Another approach, known as the blade element theory (BET) and suggested by Drzewiecki [31], treats each blade section as a 2-D airfoil producing aerodynamic forces and moments. However, the interaction between two adjacent blade sections is ignored. Rotor performance can be obtained by integrating the airloads over the rotor blade length. The principles of the momentum theory and the blade element theory were combined by Gustafson and Gessow [32], to form the hybrid blade element momentum theory (BEMT). Such an approach invokes the equivalence between circulation and momentum theories of lift, and results in a nonlinear spanwise variation of inflow. The BEMT was later refined to include the influence of the vortical wake, the presence of multiple blades, and three-dimensional effects such as root and tip losses [33].

Additionally, techniques for modeling the unsteady airloads acting on an airfoil were investigated by several researchers. The classical unsteady aerodynamic theories of Wagner [34] in the time domain, and of Theodorsen [35] in the frequency domain, form the roots of unsteady rotor analyses. In these theories, airfoils experiencing pitching and plunging harmonic oscillations in a flow of steady velocity are considered. Due to the oscillations, vorticity is shed to the wake, which changes the downwash velocity over the airfoil, and therefore affects the airloads. Theodorsen's approach involves the use of a complex valued transfer function between the forcing (angle of attack) and the aerodynamic response. This theory, initially derived for fixed-wing analysis, was extended by Loewy [36] to rotating blades, by including the effect of

the returning wake shed by blades in previous revolutions.

The blade element momentum theory along with Loewy's unsteady aerodynamic theory form the basis of most modern analyses of helicopter rotor aerodynamics. Efforts to improve these theories involved the refinement of rotor wake modeling, for more accurate predictions of the rotor inflow. In particular, theories based on a prescribed wake geometry [37], or on a free wake geometry [38, 39] have been developed. Nowadays, lifting-line theory based methods are replaced by computation fluid dynamics (CFD) methods for calculating rotorcraft flows. A review of the most modern theories can be found in Datta *et al.* [40] and Leishman [41].

All the analyses described above were developed with the purpose of providing a comprehensive set of tools to support the design of helicopter rotors. In particular, the derivations were gradually extended to cover a wide variety of rotor blade designs, operating in various conditions. The case of an extremely flexible rotor with negligible structural stiffness, operating in hover, is one subset which should be accurately modeled by the most modern theories. However, it has received limited attention in the past. The objective of this dissertation is to fill this gap. In order to develop a fundamental understanding of the physical effects governing the dynamics of an extremely flexible rotor blade, an analysis is systematically derived, starting from first principles.

In the next section, the few analyses tailored to rotor blades with negligible structural stiffness are reviewed.

### 1.2.1.3 Aeroelastic analyses for rotor blades with negligible structural stiffness

The aeroelastic behavior of a rotor blade with extremely low structural stiffness is dominated by centrifugal forces. In particular, centrifugal forces stiffen the blade in the torsional degree of freedom in two ways: the tennis racquet effect and the trapeze effect. The tennis racquet effect, also known as the propeller moment, arises due to the tendency of the centrifugal forces to rotate the rotor blade to flat pitch. The trapeze effect, or bifilar effect, arises from the tendency of the centrifugal forces to untwist the blade. As a result of the trapeze effect, the torsional rigidity of the rotor blade is increased, varying nonlinearly with the twist angle. In conventional rotor blades, the propeller moment is dominant. But in the case of a blade with high torsional flexibility, the elastic twist angles can be large and the trapeze effect becomes important. The modeling of the trapeze effect is essential to obtain accurate predictions of blade deformation and stability boundaries. However, it has always been neglected in analyses focused on extremely flexible rotor blades.

Winston [11, 12] developed one of the first analyses of an extremely flexible rotor blade. He studied a blade consisting of a thin non-porous fabric sheet attached to two steel rods that formed the leading and trailing edges. A mass with an aerodynamic stabilizer was attached to the blade tip. This research was focused primarily on the planform and tip mass distribution required to prevent luffing instability. Using a method derived by Nielsen [42] for the design of non-luffing rotor blade, Winston showed that stable operation was

achievable by appropriate choice of the mass and chordwise position of the tip body. The study also included an aeroelastic analysis of the factors involved in the static divergence and flutter of extremely flexible rotors. The model considered the coupled first flapwise bending mode and first torsional mode of an extremely flexible blade, both assumed to be linear functions of the radial location. In addition, the analysis assumed that for a large, slowly turning rotor, frequencies of oscillations were so low that a quasi-steady aerodynamic model was valid. The key result was that aeroelastic stability was found to be independent of the rotational speed. Furthermore, it was shown that the rotor was free from flutter and divergence under the condition that the elastic axis and center of gravity were located forward of the aerodynamic center. Similar conclusions were obtained in other analytical studies by Goldman [9] and Roeseler [43]. However, these conclusions contrast with the classical criterion for aeroelastic stability of a conventional rigid rotor blade [44], which only requires the blade to be mass balanced in such a way that the center of gravity is ahead of the aerodynamic center, and where the location of the elastic axis is of no importance. These results also contradict the experiments performed by Sicard and Sirohi [45]. Specifically, these experiments indicated that an extremely flexible rotor blade with coincident shear center and aerodynamic center is unstable even with the center of gravity located forward of the aerodynamic center. In addition, the rotor stability was observed to depend on the rotational speed as well as the collective pitch angle. These discrepancies between analyses available in the literature and recent experimental findings

confirm that a linear analysis cannot capture the aeroelastic behavior of an extremely flexible rotor. The nonlinear extension-torsion coupling terms, arising in the equations of motion from the centrifugal effects, must be included.

Finally, to cover the full range of operation of a variable-diameter rotor blade, the effect of a change in rotor diameter on the performance, loads and dynamic stability must be systematically investigated. The effect of changing rotor diameter has only been reported in the literature with respect to performance metrics [46, 47, 48, 49] and not stability. Particularly, Bowen-Davies and Chopra [49] evaluated the performance gain resulting from a change in rotor radius for a UH-60A Black Hawk helicopter. Using the aeromechanics code UMARC [50], they showed that, for a representative gross weight, no more than 10% radius change yielded continued performance benefits and thereafter performance degraded. However the effect of rotor diameter change on rotor stability has not been explored to date.

### **1.2.2 Measurement of blade deformation**

The experimental measurement of rotor blade deformation is a very challenging task. The conventional method using strain gages bonded to the blade surface at discrete spanwise locations is unsuitable for multiple reasons. First, this technique requires extensive on-blade instrumentation and wiring, as well as an electric slip ring, which are not feasible at the scale of the rotor analyzed in this dissertation. In addition, because of limited spatial resolution, this technique is incapable of showing strain gradients and can miss strain hot

spots. In the case where the shear moduli of the blade material and the strain gage are on the same order of magnitude, the presence of the installed gage may significantly alter the specimen strain distribution. Finally, measurement of extension, flap and lead-lag bending and torsion requires four separate sets of strain gage installations, one for each of the measured quantities.

Due to these limitations, optical techniques have been considered to measure the deformation of the flexible rotor blade. These techniques are advantageous, as they are able to generate full-field deformations [51], without instrumenting the structure and in a non-contact fashion. Interest in optical deformation measurement techniques has been rising since the beginning of the 1990s. However, a limited number of studies exist on their application to the measurement of rotating blade and deformation. Fleming *et al.* [52, 53] demonstrated the capability of Projection Moiré Interferometry (PMI) to measure azimuthal variations of rotor blade deflections at different advance ratios, in or out of fuselage influence. This study was extended to the test of a model-scale rotor in the NASA Langley 14×22 feet subsonic wind tunnel hover facility [54]. Olson *et al.* [55] and Abrego *et al.* [56] used stereo photogrammetry to measure the deformation of full-scale UH-60A helicopter blades at various advance ratios, thrust coefficients and drive shaft angles. The experiment used reflective circular targets attached at specific locations on the blade and produced results that closely matched the design parameters. Sirohi and Lawson [57] investigated the application of stereoscopic digital image correlation (DIC) to the measurement of flap bending and torsion of rotating micro-helicopter

blades (diameters of 61 and 99 cm). While the DIC technique was successfully validated in the nonrotating frame by measuring the deformation of a vibrating cantilever beam, no validation was performed in the rotating frame. However, the DIC technique was found to be very attractive as it allows for three-dimensional contours as well as nonplanar displacements and strains. In the DIC technique, a high contrast random speckle pattern is painted on the rotor blades. Cross-correlation of the images at different loading conditions, in conjunction with photogrammetry, is used to calculate three-dimensional displacements of points on the surface [58].

### 1.3 Present Approach

The objective of this dissertation is to design, analyze, fabricate and test an extremely flexible, variable-diameter rotor.

An aeroelastic analysis specifically tailored to rotor blades with negligible structural stiffness is developed. The derivation relies on the extended Hamilton's principle and is adapted from the analysis by Hodges and Dowell [21], which includes the trapeze effect. In particular, the ordering scheme is modified to reflect the large magnitude of twist angles observed during experiments [45]. The blades are discretized into second-order isotropic Euler-Bernoulli beam elements, with extension, flap, lag and torsion degrees of freedom. In addition, energies due to the tip mass are included in the model. The work done by airloads is calculated using a 2-D section approach and added to the Hamiltonian. Unsteady aerodynamic terms are included based on

Theodorsen’s theory [35]. The inflow ratio at each blade station is calculated using BEMT. Lift, drag and moment coefficients are extracted from tables of experimental data collected at a low Reynolds number ( $Re \sim 16,160$ ) [59, 60]. The nonlinear equations of motion are solved using the finite element method.

Additionally, rotor blade deformations are measured using three-dimensional DIC. This technique is first validated in the rotating frame by correlating DIC measurements on a stiff rotor blade of known geometry with measurements made by two other laser sensors. Then, DIC is used to measure the deformation of extremely flexible rotors spinning at 1200 RPM.

The measured deformations are compared to analytical predictions. Upon validation, the model is used to explore the aeroelastic stability of the extremely flexible rotor blades. The stability analysis is conducted in the frequency domain by conducting an eigenanalysis of the state matrix associated with the perturbed equations of motion. The effect of control inputs and design parameters on the stability boundaries is explored. In particular, the influence of the rotational speed, the collective pitch and the chordwise position of the tip mass on the blade stability is studied. Finally, the effect of a change in rotor diameter on the stability margin is also investigated.

## 1.4 Contribution of the Present Research

This research involves parallel experimental and analytical studies of the aeroelastic behavior of a hovering rotor with extremely flexible blades. The analysis was systematically developed from first principles. New experimental

techniques were developed and used to validate the analysis at every stage. The validated analysis can be used to design variable diameter rotors with flexible blades and to predict their stability boundaries. The key contributions of this research can be grouped under two categories:

- **Analytical:** A detailed understanding of the aeroelastic behavior of a hovering rotor with extremely flexible blades.
- **Experimental:** A novel technique to measure the three-dimensional, whole-field deformation of rotating blades.

Specific contributions are listed below:

**Analytical:**

1. An aeroelastic analysis tailored towards rotor blades with negligible structural stiffness. The structural part of the analysis includes coupled axial elongation, lead-lag bending, flap bending and torsion degrees of freedom. Terms that are important for blades experiencing large twist angles are retained; these terms have typically been neglected in similar analyses of conventional rotor blades. The aerodynamic part of the analysis includes unsteady terms based on two-dimensional strip theory.
2. A systematic analytical investigation of the axial displacement, restoring moment, centrifugal stiffening and torsional frequency associated with the trapeze (or bifilar) effect. Unlike the linear centrifugal stiffening due to the propeller moment, which adds up to the blade structural stiffness,

the centrifugal stiffening due to the trapeze effect is nonlinear, because it depends on the deformed state of the blade.

3. A finite element based numerical model to solve the aeroelastic equations of motion. The model predicts the blade trim condition and uses the  $p$ - $k$  method to calculate blade stability boundaries.
4. Identification of the stability boundaries of a hovering rotor with extremely flexible blades. The coupled modes responsible for the instability are identified. The flutter boundaries are shown to depend on collective pitch, rotor speed, chordwise mass distribution and rotor diameter.

### **Experimental:**

1. Design of a flexible rotor blade featuring a tip body attached at an index angle relative to the blade chord. A rotor with these blades has the same hovering efficiency and maximum thrust as a rotor with rigid blades of the same planform and solidity.
2. A non-contact technique to measure three-dimensional, whole-field deformation of a rotating blade. This technique is based on Digital Image Correlation and does not require any on-blade instrumentation. Blade deformation measurements with a spatial resolution of 1.04% rotor radius and a theoretical accuracy of 15  $\mu\text{m}$  are demonstrated.

## 1.5 Organization of the Dissertation

Chapter 1 presents the extremely flexible, variable-diameter rotor concept and motivates its development for micro-helicopter applications. In addition, Chapter 1 surveys the evolution and state of the art in rotor blade analyses, as well as rotor blade deformation measurements. The approach of the present research is discussed and the key contributions are formulated.

Chapter 2 shows the derivation of the equations of motion for a rotor blade with negligible structural stiffness. In particular, the kinematics and the mechanics of the trapeze effect are systematically explored. In addition, the expressions for the rotor blade kinetic and potential energies, as well as the work done by the aerodynamic loads are derived.

Chapter 3 presents the numerical model implemented to solve the flexible blade equations of motion. This model is used to compute the trim solution as well as the blade stability boundaries. A flow chart of the computer program is shown.

Chapter 4 describes the experimental procedures. The design and fabrication of the rotor blades are presented. In addition, the experimental setup, including the hover test stand and the equipment needed for the measurement of blade deformation by DIC are described. The procedure for the measurement using DIC is documented in detail.

Chapter 5 discusses the results of the experimental testing of flexible rotor blades. It also presents a validation of the DIC technique for the mea-

surement of rotor blade deformation, as well as a validation of the analytical model derived in this dissertation. In addition, the analytical model is used to investigate the aeroelastic behavior of a flexible rotor, including the trim state, the stability boundaries and the effect of a change in rotor diameter.

Finally, Chapter 6 states the key conclusions of the present research along with recommendations for future work.

# Chapter 2

## Analytical Study

This chapter presents the derivation of the nonlinear coupled equations of motion of a rotor blade with negligible structural stiffness. The general procedure, based on the extended Hamilton's principle, is introduced in § 2.1. Coordinate systems are defined in § 2.2, with respect to the undeformed and deformed positions of the blade. Blade displacement variables are introduced in § 2.3. An ordering scheme is defined in § 2.4 to eliminate higher-order terms in the Hamiltonian. A structural model, based on engineering beam theory, is derived in § 2.5 to determine the kinetic energy and strain energy of the rotor blade as well as the tip mass. The rotor blades are assumed to be hingeless, slender, with no structural twist and uniform. No assumption is made regarding the symmetry of the cross-section relative to any axis, and pre-cone angles are not included. The equations are derived for arbitrarily non-coincident elastic center, mass centroid, and area centroid. The blade deformation is assumed to consist of extensional, flap bending, lead-lag bending and twist degrees of freedom. An aerodynamic model including unsteady and quasi-steady forcing terms is presented in § 2.6. The unsteady aerodynamic model is based on strip theory in conjunction with Theodorsen's theory.

## 2.1 General Procedure

The derivation of the equations of motion follows an energy approach and relies on the extended Hamilton's principle (EHP), written for  $N$  degrees of freedom as

if  $\delta q_i |_{t_1} = \delta q_i |_{t_2} = 0$ , ( $i = 1, \dots, N$ ) then

$$\int_{t_1}^{t_2} (\delta T - \delta V + \delta W_{nc}) dt = 0 \quad (2.1)$$

where  $\delta q_i$  are generalized coordinates,  $\delta T$  and  $\delta V$  are the variations of kinetic and potential energies respectively, and  $\delta W_{nc}$  is the virtual work done by non-conservative forces. Including the kinetic and potential energies associated with the tip mass, and expanding the potential energy of the blade into the sum of the strain energy  $\delta U$ , the gravitational potential energy  $\delta V_g$  and the energy contained in torsional springs at the root of the blade  $\delta V_{sp}$ , Eq. (2.1) becomes

$$\int_{t_1}^{t_2} \left[ (\delta T - \delta U - \delta V_g - \delta V_{sp} + \delta W_a)_b + (\delta T - \delta V_g)_m \right] dt = 0 \quad (2.2)$$

The subscripts  $( )_b$  and  $( )_m$  indicate energies of the blade airfoil and the tip mass respectively, and  $\delta W_a$  accounts for the virtual work done by aerodynamic loads. From this equation, the steady-state deformation and the stability boundaries of the rotor blade are obtained, as described hereafter.

### 2.1.1 Trim solution

The trim state of the rotor, also called steady-state, is defined by the blade deformation variables  $q_i$ 's and the inflow ratios  $\lambda_i$ 's required to produce

a nominal thrust in hover. It is the solution of the steady-state equilibrium equations, which are obtained by retaining the time-invariant terms in Eq. (2.2) and considering the work done by quasi-steady aerodynamic forces only. The equation of motion governing the trim solution is

$$(\delta T_0 - \delta U - \delta V_g - \delta V_{sp} + \delta W_{aQS})_b + (\delta T_0 - \delta V_g)_m = 0 \quad (2.3)$$

Note that in the absence of aerodynamic forces, Eq. (2.3) reduces to

$$\begin{aligned} (\delta T_0 - \delta U - \delta V_g - \delta V_{sp})_b + (\delta T_0 - \delta V_g)_m &= 0 \\ \Leftrightarrow \delta H &= 0 \end{aligned} \quad (2.4)$$

where  $H$  is the Hamiltonian. Equation. (2.4) indicates that the Hamiltonian is conserved, which is a typical property of conservative gyroscopic (or non-natural) systems.

### 2.1.2 Perturbed equations of motion

Once the trim condition is known, small perturbations are applied to the state variables, as follows

$$\begin{aligned} \mathbf{q} &= \mathbf{q}_0 + \Delta \mathbf{q} \\ \boldsymbol{\lambda} &= \boldsymbol{\lambda}_0 + \Delta \boldsymbol{\lambda} \end{aligned} \quad (2.5)$$

where the subscript  $( )_0$  denotes the trimmed values. In addition, the variations of the perturbed state variables are

$$\begin{aligned} \delta \mathbf{q} &= \delta \mathbf{q}_0 + \delta \Delta \mathbf{q} \\ \delta \boldsymbol{\lambda} &= \delta \boldsymbol{\lambda}_0 + \delta \Delta \boldsymbol{\lambda} \end{aligned} \quad (2.6)$$

Note that  $\delta(\ )$  refers to the variations, whereas  $\Delta(\ )$  refers to the perturbation values. Since  $\mathbf{q}_0$  and  $\boldsymbol{\lambda}_0$  are known, we must have

$$\begin{aligned}\delta\mathbf{q}_0 &= \mathbf{0} \\ \delta\boldsymbol{\lambda}_0 &= \mathbf{0}\end{aligned}\tag{2.7}$$

Substitution of Eq. (2.5) and (2.6) into Eq. (2.1) leads to

$$\int_{t_1}^{t_2} (\delta T - \delta V + \delta W_a)_0 dt + \int_{t_1}^{t_2} (\delta\Delta T - \delta\Delta V + \delta\Delta W_a) dt = 0\tag{2.8}$$

where for instance,  $\delta T = \delta T(\mathbf{q}_0, \delta\Delta\mathbf{q})$  and  $\delta\Delta T = \delta\Delta T(\Delta\mathbf{q}, \delta\Delta\mathbf{q})$ . The first integral in Eq. (2.8) satisfies the trim equation (Eq. (2.2)), hence it equals zero. Therefore, the equation describing the perturbed motion of the rotor blade about the trim position is

$$\int_{t_1}^{t_2} (\delta\Delta T - \delta\Delta V + \delta\Delta W_a) dt = 0\tag{2.9}$$

Since the perturbations are small, it is appropriate to linearize nonlinear terms in Eq. (2.9) about the trim position using a first-order Taylor series approximation. In this process, the trimmed velocities and accelerations are assumed to be equal to zero.

Upon linearization, Eq. (2.9) can be written in matrix form as

$$\delta\Delta\mathbf{q}^T (\mathbf{M}\Delta\ddot{\mathbf{q}} + \mathbf{G}\Delta\dot{\mathbf{q}} + \mathbf{K}\Delta\mathbf{q}) = \delta\Delta\mathbf{q}^T \Delta\mathbf{F}\tag{2.10}$$

The matrices  $\mathbf{M}$ ,  $\mathbf{G}$  and  $\mathbf{K}$  denote respectively the mass, gyroscopic and stiffness matrices, and are obtained from the kinetic and potential energies of the

rotor blade with tip mass. Consequently,  $\mathbf{M}$  and  $\mathbf{K}$  are symmetric, positive definite matrices and  $\mathbf{G}$  is skew-symmetric.  $\Delta\mathbf{F}$  is the perturbed force vector obtained from the non-conservative work done by the aerodynamic forces and moments, and is a function of the perturbed generalized displacements, velocities and accelerations, as well as the perturbed inflow ratio. Assuming the effect on the aerodynamic loads of a small perturbation of the inflow negligible,  $\Delta\mathbf{F}$  can be decomposed as

$$\begin{aligned}\Delta\mathbf{F} &= \frac{\partial\Delta\mathbf{F}}{\partial\mathbf{q}}\Delta\mathbf{q} + \frac{\partial\Delta\mathbf{F}}{\partial\dot{\mathbf{q}}}\Delta\dot{\mathbf{q}} + \frac{\partial\Delta\mathbf{F}}{\partial\ddot{\mathbf{q}}}\Delta\ddot{\mathbf{q}} \\ &= \mathbf{K}^a\Delta\mathbf{q} + \mathbf{C}^a\Delta\dot{\mathbf{q}} + \mathbf{M}^a\Delta\ddot{\mathbf{q}}\end{aligned}\quad (2.11)$$

Moving the terms in Eq. (2.11) to the left hand side of Eq. (2.10) and invoking the arbitrariness of  $\delta\Delta\mathbf{q}^T$ , we obtain

$$(\mathbf{M} - \mathbf{M}^a)\Delta\ddot{\mathbf{q}} + (\mathbf{G} - \mathbf{C}^a)\Delta\dot{\mathbf{q}} + (\mathbf{K} - \mathbf{K}^a)\Delta\mathbf{q} = \mathbf{0}\quad (2.12)$$

which is the homogeneous system of equations for small perturbations about the rotor blade trim state. Note that due to the non-conservative aerodynamic forces and moments, the resulting mass and stiffness matrices are no longer symmetric.

### 2.1.3 Stability analysis

The stability analysis is conducted in the frequency domain. First, Eq.(2.12) is rewritten in state-space form, as follows

$$\begin{Bmatrix} \Delta\dot{\mathbf{q}} \\ \Delta\ddot{\mathbf{q}} \end{Bmatrix} = \mathbf{A} \begin{Bmatrix} \Delta\mathbf{q} \\ \Delta\dot{\mathbf{q}} \end{Bmatrix}\quad (2.13)$$

where  $\mathbf{A}$  is the state matrix, defined as

$$\mathbf{A} = \begin{bmatrix} \mathbf{0} & \mathbf{I} \\ -(\mathbf{M} - \mathbf{M}^a)^{-1}(\mathbf{K} - \mathbf{K}^a) & -(\mathbf{M} - \mathbf{M}^a)^{-1}(\mathbf{G} - \mathbf{C}^a) \end{bmatrix} \quad (2.14)$$

Then, the rotor blade stability boundaries are obtained by an eigenanalysis of the state matrix.

The next section presents the coordinate systems and displacement variables used in the present analysis.

## 2.2 Blade Coordinate Systems

Four coordinate systems (shown in Fig. 2.1) are used to derive the blade equations of motion.

1.  $\{X_I, Y_I, Z_I\}$  is a Newtonian coordinate system, with the positive  $Z_I$ -axis directed upward. Unit vectors  $(\mathbf{i}_{X_I}, \mathbf{j}_{Y_I}, \mathbf{k}_{Z_I})$  are associated to this system.
2.  $\{X, Y, Z\}$  is fixed to the rotor hub, with its origin at the center of the hub, and unit vectors  $(\mathbf{i}_X, \mathbf{j}_Y, \mathbf{k}_Z)$ . It rotates about the positive  $Z_I$ -axis at the constant angular velocity  $\Omega$ . The  $X$ -axis is coincident with the elastic axis of the undeformed blade. This particular axis will be defined in § 2.5.4 of this dissertation.
3.  $\{x_0, y_0, z_0\}$ , with unit vectors  $(\mathbf{i}_0, \mathbf{j}_0, \mathbf{k}_0)$ , is centered on the deformed elastic axis and results from the translations  $u$ ,  $v$  and  $w$  of the coordinate system  $\{X, Y, Z\}$  along the  $X$ -,  $Y$ - and  $Z$ - axes respectively. The

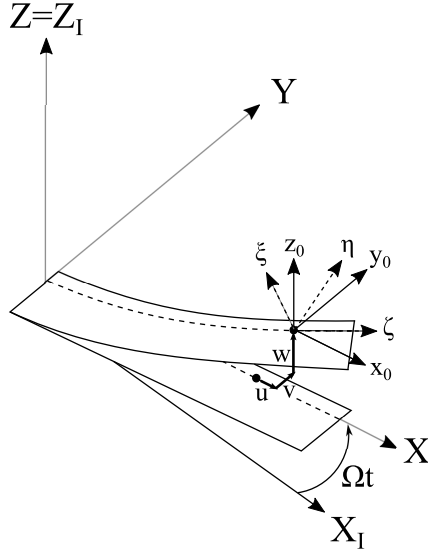


Figure 2.1: Coordinate systems

translation  $u$  is called the *axial displacement*; the translations  $v$  and  $w$  are respectively the *flap bending* and *lead-lag bending* displacements.

4.  $\{\zeta, \eta, \xi\}$  is attached to the deformed blade and is centered on the deformed elastic axis. The  $\eta$ - and  $\xi$ -axes are coplanar with the deformed blade cross-section, and  $\zeta$  is tangent to the deformed elastic axis. The unit vectors defining this coordinate system are  $(\mathbf{i}_\zeta, \mathbf{j}_\eta, \mathbf{k}_\xi)$ . Bending displacements along the  $\eta$  and  $\xi$  axis are called *chordwise bending* ( $v^*$ ) and *flatwise bending* ( $w^*$ ) respectively.

One way to relate the  $\{\zeta, \eta, \xi\}$  coordinate system to the  $\{x_0, y_0, z_0\}$  coordinate system is to use Rodriguez parameters [61]. Another way, employed for the present derivation, is to use successive rotations of the  $\{x_0, y_0, z_0\}$  coordinate system about Euler angles (see Fig. 2.2). In this case,  $\{\zeta, \eta, \xi\}$  can be related

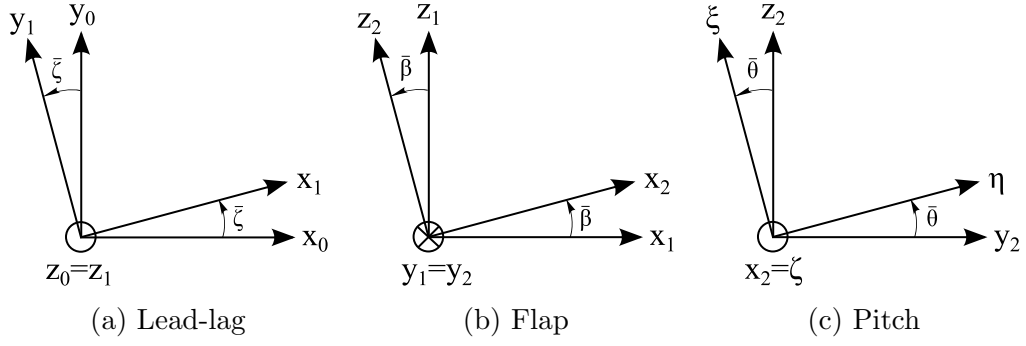


Figure 2.2: Euler angles for a lag-flap-pitch sequence

to  $\{x_0, y_0, z_0\}$  by means of a transformation matrix  $\mathbf{T}$ , defined such that

$$\begin{Bmatrix} i_\zeta \\ j_\eta \\ k_\xi \end{Bmatrix} = \mathbf{T} \begin{Bmatrix} i_0 \\ j_0 \\ k_0 \end{Bmatrix} \quad (2.15)$$

The matrix  $\mathbf{T}$  can be written as the product of three matrices corresponding to each Euler rotation, as follows

$$\begin{aligned} \mathbf{T} &= \begin{bmatrix} 1 & 0 & 0 \\ 0 & \cos \bar{\theta} & \sin \bar{\theta} \\ 0 & -\sin \bar{\theta} & \cos \bar{\theta} \end{bmatrix} \times \begin{bmatrix} \cos \bar{\beta} & 0 & \sin \bar{\beta} \\ 0 & 1 & 0 \\ -\sin \bar{\beta} & 0 & \cos \bar{\beta} \end{bmatrix} \times \begin{bmatrix} \cos \bar{\zeta} & \sin \bar{\zeta} & 0 \\ -\sin \bar{\zeta} & \cos \bar{\zeta} & 0 \\ 0 & 0 & 1 \end{bmatrix} \\ &= \begin{bmatrix} \cos \bar{\beta} \cos \bar{\zeta} & \sin \bar{\zeta} \cos \bar{\beta} & \sin \bar{\beta} \\ -\sin \bar{\zeta} \cos \bar{\theta} - \cos \bar{\zeta} \sin \bar{\beta} \sin \bar{\theta} & \cos \bar{\zeta} \cos \bar{\theta} - \sin \bar{\zeta} \sin \bar{\beta} \sin \bar{\theta} & \cos \bar{\beta} \sin \bar{\theta} \\ -\cos \bar{\zeta} \sin \bar{\beta} \cos \bar{\theta} + \sin \bar{\zeta} \sin \bar{\theta} & -\cos \bar{\zeta} \sin \bar{\theta} - \sin \bar{\zeta} \sin \bar{\beta} \cos \bar{\theta} & \cos \bar{\beta} \cos \bar{\theta} \end{bmatrix} \end{aligned} \quad (2.16)$$

where  $\bar{\zeta}$ ,  $\bar{\beta}$  and  $\bar{\theta}$  are the Euler angles.

Singularities can arise when two of the axes about which rotations occur are coincident [62]. Therefore, instead of Euler angles, modified Euler angles are used where the axes do not approach one another for rotations in the neighborhood of zero.

Additionally, the order of the rotations shown in Fig. 2.2 corresponds to a “lag-flap-pitch” blade motion sequence. This combination was chosen arbitrarily among a total of six possible sequences. In the case of an articulated rotor blade, the order of the successive rotations is dictated by the kinematics of the blade hinges. But for a hingeless blade, as in the present study, no physical justification supports the choice of rotation sequence. In fact, it can be shown that the entire formulation of the equations of motion is independent of the sequence of the three rotations [63]. Differences in the equations from one sequence to another are in form only. They vanish after adequate changes of variable.

### 2.3 Blade Displacement Variables

Effectively, the deformed position of the blade can be fully described using six variables:

- three elastic displacements  $u$ ,  $v$  and  $w$ , representing the extensional, lead-lag bending and flap bending deflections of points located on the elastic axis. These deflections are defined to be positive along the  $X$ -,  $Y$ - and  $Z$ - axes respectively.
- three rotations defined by the Euler angles.

However, in the context of an Euler-Bernoulli beam, the beam cross-sections are assumed to remain planar and normal to the beam elastic axis at all times.

Thus, two of the three angles can be eliminated by expressing them in terms of derivatives of the deflection variables, as shown hereafter.

First, consider the position vector of a particle on the deformed elastic axis

$$\mathbf{r} = (x + u) \mathbf{i}_0 + v \mathbf{j}_0 + w \mathbf{k}_0 \quad (2.17)$$

By taking the partial derivative of the position vector  $\mathbf{r}$  with respect to the curvilinear coordinate along the deformed elastic axis  $r$ , we obtain the unit vector tangent to the elastic axis of the deformed blade

$$\frac{\partial \mathbf{r}}{\partial r} = (x + u)^+ \mathbf{i}_0 + v^+ \mathbf{j}_0 + w^+ \mathbf{k}_0 \quad (2.18)$$

where  $(\ )^+ = \partial/\partial r$ . Note that the unit vectors  $(\mathbf{i}_0, \mathbf{j}_0, \mathbf{k}_0)$  are independent of the blade deformation, hence their partial derivative with respect to  $r$  is zero.

In terms of the elements of the transformation matrix, we then have

$$\frac{\partial \mathbf{r}}{\partial r} = \mathbf{i}_\zeta = T_{11} \mathbf{i}_0 + T_{12} \mathbf{j}_0 + T_{13} \mathbf{k}_0 \quad (2.19)$$

Thus, combining Eq. (2.18) and (2.19), we get

$$\begin{cases} T_{11} &= (x + u)^+ \\ T_{12} &= v^+ \\ T_{13} &= w^+ \end{cases} \quad (2.20)$$

Additionally, since  $\mathbf{T}$  is orthonormal, we must have

$$T_{11}^2 + T_{12}^2 + T_{13}^2 = 1 \quad (2.21)$$

and therefore

$$(x + u)^+ = \sqrt{1 - v^{+2} - w^{+2}} \quad (2.22)$$

From Eq. (2.16), (2.20) and (2.22), it can be deduced that

$$\left\{ \begin{array}{l} \sin \bar{\beta} = w^+ \\ \cos \bar{\beta} = \sqrt{1 - w^{+2}} \\ \sin \bar{\zeta} = \frac{v^+}{\sqrt{1 - w^{+2}}} \\ \cos \bar{\zeta} = \frac{\sqrt{1 - v^{+2} - w^{+2}}}{\sqrt{1 - w^{+2}}} \end{array} \right. \quad \begin{array}{l} (2.23a) \\ (2.23b) \\ (2.23c) \\ (2.23d) \end{array}$$

These formulas agree with those derived in [64]. The transformation matrix can now be re-written as a function of the bending deflections and the modified Euler angle  $\bar{\theta}$  as follows

$$\mathbf{T} = \begin{bmatrix} \sqrt{1 - v^{+2} - w^{+2}} \\ -\frac{v^+}{\sqrt{1 - w^{+2}}} \cos \bar{\theta} - \frac{w^+ \sqrt{1 - v^{+2} - w^{+2}}}{\sqrt{1 - w^{+2}}} \sin \bar{\theta} \\ -\frac{w^+ \sqrt{1 - v^{+2} - w^{+2}}}{\sqrt{1 - w^{+2}}} \cos \bar{\theta} + \frac{v^+}{\sqrt{1 - w^{+2}}} \sin \bar{\theta} \\ \frac{v^+}{\sqrt{1 - v^{+2} - w^{+2}}} \cos \bar{\theta} - \frac{v^+ w^+}{\sqrt{1 - w^{+2}}} \sin \bar{\theta} \\ -\frac{v^+}{\sqrt{1 - v^{+2} - w^{+2}}} \sin \bar{\theta} - \frac{v^+ w^+}{\sqrt{1 - w^{+2}}} \cos \bar{\theta} \\ \frac{w^+}{\sqrt{1 - w^{+2}}} \sin \bar{\theta} \\ \frac{w^+}{\sqrt{1 - w^{+2}}} \cos \bar{\theta} \end{bmatrix} \quad (2.24)$$

Note that the transformation matrix at this stage of the derivation is exact. The remaining Euler angle  $\bar{\theta}$  must now be replaced by some measurable quantities, independent of the sequence of rotations. Consequently, the angle of twist  $\phi$  is introduced and defined, in the absence of built-in pre-twist, as

$$\phi^+ = \kappa_1 \quad (2.25)$$

where  $\kappa_1$  is the torsion, or angle of twist per unit length, about the  $x_1$ -axis (see Fig. 2.2 for a definition of  $x_1$ ).  $\kappa_2$  and  $\kappa_3$  are the bending curvatures about the  $x_2$ - and  $x_3$ -axes. These three curvatures may be deduced with the use of Kirchhoff's kinetic analogue, which states that [65]

*“The equations of equilibrium of a thin rod, straight and prismatic when unstressed, and held bent and twisted by forces and couples applied at its ends alone, can be identified with the equations of motion of a heavy rigid body turning about a fixed point.”*

In this context, the two bending curvatures and the torsion are analogous to the three components of the angular velocity of a body, whose rotations are prescribed by the three Euler angles shown in Fig. 2.2. The components of the angular velocity vector are

$$\boldsymbol{\omega} = \dot{\zeta} \mathbf{k}_1 - \dot{\beta} \mathbf{j}_2 + \dot{\theta} \mathbf{i}_\zeta \quad (2.26)$$

Upon projection in the  $\{\zeta, \eta, \xi\}$  coordinate system, the angular velocity vector becomes

$$\boldsymbol{\omega} = \left( \dot{\zeta} \sin \bar{\beta} + \dot{\theta} \right) \mathbf{i}_\zeta + \left( \dot{\zeta} \cos \bar{\beta} \sin \bar{\theta} - \dot{\beta} \cos \bar{\theta} \right) \mathbf{j}_\eta + \left( \dot{\zeta} \cos \bar{\beta} \cos \bar{\theta} + \dot{\beta} \sin \bar{\theta} \right) \mathbf{k}_\xi \quad (2.27)$$

Therefore, using Kirchhoff's analogue and replacing the time derivatives in Eq. (2.27) by spatial derivatives, the torsion and bending curvatures are

$$\left\{ \begin{array}{l} \kappa_1 = \bar{\zeta}^+ \sin \bar{\beta} + \bar{\theta}^+ \\ \kappa_2 = \bar{\zeta}^+ \cos \bar{\beta} \sin \bar{\theta} - \bar{\beta}^+ \cos \bar{\theta} \\ \kappa_3 = \bar{\zeta}^+ \cos \bar{\beta} \cos \bar{\theta} + \bar{\beta}^+ \sin \bar{\theta} \end{array} \right. \quad \begin{array}{l} (2.28a) \\ (2.28b) \\ (2.28c) \end{array}$$

Furthermore,  $\kappa_1$  can be re-written as a function of the blade deflections by deriving an expression for  $\bar{\zeta}^+$  in terms of  $v$ ,  $w$  and their derivatives. This expression is obtained by differentiating Eq. (2.23c) with respect to  $r$ . The result of this operation is

$$\bar{\zeta}^+ = \frac{v^{++}}{\sqrt{1-v^{+2}-w^{+2}}} + \frac{v^+w^+w^{++}}{(1-w^{+2})\sqrt{1-v^{+2}-w^{+2}}} \quad (2.29)$$

Finally, combining Eq. (2.23a), (2.25) and (2.29) into (2.28a), the partial derivative of the third Euler angle with respect to the curvilinear coordinate  $r$  is

$$\bar{\theta}^+ = \phi^+ - \frac{w^+}{\sqrt{1-v^{+2}-w^{+2}}} \left( v^{++} + \frac{v^+w^+w^{++}}{1-w^{+2}} \right) \quad (2.30)$$

Upon integration in  $r$ , we get

$$\bar{\theta} = \theta_0 + \phi - \int_0^r \frac{w^+}{\sqrt{1-v^{+2}-w^{+2}}} \left( v^{++} + \frac{v^+w^+w^{++}}{1-w^{+2}} \right) dr \quad (2.31)$$

where  $\theta_0 = \phi|_{r=0}$  is defined as the *root pitch angle*. Note that Eq. (2.31) is also exact.

Finally, we can relate the spatial derivative in  $r$  denoted by  $( )^+$  to the one in  $x$  denoted by  $( )'$ , according to the following chain rule

$$( )' = \frac{\partial( )}{\partial x} = \frac{\partial( )}{\partial r} \frac{\partial r}{\partial x} = \frac{\partial( )}{\partial r} r' \quad (2.32)$$

in which  $r'$  is obtained by differentiating Eq. (2.17) with respect to  $x$ . This operation yields

$$r' = \sqrt{(1 + u')^2 + v'^2 + w'^2} \quad (2.33)$$

Recall also the expression for the extensional strain, in the Green-Lagrangian sense

$$\epsilon_{xx} = u' + \frac{1}{2} (u'^2 + v'^2 + w'^2) \quad (2.34)$$

Comparing Eq. (2.33) and (2.34), we can write

$$r'^2 = 1 + 2\epsilon_{xx} \quad (2.35)$$

Plugging this last result into Eq (2.32), we obtain

$$(\ )' = \sqrt{1 + 2\epsilon_{xx}} (\ )^+ \quad (2.36)$$

Finally, for small strain assumptions, Eq. (2.36) implies that  $(\ )^+ = (\ )'$ , and

$$\bar{\theta} = \theta_0 + \phi - \int_0^x \frac{w'}{\sqrt{1 - v'^2 - w'^2}} \left( v'' + \frac{v'w'w''}{1 - w'^2} \right) d\chi \quad (2.37)$$

For conciseness, we define the *elastic pitch angle*  $\theta$  as

$$\theta = \phi - \int_0^x \frac{w'}{\sqrt{1 - v'^2 - w'^2}} \left( v'' + \frac{v'w'w''}{1 - w'^2} \right) d\chi \quad (2.38)$$

This angle includes both a contribution from the elastic twist deformation  $\phi$  and a kinematic integral component that depends on the derivatives of the bending deflections. Note that an accurate expression for the angle  $\theta$  is important, as it affects the blade sectional angle of incidence, which drives the aerodynamics loads.

The elastic pitch angle  $\theta$  defined above, along with the three elastic displacements  $u$ ,  $v$  and  $w$  constitute the set of unknown variables in terms of which the equations of motion are derived. The following section introduces the ordering scheme and the truncation rules adopted in the present analysis.

## 2.4 Ordering Scheme

The exact derivation of the EHP, using the displacements  $u$ ,  $v$  and  $w$ , and the elastic pitch angle  $\theta$  as variables, leads to an extremely large amount of algebra if all the terms in the equations are to be retained. To circumvent this difficulty, the equations in the present analysis are truncated to second-order accuracy. A set of rules must be followed to obtain a consistent truncation scheme. Specifically, the truncation of terms should not destroy the self-adjoint property of the structural and inertial operators. In practice, the mass and stiffness matrices must remain symmetric and the gyroscopic matrix must remain anti-symmetric after the truncation. In addition, when combining kinetic and potential energies in the Hamiltonian, the relative order of magnitude of inertial terms with respect to structural terms must be studied and an appropriate ordering scheme must be chosen such that all physically significant terms are retained.

Along the lines of previous studies [21, 22, 50], an ordering scheme is defined where each physical quantity is compared to a small parameter  $\epsilon$ , on the order of the normalized flap bending deflection  $w/R$ . The ordering scheme is summarized in Table 2.1. Note that this scheme differs from the scheme em-

Table 2.1: Ordering scheme

$\theta_0, \theta, \frac{x}{R}, \frac{\partial}{\partial x}, \frac{\partial}{\partial t}$	= $\mathcal{O}(1)$
$\frac{v}{R}, \frac{w}{R}, \frac{\eta}{R}, \frac{\xi}{R}, \frac{c}{R}$	= $\mathcal{O}(\epsilon)$
$\frac{u}{R}$	= $\mathcal{O}(\epsilon^2)$

ployed in previous studies [21, 22, 50] by considering arbitrarily large elastic pitch angles  $\theta$ , of order  $\mathcal{O}(1)$ . In addition, the normalized extensional deformation is considered to be one order smaller than the magnitude of bending deflection.

In addition, a truncation method is defined. Two different strategies can be found in the literature. In some analyses [21, 50], the orders of the largest terms in the kinetic and potential energies are first identified. Denoting these two orders of magnitude as  $\epsilon^k$  and  $\epsilon^p$ , all the terms in the kinetic and potential energies of magnitude smaller than or equal to  $\epsilon^{k+2}$  and  $\epsilon^{p+2}$  respectively are truncated. This truncation method results in structural terms in the strain energy of order  $\mathcal{O}(\epsilon^4)$  and  $\mathcal{O}(\epsilon^5)$ , and inertial terms in the kinetic energy of order  $\mathcal{O}(\epsilon^2)$  and  $\mathcal{O}(\epsilon^3)$ . But some exceptions are made under which three structural terms of order  $\mathcal{O}(\epsilon^6)$  and one inertial term of order  $\mathcal{O}(\epsilon^4)$  are retained. These terms contribute to the torsion equation of motion in the form of coupling between extension and twist. Physically, they are associated with blade warping and the trapeze effect, thus to retain them is justified. However,

Table 2.2: Order of terms retained for each equation of motion in Kaza and Kvaternik, 1977

	Strain energy terms	Kinetic energy terms
Extension equation	$\mathcal{O}(\epsilon^3)$	$\mathcal{O}(\epsilon^3)$
Bending equation	$\mathcal{O}(\epsilon^4)$	$\mathcal{O}(\epsilon^2)$
Torsion equation	$\mathcal{O}(\epsilon^5)$	$\mathcal{O}(\epsilon^3)$

from a mathematical stand point, it does not seem rigorous to arbitrarily retain terms while discarding others of equal magnitude. Another strategy [22] consists of truncating the extensional, bending and torsional equations of motion to different orders, as shown in Table 2.2. In particular, terms of higher order are retained in the torsional equation, so as to systematically retain terms of the same order of magnitude as the trapeze effect. However, truncating each equation of motion to a different order can lead to a loss of the self-adjoint property of the operators, hence some care must be taken in this process.

The truncation strategy employed in the present analysis consists of a mathematically rigorous generalization of the two methods described previously. In particular, higher order terms are discarded in the energies, with no distinction of their belonging to the extension, bending or torsion equations of motion. As a result, all the strain energy terms of order  $\mathcal{O}(\epsilon^5)$  or less are retained, as well as all the kinetic energy terms of order  $\mathcal{O}(\epsilon^3)$  or less, as summarized in Table 2.3. It can be seen that such truncation strategy automatically retains all the terms associated with the trapeze effect and the propeller moment.

Table 2.3: Truncation strategy

	Terms retained in energies	Terms associated to the trapeze effect	Terms associated to the propeller moment
Strain energy	$\mathcal{O}(\epsilon^5)$	$\mathcal{O}(\epsilon^4)$	-
Kinetic energy	$\mathcal{O}(\epsilon^3)$	$\mathcal{O}(\epsilon^3)$	$\mathcal{O}(\epsilon^2)$

## 2.5 Structural Model

The structural model gives rise to the rotor blade strain energy, kinetic energy and gravitational energy. It can be derived following several approaches, all yielding equivalent formulations. In addition, the trapeze effect can be represented in various ways. The analytical treatment of the trapeze effect is described in § 2.5.1. Other extension-torsion coupling effects are discussed in § 2.5.2, and the kinematic foreshortening due to bending is derived in § 2.5.3. Since the rotor blades are modeled as one-dimensional beams, a reference axis about which cross-sectional quantities are reduced must be defined. The choice of the elastic axis as the reference axis is explained in § 2.5.4. In addition, an overview of the various approaches to derive the equations of motion is given in § 2.5.5 and the choice for the formulation employed in the present dissertation is motivated. Finally, the derivation of the strain, kinetic and gravitational energies is presented.

### 2.5.1 Modeling of the trapeze effect

The trapeze effect, also called bifilar effect, was first observed by Campbell [66] and Pealing [67], who studied the torsional rigidity of phosphor bronze strips in vibration galvanometers. In particular, Campbell [66] found that “*in a phosphor-bronze strip under tension, the torsional rigidity is considerably increased as the tension is raised.*” The mechanics of the trapeze effect can be physically described in various analogous ways. It is the tendency of a pre-twisted beam to untwist under the action of an axial load, or similarly the tendency of a beam under an axial load to resist torsion. The theoretical explanation for this effect was first given by Buckley [68]. He showed that the geometric change of direction of the twisted fibers of a member induces a fore-shortening responsible for the increase in torsional rigidity. The trapeze effect applies particularly to the case of rotor blades subjected to large centrifugal loads. Conventional rotor blades typically exhibit a high structural torsional stiffness, preventing large angles of twist, therefore limiting the action of the trapeze effect. But for the case of torsionally soft blades with negligible structural stiffness, the trapeze effect plays a significant role on the deformation and the aeroelastic stability. The objective of the following analytical study is to describe the modeling of the trapeze effect. In addition, a parametric study showing the impact of the trapeze effect on the torsional frequency of a rotor blade is conducted. A systematic approach to the problem is proposed, first looking at the kinematics of a trapeze, and adding complexity to the problem to finally model a rotor blade with tip mass.

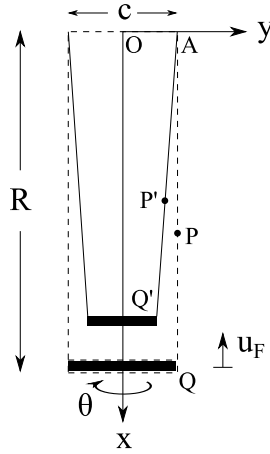


Figure 2.3: Undeformed and deformed shape of a trapeze in torsion

### 2.5.1.1 Kinematics relationships

**Case 1: Classical trapeze** It is natural to consider first the extension-torsion behavior of a simple trapeze, consisting of a rigid bar of length  $c$  suspended from its ends by inextensible cables of length  $R$  (see Fig. 2.3). When twisted, the tip of the trapeze makes an angle relative to the root equal to  $\theta$ . Because the cables are inextensible, the twisting results in a shortening of the trapeze by an amount  $u_F$ ; this is called axial foreshortening. Points  $P$  and  $Q$ , at a distance equal to  $x$  and  $R$  respectively from the root, displace to  $P'$  and  $Q'$  after deformation. The objective is to derive an expression for the axial displacement  $u_F$  as a function of the spanwise coordinate  $x$ .

The position of  $P'$  relative to  $A$ , projected in the fixed coordinate system  $\{x, y, z\}$ , is given by

$$\mathbf{AP}' = (x - u_F(x)) \mathbf{i} + \left(y_{P'} - \frac{c}{2}\right) \mathbf{j} + z_{P'} \mathbf{k} \quad (2.39)$$

where  $(\mathbf{i}, \mathbf{j}, \mathbf{k})$  are unit vectors directed along the  $x$ -,  $y$ - and  $z$ - direction respectively. In addition, because the cables forming the trapeze are inextensible, we can deduce that

$$\|\mathbf{AP}'\| = \|\mathbf{AP}\| = x \quad (2.40)$$

Combining Eq. (2.39) and (2.40), we obtain a quadratic equation in  $u_F$ . Only one of the two roots of this polynomial is physically meaningful. This root is given by

$$u_F(x) = x - \sqrt{x^2 - y_{P'}^2 - z_{P'}^2 - \frac{c^2}{4} + c y_{P'}} \quad (2.41)$$

In order to relate  $y_{P'}$  and  $z_{P'}$  to the variable  $x$  and  $\theta$ , we must express the vector  $\mathbf{AQ}'$  and then enforce the condition that  $\mathbf{AP}'$  and  $\mathbf{AQ}'$  are always collinear. The components of  $\mathbf{AQ}'$  projected in  $\{x, y, z\}$  are

$$\mathbf{AQ}' = (R - u_F(R)) \mathbf{i} + \frac{c}{2} (\cos \theta - 1) \mathbf{j} + \frac{c}{2} \sin \theta \mathbf{k} \quad (2.42)$$

From the inextensible cables assumption, we deduce that  $\|\mathbf{AQ}'\| = R$ , hence

$$u_F(R) = R - \sqrt{R^2 - \frac{c^2}{2} (1 - \cos \theta)} \quad (2.43)$$

Since  $\mathbf{AP}'$  and  $\mathbf{AQ}'$  are collinear, we must have

$$\mathbf{AP}' \times \mathbf{AQ}' = \mathbf{0} \quad (2.44)$$

which results in a system of three equations. Two of these three equations are independent and give expressions for  $y_{P'}$  and  $z_{P'}$ , as

$$\begin{cases} y_{P'} &= \frac{c(R - x + x \cos \theta)}{2R} \\ z_{P'} &= \frac{c x \sin \theta}{2R} \end{cases} \quad (2.45)$$

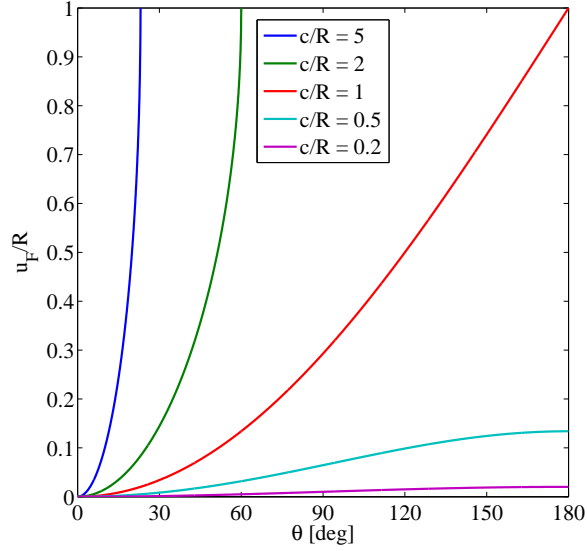


Figure 2.4: Kinematic foreshortening induced in a twisted trapeze, for various chord over length ratios

Finally, substituting Eq. (2.45) into Eq. (2.41), we obtain the foreshortening at any location  $x$ , given by

$$u_F(x) = x - \frac{x}{R} \sqrt{R^2 - \frac{c^2}{2}(1 - \cos \theta)} \quad \text{for } \theta \in [0; \pi] \quad (2.46)$$

This formula is exact and valid for any arbitrarily large angle  $\theta$ . However, when  $\theta = \pi$ , the two cables have come in contact and the kinematics of the trapeze changes. If one assumes that the diameter of the cables is infinitesimally small, then the motion of the trapeze outboard of the contact point is a pure rotation about a fixed point, which induces no additional foreshortening.

The tip displacement  $u_F(R)$  normalized by the trapeze length  $R$  is plotted in Fig. 2.4 as a function of the tip twist  $\theta$ , for various trapeze geometries. It

can be seen that the axial foreshortening, and consequently the trapeze effect, increases as  $c/R$  increases. In addition, for  $c/R > 1$ , the maximum twist angle at the end of the trapeze is kinematically limited to a value less than  $180^\circ$ . Note also that for  $c = R$ , the total foreshortening when  $\theta = 180^\circ$  is equal to the trapeze length.

In the case treated above, the two cables are not constrained in the chordwise direction, i.e. they are free to penetrate a virtual cylinder of diameter equal to the root chord  $c$ . However, in the case of a rotor blade, each longitudinal fiber is prevented from translating in the chordwise direction because of the presence of the neighboring fibers. In the following paragraph, the kinematics of a thin flexible ribbon in torsion is investigated.

**Case 2: Thin ribbon** A rotor blade can be modeled as a thin ribbon composed of an infinite number of fibers, aligned parallel to the spanwise direction. When a torsional moment is applied to the blade at a given section, that section rotates about a point called the torsional center. The loci of torsional centers at every section constitute the torsional axis [69]. In the case of a ribbon of rectangular cross-section, the torsional axis is coincident with the mid-chord. Hence, when the blade is twisted, the central fiber remains straight while the outer fibers take an helicoidal shape, as shown in Fig. 2.5. The radius of the helix made by a deformed fiber is equal to the chordwise distance from the fiber to the torsional axis, denoted as  $\eta$  in Fig. 2.5. If the end of the ribbon is prevented from warping, as it is for the rotor blade of interest

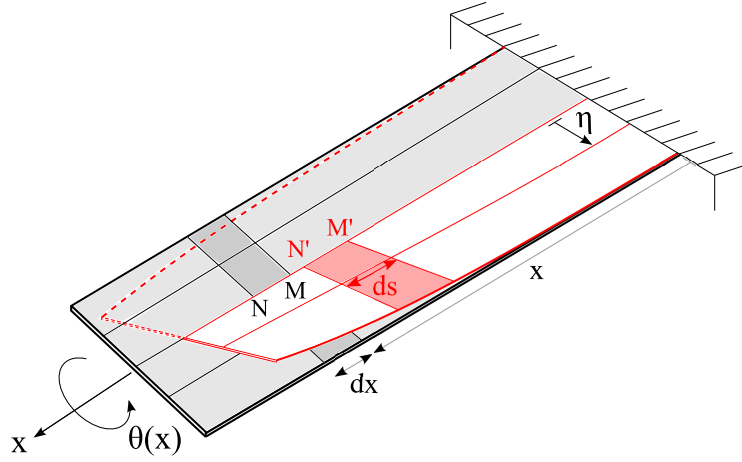


Figure 2.5: Undeformed and deformed shape of a thin ribbon in torsion

in this dissertation, then tensile stresses are created in the outer fibers, and compressive stresses occur in the inner fibers. One fiber on both sides of the torsional axis is strain-free. Enforcing the free-end condition at the tip of the ribbon, it can be shown that the resultant normal stress must be zero. From this condition, the foreshortening of the elastic axis can be deduced. The objective of the following derivation is to relate the axial displacement of each cross-section of the ribbon  $u_F(x)$  to the twist angle  $\theta(x)$ .

As a preliminary, the formula for the length of an helix must be derived. A circular helix of radius  $\eta$  and pitch  $2\pi b$  (see Fig. 2.6) is described by the following parametrization

$$\begin{cases} x(\theta) = b\theta \\ y(\theta) = \eta \sin \theta \\ z(\theta) = \eta \cos \theta \end{cases} \quad (2.47)$$

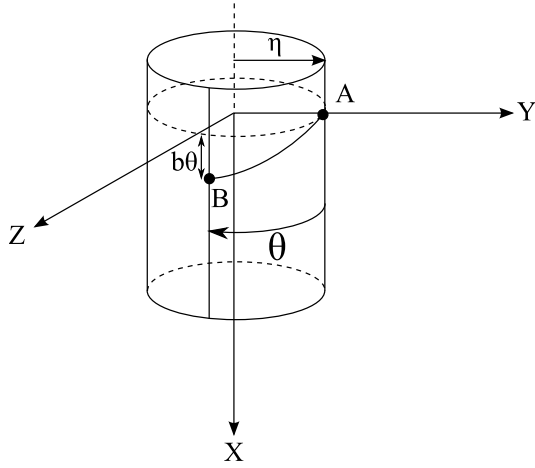


Figure 2.6: Parametrization of a helix

Hence, the arclength ( $AB$ ) is equal to

$$\begin{aligned}
 (AB) &= \int_A^B ds \\
 &= \int_A^B \sqrt{dx^2 + dy^2 + dz^2} \\
 &= \int_0^\theta \sqrt{(\eta d\theta)^2 + (dx)^2} \\
 &= \int_0^\theta \sqrt{\eta^2 + \left(\frac{dx}{d\theta}\right)^2} d\theta \\
 &= \sqrt{\eta^2 + b^2} \int_0^\theta d\theta \\
 &= \sqrt{\eta^2 + b^2} \theta
 \end{aligned} \tag{2.48}$$

Next, we can derive the axial strain in the central fiber and a fiber located at a distance  $\eta$  from the torsional axis (see Fig. 2.5). The compressive

strain in the middle fiber is

$$\begin{aligned}
\epsilon_0 &= \frac{\|\mathbf{M}'\mathbf{N}'\| - \|\mathbf{MN}\|}{\|\mathbf{MN}\|} \\
&= \frac{[(x + dx + u_F(x + dx)) - (x + u_F(x))] - dx}{dx} \\
&= u'_F(x)
\end{aligned} \tag{2.49}$$

And the strain in the fiber located at a distance  $\eta$  from the torsional axis is

$$\epsilon(\eta) = \frac{ds - dx}{dx} \tag{2.50}$$

Using Eq. (2.48), we have

$$ds = [\theta(x + dx) - \theta(x)] \sqrt{\eta^2 + b^2} \tag{2.51}$$

Thus,

$$\epsilon(\eta) = \theta'(x) \sqrt{\eta^2 + b^2} - 1 \tag{2.52}$$

In addition, by expressing the strain in the middle fiber as a function of the parameter of the helix  $b$ , we find that

$$b = \frac{\epsilon_0 + 1}{\theta'} \tag{2.53}$$

Therefore, we can write the strain in a fiber located at a distance  $\eta$  from the torsional axis as a function of  $\epsilon_0$  and  $\theta'$

$$\begin{aligned}
\epsilon(\eta) &= \sqrt{(\theta' \eta)^2 + (\epsilon_0 + 1)^2} - 1 \\
&= \sqrt{1 + 2\epsilon_0 + \epsilon_0^2 + \theta'^2 \eta^2} - 1 \\
&\simeq \epsilon_0 + \frac{1}{2} \epsilon_0^2 + \frac{1}{2} \theta'^2 \eta^2 \\
&\simeq \epsilon_0 + \frac{1}{2} \theta'^2 \eta^2
\end{aligned} \tag{2.54}$$

Since the ribbon is under pure torsion, the net axial force integrated over the blade cross-section should be zero. Hence,

$$\int_{-c/2}^{c/2} \epsilon(\eta) d\eta = 0 \quad (2.55)$$

$$\Leftrightarrow \epsilon_0 = -\frac{c^2}{12} \frac{\theta'^2}{2} \quad (2.56)$$

Finally, using Eq. (2.49), we conclude that

$$u_F(x) = -\int_0^x \frac{c^2}{12} \frac{\theta'^2}{2} dx \quad (2.57)$$

It is interesting to note that the neutral fiber (or strain free fiber) is located at a distance equal to  $\sqrt{c^2/12}$  on each side of the torsional axis. This value corresponds to the radius of gyration of a rectangular blade section of unit thickness and chord length  $c$  about its middle axis.

Generalizing the above derivation to the case of a rotor blade of thickness  $t$ , it is straightforward to show that the longitudinal strain in a fiber located at distances  $\eta$  and  $\xi$  from the torsional axis, in the chordwise and flatwise direction respectively, is

$$\epsilon(\eta, \xi) = \epsilon_0 + \frac{1}{2} \theta'^2 (\eta^2 + \xi^2) \quad (2.58)$$

In addition, in the absence of net axial force, the previous equation becomes

$$\epsilon(\eta, \xi) = \frac{\theta'^2}{2} (\eta^2 + \xi^2 - k_A^2) \quad (2.59)$$

where  $k_A$  is the polar radius of gyration of the rotor blade cross-section about the torsional axis. For a blade with rectangular cross-section,

$$k_A^2 = \frac{c^2 + t^2}{12} \quad (2.60)$$

Finally, the expression for the foreshortening due to the trapeze effect is

$$u_F(x) = - \int_0^x k_A^2 \frac{\theta'^2}{2} dx \quad (2.61)$$

Next, the restoring torque induced by the longitudinal stresses in the blade fibers is derived.

### 2.5.1.2 Restoring moment relationships

It can be seen from Eq. (2.59) that the longitudinal tensile stress in a fiber of a twisted rotor blade with zero net axial force is

$$\sigma(\eta, \xi) = E \frac{\theta'^2}{2} (\eta^2 + \xi^2 - k_A^2) \quad (2.62)$$

If the blade cross-section is rectangular, the maximum tensile stress occurs in the fiber most distant from the torsional axis ( $\eta=c/2$ ,  $\xi=t/2$ ). Thus

$$\sigma_{max} = \frac{E\theta'^2 (c^2 + t^2)}{12} \quad (2.63)$$

The minimum stress (compressive stress) occurs at the center of the blade ( $\eta=0$ ,  $\xi=0$ ) is

$$\sigma_{min} = - \frac{E\theta'^2 (c^2 + t^2)}{24} \quad (2.64)$$

The magnitude of these longitudinal stresses can be compared to the maximum shear stress which also arises in the twisted blade, predicted by Saint-Venant theory. For a narrow rectangular cross-section, it can be shown that [70]

$$\tau_{max} = tG\theta' \quad (2.65)$$

Substituting  $\theta'$  into Eq. (2.63) and (2.64), we obtain

$$\begin{cases} \sigma_{max} = \frac{E\tau_{max}^2}{12G^2} \left( \frac{c^2}{t^2} + 1 \right) \\ \sigma_{min} = -\frac{E\tau_{max}^2}{24G^2} \left( \frac{c^2}{t^2} + 1 \right) \end{cases} \quad (2.66)$$

As noted in Ref. [70], the above longitudinal stresses, which arise due to the trapeze effect, are proportional to  $\tau_{max}^2$ ; hence, the importance of these stresses increases with increasing  $\tau_{max}$ , i.e. with increasing angle of twist. For most metallic materials, such as aluminum or steel,  $\tau_{max}$  is always very small in comparison with  $G$ , and the magnitude of  $\sigma_{max}$  is therefore small in comparison with  $\tau_{max}$ . However, for a composite material with low shear modulus on the order of a few megapascals,  $\tau_{max}$  may be of the same order of magnitude as  $G$ . Hence,  $\sigma$  must be taken into consideration. Note also that the ratio  $E/G$  is approximately equal to 2.6 for isotropic and homogeneous materials with a Poisson's ratio of 0.3. But it can be significantly larger for anisotropic materials, around 21 for a carbon/epoxy (AS4/3501-6) unidirectional composite. Finally, Eq. (2.66) shows that the magnitude of  $\sigma_{max}$ , or in other words the importance of the trapeze effect, increases when  $c \gg t$ .

The longitudinal stresses in the deformed fibers create a restoring torque about the blade torsional axis, as shown in Fig. 2.7. The projection of  $\sigma$  in a plane perpendicular to the torsional axis is

$$\sigma^t = \sigma \sin \gamma \quad (2.67)$$

where  $\gamma$  is the angle the displaced fiber makes with the vertical. From Fig. 2.7,

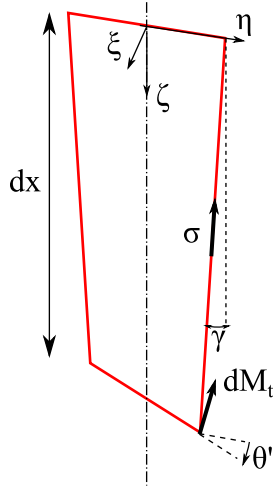


Figure 2.7: Restoring torque induced by longitudinal stresses in the fibers

it can be seen that

$$\sin \gamma = \sqrt{\eta^2 + \xi^2} \theta' \quad (2.68)$$

Hence, the restoring torque produced by the stretched fiber, about the torsional axis is

$$dM_t = E \frac{\theta'^3}{2} (\eta^2 + \xi^2 - k_A^2) (\eta^2 + \xi^2) d\eta d\xi \quad (2.69)$$

Integrating over the blade cross-section, the torque due to the trapeze effect is

$$M_t = E \frac{\theta'^3}{2} (B_1 - Ak_A^4) \quad (2.70)$$

where  $B_1 = \iint_A (\eta^2 + \xi^2)^2 dA$ . Combining this torque with the torque due to the shear stress  $T_{SV}$  (predicted according to Saint-Venant's theory), the total restoring torque acting on the rotor blade is

$$M_t = T_{SV} + E \frac{\theta'^3}{2} (B_1 - Ak_A^4) \quad (2.71)$$

This last result was specialized by Timoshenko [70] and Biot [71, 72] to the case of a narrow rectangular cross-section and it was shown that in this case,

$$\begin{aligned} M_t &= \frac{ct^3}{3} G \theta' + \frac{1}{360} E t c^5 \theta'^3 \\ &= \frac{ct^3}{3} G \theta' \left( 1 + \frac{1}{120} \frac{E c^4}{G t^2} \theta'^2 \right) \end{aligned} \quad (2.72)$$

It can be seen that when  $c \gg t$  and the angles of twist are large, the restoring moment associated with the trapeze effect may contribute an important portion of the total torque.

Finally, we need to consider the influence of a uniform axial load, such as the centrifugal forces acting on rotor blades on the total restoring torque. With this new boundary condition, the equilibrium equation for calculating the strain along the torsional axis (Eq. (2.55)) becomes

$$\iint_A E \epsilon(\eta, \xi) dA = \sigma_0 A \quad (2.73)$$

$$\Leftrightarrow \epsilon_0 = \frac{\sigma_0}{E} - k_A^2 \frac{\theta'^2}{2} \quad (2.74)$$

The expression for the longitudinal stress becomes

$$\sigma(\eta, \xi) = E \frac{\theta'^2}{2} (\eta^2 + \xi^2 - k_A^2) + \sigma_0 \quad (2.75)$$

And the total restoring torque acting on a blade cross-section, including the Saint-Venant's torque  $T_{SV}$ , is

$$M_t = T_{SV} + E \frac{\theta'^3}{2} (B_1 - A k_A^4) + \sigma_0 A k_A^2 \theta' \quad (2.76)$$

Consequently, it can be seen in Eq. (2.76) that the action of the tensile stress  $\sigma_0$  is to reduce the rate of twist per unit length  $\theta'$ . In addition, we note that

the untwisting effect due to the axial load is purely linear in the twist per unit length  $\theta'$ , unlike the restoring moment due to the change in fibers shape and geometry, which is proportional to  $\theta'^3$ . Finally, the Saint-Venant restoring moment is also a linear term in  $\theta'$ , which for instance is equal to  $GJ\theta'$  for the case of a circular cross-section.

To summarize, we have shown that for a rotor blade with low shear modulus and small thickness-to-chord ratio, non-negligible longitudinal stresses arise in the deformed fibers as a result of the trapeze effect. In addition, the restoring torque produced by these stresses is nonlinear, and is of the same order of magnitude as the torque due to the shear stress, classically predicted by Saint-Venant's theory. Finally, a net axial force giving rise to a uniform tensile stress tends to decrease the twist of the blade in a linear fashion.

In the next section, the impact of the trapeze effect on the rotor blade torsional frequency is investigated.

### **2.5.1.3 Torsional frequency**

Conventional helicopter rotor blades are relatively stiff in torsion, due to the skin of the blade acting as a closed torque box. The torsional stiffness is due predominantly to the control system stiffness and the restoring propeller moment. Therefore, typical values for the first torsional frequency are on the order of 5 per revolution (5/rev). In contrast, the torsional frequency of a rotor blade with negligible structural stiffness is essentially dictated by centrifugal effects, namely the propeller moment and the trapeze effect. The

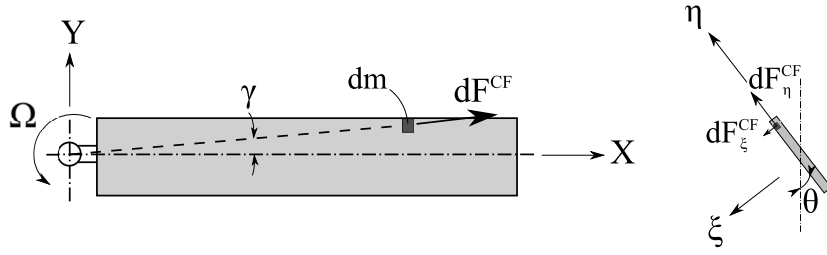


Figure 2.8: Schematic of propeller moment acting on a rotating blade

torsional frequencies associated with each of these effects individually, and to the combination of both, are derived below.

**Uncoupled propeller moment** We consider first the torsional dynamics of a rigid, untwisted rotating blade, with feathering hinge at the root, as shown in Fig. 2.8. Because the blade is rigid and untwisted, the restoring moment due to the trapeze effect equals zero. If the blade cross-section is not axisymmetric about the feathering axis, then the propeller moment stiffens the torsional degree of freedom. The expression for the propeller moment is derived hereafter.

The centrifugal force acting on an infinitesimal blade element of mass  $dm$  is

$$\mathbf{dF}^{\text{CF}} = dm \Omega^2 [x \mathbf{i}_X + (\eta \cos \theta - \xi \sin \theta) \mathbf{j}_Y] \quad (2.77)$$

Projected in the blade-fixed reference frame  $\{\zeta, \eta, \xi\}$ , the components of this

vector are

$$\mathbf{dF}^{\mathbf{CF}} = dF_{\zeta}^{\mathbf{CF}} \mathbf{e}_{\zeta} + dF_{\eta}^{\mathbf{CF}} \mathbf{e}_{\eta} + dF_{\xi}^{\mathbf{CF}} \mathbf{e}_{\xi} \quad (2.78)$$

$$\begin{aligned} &= dm \Omega^2 \left[ x \mathbf{e}_{\zeta} + (\eta \cos^2 \theta - \xi \sin \theta \cos \theta) \mathbf{e}_{\eta} \right. \\ &\quad \left. - (\eta \sin \theta \cos \theta - \xi \sin^2 \theta) \mathbf{e}_{\xi} \right] \quad (2.79) \end{aligned}$$

Thus, a pitching moment about the  $X$ -axis (which is coincident with the  $\zeta$ -axis) is created, of magnitude

$$dM_{\theta} = dF_{\xi}^{\mathbf{CF}} \eta - dF_{\eta}^{\mathbf{CF}} \xi \quad (2.80)$$

$$= dm \Omega^2 \left[ (\xi^2 - \eta^2) \sin \theta \cos \theta + \eta \xi (\sin^2 \theta - \cos^2 \theta) \right] \quad (2.81)$$

Integrating over the blade cross-section, we obtain an expression for the propeller moment, defined positive nose-up, as

$$M_{\theta} = m_0 \Omega^2 \left[ \left( k_{m_{\eta}}^2 - k_{m_{\xi}}^2 \right) \sin \theta \cos \theta + k_{m_{\eta\xi}}^2 (\sin^2 \theta - \cos^2 \theta) \right] \quad (2.82)$$

where  $m_0$  is the mass of the blade per unit length, and  $k_{m_{\eta}}$ ,  $k_{m_{\xi}}$ ,  $k_{m_{\eta\xi}}$  are radii of gyration about the feathering axis. Finally, we can write the equation of motion as

$$m_0 k_m^2 \ddot{\theta} + m_0 \Omega^2 \left[ \left( k_{m_{\xi}}^2 - k_{m_{\eta}}^2 \right) \sin \theta \cos \theta + k_{m_{\eta\xi}}^2 (\cos^2 \theta - \sin^2 \theta) \right] = 0 \quad (2.83)$$

For a rotor blade with a narrow rectangular cross-section, experiencing small pitch angles, it can be shown that the previous equation reduces to

$$\ddot{\theta} + \Omega^2 \theta = 0 \quad (2.84)$$

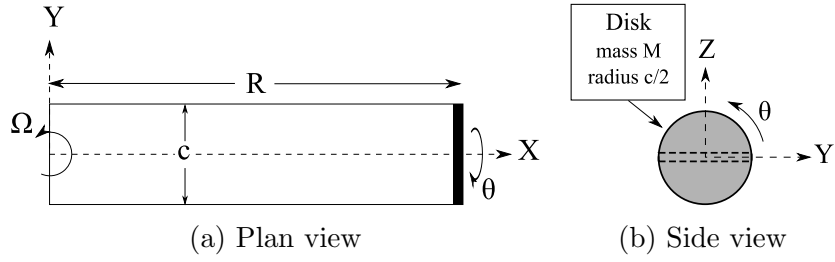


Figure 2.9: Cable rotor with disk at the tip

In non-dimensionalized form, this equation rewrites

$$\theta^{**} + \theta = 0 \quad (2.85)$$

where  $(\ )^{**} = \frac{1}{\Omega^2} \frac{\partial^2}{\partial t^2}$ . Therefore, it can be seen that the dimensionless torsional frequency due to the propeller moment is equal to 1/rev.

Next, the torsional frequency associated with the uncoupled trapeze effect is derived.

**Uncoupled trapeze effect** The kinematic relationship derived in § 2.5.1.1 (see Eq. (2.46)) can be used to find the torsional frequency of a trapeze rotating at a constant angular velocity  $\Omega$  (see Fig. 2.9). This system is typically described in the literature as a cable rotor. To isolate the action of the trapeze effect from the action of the propeller moment, the tip body must be axisymmetric (i.e.  $k_{m_\eta} = k_{m_\xi}$  and  $k_{m_{\eta\xi}} = 0$  in Eq. (2.82)). In the present example, a disk of mass  $M$  and radius  $c/2$  is chosen.

The total kinetic energy of this system, including the rotational part due to

twist and the translational part due to foreshortening, is

$$T = \frac{1}{2}M\dot{u}_F^2 + \frac{1}{2}M(R + u_F)^2\Omega^2 + \frac{1}{2}I\dot{\theta}^2 \quad (2.86)$$

where  $u_F = u_F(R)$  is the foreshortening defined by Eq. (2.46). Additionally, the cables at the leading-edge and trailing-edge are assumed to be inextensible. Therefore, the potential energy of the system is zero. Equation (2.46) evaluated at  $x = R$  can be differentiated with respect to time and inserted in Eq. (2.86) to get the kinetic energy as a function of the generalized coordinate  $\theta$  and its time derivative. Finally, using Lagrange's equation, we obtain the equation of motion of the cable blade as follows

$$\begin{aligned} \left[ I + Mc^4 \frac{\sin^2 \theta}{4R^2 - 2c^2(1 - \cos \theta)} \right] \ddot{\theta} \\ + \left[ \frac{Mc^2 \sin \theta [c^2 \cos^2 \theta + 2 \cos \theta (2R^2 - c^2) + c^2]}{4(c^2 \cos \theta + 2R^2 - c^2)^2} \right] \dot{\theta}^2 \\ + \frac{Mc^2}{4} \Omega^2 \sin \theta = 0 \quad (2.87) \end{aligned}$$

The steady-state solution of this equation is trivial ( $\theta_e = 0$ ). A small perturbation of the steady-state solution allows to linearize the equation of motion. Note in particular that the term proportional to  $\dot{\theta}^2$  does not contribute to the linearized stability analysis and was included in Eq. (2.87) only for completeness. The perturbed equation of motion, upon non-dimensionalization, becomes

$$\Delta\theta + \frac{Mc^2}{4I} \Delta\theta = 0 \quad (2.88)$$

and the torsional natural frequency is given as

$$\nu_\theta = \sqrt{\frac{Mc^2}{4I}} \quad (2.89)$$

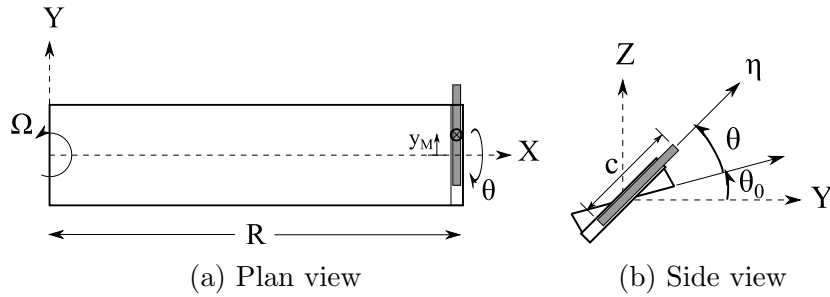


Figure 2.10: Cable rotor with solid rod at the tip

Therefore, it can be seen that the torsional frequency associated with the trapeze effect depends on the geometry of the tip body. If the tip body is a solid disk, then  $I = Mc^2/8$  and the torsional frequency is  $\nu_\theta = \sqrt{2} \sim 1.41/\text{rev}$ . Moreover, if the tip body is comprised of two bars attached perpendicularly to each other at their center, then  $I = Mc^2/12$  and  $\nu_\theta = \sqrt{3} \sim 1.73/\text{rev}$  (see an alternative derivation of this frequency in Appendix A).

**Coupled propeller moment and trapeze effect** The axisymmetric tip body considered in the previous case is now replaced by a solid rod, oriented perpendicularly to the spanwise direction (see Fig. 2.10). The length of the rod is arbitrarily taken equal to the blade chord  $c$ , and its center of mass offset from the torsional axis is denoted by  $y_M$ . Its mass is equal to  $M$  and its moment of inertia about the torsional axis is  $I$ . Note also in Fig. 2.10b the presence of a root pitch angle  $\theta_0$ . In this situation, both the propeller moment and the trapeze effect produce a torque on the rotor blade. The propeller moment tends to rotate the blade to flat pitch (i.e. tip body axis perpendicular to axis of rotation) whereas the trapeze effect tends to untwist the two cables (i.e.

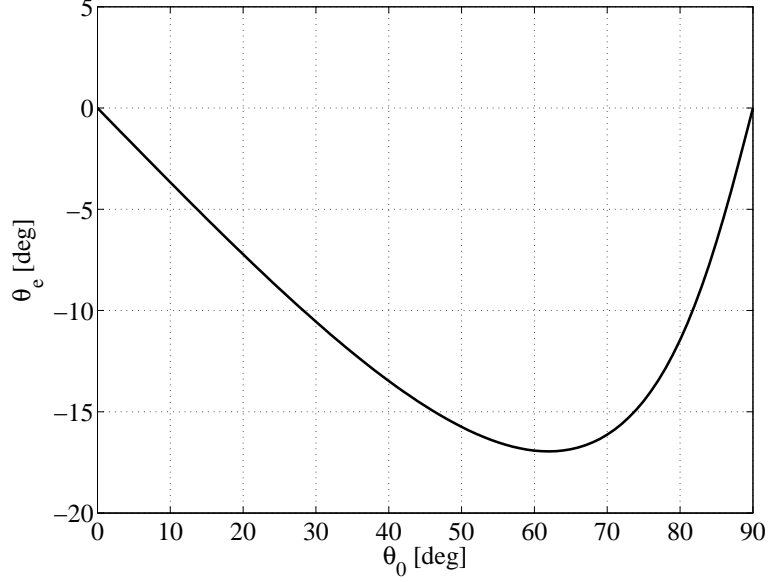


Figure 2.11: Variation of the steady-state twist angle with the root pitch

both cables lie in the same plane). As a result, the equation of motion is

$$\left[ I + Mc^4 \frac{\sin^2 \theta}{4R^2 - 2c^2(1 - \cos \theta)} \right] \ddot{\theta} + \left[ I\Omega^2 \cos \bar{\theta} \sin \bar{\theta} + \frac{Mc^2}{4} \Omega^2 \sin \theta \right] = 0 \quad (2.90)$$

where  $\bar{\theta} = \theta_0 + \theta$ . The steady-state twist angle  $\theta_e$ , solution of the nonlinear Eq. (2.91) below, is plotted as a function of the root pitch in Fig. 2.11.

$$I \cos(\theta_0 + \theta_e) \sin(\theta_0 + \theta_e) + \frac{1}{4} Mc^2 \sin \theta_e = 0 \quad (2.91)$$

It can be observed that  $\theta_e$  is equal to zero when the root pitch equals 0 or 90 degrees, cases where the propeller moment and the restoring torque due to the trapeze effect are zero. It is negative for any other root pitch angle.

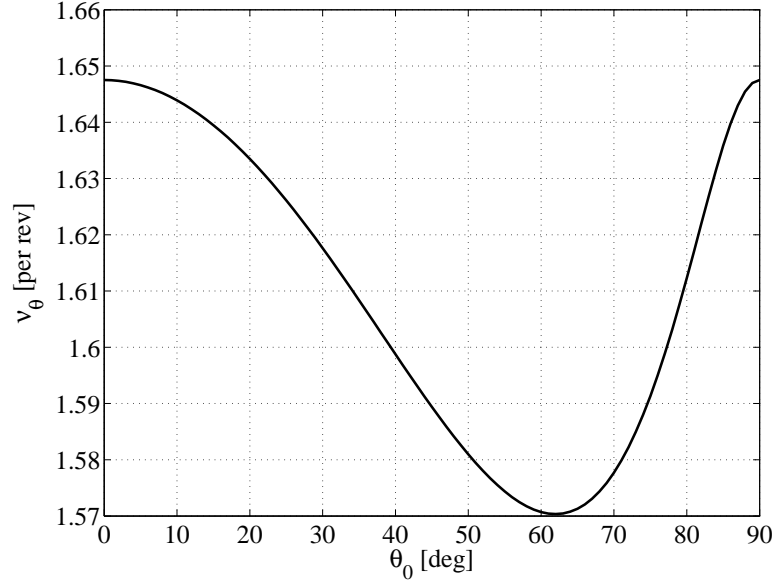


Figure 2.12: Variation of the torsional frequency with the root pitch ( $y_m/c = 0.25$ )

Additionally, the linearized perturbed equation of motion is

$$\left[ I + Mc^4 \frac{\sin^2 \theta_e}{4R^2 - 2c^2(1 - \cos \theta_e)} \right] \Delta \ddot{\theta} + \left[ I\Omega^2 \cos 2\theta_e + \frac{Mc^2}{4} \Omega^2 \cos \theta_e \right] \Delta \theta = 0 \quad (2.92)$$

From this equation, the torsional frequency can be extracted, as

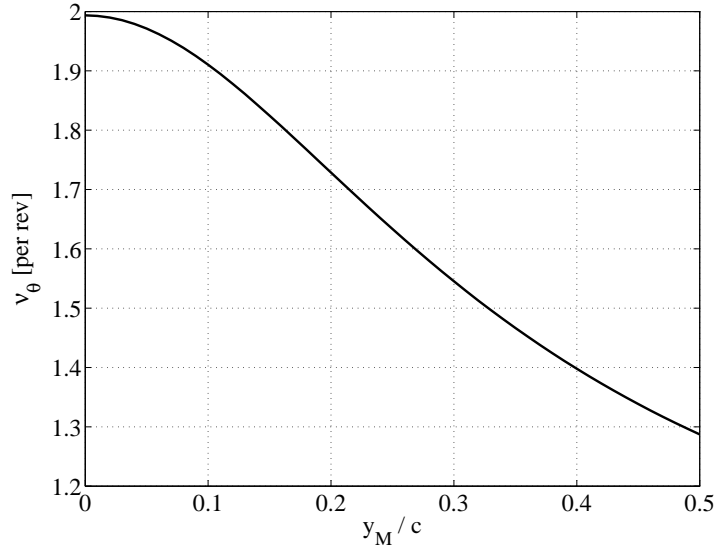
$$\nu_\theta^2 = \frac{I \cos 2\theta_e + \frac{Mc^2}{4} \cos \theta_e}{I + Mc^4 \frac{\sin^2 \theta_e}{4R^2 - 2c^2(1 - \cos \theta_e)}} \quad (2.93)$$

Equation (2.93) is illustrated by Fig. 2.12, showing the variation of torsional frequency as a function of root pitch angle. First, it can be seen that the torsional frequency resulting from the combined action of the propeller moment

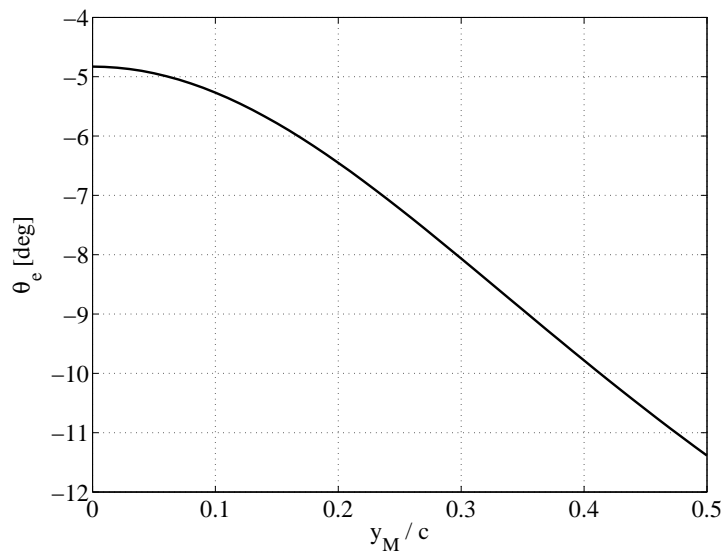
and the trapeze effect is approximately 1.6 times greater than the frequency induced by the propeller moment alone, equal to 1 per rev. Secondly, as the root pitch departs from 0 or 90 degrees, the torsional frequency decreases. This is due to the fact that when the blade is twisted, the trapeze effect opposes the action of the propeller moment. Hence the overall stiffening is less than for the cases  $\theta_0 = 0^\circ$  or  $\theta_0 = 90^\circ$ , in which the actions of the trapeze effect and the propeller moment add up.

The chordwise position of the tip mass also affects the torsional frequency of the blade, by changing its moment of inertia  $I$ . In particular, it can be seen in Fig. 2.13a that the highest torsional frequency is obtained when the tip mass is centered at the mid-chord. In addition, as the tip mass moves toward the leading-edge, the propeller moment increases, which results in an increase in twist (see Fig. 2.13b). Although an increase in twist also implies an increase in the trapeze effect, it can be seen in Fig. 2.13a that the torsional frequency tends towards 1 per rev as  $y_M/c$  becomes larger, which means that the propeller moment dominates.

In summary, it was shown that the torsional frequency associated with the uncoupled trapeze effect acting on a cable rotor is equal to  $\sqrt{2}/\text{rev}$  when the tip body is a solid disk, and  $\sqrt{3}/\text{rev}$  when the tip body is comprised of two perpendicular cross-bars. These frequencies are of the same order of magnitude as the classical frequency due to propeller moment, equal to  $1/\text{rev}$ . In addition, this study has shown that in the case of a rotor blade with concentrated tip mass, the torsional frequency varies with the collective pitch as well



(a) Torsional frequency



(b) Twist angle

Figure 2.13: Variation of the torsional frequency and twist of a cable rotor, as a function of the tip mass chordwise position ( $\theta_0 = 20^\circ$ )

as the chordwise position of the tip mass. It was found that the maximum torsional stiffness is obtained when the center of gravity of the tip mass is located at the mid-chord. These conclusions motivate the accurate modeling of both the propeller moment and the trapeze effect, to obtain accurate predictions of torsional deformations and natural frequencies of a rotor blade with negligible torsional stiffness. Finally, note that the extension-torsion couplings due to warping functions, as well as anisotropic composite laminates, have been ignored in the previous derivations. These couplings are addressed in the next section.

## **2.5.2 Modeling of other extension-torsion coupling effects**

### **2.5.2.1 Vlasov effect**

In the previous derivations, warping of the blade cross-sections was not mentioned, although thin rectangular cross-sections, which typically warp, were considered. This is because the rotor blades studied in this dissertation are prevented from warping at both of their ends. The question arises how this restrained warping affects the angle of twist and the distribution of stresses. In fact, it can be shown that when warping of a twisted member is restrained, longitudinal stresses arise that induce resistance to torsion. This phenomenon is called the Vlasov effect [73], and is analytically described next.

Two approaches to analytically model the restrained warping effect can be found in the literature. The first approach was presented by Wagner [74] who studied the torsion and buckling of a thin-walled, open section beam of

length  $L$ , with torsional moments of magnitude  $M$  acting on its ends, and a distributed external torque of magnitude  $m$  acting along its length. In addition, warping was prevented at both ends of the beam. Due to the longitudinal stresses arising from the restrained warping, the internal work of deformation (or strain energy) was found to be

$$W_i = \frac{1}{2} GJ \int_0^L \theta'^2 dx + \frac{1}{2E} \int_0^L \iint_A \sigma^2 dA dx \quad (2.94)$$

The longitudinal stress was expressed in terms of the warping function  $\lambda$  as

$$\sigma = E\theta''\lambda \quad (2.95)$$

where  $\lambda$  is a function of the cross-sectional coordinates and is obtained by solving the Laplace's equation [75].

According to the principle of virtual work, equating the internal virtual work to the external virtual work results in

$$GJ \int_0^L \theta' \delta\theta' dx + E \left( \iint_A \lambda^2 dA \right) \int_0^L \theta'' \delta\theta'' dx - \int_0^L m \delta\theta dx = 0 \quad (2.96)$$

Integrating by parts, and for arbitrary virtual displacement  $\delta\theta$ , we obtain

$$EC_1\theta'''' - GJ\theta'' = m \quad (2.97)$$

where  $C_1 = \iint_A \lambda^2 dA$  is defined as the warping rigidity. From Eq. (2.97), Wagner showed that the longitudinal stresses resulting from the restrained warping created a torsional moment of magnitude

$$T_\lambda = -EC_1\theta''' \quad (2.98)$$

Comparing the magnitude of  $T_\lambda$  with that of the restoring moment predicted by Saint-Venant's theory ( $T_{SV} = GJ\theta'$ ) gives information on the relevance of the Vlasov effect in the modeling of the torsional degree of freedom of a rotor blade. For rotor blades with closed cross-sections, as in the case of this dissertation, this effect is negligible [26]. However, in the case of open cross-sections, such as I-beams for instance, the Vlasov effect must be considered.

Another analytical model of the Vlasov effect was presented by Timoshenko and Goodier [75]. To enforce the no-warping condition, they assumed the presence of a normal stress distributed over the beam cross-section, proportional to the warping displacement

$$\sigma(x) = mEe^{-mx} u_\lambda \quad (2.99)$$

The other components of stress were deduced from the equilibrium equations and boundary conditions of a bar, with a torque  $M$  applied to its ends. Then, the total twist angle due to the combined Saint-Venant shear stress and prescribed normal stress was derived. In the case of a thin rectangular cross-section, it was found that

$$\theta = \frac{3M_t}{ct^3G} \left[ R - \frac{\sqrt{5(1+\nu)}}{6} c \right] \quad (2.100)$$

where  $\nu$  is the Poisson's ratio of the bar. Comparing this result with the angle of twist of a thin rectangular bar free to warp ( $\theta = \frac{3M_t R}{ct^3G}$ ), it can be seen that by preventing the cross-sections from warping, the torsional rigidity of the bar is increased. The effect on the twist angle is however small if  $c \ll R$ . In the

case of the rotor blade analyzed in this dissertation,  $c/R \sim 0.11$  therefore to ignore the Vlasov effect is justified.

To summarize, the restrained warping in effect for the rotor blades studied in this dissertation induces an increase in the blade torsional stiffness. However, this effect is negligible for blades with closed cross-sections and large aspect ratio, as in this dissertation. Therefore, it is neglected.

### 2.5.2.2 Composite material coupling

Extension-torsion coupling can also result from elastic tailoring of a composite lay-up. The force resultant/strain and moment resultant/curvature relationships of a general composite laminate are recalled below. In addition, the equations are specialized to the case of a two-ply, symmetric  $[+45^\circ/-45^\circ]_s$  laminate, representative of the composite blade analyzed in this dissertation. It is shown that the structural coupling induced by the composite lay-up is negligible, hence the blade material can be modeled as isotropic.

For a general composite laminate, the forces and moments shown on Fig. 2.14 are related to reference plane strains and curvatures as follows [76]

$$\begin{Bmatrix} N_x \\ N_y \\ N_{ss} \\ M_x \\ M_y \\ M_{ss} \end{Bmatrix} = \begin{bmatrix} A_{xx} & A_{xy} & A_{xs} & B_{xx} & B_{xy} & B_{xs} \\ A_{yx} & A_{yy} & A_{ys} & B_{yx} & B_{yy} & B_{ys} \\ A_{sx} & A_{sy} & A_{ss} & B_{sx} & B_{sy} & B_{ss} \\ B_{xx} & B_{xy} & B_{xs} & D_{xx} & D_{xy} & D_{xs} \\ B_{yx} & B_{yy} & B_{ys} & D_{yx} & D_{yy} & D_{ys} \\ B_{sx} & B_{sy} & B_{ss} & D_{sx} & D_{sy} & D_{ss} \end{bmatrix} \begin{Bmatrix} \epsilon_x^o \\ \epsilon_y^o \\ \gamma_s^o \\ \kappa_x \\ \kappa_y \\ \kappa_{ss} \end{Bmatrix} \quad (2.101)$$

where  $\mathbf{A}$ ,  $\mathbf{B}$  and  $\mathbf{D}$ , are respectively the extensional, extensional-bending, and flexural stiffness matrices of the composite. In the particular case where the

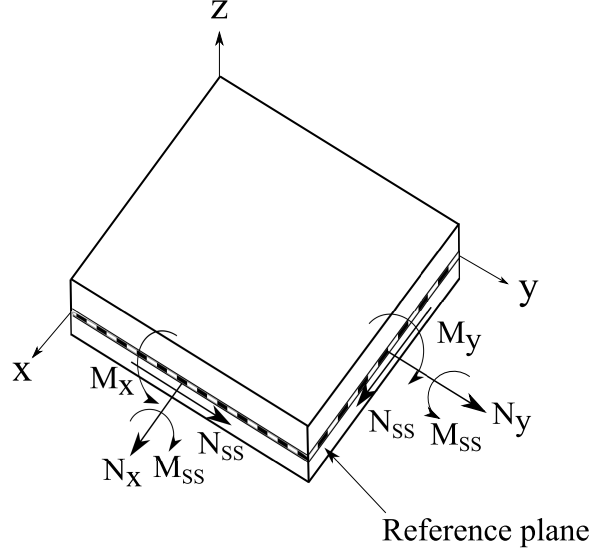


Figure 2.14: Laminated element with force and moment resultants

laminated element is symmetric, the extensional-bending matrix becomes null. In addition, a  $[+45^\circ/-45^\circ]_S$  composite is a cross-ply regular laminate, for which it can be shown that  $A_{is} = 0$  and  $D_{is} = 0$  (where  $i = x, y$ ) [76]. Therefore, the force resultant/strain and moment resultant/curvature equations become

$$\begin{pmatrix} N_x \\ N_y \\ N_{ss} \\ M_x \\ M_y \\ M_{ss} \end{pmatrix} = \begin{bmatrix} A_{xx} & A_{xy} & 0 & 0 & 0 & 0 \\ A_{yx} & A_{yy} & 0 & 0 & 0 & 0 \\ 0 & 0 & A_{ss} & 0 & 0 & 0 \\ 0 & 0 & 0 & D_{xx} & D_{xy} & 0 \\ 0 & 0 & 0 & D_{yx} & D_{yy} & 0 \\ 0 & 0 & 0 & 0 & 0 & D_{ss} \end{bmatrix} \begin{pmatrix} \epsilon_x^o \\ \epsilon_y^o \\ \gamma_s^o \\ \kappa_x \\ \kappa_y \\ \kappa_{ss} \end{pmatrix} \quad (2.102)$$

and it can be seen that no extension-torsion or extension-shear coupling is induced. In addition, by modeling the blade as an Euler-Bernoulli beam, we assume the stress state to be uniaxial, i.e.  $\sigma_{yy} = 0$ . Hence,  $N_y$  and  $M_y$  are

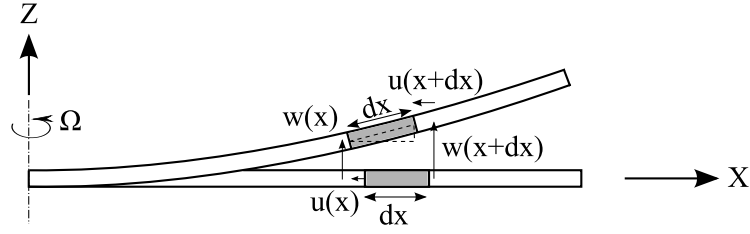


Figure 2.15: Foreshortening associated with out-of-plane bending

ignored and we have

$$\begin{Bmatrix} N_x \\ N_{ss} \\ M_x \\ M_{ss} \end{Bmatrix} = \begin{bmatrix} A_{xx} & 0 & 0 & 0 \\ 0 & A_{ss} & 0 & 0 \\ 0 & 0 & D_{xx} & 0 \\ 0 & 0 & 0 & D_{ss} \end{bmatrix} \begin{Bmatrix} \epsilon_x^o \\ \gamma_s^o \\ \kappa_x \\ \kappa_{ss} \end{Bmatrix} \quad (2.103)$$

This final form of the force resultant/strain and moment resultant/curvature equations motivate the modeling of the rotor blade in this dissertation as an isotropic structure.

### 2.5.3 Modeling of the kinematic foreshortening due to bending

Bending deformations are also responsible for an axial displacement of the blade cross-sections along the hub-fixed  $X$ -axis. This displacement is proportional to the square of the bending slope, as shown next.

Consider the out-of-plane bending of the rotor blade shown in Fig. 2.15. In particular, we consider the axial displacement of an infinitely small blade element of length  $dx$ . From Pythagorean theorem, we have

$$dx^2 = [dx + u(x + dx) - u(x)]^2 + [w(x + dx) - w(x)]^2 \quad (2.104)$$

Introducing the axial foreshortening  $u_F(x)$

$$u'_F(x) = \frac{u(x+dx) - u(x)}{dx} \quad (2.105)$$

Eq. (2.104) rewrites as

$$\begin{aligned} 1 &= (1 + u'_F)^2 + w'^2 \\ \Leftrightarrow u'_F &= \left( \sqrt{1 - w'^2} - 1 \right) \end{aligned} \quad (2.106)$$

For arbitrarily small  $w'$

$$u'_F = -\frac{w'^2}{2} + \mathcal{O}(w'^4) \quad (2.107)$$

Integrating from 0 to  $x$ , the axial foreshortening displacement associated with bending is

$$u_F(x) = -\int_0^x \frac{w'^2}{2} d\chi \quad (2.108)$$

From the superposition principle, it can be shown that the foreshortening due to the combined action of lead-lag and flap bending is

$$u_F(x) = -\int_0^x \left( \frac{v'^2}{2} + \frac{w'^2}{2} \right) d\chi \quad (2.109)$$

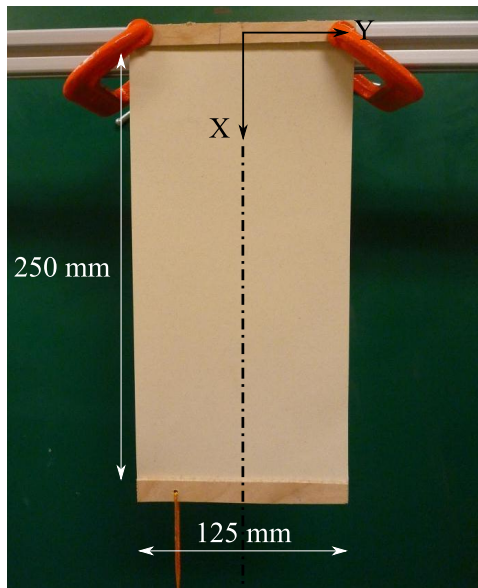
#### 2.5.4 Definition of the reference axis

In this dissertation, the rotor blade deformations are modeled by three displacements and one rotation with respect to a reference axis. In addition, two-dimensional cross-sectional properties are integrated and reduced to that same reference axis, consistent with a one-dimensional beam representation of the blade. In terms of the system of axes defined in § 2.2, the reference

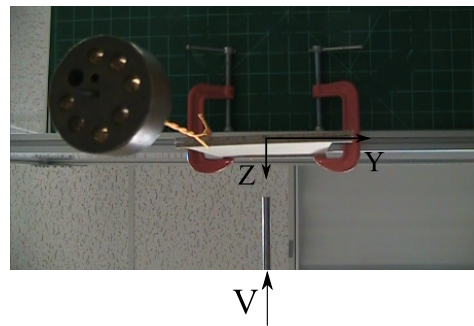
axis is coincident with the  $X$ -axis when the rotor blade is undeformed. After deformation, it is defined by the curvilinear coordinate  $\zeta$ . There are several ways to define this axis with respect to the blade geometry.

Some studies [21, 22, 77, 78] have suggested the use of the elastic axis as the reference axis. In Ref. [21], the elastic axis was defined as the spanwise locus of the blade cross-sectional shear centers. In Ref. [22], the reference axis was arbitrarily defined to be coincident with the blade feathering axis placed at quarter-chord. In both studies, the motivation was to simplify the beam analysis by decoupling the bending due to transverse loads from the twisting due to torques. However, the effect of an axial load (i.e centrifugal forces) on the bending/torsion relationship was ignored. This dissertation investigates how twist deformation can be decoupled from the application of a shear force, when it is combined with an axial force. In addition, the investigation is focused on beams with negligible structural stiffness. Accordingly, the following experiment is conducted.

A 250 mm long, extremely soft beam is fabricated out of a 0.15 mm thick and 125 mm wide sheet of paper, shown in Fig. 2.16 (note that the sheet of paper is assumed to behave like a beam, although the length is of the same order of magnitude as the width). Before any external loading is applied, the beam, clamped at one end and free at the other end, is hanging under the action of gravity. In addition, both ends of the beam are prevented from warping. An axial gravity load of magnitude  $P$  can be applied at a distance  $e$  from the middle axis. In addition, a transverse shear force  $V$  can be applied

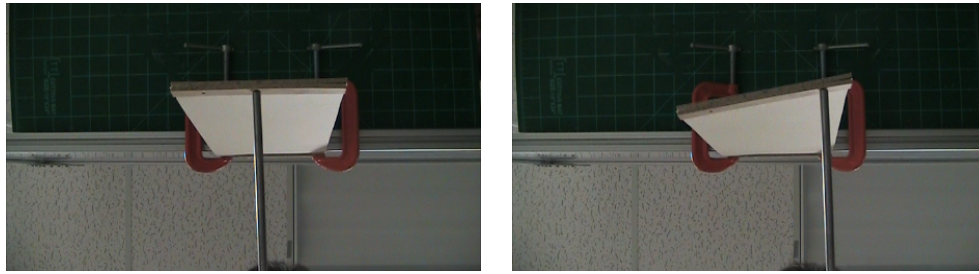


(a) Plan view



(b) Bottom view

Figure 2.16: Infinitely soft beam under combined axial loading ( $P$ ) and shear loading ( $V$ )



(a) Shear force acting at  $y = 0$

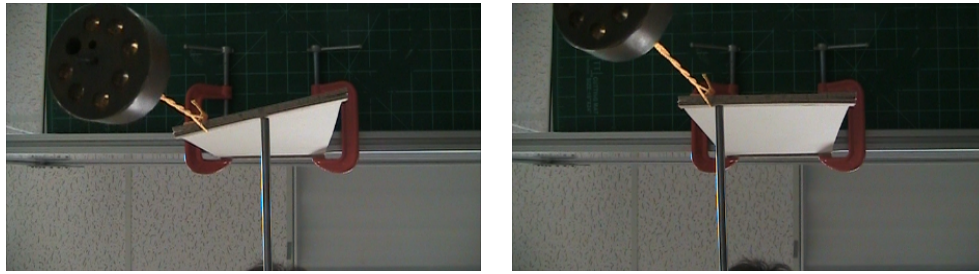
(b) Shear force acting at  $y = e$

Figure 2.17: Bending/twist deformation due to a shear force ( $P = 0$ )

at any location along the chord of the beam (i.e. along the  $Y$ -axis).

First, the deformation of the beam under the action of a shear force is observed for the case where  $P = 0$ . When the shear force  $V$  is applied at the middle of the beam end (i.e. at  $y = 0$ ) as shown in Fig. 2.17a, the beam experiences pure bending and no twist. In contrast, when the shear force acts at a distance  $y = e$  from the middle of the beam (Fig. 2.17b), a combination of bending and twist deformation can be observed. These experimental results confirm that twist deformation is decoupled from the action of a shear force when the shear force is acting at the shear center. As a matter of fact, the shear center, in the case of a beam of rectangular cross-section, is coincident with the middle of the cross-section.

Secondly, these experiments are repeated for the case where an axial load is applied (i.e.  $P \neq 0$ ) at a distance  $y = e$  from the middle axis. It can be seen in Fig. 2.18a that under this condition, a shear force applied at the middle of the beam induces both bending and twist deformations. However, when the shear force acts at the point of application of the axial load, as shown



(a) Shear force acting at  $y = 0$

(b) Shear force acting at  $y = e$

Figure 2.18: Bending/twist deformation due to a shear force ( $P \neq 0$ )

in Fig. 2.18b, then only bending deformation is observed.

Therefore, the experiments described above indicate that in the presence of an axial load, a shear force acting on an extremely soft beam will produce no twist only if it is applied at the point of application of the axial load, or more generally at the centroid of the axial stress field.

To theoretically explain this experimental conclusion, a more general definition of the elastic axis than the ones cited above and employed in Ref. [21, 22] must be used. Indeed, the elastic axis can be defined as the spanwise locus of the beam cross-sectional elastic centers [77, 79]. In addition, recall the following definitions, extracted from Ref. [69, 79]:

- The elastic center of a given cross-section of a beam is the point in the plane of the section lying between the shear center and the torsional center.
- The shear center of a given cross-section of a beam is the point in the plane of the section through which a transverse load, applied at that

section, must act to produce bending deflections only and no twist of the section.

- The torsional center of a given cross-section of a beam is the point about which the section rotates when a twisting couple is applied at that section.

Therefore, to find the location of the elastic center, the locations of the shear center and the torsional center must be known. The location of the shear center is always dictated by the sectional shear flow. However, the position of the torsional center does not necessarily depend on the shear flow, as explained below.

In the case of conventional rigid rotor blades experiencing negligible twist, it was shown in § 2.5.1 (see Eq. (2.76) with  $\theta'$  chosen arbitrarily small) that the twist due to an applied torque is well predicted by Saint-Venant's theory and is predominantly due to the sectional shear flow. Therefore, the locations of the shear center and the torsional center are dictated by the same stress field and are coincident. However, in the case of a torsionally soft rotor loaded by centrifugal forces, the twist distribution also depends on the axial stress distribution (due to the trapeze effect). Therefore, the shear center and the torsional center are prescribed by distinct stress fields and it can no longer be assumed that they are coincident. To derive the position of the torsional center, the following case is considered.

The objective is to compute the spanwise locus of torsional centers for

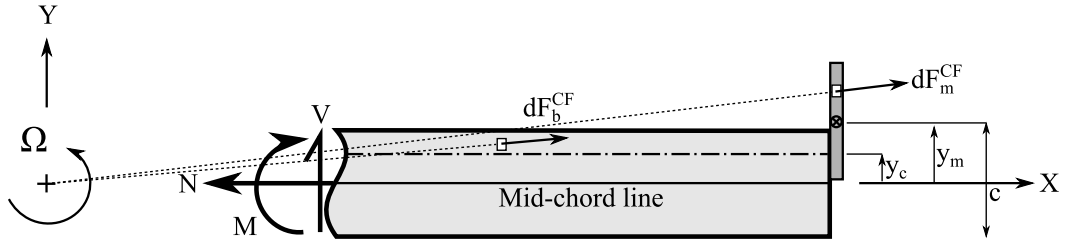


Figure 2.19: Free-body-diagram of the forces and moments applied to a rotor blade with tip mass

the rotor blade with tip mass, shown in Fig. 2.19, assumed to experience large twist angles. In addition, the torsional center of every blade cross-section is assumed to be located at a distance  $y_c(x)$  from the blade neutral axis ( $X$ -axis). For simplicity, the locus of torsional centers are shown by a straight dashed-line in Fig. 2.19. However, the following analysis is derived for a given blade station, and does not assume that the torsional axis is straight.

From equilibrium, the internal normal force and bending moment acting at a spanwise location  $x$  are

$$N(x) = m_0 \Omega^2 \frac{R^2 - x^2}{2} + M_m \Omega^2 R \quad (2.110)$$

$$M(x) = -M_m \Omega^2 y_m x \quad (2.111)$$

where  $m_0$  is the mass of the blade per unit length,  $M_m$  is the tip mass, and  $y_m$  is the distance from the mid-chord (passing through the lead-lag hinge) to the center of gravity of the tip mass.

Using the superposition principle, the axial stress at any spanwise location  $x$  and distance  $y$  from the neutral axis is

$$\sigma(x, y) = \frac{N(x)}{A} - \frac{M(x)y}{I_Z} \quad (2.112)$$

In addition, it was shown in Eq. (2.67) that the tangential component of the stress in a deformed blade fiber, responsible for a restoring torque about the torsional axis is

$$\sigma_t(x, y) = \sigma(x, y) \sin \gamma \quad (2.113)$$

$$= \sigma(x, y) (y - y_c) \theta' \quad (2.114)$$

where  $\gamma$  is the angle made by the deformed fiber relative to the torsional axis. Multiplying Eq. (2.114) by the width of a fiber, the force responsible for the restoring torque due to the trapeze effect, directed perpendicularly to the blade chord, is obtained as

$$dF_t(x, y) = \sigma(x, y) (y - y_c) \theta' dy \quad (2.115)$$

But it can be seen from Fig. 2.19 that the resultant shear force along the direction perpendicular to the blade chord equals zero. Therefore,

$$\int_{-c/2}^{c/2} dF_t(x, y) dy = 0 \quad (2.116)$$

Substituting Eq. (2.112) and (2.115) into Eq. (2.116), we obtain

$$y_c(x) = -\frac{M(x)}{N(x)} \frac{A}{I} \frac{c^2}{12} \quad (2.117)$$

Thus, Eq. (2.117) shows that the torsional center is coincident with the cen-

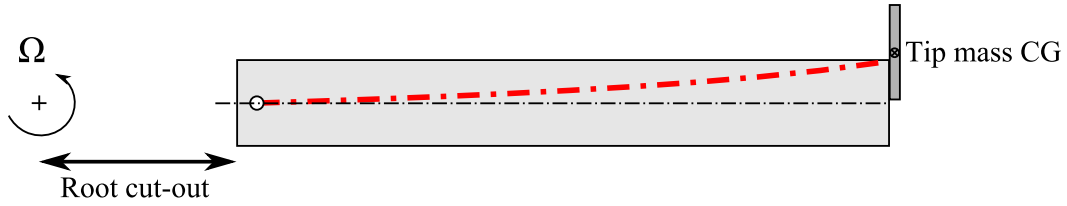


Figure 2.20: Spanwise locus of centroid of the axial stress field

centroid of the axial stress distribution, which can alternatively be defined as

$$y_c(x) = \frac{\int_{-c/2}^{c/2} y \sigma(x, y) dy}{\int_{-c/2}^{c/2} \sigma(x, y) dy} \quad (2.118)$$

$$= -\frac{M(x)}{N(x)} \frac{A}{I} \frac{c^2}{12} \quad (2.119)$$

For a given set of design parameters, we can plot the centroid of the axial stress field along the blade span (see Fig. 2.20). First, it can be seen from Eq. (2.117) that the result is independent of the rotational speed. Secondly, Fig. 2.20 shows that the shear centers, located along the mid-chord for a rotor blade with rectangular cross-section, are not coincident with the centroids of the axial stress field. Finally, note that flapwise and lead-lag bending deformations of the rotor blade induce a modification of the mass distribution, leading to a change of the radial stress field and therefore of its centroid. However, following a similar analysis as the one leading to Eq. (2.117), it can be shown that for small bending deformations, the result given in Eq. (2.117) remains unchanged.

To summarize, we have shown that in the case of torsionally soft rotors,

subjected to the combination of axial loads, shear loads and twisting moments, the torsional centers are generally not coincident with the shear centers. The locus of torsional centers are dictated by the axial stress field distribution, while the locus of shear centers are governed by the sectional shear flow. Consequently, the elastic axis passes between the loci of torsional centers and shear centers. However, the position of this axis cannot be exactly determined. We will assume that the elastic axis is a curve parallel to the deformed blade leading-edge, passing through the quarter-chord point at every blade section.

### 2.5.5 Choice of coordinates

The coordinates chosen as degrees of freedom for this dissertation are the displacements of the elastic axis along the  $X$ -,  $Y$ - and  $Z$ -directions ( $u$ ,  $v$  and  $w$  respectively), and the elastic pitch angle  $\theta$ . This angle corresponds to the elastic part of the rotation of the blade cross-section about the deformed elastic axis ( $\zeta$ -axis). It depends on both twist and bending deformations.

However, other sets of coordinates could be used to describe the same rotor blade motion. For example, instead of deriving the equations of motion as a function of the elastic pitch angle  $\theta$ , defined by Eq. (2.38), one could use the elastic twist angle  $\phi$ , defined by Eq. (2.25). The relationship between these two angles is given, approximated to second-order, in § 2.5.5.1.

In addition, the axial displacement variable  $u$  could be replaced by the sum of the elongation of the elastic axis, denoted  $u_e$ , and the kinematic foreshortening due to bending and twist. The two alternative approaches,

making use of the variables  $u$  or  $u_e$ , correspond respectively to an implicit or explicit consideration of the kinematic foreshortening due to bending and torsion. These two approaches are described in § 2.5.5.2.

In § 2.5.5.3, it is shown that the variables  $u$  and  $\theta$  are true coordinates, whereas  $u_e$  and  $\phi$  are quasi-coordinates. The validity of Lagrange's equations for quasi-coordinates is demonstrated.

Finally in § 2.5.5.4, the equivalence of two formulations derived using true or quasi-coordinates is shown by means of a simple example. Specifically, the flap dynamics of an elastic rotor blade is derived.

#### 2.5.5.1 Elastic pitch angle $\theta$ vs. twist angle $\phi$

The exact relationship between  $\theta$  and  $\phi$ , given by Eq. (2.38), can be approximated to second-order using the ordering scheme defined by Table. 2.1. A Taylor-Lagrange expansion of the integrand in Eq. (2.38) gives

$$\theta = \phi - \int_0^x w' \left[ 1 + \frac{v'^2 + w'^2}{2} + \mathcal{O}(\epsilon^4) \right] \left[ v'' + v'w'w'' (1 + w'^2 + \mathcal{O}(\epsilon^4)) \right] d\chi \quad (2.120)$$

Retaining terms up to second-order, we obtain

$$\begin{aligned} \theta &= \phi - \int_0^x v''w' d\chi + \mathcal{O}(\epsilon^4) \\ &\sim \phi - \int_0^x v''w' d\chi \end{aligned} \quad (2.121)$$

Hence, it can be seen that the elastic pitch angle  $\theta$  can be expressed as a function of the twist angle  $\phi$  and an integral of the bending deflection derivatives. To simplify the formulation, this dissertation uses the angle  $\theta$  as the

independent variable, avoiding the need for the integral term in Eq. (2.121). However, other studies such as [21, 22] have instead used the angle of twist  $\phi$  as the independent variable. Although the final equations of motion in the two approaches differ in form, they can be reduced to the same expression once the change of variable defined by Eq. (2.121) is introduced.

### 2.5.5.2 Implicit vs. explicit kinematic foreshortening

The total axial displacement of a point on the blade elastic axis is represented in this dissertation by the variable  $u$ . It can be decomposed into the sum of the elongation due to radial forces  $u_e$ , and the kinematic foreshortening due to bending and torsion  $u_F$ . Hence, we have

$$u = u_e + u_F \quad (2.122)$$

The foreshortening displacement due to torsion (trapeze effect) is given by Eq. (2.61), and the foreshortening due to bending is expressed by Eq. (2.109). Superposing the two results, we obtain

$$u = u_e - \frac{1}{2} \int_0^x (v'^2 + w'^2 + k_A^2 \theta') d\chi \quad (2.123)$$

An alternative approach to the one followed in this dissertation is to consider  $u_e$  to be the independent variable, and to include explicitly the expression for the foreshortening  $u_F$  in the position vector.

When  $u_e$  is chosen as the independent variable and the foreshortening of the elastic axis is explicitly included, centrifugal stiffening terms appear in the

kinetic energy. These terms are integral functions of the blade deformations, which can, only in some cases, be computed analytically.

In contrast, when the variable  $u$  is used, the foreshortening of the elastic axis is implicitly present in the expression for the longitudinal strains. In that case, the stiffening due to the centrifugal forces appears as additional terms in the strain energy.

The two formulations described above, although different in form, are fundamentally equivalent. However, the numerical implementation is simplified in the case where the foreshortening is considered implicitly. This is why  $u$  is used as the independent variable in this dissertation.

### 2.5.5.3 True vs. quasi coordinates

The coordinates chosen in this dissertation  $q_k = (u, v, w, \theta)$  are qualified as true coordinates, in a sense that if the velocities  $\dot{q}_k$  are known functions of time, an integration with respect to time yields the corresponding coordinates  $q_k$  [62]. But we have seen that other coordinates, such as  $u_e$  or  $\phi$  could equivalently be employed. The coordinates  $u_e$  and  $\phi$  are called quasi-coordinates because they are related to physical angles and displacements through integrals that cannot be evaluated in closed form (see Eq. (2.121) and (2.123)). In general, the formulation of the Lagrange's equations (and therefore the EHP) for quasi-coordinates differs from the classical formulation given by equation (2.1) which is valid for true coordinates [62]. It is natural to verify that for the special case of the quasi-coordinates  $u_e$  and  $\phi$ , the classical formulation holds true.

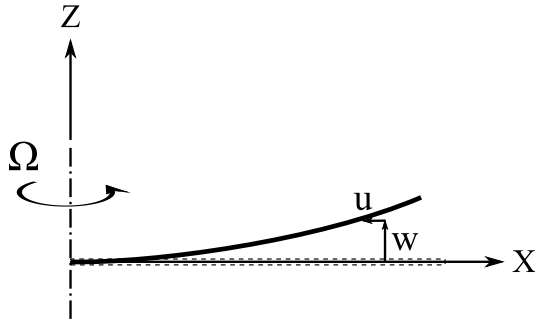


Figure 2.21: Elastic string undergoing pure flap

The elements of this derivation was presented in Ref. [63]. It is detailed for the specific case of the quasi-coordinates  $u_e$  and  $\phi$  in Appendix B.

#### 2.5.5.4 Example: Elastic rotor blade undergoing coupled extension-flap motion

An example will illustrate the equivalence between the implicit and explicit foreshortening formulations. The objective is to derive the equation of motion of a rotor blade undergoing pure flap, and to show that the equations obtained by including the kinematic foreshortening of the elastic axis implicitly or explicitly are equivalent. For simplicity, we assume that the blade cross-section is infinitely small, therefore we simply consider the dynamics of the rotating string shown in Fig. 2.21.

**Implicit formulation of the kinematic foreshortening** In this approach, the independent variables are the axial displacement  $u$ , directed along the hub-fixed  $X$ -axis, and the vertical deflection  $w$ .

The position of a particle on the deformed string is given by

$$\mathbf{r} = (x + u) \mathbf{i}_X + w \mathbf{k}_Z \quad (2.124)$$

And the velocity of the same point is

$$\dot{\mathbf{r}} = \dot{u} \mathbf{i}_X + (x + u)\Omega \mathbf{i}_Y + \dot{w} \mathbf{k}_Z \quad (2.125)$$

In addition, it can be shown that the longitudinal strain, defined in the Lagrangian sense, inside the string, is

$$\epsilon_{xx} = u' + \frac{w'^2}{2} + \mathcal{O}(\epsilon^4) \quad (2.126)$$

Consequently, the strain energy can be derived as

$$\begin{aligned} U &= \frac{1}{2} \int_R \iint_A E \epsilon_{xx}^2 dA dx \\ &= \frac{1}{2} \int_R \left( EAu'^2 + EA \frac{w'^4}{4} + EAu'w'^2 \right) dx + \mathcal{O}(\epsilon^6) \end{aligned} \quad (2.127)$$

Taking the variation, we obtain

$$\delta U = \int_R \left[ \left( EAu' + \underline{\underline{EA \frac{w'^2}{2}}} \right) \delta u' + \left( \underline{\underline{EA \frac{w'^3}{2}}} + \underline{\underline{EAu'w'}} \right) \delta w' \right] dx + \mathcal{O}(\epsilon^6) \quad (2.128)$$

Note that the underlined terms are the terms which differ from one formulation to one another, as shown later. Additionally, the kinetic energy is

$$\begin{aligned} T &= \frac{1}{2} \int_R \iint_A \rho (\dot{\mathbf{r}} \cdot \dot{\mathbf{r}}) dA dx \\ &= \frac{1}{2} \int_R m_0 (x^2 \Omega^2 + 2xu\Omega^2 + \dot{w}^2) dx + \mathcal{O}(\epsilon^4) \end{aligned} \quad (2.129)$$

And the variation of kinetic energy is

$$\delta T = \int_R (m_0 x \Omega^2 \delta u + m_0 \dot{w} \delta \dot{w}) dx + \mathcal{O}(\epsilon^4) \quad (2.130)$$

Using the results above, we can write the EHP, as follows

$$\int_{t_1}^{t_2} \int_R \left[ m_0 x \Omega^2 \delta u - \left( EA u' + EA \frac{w'^2}{2} \right) \delta u' + m_0 \dot{w} \delta \dot{w} - \left( EA \frac{w'^3}{2} + EA u' w' \right) \delta w' \right] dx dt = 0 \quad (2.131)$$

where higher-order terms have been truncated. Finally, we make the following change of variable

$$u = u_e - \int_0^x \frac{w'^2}{2} d\chi \quad (2.132)$$

$$u' = u'_e - \frac{w'^2}{2} \quad (2.133)$$

$$\delta u = \delta u_e - \int_0^x w' \delta w' d\chi \quad (2.134)$$

$$\delta u' = \delta u'_e - w' \delta w' \quad (2.135)$$

and after simplification, we obtain

$$\int_{t_1}^{t_2} \int_R \left[ m_0 x \Omega^2 \delta u_e - EA u'_e \delta u'_e + m_0 \dot{w} \delta \dot{w} - m_0 x \Omega^2 \int_0^x w' \delta w' d\chi \right] dx dt = 0 \quad (2.136)$$

**Explicit formulation of the kinematic foreshortening** An alternative approach is to choose  $u_e$  and  $w$  as the independent variables. In this case, the position vector of a particle on the deformed string is

$$\mathbf{r} = \left( x + u_e - \int_0^x \frac{w'^2}{2} d\chi \right) \mathbf{i}_X + w \mathbf{k}_Z \quad (2.137)$$

And the corresponding velocity vector is

$$\dot{\mathbf{r}} = \left( \dot{u}_e - \int_0^x w' \dot{w}' d\chi \right) \mathbf{i}_X + \left( x + u_e - \int_0^x \frac{w'^2}{2} d\chi \right) \Omega \mathbf{i}_Y + \dot{w} \mathbf{k}_Z \quad (2.138)$$

It can also be shown that the longitudinal strain is

$$\epsilon_{xx} = u'_e + \mathcal{O}(\epsilon^4) \quad (2.139)$$

Consequently, the variations of strain energy and kinetic energy, in this formulation, are

$$\delta U = \int_R EA u'_e \delta u'_e dx + \mathcal{O}(\epsilon^6) \quad (2.140)$$

$$\delta T = \int_R \left( m_0 x \Omega^2 \delta u_e - \underline{\underline{m_0 \Omega^2 \int_0^x w' \delta w' d\chi}} + m_0 \dot{w} \delta \dot{w} \right) dx + \mathcal{O}(\epsilon^4) \quad (2.141)$$

We can compare Eq. (2.128) and (2.130) to Eq. (2.140) and (2.141) respectively, and notice the additional terms in each formulation. Specifically, the centrifugal stiffening terms contained inside the strain energy in the implicit formulation, are present in the kinetic energy in the explicit formulation. Additionally, when the kinematic foreshortening is formulated explicitly, the final EHP is

$$\int_{t_1}^{t_2} \int_R \left[ m_0 x \Omega^2 \delta u_e - EA u'_e \delta u'_e + m_0 \dot{w} \delta \dot{w} - m_0 x \Omega^2 \int_0^x w' \delta w' d\chi \right] dx dt = 0 \quad (2.142)$$

which is identical to the expression shown in Eq. (2.136). Therefore, we have shown, by means of a simple example, the equivalence between two different formulations to describe the dynamics of a rotor blade. In the next section, the inextensible beam assumption is discussed.

### 2.5.6 Inextensible blade assumption

In many situations, the equations of motion of a rotor blade, modeled as beam elements, can be simplified by assuming the beams to be inextensible. This assumption implies that the extension of the elastic axis,  $u_e$ , and all its derivatives are equal to zero. However, the procedure allowing to make this simplification differs depending on the approach followed to derive the equations of motion.

If the axial displacement variable  $u$  is used to derive the equations, then the simplification can only be made a posteriori, in the final form of the equations of motion. Specifically, the derivatives and variation of  $u$  are replaced by the derivatives and the variation of the kinematic foreshortening  $u_F$ . However, if the kinematic foreshortening of the elastic axis is considered explicitly in the derivation, then the simplification can be made a priori, by setting  $u_e$  and its derivatives equal to zero.

From this description, it appears that if the inextensible blade assumption is applicable, then it is favorable to include the kinematic foreshortening of the elastic axis explicitly, and to use  $u_e$  as the independent variable, in place of  $u$ , to simplify the equations as early as possible. Nonetheless, the use of  $u_F$  yields integral terms in the equations of motion, whose integrand are functions of the deformations. The numerical modeling of such terms is computationally very inefficient, as it destroys the sparseness of the mass, damping and stiffness operators. For this reason, the inextensible blade assumption is made a posteriori in this dissertation.

In § 2.5.1 to 2.5.6, the choice of procedure adopted to derive the equations of motion in this dissertation was justified. In addition, a series of assumptions was made. From these preliminaries, the strain and kinetic energies can be derived.

### 2.5.7 Blade strain energy

The general formulation for the strain energy of a long, slender, isotropic beam is

$$U = \frac{1}{2} \int_0^R \iint_A (\sigma_{xx} \epsilon_{xx} + \tau_{x\eta} \gamma_{x\eta} + \tau_{x\xi} \gamma_{x\xi}) d\eta d\xi dx \quad (2.143)$$

where  $\epsilon_{xx}$  is the axial strain,  $\gamma_{x\eta}$  and  $\gamma_{x\xi}$  are the Cauchy or engineering shear strains. Using Hooke's law and introducing the true strains, the strain energy becomes

$$U = \frac{1}{2} \int_0^R \iint_A (E\epsilon_{xx}^2 + 4G\epsilon_{x\eta}^2 + 4G\epsilon_{x\xi}^2) d\eta d\xi dx \quad (2.144)$$

To compute this integral, the strain tensor associated with the combined extension, bending and torsion of an elastic blade must be derived.

#### 2.5.7.1 Strain tensor

The strain tensor  $\epsilon$  can be defined in the Lagrangian sense by the following equation

$$\mathbf{dr}_1 \cdot \mathbf{dr}_1 - \mathbf{dr}_0 \cdot \mathbf{dr}_0 = 2 \{dx d\eta d\xi\} [\epsilon] \begin{Bmatrix} dx \\ d\eta \\ d\xi \end{Bmatrix} \quad (2.145)$$

where  $dx$ ,  $d\eta$  and  $d\xi$  are increments along the  $X$ -,  $\eta$ - and  $\xi$ -axes in their configuration before deformation.  $\mathbf{dr}_0$  and  $\mathbf{dr}_1$  are the total differentials of

the position vectors  $\mathbf{r}_0$  and  $\mathbf{r}_1$ . The subscripts  $( )_0$  and  $( )_1$  refer respectively to the blade position before and after deformation.

In the  $\{X, Y, Z\}$  coordinate system, the position of a particle on the undeformed blade is

$$\mathbf{r}_0 = \begin{Bmatrix} x_0 \\ y_0 \\ z_0 \end{Bmatrix} = \begin{Bmatrix} x \\ \eta \cos \theta_0 - \xi \sin \theta_0 \\ \eta \sin \theta_0 + \xi \cos \theta_0 \end{Bmatrix} \quad (2.146)$$

Likewise, the position of a particle on the deformed blade is

$$\mathbf{r}_1 = \begin{Bmatrix} x_1 \\ y_1 \\ z_1 \end{Bmatrix} = \begin{Bmatrix} x + u \\ v \\ w \end{Bmatrix} + \mathbf{T}^T \begin{Bmatrix} 0 \\ \eta \\ \xi \end{Bmatrix} \quad (2.147)$$

where  $\mathbf{T}$  is the transformation matrix relating the coordinate system  $\{X, Y, Z\}$  to the coordinate system  $\{\zeta, \eta, \xi\}$ , introduced previously (see the exact expression in Eq. (2.24)). Using the ordering scheme defined in § 2.4, the transformation matrix can be approximated to second-order as

$$\mathbf{T} = \begin{bmatrix} 1 - \frac{v'^2}{2} - \frac{w'^2}{2} & v' & w' \\ -v' \cos \bar{\theta} - w' \sin \bar{\theta} & \left(1 - \frac{v'^2}{2}\right) \cos \bar{\theta} - v'w' \sin \bar{\theta} & \left(1 - \frac{w'^2}{2}\right) \sin \bar{\theta} \\ v' \sin \bar{\theta} - w' \cos \bar{\theta} & -\left(1 - \frac{v'^2}{2}\right) \sin \bar{\theta} - v'w' \cos \bar{\theta} & \left(1 - \frac{w'^2}{2}\right) \cos \bar{\theta} \end{bmatrix} \quad (2.148)$$

Consequently, the position vector  $\mathbf{r}_1$  becomes

$$\mathbf{r}_1 = \begin{Bmatrix} x_1 \\ y_1 \\ z_1 \end{Bmatrix} = \begin{Bmatrix} x + u - w' (\eta \sin \bar{\theta} + \xi \cos \bar{\theta}) - v' (\eta \cos \bar{\theta} - \xi \sin \bar{\theta}) \\ v + \left(1 - \frac{v'^2}{2}\right) (\eta \cos \bar{\theta} - \xi \sin \bar{\theta}) - v'w' (\eta \sin \bar{\theta} + \xi \cos \bar{\theta}) \\ w + \left(1 - \frac{w'^2}{2}\right) (\eta \sin \bar{\theta} + \xi \cos \bar{\theta}) \end{Bmatrix} \quad (2.149)$$

In addition, the total differentials of the position vectors are

$$\mathbf{dr}_0 = \begin{Bmatrix} dx_0 \\ dy_0 \\ dz_0 \end{Bmatrix} = \begin{Bmatrix} 1 dx \\ \cos \theta_0 d\eta - \sin \theta_0 d\xi \\ \sin \theta_0 d\eta + \cos \theta_0 d\xi \end{Bmatrix} \quad (2.150)$$

and

$$\mathbf{dr}_1 = \begin{Bmatrix} dx_1 \\ dy_1 \\ dz_1 \end{Bmatrix} \quad (2.151)$$

where

$$\left\{ \begin{array}{l} dx_1 = \left[ 1 + u' - w'' (\eta \sin \bar{\theta} + \xi \cos \bar{\theta}) - w' \theta' (\eta \cos \bar{\theta} - \xi \sin \bar{\theta}) \right. \\ \quad \left. - v'' (\eta \cos \bar{\theta} - \xi \sin \bar{\theta}) + v' \theta' (\eta \sin \bar{\theta} + \xi \cos \bar{\theta}) \right] dx \\ \quad + [-w' \sin \bar{\theta} - v' \cos \bar{\theta}] d\eta + [-w' \cos \bar{\theta} + v' \sin \bar{\theta}] d\xi \\ dy_1 = \left[ v' - v' v'' (\eta \cos \bar{\theta} - \xi \sin \bar{\theta}) - \left( 1 - \frac{v'^2}{2} \right) \theta' (\eta \sin \bar{\theta} + \xi \cos \bar{\theta}) \right. \\ \quad \left. - (v'' w' + v' w'') (\eta \sin \bar{\theta} + \xi \cos \bar{\theta}) - v' w' \theta' (\eta \cos \bar{\theta} - \xi \sin \bar{\theta}) \right] dx \\ \quad + \left[ \left( 1 - \frac{v'^2}{2} \right) \cos \bar{\theta} - v' w' \sin \bar{\theta} \right] d\eta + \left[ - \left( 1 - \frac{v'^2}{2} \right) \sin \bar{\theta} - v' w' \cos \bar{\theta} \right] d\xi \\ dz_1 = \left[ w' - w' w'' (\eta \sin \bar{\theta} + \xi \cos \bar{\theta}) + \left( 1 - \frac{w'^2}{2} \right) \theta' (\eta \cos \bar{\theta} - \xi \sin \bar{\theta}) \right] dx \\ \quad + \left[ \left( 1 - \frac{w'^2}{2} \right) \sin \bar{\theta} \right] d\eta + \left[ \left( 1 - \frac{w'^2}{2} \right) \cos \bar{\theta} \right] d\xi \end{array} \right. \quad (2.152)$$

Therefore, the left-hand side of Eq. (2.145) can be rewritten (see expansion in

Eq. (C.1) of Appendix C, from which we obtain the following strains

$$\begin{aligned}\epsilon_{xx} = & u' + \frac{v'^2}{2} + \frac{w'^2}{2} - v'' (\eta \cos \bar{\theta} - \xi \sin \bar{\theta}) - w'' (\eta \sin \bar{\theta} + \xi \cos \bar{\theta}) \\ & + \frac{\theta'^2}{2} (\eta^2 + \xi^2) + \mathcal{O}(\epsilon^4)\end{aligned}\quad (2.153)$$

$$\begin{aligned}\epsilon_{x\eta} = & -\theta' \frac{\xi}{2} - v'' w' \frac{\xi}{2} + \left\{ -\frac{u'}{2} (v' \cos \bar{\theta} + w' \sin \bar{\theta}) - \frac{v'^3}{4} \cos \bar{\theta} - \frac{w'^3}{4} \sin \bar{\theta} \right. \\ & \left. - \frac{v'^2 w'}{2} \sin \bar{\theta} \right\} + \mathcal{O}(\epsilon^4)\end{aligned}\quad (2.154)$$

$$\begin{aligned}\epsilon_{x\xi} = & \theta' \frac{\eta}{2} + v'' w' \frac{\eta}{2} + \left\{ \frac{u'}{2} (v' \sin \bar{\theta} - w' \cos \bar{\theta}) + \frac{v'^3}{4} \sin \bar{\theta} - \frac{w'^3}{4} \cos \bar{\theta} \right. \\ & \left. - \frac{v'^2 w'}{2} \cos \bar{\theta} \right\} + \mathcal{O}(\epsilon^4)\end{aligned}\quad (2.155)$$

Terms up to order  $\mathcal{O}(\epsilon^3)$  were retained, as required to obtain a second-order accurate expression for the strain energy [80].

Each component of the longitudinal strain is plotted in Fig. 2.22. The first three terms are the typical components of the Green-Lagrangian longitudinal strain. The fourth and fifth terms, proportional to  $v''$  and  $w''$ , are the bending strains. On the neutral axis, these terms vanish. The last term accounts for the longitudinal strain which arises due to the trapeze effect.

Additionally, note that definitions of strains other than the Green-Lagrangian strains are found in the literature, such as the Eulerian strains for instance. However, for small deformations, all these definitions coalesce. In particular, it can be seen that the Lagrangian strain field shown by Eq. (2.153)-(2.155) is similar, up to second-order, to the Eulerian strain field derived by Hodges and Dowell [21].

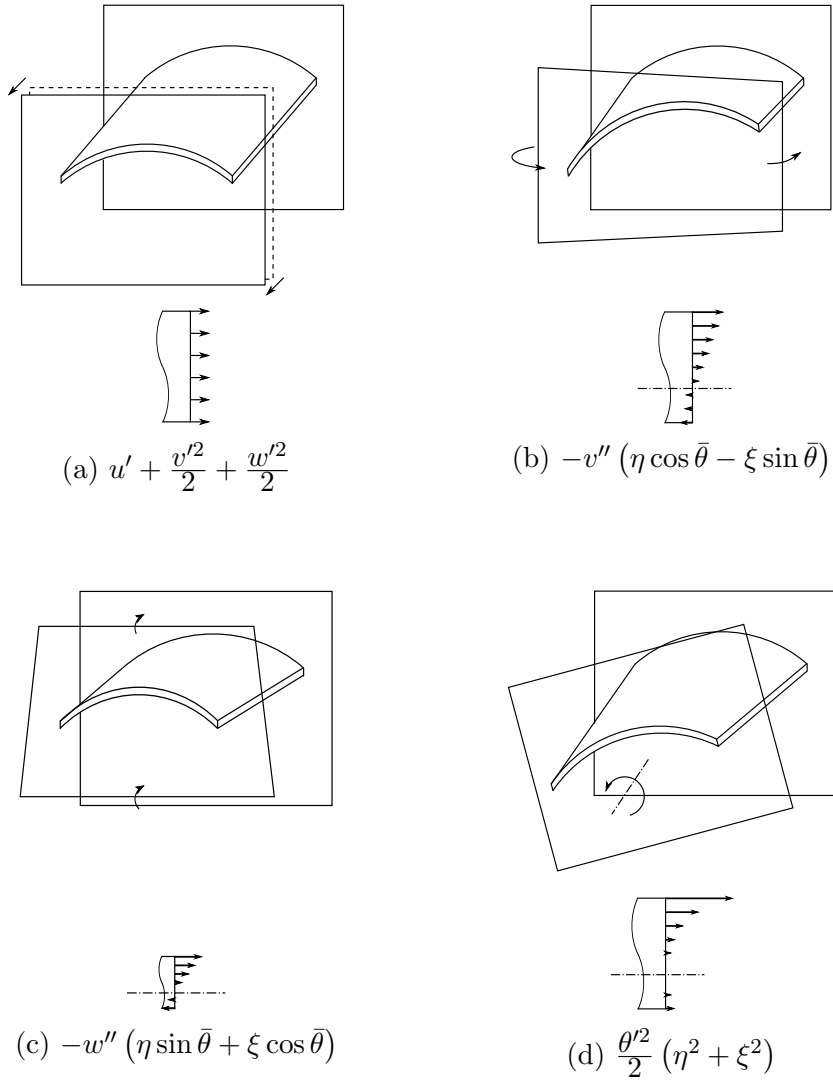


Figure 2.22: Components of the longitudinal strain

Next, the square of the strains can be computed (see expansion in Eq. (C.2)-(C.4) of Appendix C), substituted into Eq. (2.144), and then integrated over the blade cross-sectional area.

### 2.5.7.2 Structural cross-sectional constants

For simplicity, we define the following set of cross-section constants:

$$\begin{aligned}
\iint_A d\eta d\xi &= A & \iint_A \eta^2 d\eta d\xi &= I_\xi & \iint_A (\eta^2 + \xi^2) d\eta d\xi &= B_1 \\
\iint_A \eta d\eta d\xi &= Ae_\eta & \iint_A \xi^2 d\eta d\xi &= I_\eta & \iint_A \eta (\eta^2 + \xi^2) d\eta d\xi &= B_2 \\
\iint_A \xi d\eta d\xi &= Ae_\xi & \iint_A \eta\xi d\eta d\xi &= I_{\eta\xi} & \iint_A \xi (\eta^2 + \xi^2) d\eta d\xi &= B_3 \\
\iint_A (\eta^2 + \xi^2) d\eta d\xi &= J = Ak_A^2
\end{aligned}$$

It can be seen that  $e_\eta$  and  $e_\xi$  are the coordinates of the tensile axis (loci of the area centroids) relative to the elastic axis, positive in the direction of the  $\eta$ - and  $\xi$ - axes respectively.

Using the constants defined above, the expression for the blade strain energy is

$$\begin{aligned}
(U)_b &= \frac{1}{2} \int_R EA \left( u' + \frac{v'^2}{2} + \frac{w'^2}{2} \right)^2 + E Ak_A^2 \left( u' + \frac{v'^2}{2} + \frac{w'^2}{2} \right) \theta'^2 \\
&\quad + EI_\xi (v''^2 \cos^2 \bar{\theta} + w''^2 \sin^2 \bar{\theta} + v'' w'' \sin 2\bar{\theta}) \\
&\quad + EI_\eta (v''^2 \sin^2 \bar{\theta} + w''^2 \cos^2 \bar{\theta} - v'' w'' \sin 2\bar{\theta}) \\
&\quad + EI_{\eta\xi} ((w''^2 - v''^2) \sin 2\bar{\theta} + 2v'' w'' \cos 2\bar{\theta})
\end{aligned}$$

$$\begin{aligned}
& + EB_1 \frac{\theta'^4}{4} + EB_2 \theta'^2 (-v'' \cos \bar{\theta} - w'' \sin \bar{\theta}) \\
& + EB_3 \theta'^2 (v'' \sin \bar{\theta} - w'' \cos \bar{\theta}) \\
& + EAe_\eta ((-2u' - v'^2 - w'^2)(v'' \cos \bar{\theta} + w'' \sin \bar{\theta})) \\
& + EAe_\xi ((2u' + v'^2 + w'^2)(v'' \sin \bar{\theta} - w'' \cos \bar{\theta})) \\
& + GJ(\theta'^2 + 2v''w'\theta') \\
& + GAe_\eta (-2u'\theta'(w' \cos \bar{\theta} - v' \sin \bar{\theta}) - 2v'^2w'\theta' \cos \bar{\theta} \\
& \quad + v'^3\theta' \sin \bar{\theta} - w'^3\theta' \cos \bar{\theta}) \\
& + GAe_\xi (2u'\theta'(w' \sin \bar{\theta} + v' \cos \bar{\theta}) + 2v'^2w'\theta' \sin \bar{\theta} \\
& \quad + v'^3\theta' \cos \bar{\theta} + w'^3\theta' \sin \bar{\theta}) \\
& + \mathcal{O}(\epsilon^6) \tag{2.156}
\end{aligned}$$

Note that although the order of the truncated terms in Eq. (2.156) is  $\mathcal{O}(\epsilon^6)$ , this equation does not contain any term of order  $\mathcal{O}(\epsilon^5)$ , while the strain energy derived in other studies [21, 22, 50] does. The absence of terms of order  $\mathcal{O}(\epsilon^5)$  in the present derivation is due to the order scheme, particularly the twist angles considered of order  $\mathcal{O}(1)$ .

### 2.5.7.3 Variation in the strain energy

The variation in the strain energy are given by

$$\delta U = \int_R \iint_A (E\epsilon_{xx}\delta\epsilon_{xx} + 4G\epsilon_{x\eta}\delta\epsilon_{x\eta} + 4G\epsilon_{x\xi}\delta\epsilon_{x\xi}) d\eta d\xi dx \tag{2.157}$$

The variations in the strains ( $\delta\epsilon_{xx}$ ,  $\delta\epsilon_{x\eta}$  and  $\delta\epsilon_{x\xi}$ ) can be computed from the strain field formulated previously (see derivation in Eq. (C.5)-(C.7)). Subsequently, the variation in the strain energy becomes

$$(\delta U)_b = \int_R (s_{u'}\delta u' + s_{v'}\delta v' + s_{v''}\delta v'' + s_{w'}\delta w' + s_{w''}\delta w'' + s_\theta\delta\theta + s_{\theta'}\delta\theta') dx + \mathcal{O}(\epsilon^6) \quad (2.158)$$

where

$$s_{u'} = EA \left( u' + \frac{v'^2}{2} + \frac{w'^2}{2} \right) + \underline{\underline{EA \frac{k_A^2}{2} \theta'^2}} - (EA v'' + \underline{\underline{GA \theta' w'}})(e_\eta \cos \bar{\theta} - \underline{\underline{e_\xi \sin \bar{\theta}}}) - (EA w'' - \underline{\underline{GA \theta' v'}})(e_\eta \sin \bar{\theta} + \underline{\underline{e_\xi \cos \bar{\theta}}}) \quad (2.159)$$

$$s_{v'} = EA \left( u' + \frac{v'^2}{2} + \frac{w'^2}{2} \right) v' + \underline{\underline{EA \frac{k_A^2}{2} v' \theta'^2}} - (EA v' v'' + \underline{\underline{2GA v' w' \theta'}})(e_\eta \cos \bar{\theta} - \underline{\underline{e_\xi \sin \bar{\theta}}}) - \left( EA v' w'' - \underline{\underline{GA u' \theta'}} - \underline{\underline{\frac{3}{2} GA v'^2 \theta'}} \right) (e_\eta \sin \bar{\theta} + \underline{\underline{e_\xi \cos \bar{\theta}}}) \quad (2.160)$$

$$s_{v''} = \left[ EI_\xi \cos^2 \bar{\theta} + EI_\eta \sin^2 \bar{\theta} - \underline{\underline{EI_{\eta\xi} \sin 2\bar{\theta}}} \right] v'' + \frac{1}{2} \left[ (EI_\xi - EI_\eta) \sin 2\bar{\theta} + \underline{\underline{2EI_{\eta\xi} \cos 2\bar{\theta}}} \right] w'' - \underline{\underline{\frac{EB_2}{2} \theta'^2 \cos \bar{\theta}}} + \underline{\underline{\frac{EB_3}{2} \theta'^2 \sin \bar{\theta}}} - EA \left( u' + \frac{v'^2}{2} + \frac{w'^2}{2} \right) (e_\eta \cos \bar{\theta} - \underline{\underline{e_\xi \sin \bar{\theta}}}) + GJ \theta' w' \quad (2.161)$$

$$s_{w'} = EA \left( u' + \frac{v'^2}{2} + \frac{w'^2}{2} \right) w' + \underline{\underline{EA \frac{k_A^2}{2} w' \theta'^2}}$$

$$\begin{aligned}
& - (EAw'v'' + \underbrace{GAu'\theta'} + \underbrace{GAv'^2\theta'} + \frac{3}{2}\underbrace{GAw'^2\theta'}) (e_\eta \cos \bar{\theta} - \underline{e_\xi \sin \bar{\theta}}) \\
& - EAw'w'' (\underline{e_\eta \sin \bar{\theta}} + \underline{e_\xi \cos \bar{\theta}}) + GJv''\theta' \tag{2.162}
\end{aligned}$$

$$\begin{aligned}
s_{w''} &= \left[ EI_\xi \sin^2 \bar{\theta} + EI_\eta \cos^2 \bar{\theta} + \underline{EI_{\eta\xi} \sin 2\bar{\theta}} \right] w'' \\
&+ \frac{1}{2} \left[ (EI_\xi - EI_\eta) \sin 2\bar{\theta} + \underline{2EI_{\eta\xi} \cos 2\bar{\theta}} \right] v'' \\
&- \frac{EB_2}{2} \theta'^2 \sin \bar{\theta} - \frac{EB_3}{2} \theta'^2 \cos \bar{\theta} \\
&- EA \left( u' + \frac{v'^2}{2} + \frac{w'^2}{2} \right) (\underline{e_\eta \sin \bar{\theta}} + \underline{e_\xi \cos \bar{\theta}}) \tag{2.163}
\end{aligned}$$

$$\begin{aligned}
s_\theta &= \frac{1}{2} \left[ (EI_\xi - EI_\eta) \sin 2\bar{\theta} + \underline{2EI_{\eta\xi} \cos 2\bar{\theta}} \right] w''^2 \\
&- \frac{1}{2} \left[ (EI_\xi - EI_\eta) \sin 2\bar{\theta} + \underline{2EI_{\eta\xi} \cos 2\bar{\theta}} \right] v''^2 \\
&+ \left[ (EI_\xi - EI_\eta) \cos 2\bar{\theta} - \underline{2EI_{\eta\xi} \sin 2\bar{\theta}} \right] v''w'' \\
&- \left( \frac{EB_2}{2} \cos \bar{\theta} - \frac{EB_3}{2} \sin \bar{\theta} \right) w''\theta'^2 + \left( \frac{EB_2}{2} \sin \bar{\theta} + \frac{EB_3}{2} \cos \bar{\theta} \right) v''\theta'^2 \\
&+ \left[ EA \left( u' + \frac{v'^2}{2} + \frac{w'^2}{2} \right) v'' + \underbrace{GAu'w'\theta'} + \underbrace{GAv'^2w'\theta'} \right. \\
&\quad \left. + \underbrace{GA \frac{w'^3\theta'}{2}} \right] (\underline{e_\eta \sin \bar{\theta}} + \underline{e_\xi \cos \bar{\theta}}) \\
&+ \left[ -EA \left( u' + \frac{v'^2}{2} + \frac{w'^2}{2} \right) w'' + \underbrace{GAu'v'\theta'} \right. \\
&\quad \left. + \underbrace{GA \frac{v'^3\theta'}{2}} \right] (\underline{e_\eta \cos \bar{\theta}} - \underline{e_\xi \sin \bar{\theta}}) \tag{2.164}
\end{aligned}$$

$$\begin{aligned}
s_{\theta'} = & \underline{\underline{E A k_A^2}} \left( \underline{\underline{u' + \frac{v'^2}{2} + \frac{w'^2}{2}}} \right) \underline{\underline{\theta'}} + \left( \frac{E B_1}{2} \right) \theta'^3 - \left( \underline{E B_2 \sin \bar{\theta}} + \underline{E B_3 \cos \bar{\theta}} \right) w'' \theta' \\
& - \left( \underline{E B_2 \cos \bar{\theta}} - \underline{E B_3 \sin \bar{\theta}} \right) v'' \theta' + G J \theta' + G J v'' w' \\
& - \left( \underline{G A u' w'} + \underline{G A v'^2 w'} + \frac{G A w'^3}{2} \right) \left( \underline{e_\eta \cos \bar{\theta}} - \underline{e_\xi \sin \bar{\theta}} \right) \\
& + \left( \underline{G A u' v'} + \frac{G A v'^3}{2} \right) \left( \underline{e_\eta \sin \bar{\theta}} + \underline{e_\xi \cos \bar{\theta}} \right) \tag{2.165}
\end{aligned}$$

---



---

Underline	Meaning
-----------	---------

<u>      </u>	Extension-torsion terms associated with trapeze effect
<u>      </u>	Bending-torsion terms significant for large twist angles
- - -	Non-vanishing terms for arbitrary asymmetric cross-sections
~~~~~	Higher-order terms retained consistently with truncation scheme

---



---

The terms indicated by a double underline correspond to the extension-torsion coupling due to the trapeze effect. In addition, the terms with a single underline are related to bending-torsion coupling. They vanish for rotor blades with small angles of twist. Hence, they do not appear in conventional rotor blade studies, such as [21, 22, 50]. However, they are important for this dissertation. The terms with a dashed underline must be kept for arbitrary non-symmetric cross-sections. Finally, the wavy underlined terms are retained consistent with the mathematically rigorous ordering scheme presented in § 2.4. These terms were arbitrarily neglected in other rotor blade analyses [21, 50].

It will be shown in Chapter 3 of this dissertation that the equations

of motion are solved in their linear form, according to the Newton-Raphson method. Consequently, the linearized expression for the strain energy is derived next.

#### 2.5.7.4 Linearized strain energy

The nonlinear expression for the strain energy can be linearized by first-order Taylor expansion about the equilibrium (or trim) position, as follows

$$(\delta U)_{bLin} = (\delta U)_{b0} + \sum_{i=1}^N \left( \frac{\partial \delta U}{\partial q_i} \right)_0 \Delta q_i \quad (2.166)$$

where the magnitude of the truncated terms is on the order of  $(\Delta q_i)^2$  or less. This equation can be written in matrix form, as

$$(\delta U)_{bLin} = (\delta U)_{b0} + \delta \mathbf{q}^T \mathbf{K} \Delta \mathbf{q} \quad (2.167)$$

The matrix of gradients  $\mathbf{K}$  shown in the above equation corresponds to the structural part of the Jacobian matrix. It is given in Appendix [D.1](#).

#### 2.5.8 Blade kinetic energy

The general formulation for the blade kinetic energy is

$$T = \frac{1}{2} \int_R \iint_A \rho \left( \frac{d\mathbf{r}_1}{dt} \cdot \frac{d\mathbf{r}_1}{dt} \right) d\eta d\xi dx \quad (2.168)$$

where

$$\begin{aligned} \frac{d\mathbf{r}_1}{dt} &= \dot{\mathbf{r}}_1 + \boldsymbol{\Omega} \times \mathbf{r}_1 \\ &= \begin{Bmatrix} \dot{x}_1 - \Omega y_1 \\ \dot{y}_1 + \Omega x_1 \\ \dot{z}_1 \end{Bmatrix} \end{aligned} \quad (2.169)$$

In addition, the time derivative of the position vector, relative to the rotor blade fixed coordinate system, is

$$\dot{\mathbf{r}}_1 = \begin{Bmatrix} \dot{x}_1 \\ \dot{y}_1 \\ \dot{z}_1 \end{Bmatrix} \quad (2.170)$$

where

$$\begin{cases} \dot{x}_1 &= \dot{u} - \dot{w}' (\eta \sin \bar{\theta} + \xi \cos \bar{\theta}) - w' \dot{\theta} (\eta \cos \bar{\theta} - \xi \sin \bar{\theta}) \\ &\quad - \dot{v}' (\eta \cos \bar{\theta} - \xi \sin \bar{\theta}) + v' \dot{\theta} (\eta \sin \bar{\theta} + \xi \cos \bar{\theta}) \\ \dot{y}_1 &= \dot{v} - \left(1 - \frac{v'^2}{2}\right) \dot{\theta} (\eta \sin \bar{\theta} + \xi \cos \bar{\theta}) - v' \dot{v}' (\eta \cos \bar{\theta} - \xi \sin \bar{\theta}) \\ &\quad - \dot{v}' w' (\eta \sin \bar{\theta} + \xi \cos \bar{\theta}) - v' \dot{w}' (\eta \sin \bar{\theta} + \xi \cos \bar{\theta}) \\ &\quad - v' w' \dot{\theta} (\eta \cos \bar{\theta} - \xi \sin \bar{\theta}) \\ \dot{z}_1 &= \dot{w} + \left(1 - \frac{w'^2}{2}\right) \dot{\theta} (\eta \cos \bar{\theta} - \xi \sin \bar{\theta}) - w' \dot{w}' (\eta \sin \bar{\theta} + \xi \cos \bar{\theta}) \end{cases} \quad (2.171)$$

Expanding the dot product in Eq. (2.168) (see expansion in Eq. (C.8)) and integrated over the blade cross-sectional area, we obtain the expression for the blade kinetic energy.

### 2.5.8.1 Inertial cross-sectional constants

For simplicity, we define the following set of inertial cross-sectional constants:

$$\begin{aligned} \int_A \rho \, d\eta d\xi &= m_0 & \int_A \rho \eta^2 \, d\eta d\xi &= m_0 k_{m\xi}^2 & \int_A \rho (\eta^2 + \xi^2) \, d\eta d\xi &= m_0 k_m^2 \\ \int_A \rho \eta \, d\eta d\xi &= m_0 d_\eta & \int_A \rho \xi^2 \, d\eta d\xi &= m_0 k_{m\eta}^2 \\ \int_A \rho \xi \, d\eta d\xi &= m_0 d_\xi & \int_A \rho \eta \xi \, d\eta d\xi &= m_0 k_{m\eta\xi}^2 \end{aligned}$$

where  $m_0$  represents the mass per unit length of the rotor blade.  $d_\eta$  and  $d_\xi$  are the mass centroid offsets from the elastic axis, respectively in the  $\eta$  and  $\xi$  directions.  $m_0k_{m_\xi}^2$  and  $m_0k_{m_\eta}^2$  are the chordwise and flatwise mass moment of inertia of the blade section about the elastic axis.

Consequently, the kinetic energy can be rewritten as

$$\begin{aligned}
(T)_b = & \frac{1}{2} \int_R m_0 (\dot{v}^2 + \dot{w}^2 + \Omega^2 v^2 + \Omega^2 x^2 + 2\Omega^2 xu - 2\Omega v\dot{u} + 2\Omega x\dot{v} + 2\Omega\dot{v}u) \\
& + m_0 d_\eta \left[ -2\dot{v}\dot{\theta} \sin \bar{\theta} + 2\dot{w}\dot{\theta} \cos \bar{\theta} - 2x\Omega^2 (w' \sin \bar{\theta} + v' \cos \bar{\theta}) \right. \\
& \quad + 2\Omega^2 v \cos \bar{\theta} + 2\Omega v\dot{w}' \sin \bar{\theta} + 2\Omega v w' \dot{\theta} \cos \bar{\theta} + 2\Omega v \dot{v}' \cos \bar{\theta} \\
& \quad - 2\Omega v v' \dot{\theta} \sin \bar{\theta} - 2\Omega \dot{u} \cos \bar{\theta} - 2\Omega x \left( 1 - \frac{v'^2}{2} \right) \dot{\theta} \sin \bar{\theta} \\
& \quad - 2x\Omega (v' \dot{v}' \cos \bar{\theta} + \dot{v}' w' \sin \bar{\theta} + v' \dot{w}' \sin \bar{\theta}) - 2\Omega x v' w' \dot{\theta} \cos \bar{\theta} \\
& \quad \left. - 2\Omega u \dot{\theta} \sin \bar{\theta} - 2\Omega w' \dot{v} \sin \bar{\theta} - 2\Omega v' \dot{v} \cos \bar{\theta} \right] \\
& + m_0 d_\xi \left[ -2\dot{v}\dot{\theta} \cos \bar{\theta} - 2\dot{w}\dot{\theta} \sin \bar{\theta} - 2x\Omega^2 (w' \cos \bar{\theta} - v' \sin \bar{\theta}) - 2\Omega^2 v \sin \bar{\theta} \right. \\
& \quad + 2\Omega v \dot{w}' \cos \bar{\theta} - 2\Omega v w' \dot{\theta} \sin \bar{\theta} - 2\Omega v \dot{v}' \sin \bar{\theta} - 2\Omega v v' \dot{\theta} \cos \bar{\theta} \\
& \quad + 2\Omega \dot{u} \sin \bar{\theta} - 2\Omega x \left( 1 - \frac{v'^2}{2} \right) \dot{\theta} \cos \bar{\theta} \\
& \quad + 2x\Omega (v' \dot{v}' \sin \bar{\theta} - \dot{v}' w' \cos \bar{\theta} - v' \dot{w}' \cos \bar{\theta}) \\
& \quad \left. + 2\Omega x v' w' \dot{\theta} \sin \bar{\theta} - 2\Omega u \dot{\theta} \cos \bar{\theta} - 2\Omega w' \dot{v} \cos \bar{\theta} + 2\Omega v' \dot{v} \sin \bar{\theta} \right] \\
& + m_0 k_m^2 \left[ \dot{\theta}^2 + 2\Omega w' \dot{\theta} \right] \\
& + m_0 k_{m_\xi}^2 \left[ \Omega^2 \cos^2 \bar{\theta} + 2\Omega \dot{w}' \sin \bar{\theta} \cos \bar{\theta} + 2\Omega \dot{v}' \cos^2 \bar{\theta} \right] \\
& + m_0 k_{m_\eta}^2 \left[ \Omega^2 \sin^2 \bar{\theta} - 2\Omega \dot{w}' \sin \bar{\theta} \cos \bar{\theta} + 2\Omega \dot{v}' \sin^2 \bar{\theta} \right] \\
& + m_0 k_{m_{\eta\xi}}^2 \left[ -2\Omega^2 \cos \bar{\theta} \sin \bar{\theta} + 2\Omega \dot{w}' (\cos^2 \bar{\theta} - \sin^2 \bar{\theta}) - 4\Omega \dot{v}' \cos \bar{\theta} \sin \bar{\theta} \right] \\
& + O(\epsilon^4) \tag{2.172}
\end{aligned}$$

### 2.5.8.2 Variation in the kinetic energy

Taking the variation of Eq. (2.168), we obtain

$$\delta T = \int_R \iint_A \rho \frac{d\mathbf{r}_1}{dt} \cdot \delta \left( \frac{d\mathbf{r}_1}{dt} \right) d\eta d\xi dx \quad (2.173)$$

where

$$\delta \left( \frac{d\mathbf{r}_1}{dt} \right) = \begin{Bmatrix} \delta \dot{x}_1 - \Omega \delta y_1 \\ \delta \dot{y}_1 + \Omega \delta x_1 \\ \delta \dot{z}_1 \end{Bmatrix} \quad (2.174)$$

The product in Eq. (2.173) can be expanded, as

$$\begin{aligned} \frac{d\mathbf{r}_1}{dt} \cdot \delta \left( \frac{d\mathbf{r}_1}{dt} \right) &= \dot{x}_1 \delta \dot{x}_1 + \dot{y}_1 \delta \dot{y}_1 + \dot{z}_1 \delta \dot{z}_1 - \dot{x}_1 \Omega \delta y_1 + \dot{y}_1 \Omega \delta x_1 \\ &\quad - y_1 \Omega \delta \dot{x}_1 + x_1 \Omega \delta \dot{y}_1 + y_1 \Omega^2 \delta y_1 + x_1 \Omega^2 \delta x_1 \end{aligned} \quad (2.175)$$

Note that upon writing the EHP, the time derivatives of the variations in the generalized coordinates ( $\delta \dot{x}_1$ ,  $\delta \dot{y}_1$  and  $\delta \dot{z}_1$ ) are integrated by parts. For simplicity, we can operate the integration by parts at this stage of the derivation.

Therefore, the variation in the kinetic energy becomes

$$\begin{aligned} \int_{t_1}^{t_2} \delta T dt &= \int_{t_1}^{t_2} \int_R \iint_A \rho \left[ (-\ddot{x}_1 + 2\Omega \dot{y}_1 + \Omega^2 x_1) \delta x_1 \right. \\ &\quad \left. + (\Omega^2 y_1 - \ddot{y}_1 - 2\Omega \dot{x}_1) \delta y_1 + (-\ddot{z}_1) \delta z_1 \right] d\eta d\xi dx dt \end{aligned} \quad (2.176)$$

where boundary terms were voluntarily omitted. The position and velocity vectors are given by Eq. (2.149) and (2.171) respectively. Additionally, the components of the acceleration vector and the variation in the position vector can be computed (see Eq. (C.9) and Eq. (C.12)).

In terms of the cross-sectional constants defined in § 2.5.8.1, the final form of the variation in the kinetic energy is

$$\int_{t_1}^{t_2} (\delta T)_b = \int_{t_1}^{t_2} \int_R (k_u \delta u + k_v \delta v + k_{v'} \delta v' + k_w \delta w + k_{w'} \delta w' + k_\theta \delta \theta) dx dt + \mathcal{O}(\epsilon^4) \quad (2.177)$$

where

$$\begin{aligned} k_u = & m_0 \Omega^2 x + 2m_0 \Omega \dot{v} - \underline{\underline{2m_0 \Omega \dot{\theta} (d_\eta \sin \bar{\theta} + d_\xi \cos \bar{\theta})}} \\ & - \underline{\underline{m_0 \ddot{u}}} + \underline{\underline{m_0 \ddot{w}' (d_\eta \sin \bar{\theta} + d_\xi \cos \bar{\theta})}} + \underline{\underline{m_0 \ddot{v}' (d_\eta \cos \bar{\theta} - d_\xi \sin \bar{\theta})}} \\ & + \underline{\underline{m_0 w' \ddot{\theta} (d_\eta \cos \bar{\theta} - d_\xi \sin \bar{\theta})}} - \underline{\underline{m_0 v' \ddot{\theta} (d_\eta \sin \bar{\theta} + d_\xi \cos \bar{\theta})}} \end{aligned} \quad (2.178)$$

$$\begin{aligned} k_v = & -m_0 \ddot{v} + m_0 \Omega^2 v - 2m_0 \Omega \dot{u} \\ & + \left( m_0 \Omega^2 + \underline{\underline{m_0 \dot{\theta}^2}} + 2m_0 \Omega \dot{v}' + \underline{\underline{2m_0 \Omega w' \dot{\theta}}} \right) \left( d_\eta \cos \bar{\theta} - \underline{\underline{d_\xi \sin \bar{\theta}}} \right) \\ & + \left( m_0 \ddot{\theta} + 2m_0 \Omega \dot{w}' - \underline{\underline{2m_0 \Omega v' \dot{\theta}}} \right) \left( d_\eta \sin \bar{\theta} + \underline{\underline{d_\xi \cos \bar{\theta}}} \right) \end{aligned} \quad (2.179)$$

$$\begin{aligned} k_{v'} = & -(2m_0 \Omega \dot{v} + m_0 \Omega^2 x) \left( d_\eta \cos \bar{\theta} - \underline{\underline{d_\xi \sin \bar{\theta}}} \right) \\ & + \underline{\underline{m_0 \Omega \dot{\theta} ((k_{m\xi}^2 - k_{m\eta}^2) \sin 2\bar{\theta} + 2k_{m\eta\xi}^2 \cos 2\bar{\theta})}} \\ & + \underline{\underline{m_0 \ddot{u} (d_\eta \cos \bar{\theta} - d_\xi \sin \bar{\theta})}} \end{aligned} \quad (2.180)$$

$$k_w = -m_0 \ddot{w} - m_0 \ddot{\theta} \left( d_\eta \cos \bar{\theta} - \underline{\underline{d_\xi \sin \bar{\theta}}} \right) + \underline{\underline{m_0 \dot{\theta}^2 (d_\eta \sin \bar{\theta} + d_\xi \cos \bar{\theta})}} \quad (2.181)$$

$$k_{w'} = - (2m_0 \Omega \dot{v} + m_0 \Omega^2 x) \left( d_\eta \sin \bar{\theta} + \underline{\underline{d_\xi \cos \bar{\theta}}} \right)$$

$$\begin{aligned}
& + \underline{2m_0\Omega\dot{\theta}} (k_{m\xi}^2 \sin^2 \bar{\theta} + k_{m\eta}^2 \cos^2 \bar{\theta} + k_{m\eta\xi}^2 \sin 2\bar{\theta}) \\
& + \underline{m_0\ddot{u}} (d_\eta \sin \bar{\theta} + d_\xi \cos \bar{\theta}) \tag{2.182}
\end{aligned}$$

$$\begin{aligned}
k_\theta = & - (\underline{2m_0\Omega\dot{v}w'} + m_0\Omega^2 xw' + m_0\ddot{w}) \left( d_\eta \cos \bar{\theta} - \underline{d_\xi \sin \bar{\theta}} \right) \\
& + \left( \underline{2m_0\Omega\dot{v}v'} + m_0\Omega^2 xv' - m_0\Omega^2 v + m_0\ddot{v} + \underline{2m_0\Omega\dot{u}} \right) \left( d_\eta \sin \bar{\theta} + \underline{d_\xi \cos \bar{\theta}} \right) \\
& - 2m_0\Omega\dot{w}' (k_{m\xi}^2 \sin^2 \bar{\theta} + k_{m\eta}^2 \cos^2 \bar{\theta} + k_{m\eta\xi}^2 \sin 2\bar{\theta}) \\
& - m_0\Omega\dot{v}' [(k_{m\xi}^2 - k_{m\eta}^2) \sin 2\bar{\theta} + 2k_{m\eta\xi}^2 \cos 2\bar{\theta}] \\
& - \frac{1}{2}m_0\Omega^2 \left[ (k_{m\xi}^2 - k_{m\eta}^2) \sin 2\bar{\theta} + \underline{2k_{m\xi\eta}^2 \cos 2\bar{\theta}} \right] - m_0k_m^2 \ddot{\theta} \\
& - \underline{m_0\ddot{u}v'} (d_\eta \sin \bar{\theta} + d_\xi \cos \bar{\theta}) + \underline{m_0\ddot{u}w'} (d_\eta \cos \bar{\theta} - d_\xi \sin \bar{\theta}) \tag{2.183}
\end{aligned}$$

---



---

Underline	Meaning
=====	Extension-torsion terms associated with trapeze effect
=====	Bending-torsion terms significant for large twist angles
-----	Non-vanishing terms for arbitrary asymmetric cross-sections
~~~~~	Higher-order terms retained to prevent singular eigenvalue problem

---



---

The terms with a single or double underline do not appear in other studies developed for torsionally stiff rotor blades [21, 22, 50]. However, they are important for the present analysis in which large twist angles are considered. In addition, the dash-underlined terms must generally be retained when the area centroids of the blade cross-sections are not coincident with the elastic axis (as in the case of circular arc airfoils).

Note also the presence of the wave-underlined terms, which are one order of magnitude greater than the order of truncation, defined in § 2.4. If these terms are omitted, then the elements of the mass matrix associated with the equation for the axial displacement  $u$  (i.e. the terms in Eq. (2.178)) are all zero. In that case, an eigenvalue analysis of the equations of motion is found to be singular. To circumvent this issue the additional terms, marked by a wave-underline, are retained.

As indicated in § 2.1, the computation of the trim solution requires only the time-invariant (or steady-state) kinetic energy of the rotor blade. Its expression is deduced from Eq. (2.177) and is given in the next section.

### 2.5.8.3 Time-invariant kinetic energy

Retaining only the time independent terms in Eq. (2.177), we obtain

$$\begin{aligned}
(\delta T_0)_b = & \int_R \left\{ m_0 \Omega^2 x \right\} \delta u \\
& + \left\{ m_0 \Omega^2 v + m_0 \Omega^2 (d_\eta \cos \bar{\theta} - d_\xi \sin \bar{\theta}) \right\} \delta v \\
& + \left\{ -m_0 \Omega^2 x (d_\eta \cos \bar{\theta} - d_\xi \sin \bar{\theta}) \right\} \delta v' \\
& + \left\{ -m_0 \Omega^2 x (d_\eta \sin \bar{\theta} + d_\xi \cos \bar{\theta}) \right\} \delta w' \\
& + \left\{ -m_0 \Omega^2 x w' (d_\eta \cos \bar{\theta} - d_\xi \sin \bar{\theta}) + (m_0 \Omega^2 x v' \right. \\
& \quad \left. - m_0 \Omega^2 v) (d_\eta \sin \bar{\theta} + d_\xi \cos \bar{\theta}) \right. \\
& \quad \left. - \frac{1}{2} m_0 \Omega^2 [(k_{m\xi}^2 - k_{m\eta}^2) \sin 2\bar{\theta} + 2k_{m\xi\eta}^2 \cos 2\bar{\theta}] \right\} \delta \theta \\
& + \mathcal{O}(\epsilon^4)
\end{aligned} \tag{2.184}$$

Finally, the nonlinear expression for the blade kinetic energy can be linearized about the trim state.

#### 2.5.8.4 Linearized kinetic energy

Note that when linearizing the kinetic energy, the generalized coordinates general positions, general velocities and general accelerations ( $\mathbf{q}_i$ 's,  $\dot{\mathbf{q}}_i$ 's and  $\ddot{\mathbf{q}}_i$ 's). Therefore, the expression for the first-order Taylor expansion is

$$(\delta T)_{bLin} = (\delta T)_{b0} + \sum_{i=1}^N \left[ \left( \frac{\partial \delta T}{\partial q_i} \right)_0 \Delta q_i + \left( \frac{\partial \delta T}{\partial \dot{q}_i} \right)_0 \Delta \dot{q}_i + \left( \frac{\partial \delta T}{\partial \ddot{q}_i} \right)_0 \Delta \ddot{q}_i \right] \quad (2.185)$$

or in matrix form

$$(\delta T)_{bLin} = (\delta T)_{b0} + \delta \mathbf{q}^T \mathbf{K} \Delta \mathbf{q} + \delta \mathbf{q}^T \mathbf{G} \Delta \dot{\mathbf{q}} + \delta \mathbf{q}^T \mathbf{M} \Delta \ddot{\mathbf{q}} \quad (2.186)$$

The components of the  $\mathbf{K}$  matrix are added to those obtained from linearization of the strain energy to form the stiffness matrix. In addition,  $\mathbf{G}$  and  $\mathbf{M}$  are the gyroscopic matrix and the mass matrix respectively. Note also that when the gradients are computed, the trim state generalized velocities and generalized accelerations are assumed equal to zero. This is consistent with assuming that the rotor blade at trim state has a constant deformation.

Each element of the mass, gyroscopic and stiffness matrices is shown in Appendix [D.2](#).

Finally, to complete the blade structural model, the gravitational potential energy must be derived.

### 2.5.9 Blade gravitational potential energy

The potential energy associated with the work done by gravitational forces is defined as

$$V_g = \int_R \iint_A \rho g \mathbf{r}_1 \cdot \mathbf{k}_{Z_1} \quad (2.187)$$

where  $\mathbf{r}_1$  is the position vector of a particle on the deformed blade, given by Eq. (2.149). Hence

$$\begin{aligned} V_g &= \int_R \iint_A \rho g \left[ w + \left( 1 - \frac{w'^2}{2} \right) (\eta \sin \bar{\theta} + \xi \cos \bar{\theta}) \right] \\ &= g \int_R \left[ m_0 w + m_0 \left( 1 - \frac{w'^2}{2} \right) (d_\eta \sin \bar{\theta} + d_\xi \cos \bar{\theta}) \right] \end{aligned} \quad (2.188)$$

Taking the variation, we obtain

$$\begin{aligned} (\delta V_g)_b &= g \int_R m_0 \delta w \\ &\quad - \left\{ m_0 w' (d_\eta \sin \bar{\theta} + d_\xi \cos \bar{\theta}) \right\} \delta w' \\ &\quad + \left\{ m_0 \left( 1 - \frac{w'^2}{2} \right) (d_\eta \cos \bar{\theta} - d_\xi \sin \bar{\theta}) \right\} \delta \theta \end{aligned} \quad (2.189)$$

In addition, a linear approximation of the previous equation is given in Appendix D.3.

### 2.5.10 Potential energy stored in the root springs

Rotor blades often feature stiffness singularities at the root due to the compliance of the control mechanism. To model these singularities, torsional springs can be added to the simulation. If the stiffness of the springs in the

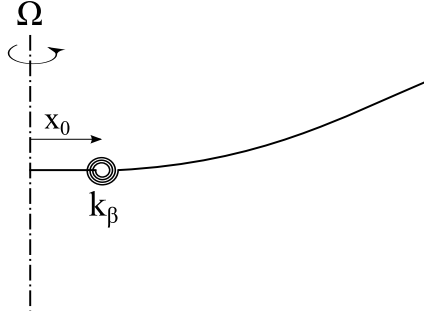


Figure 2.23: Flap torsional spring

lag, flap and twist directions are  $k_\zeta$ ,  $k_\beta$  and  $k_\theta$  respectively (see for instance a torsional spring acting on the flap degree of freedom, in Fig. 2.23), then the expression for the potential energy stored in the springs is

$$(V_{sp})_b = \frac{1}{2} k_\beta w'_{x_0}{}^2 + \frac{1}{2} k_\zeta v'_{x_0}{}^2 + \frac{1}{2} k_\theta \theta_{x_0}^2 \quad (2.190)$$

And the variation in this energy is

$$(\delta V_{sp})_b = k_\beta w'_{x_0} \delta w'_{x_0} + k_\zeta v'_{x_0} \delta v'_{x_0} + k_\theta \theta_{x_0} \delta \theta_{x_0} \quad (2.191)$$

### 2.5.11 Modeling of the tip mass

The mass secured at the tip of the blade contributes to the total kinetic energy and potential gravitational energy of the rotor. The work done by the aerodynamic forces acting on it is ignored.

Two tip mass configurations are studied. In a first configuration, labeled configuration  $BP$ , the tip mass consists of a solid rod of length  $L_m$ , secured perpendicular to the blade spanwise direction. A variable  $\theta_{ind}$  is introduced to account for the presence of an index angle between the blade chord

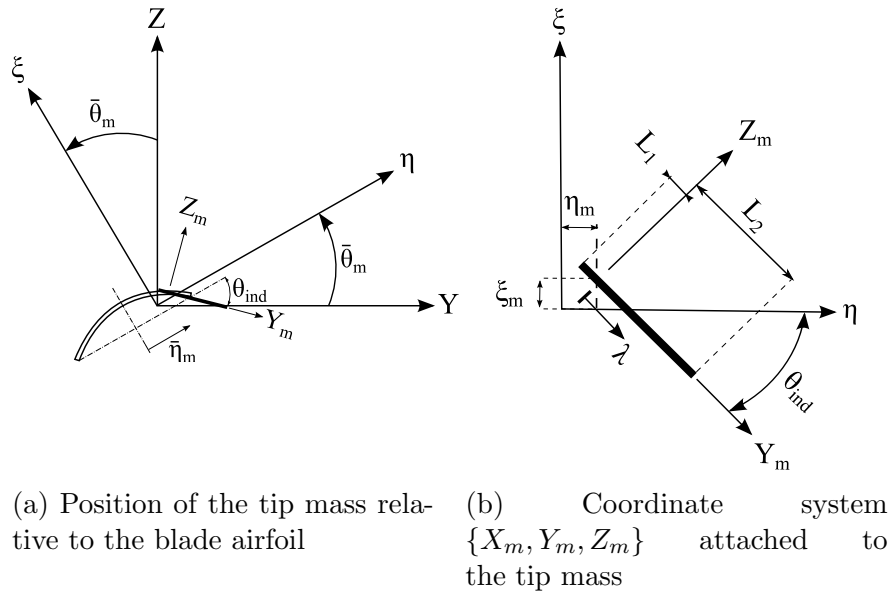


Figure 2.24: Position and orientation of the tip mass in the blade configuration BP

and the tip mass longitudinal axis. The motivation for such an index angle will be given in § 4.1.2 of this dissertation.

The second tip mass configuration, labeled configuration  $C$ , features a solid rod aligned with the blade span and secured at the leading edge. The energies added to the total energy of the rotor system, due to the presence of the tip mass, are derived below for both configurations.

### 2.5.11.1 Configuration BP

The tip mass of the flexible blade BP is a uniform circular tungsten rod, of mass  $m_m$  and density  $\rho_m$ . It is secured perpendicular to the blade spanwise direction (see Fig. 2.24a). The distances between the tip mass attachment

point and the elastic axis are  $\eta_m$  and  $\xi_m$  along the  $\eta$ -axis and  $\xi$ -axis respectively (see Fig. 2.24b). In addition, an index angle  $\theta_{ind}$  is inserted between the longitudinal axis of the tip mass and the blade chord.

The position vector  $\mathbf{r}_{1m}$  of a particle along the longitudinal axis of the tip mass can be deduced from the expression found for  $\mathbf{r}_1$  (Eq. (2.149)), in which we substitute

$$\begin{cases} x = R \\ \eta = \eta_m + \lambda \cos(\theta_{ind}) \\ \xi = \xi_m - \lambda \sin(\theta_{ind}) \end{cases} \quad (2.192)$$

where  $\lambda$  is a bound variable which takes values in the range  $[-L_1; L_2]$ . The result of the substitution is

$$\mathbf{r}_{1m} = \begin{Bmatrix} x_{1m} \\ y_{1m} \\ z_{1m} \end{Bmatrix} = \begin{Bmatrix} R + u_m - w'_m [\eta_m \sin \bar{\theta}_m + \xi_m \cos \bar{\theta}_m + \lambda \sin (\bar{\theta}_m - \theta_{ind})] \\ -v'_m [\eta_m \cos \bar{\theta}_m - \xi_m \sin \bar{\theta}_m + \lambda \cos (\bar{\theta}_m - \theta_{ind})] \\ v_m + \left(1 - \frac{v_m'^2}{2}\right) [\eta_m \cos \bar{\theta}_m - \xi_m \sin \bar{\theta}_m + \lambda \cos (\bar{\theta}_m - \theta_{ind})] \\ -v'_m w'_m [\eta_m \sin \bar{\theta}_m + \xi_m \cos \bar{\theta}_m + \lambda \sin (\bar{\theta}_m - \theta_{ind})] \\ w_m + \left(1 - \frac{w_m'^2}{2}\right) [\eta_m \sin \bar{\theta}_m + \xi_m \cos \bar{\theta}_m + \lambda \sin (\bar{\theta}_m - \theta_{ind})] \end{Bmatrix} \quad (2.193)$$

In addition, we can take the variation in the position vector  $\delta \mathbf{r}_{1m}$  (see Eq. (C.16)-(C.18)) and use the result to derive the kinetic energy and the gravitational potential energy associated with the tip mass.

**Kinetic energy** The expression for the kinetic energy can easily be derived by applying the change of variables defined by Eq. (2.192) to the general

expression for the kinetic energy of the airfoil (see Eq. (C.15)), and then integrating over the tip mass volume instead of the blade volume.

For simplicity, we define the following integrals

$$m_m = \int_{-L_1}^{L_2} \iint_{A_m} \rho_m dA_m d\lambda \quad (2.194)$$

$$\begin{aligned} m_m T_1 &= \int_{-L_1}^{L_2} \iint_{A_m} \rho_m (\eta \sin + \xi \cos) dA_m d\lambda \\ &= m_m \left[ \eta_m \sin \bar{\theta}_m + \xi_m \cos \bar{\theta}_m + \frac{L_2 - L_1}{2} \sin(\bar{\theta}_m - \theta_{ind}) \right] \end{aligned} \quad (2.195)$$

$$\begin{aligned} m_m T_2 &= \int_{-L_1}^{L_2} \iint_{A_m} \rho_m (\eta \cos - \xi \sin) dA_m d\lambda \\ &= m_m \left[ \eta_m \cos \bar{\theta}_m - \xi_m \sin \bar{\theta}_m + \frac{L_2 - L_1}{2} \cos(\bar{\theta}_m - \theta_{ind}) \right] \end{aligned} \quad (2.196)$$

$$\begin{aligned} m_m T_3 &= \int_{-L_1}^{L_2} \iint_{A_m} \rho_m (\eta \sin + \xi \cos)^2 dA_m d\lambda \\ &= m_m \left[ \eta_m^2 \sin^2 \bar{\theta}_m + \xi_m^2 \cos^2 \bar{\theta}_m + \eta_m \xi_m \sin 2\bar{\theta}_m \right. \\ &\quad + \frac{L_2 - L_1}{2} (2\eta_m \sin \bar{\theta}_m \sin(\bar{\theta}_m - \theta_{ind}) + 2\xi_m \cos \bar{\theta}_m \sin(\bar{\theta}_m - \theta_{ind})) \\ &\quad \left. + \frac{L_1^3 + L_2^3}{3(L_1 + L_2)} \sin^2(\bar{\theta}_m - \theta_{ind}) \right] \end{aligned} \quad (2.197)$$

$$\begin{aligned} m_m T_4 &= \int_{-L_1}^{L_2} \iint_{A_m} \rho_m (\eta \cos - \xi \sin)^2 dA_m d\lambda \\ &= m_m \left[ \eta_m^2 \cos^2 \bar{\theta}_m + \xi_m^2 \sin^2 \bar{\theta}_m - \eta_m \xi_m \sin 2\bar{\theta}_m \right. \\ &\quad \left. + \frac{L_2 - L_1}{2} (2\eta_m \cos \bar{\theta}_m \cos(\bar{\theta}_m - \theta_{ind}) - 2\xi_m \sin \bar{\theta}_m \cos(\bar{\theta}_m - \theta_{ind})) \right] \end{aligned}$$

$$+ \frac{L_1^3 + L_2^3}{3(L_1 + L_2)} \cos^2(\bar{\theta}_m - \theta_{ind}) \Big] \quad (2.198)$$

$$\begin{aligned} m_m T_5 &= \int_{-L_1}^{L_2} \iint_{A_m} \rho_m (\eta \sin + \xi \cos) (\eta \cos - \xi \sin) dA_m d\lambda \\ &= m_m \left[ (\eta_m^2 - \xi_m^2) \sin \bar{\theta}_m \cos \bar{\theta}_m + \eta_m \xi_m \cos 2\bar{\theta}_m \right. \\ &\quad + \frac{L_2 - L_1}{2} (\eta_m \sin(2\bar{\theta}_m - \theta_{ind}) + \xi_m \cos(2\bar{\theta}_m - \theta_{ind})) \\ &\quad \left. + \frac{L_1^3 + L_2^3}{3(L_1 + L_2)} \sin(\bar{\theta}_m - \theta_{ind}) \cos(\bar{\theta}_m - \theta_{ind}) \right] \end{aligned} \quad (2.199)$$

Therefore, the variation in the kinetic energy of the tip mass is

$$\begin{aligned} (\delta T)_m &= \left\{ m_m \Omega^2 x_m + 2m_m \Omega \dot{v}_m - 2m_m T_1 \Omega \dot{\theta}_m \right\} \delta u_m \\ &\quad + \left\{ m_m \Omega^2 v_m - m_m \ddot{v}_m - 2m_m \Omega \dot{u}_m + m_m T_1 (\ddot{\theta}_m + 2\Omega \dot{w}'_m - 2\Omega v'_m \dot{\theta}_m) \right. \\ &\quad \left. + m_m T_2 (\Omega^2 + \dot{\theta}_m^2 + 2\Omega w'_m \dot{\theta}_m + 2\Omega \dot{v}'_m) \right\} \delta v_m \\ &\quad + \left\{ 2m_m T_5 \Omega \dot{\theta}_m + m_m T_2 (-2\Omega \dot{v}_m - \Omega^2 x_m) \right\} \delta v'_m \\ &\quad + \left\{ -m_m \ddot{w}_m + m_m T_1 \dot{\theta}_m^2 - m_m T_2 \ddot{\theta}_m \right\} \delta w_m \\ &\quad + \left\{ 2m_m T_3 \Omega \dot{\theta}_m + m_m T_1 (-2\Omega \dot{v}_m - \Omega^2 x_m) \right\} \delta w'_m \\ &\quad + \left\{ m_m T_1 (2\Omega \dot{v}_m v'_m + \Omega^2 x_m v'_m - \Omega^2 v_m + \ddot{v}_m + 2\Omega \dot{u}_m) \right. \\ &\quad \left. + m_m T_2 (-2\Omega \dot{v}_m w'_m - \Omega^2 x_m w'_m - \ddot{w}_m) + m_m T_3 (-\ddot{\theta}_m - 2\Omega \dot{w}'_m) \right. \\ &\quad \left. + m_m T_4 (-\ddot{\theta}_m) + m_m T_5 (-\Omega^2 - 2\Omega \dot{v}'_m) \right\} \delta \theta_m \\ &\quad + \mathcal{O}(\epsilon^4) \end{aligned} \quad (2.200)$$

The Taylor expansion about the trim condition of this expression is given in

#### Appendix D.4.

If only the time-invariant terms in the kinetic energy are retained, we obtain the steady-state kinetic energy of the tip mass as

$$\begin{aligned}
(\delta T_0)_m &= \left\{ m_m \Omega^2 x_m \right\} \delta u_m + \left\{ m_m \Omega^2 v_m + m_m \Omega^2 T_2 \right\} \delta v_m \\
&\quad - \left\{ m_m \Omega^2 x_m T_2 \right\} \delta v'_m - \left\{ m_m \Omega^2 x_m T_1 \right\} \delta w'_m \\
&\quad + \left\{ (m_m \Omega^2 x_m v'_m - m_m \Omega^2 v_m) T_1 - m_m \Omega^2 x_m w'_m T_2 - m_m \Omega^2 T_5 \right\} \delta \theta_m \\
&\quad + \mathcal{O}(\epsilon^4) \tag{2.201}
\end{aligned}$$

The expansion of the constants  $T_1$ ,  $T_2$  and  $T_5$  in the previous expression, in terms of the geometric parameters  $\eta_m$ ,  $\xi_m$ ,  $L_1$  and  $L_2$ , give some insight into the kinematic stiffening of the rotor blade generated by the tip mass. Substituting Eq. (2.194)-(2.199) into Eq. (2.200), we obtain

$$\begin{aligned}
(\delta T_0)_m &= m_m \Omega^2 x_m \delta u_m \\
&\quad + m_m \Omega^2 \left\{ v_m + \eta_m \cos \bar{\theta}_m - \xi_m \sin \bar{\theta}_m + \frac{L_2 - L_1}{2} \cos(\bar{\theta}_m - \theta_{ind}) \right\} \delta v_m \\
&\quad - m_m \Omega^2 x_m \left\{ \eta_m \cos \bar{\theta}_m - \xi_m \sin \bar{\theta}_m + \frac{L_2 - L_1}{2} \cos(\bar{\theta}_m - \theta_{ind}) \right\} \delta v'_m \\
&\quad - m_m \Omega^2 x_m \left\{ \eta_m \sin \bar{\theta}_m + \xi_m \cos \bar{\theta}_m + \frac{L_2 - L_1}{2} \sin(\bar{\theta}_m - \theta_{ind}) \right\} \delta w'_m \\
&\quad - m_m \Omega^2 \left\{ x_m w'_m \left( \eta_m \cos \bar{\theta}_m - \xi_m \sin \bar{\theta}_m + \frac{L_2 - L_1}{2} \cos(\bar{\theta}_m - \theta_{ind}) \right) \right. \\
&\quad \left. - (x_m v'_m - v_m) \left( \eta_m \sin \bar{\theta}_m + \xi_m \cos \bar{\theta}_m + \frac{L_2 - L_1}{2} \sin(\bar{\theta}_m - \theta_{ind}) \right) \right. \\
&\quad \left. + \left( \frac{\eta_m^2}{2} - \frac{\xi_m^2}{2} \right) \sin 2\bar{\theta}_m + \eta_m \xi_m \cos 2\bar{\theta}_m + \frac{L_1^3 + L_2^3}{6(L_1 + L_2)} \sin 2(\bar{\theta}_m - \theta_{ind}) \right\} \delta \theta_m
\end{aligned}$$

$$\begin{aligned}
& + \frac{L_2 - L_1}{2} (\eta_m \sin(2\bar{\theta}_m - \theta_{ind}) + \xi_m \cos(2\bar{\theta}_m - \theta_{ind})) \} \delta\theta_m \\
& + \mathcal{O}(\epsilon^4)
\end{aligned} \tag{2.202}$$

We can further simplify this equation for the case where the tip mass is attached at its center (i.e.  $L_1 = L_2$ ), and that the attachment point is coincident with the elastic axis (i.e.  $\eta_m = \xi_m = 0$ ). The variation in the tip mass kinetic energy then reduces to a single term given by

$$(\delta T_0)_m = -m_m \Omega^2 \frac{L^2}{12} \sin [2 (\bar{\theta}_m - \theta_{ind})] \delta\theta_m \tag{2.203}$$

which can be recognized as the restoring propeller moment due to the centrifugal forces acting on the tip mass. It can be seen that this restoring moment will vanish if the index angle  $\theta_{ind}$  is equal to the pitch angle at the tip of the blade  $\bar{\theta}_m$ .

**Gravitational potential energy** The variation in the gravitational potential energy of the tip mass is given by

$$(\delta V_g)_m = m_m g \delta z_m \tag{2.204}$$

Using Eq. (C.16)-(C.18), we obtain

$$(\delta V_g)_m = m_m g \delta w_m - m_m g w'_m T_1 \delta w'_m + m_m g \left(1 - \frac{w_m'^2}{2}\right) T_2 \delta\theta_m \tag{2.205}$$

The linearization of this expression about the trim state is shown in Appendix D.5.

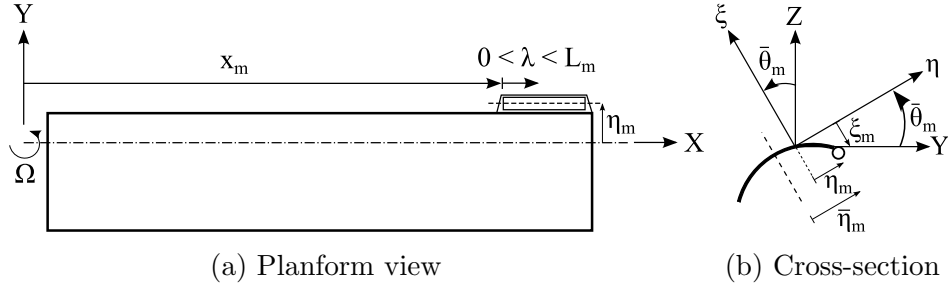


Figure 2.25: Position and orientation of the tip mass for the blade configuration C

### 2.5.11.2 Configuration C

The derivation of the energies associated with the tip mass in configuration C is similar to that corresponding to the tip mass BP. The planform view and cross-section of the flexible rotor blade C are shown in Fig. 2.25. In this case, the tip body is a solid rod of length  $L_m$  and mass  $m_m$ . The distance from the axis of rotation  $Z$  to the inboard end of the tip mass is  $x_m$ . In addition,  $\eta_m$  and  $\xi_m$  are the rod longitudinal axis offsets from the elastic axis of the blade, along the  $\eta$ - and  $\xi$ - direction respectively (see Fig. 2.25b, note that  $\eta_m > 0$  and  $\xi_m < 0$ ).

The position vector of a particle along the longitudinal axis of the tip mass is obtained from Eq. (2.149), in which we substitute

$$\begin{cases} x = x_m + \lambda \\ \eta = \eta_m \\ \xi = \xi_m \end{cases} \quad (2.206)$$

Thus, the components of the position vector in the  $\{X, Y, Z\}$  reference frame

are

$$\mathbf{r}_{1m} = \begin{Bmatrix} x_{1m} \\ y_{1m} \\ z_{1m} \end{Bmatrix} \quad (2.207)$$

where

$$\begin{cases} x_{1m} = (x_m + \lambda) + u_m - w'_m [\eta_m \sin \bar{\theta}_m + \xi_m \cos \bar{\theta}_m] - v'_m [\eta_m \cos \bar{\theta}_m - \xi_m \sin \bar{\theta}_m] \\ y_{1m} = v_m + \left(1 - \frac{v_m'^2}{2}\right) [\eta_m \cos \bar{\theta}_m - \xi_m \sin \bar{\theta}_m] - v'_m w'_m [\eta_m \sin \bar{\theta}_m + \xi_m \cos \bar{\theta}_m] \\ z_{1m} = w_m + \left(1 - \frac{w_m'^2}{2}\right) [\eta_m \sin \bar{\theta}_m + \xi_m \cos \bar{\theta}_m] \end{cases} \quad (2.208)$$

Note that as the rigid mass does not deform, twist and bending deformations of the blade airfoil for  $x \in [x_m; x_m + L_m]$  are prevented. Also noting that  $L_m \ll R$ , we can assume that

$$v_m = v(x_m + \lambda) \simeq v(x_m) \quad (2.209)$$

$$w_m \simeq w(x_m) \quad (2.210)$$

$$\theta_m \simeq \theta(x_m) \quad (2.211)$$

Subsequently, the expressions for the kinetic energy and the gravitational potential energy associated with the tip mass C are given by Eq. (2.200) and (2.205), in which  $x_m$  is replaced by  $x_m + L_m/2$ , and in which the following integral constants are substituted

$$m_m = \int_0^L \iint_{A_m} \rho_m dA_m d\lambda \quad (2.212)$$

$$m_m T_1 = \int_0^L \iint_{A_m} \rho_m (\eta_m \sin \bar{\theta}_m + \xi_m \cos \bar{\theta}_m) dA_m d\lambda$$

$$= m_m (\eta_m \sin \bar{\theta}_m + \xi_m \cos \bar{\theta}_m) \quad (2.213)$$

$$\begin{aligned} m_m T_2 &= \int_0^L \iint_{A_m} \rho_m (\eta_m \cos \bar{\theta}_m - \xi_m \sin \bar{\theta}_m) dA_m d\lambda \\ &= m_m (\eta_m \cos \bar{\theta}_m - \xi_m \sin \bar{\theta}_m) \end{aligned} \quad (2.214)$$

$$\begin{aligned} m_m T_3 &= \int_0^L \iint_{A_m} \rho_m (\eta_m \sin \bar{\theta}_m + \xi_m \cos \bar{\theta}_m)^2 dA_m d\lambda \\ &= m_m \left[ \eta_m^2 \sin^2 \bar{\theta}_m + \xi_m^2 \cos^2 \bar{\theta}_m + \eta_m \xi_m \sin 2\bar{\theta}_m \right] \end{aligned} \quad (2.215)$$

$$\begin{aligned} m_m T_4 &= \int_0^L \iint_{A_m} \rho_m (\eta_m \cos \bar{\theta}_m - \xi_m \sin \bar{\theta}_m)^2 dA_m d\lambda \\ &= m_m \left[ \eta_m^2 \cos^2 \bar{\theta}_m + \xi_m^2 \sin^2 \bar{\theta}_m - \eta_m \xi_m \sin 2\bar{\theta}_m \right] \end{aligned} \quad (2.216)$$

$$\begin{aligned} m_m T_5 &= \int_0^L \iint_{A_m} \rho_m (\eta_m \sin \bar{\theta}_m + \xi_m \cos \bar{\theta}_m) (\eta_m \cos \bar{\theta}_m - \xi_m \sin \bar{\theta}_m) \\ &= m_m \left[ \frac{1}{2} (\eta_m^2 - \xi_m^2) \sin 2\bar{\theta}_m + \eta_m \xi_m \cos 2\bar{\theta}_m \right] \end{aligned} \quad (2.217)$$

The calculation of the energies related to the presence of the tip mass completes the derivation of the structural model. In the next section, the aerodynamic model is derived.

## 2.6 Aerodynamic Model

The virtual work done by aerodynamic forces and moments is calculated from 2-D strip theory assuming incompressible flow. In addition, we assume

that the aerodynamic loading is only influenced by the apparent velocity in the plane of the deformed blade cross-section. A general aerodynamic model is developed for unsteady flow, in which the airfoil is assumed to experience harmonic pitching and heaving motion. The resulting expressions are then specialized to the case of quasi-steady flow. In both cases, 2-D aerodynamic coefficients are extracted from lookup tables developed from experimental measurements. In addition, the steady induced inflow is calculated from classical blade element-momentum theory (BEMT).

### 2.6.1 Unsteady aerodynamic model

To accurately predict unsteady aeroelastic phenomena, such as dynamic instabilities (flutter or limit cycle oscillations), unsteady aerodynamic effects must be considered, and their impact on the aerodynamic loads must be assessed. In particular, blade motion (pitching or flapping), blade deformations (elastic twist or bending) and perturbation of the downwash produced by discrete tip vortices are various sources that may affect the blade aerodynamic loads [41].

One important parameter used to quantify the degree of unsteadiness of the aerodynamics of an airfoil is the reduced frequency. This dimensionless parameter is defined as

$$k = \frac{\omega c}{2V_\infty} \quad (2.218)$$

where  $\omega$  is the frequency of oscillations of the airfoil and  $V_\infty$  is the free-stream velocity. Using a dimensional analysis, it can be shown that the resultant

aerodynamic forces acting on an oscillating airfoil can be written as a function of the reduced frequency, in addition to the Reynolds number and the Mach number. According to the value of the reduced frequency, assumptions regarding the flow can be made, as follows

$$\left\{ \begin{array}{ll} k = 0 & \text{steady flow} \\ 0 \leq k \leq 0.05 & \text{quasi-steady flow} \\ 0.05 \leq k \leq 0.2 & \text{unsteady flow} \\ k > 0.2 & \text{highly unsteady flow} \end{array} \right. \quad (2.219)$$

Note that for a helicopter rotor blade, the reduced frequency (like the Reynolds number or the Mach number) is an ambiguous parameter as it depends upon the local air velocity, which varies radially. One convention is to calculate this parameter at the 75% radius location. This approach is employed in this dissertation, and the corresponding reduced frequency is denoted  $k_{75}$ .

In the next two sections, the equations for the unsteady lift and pitching moment acting on an airfoil are derived. First, Theodorsen's theory, focused on the unsteady aerodynamics of a flat plate, is recalled. Then, the theory is adapted to the case of a rotor blade operating in hover.

### 2.6.1.1 Theodorsen's theory for a flat plate

The following derivation is based on Theodorsen's theory [35, 81] for a thin flat plate experiencing oscillatory pitching and heaving motion in a steady flow. The flow surrounding the plate is assumed to be inviscid, incompressible, and to always remain attached to the airfoil. In addition, it is assumed that the thin airfoil has a chord of length  $2b$ , and is pitching at a rate  $\dot{\alpha}$  about

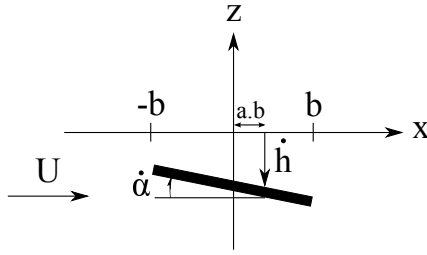


Figure 2.26: Thin airfoil section undergoing pitching and heaving motion

a point located a distance  $x = a \cdot b$  from the mid-chord.  $x$  is the chordwise coordinate, directed from the leading-edge towards the trailing-edge, as shown in Fig. 2.26. Finally, the vertical heaving velocity is  $\dot{h}$ , defined to be positive downward.

The lift and moment acting on the section shown in Fig. 2.26 can be expressed in terms of circulatory components ( $L_C$ ,  $M_C$ ) and noncirculatory components ( $L_{NC}$ ,  $M_{NC}$ ) as

$$L = L_C + L_{NC} \quad (2.220)$$

$$M = M_C + M_{NC} \quad (2.221)$$

The circulatory lift is obtained from potential flow theory. In this theory, the presence of the airfoil in a flow field is represented by a vortex sheet placed along the chordline, resulting in a net vorticity called the bound circulation. When the bound circulation of the airfoil is suddenly changed, under the action of pitching or heaving motion for instance, an equal and opposite amount of vorticity is shed into the wake, as required by Kelvin's circulation theorem. The shed vorticity in the wake induces velocity at the airfoil (which can be

calculated using the Biot-Savart Law) that opposes the change in lift associated with the unsteady pitching or heaving. This “lift deficiency” effect decays as the shed vortex travels downstream, hence it depends on the free-stream velocity and on the frequency of oscillation of the airfoil. The wake-induced lift deficiency is commonly represented by a complex function of the reduced frequency  $k$ , called the *Theodorsen lift deficiency function* [35], and is equal to

$$C(k) = F(k) + iG(k) = \frac{H_1^{(2)}(k)}{H_1^{(2)}(k) + iH_0^{(2)}(k)} \quad (2.222)$$

The Hankel function is defined as  $H_\nu^{(2)} = J_\nu - iY_\nu$ , with  $J_\nu$  and  $Y_\nu$  being Bessel functions of the first and second kind, respectively.

As a result, the circulatory lift can be rewritten [77, 78] as

$$L_C = L_{QS}C(k) \quad (2.223)$$

$$= 2\pi\rho_\infty Ub \left[ U\alpha + \dot{h} + \left( \frac{1}{2} - a \right) b\dot{\alpha} \right] C(k) \quad (2.224)$$

where  $L_{QS}$  is the quasi-steady lift and  $\rho_\infty$  is the density of air. The magnitude and phase of the Theodorsen function  $C(k)$  are shown in Fig. 2.27.

Note that the third term inside the square bracket of Eq. (2.224) vanishes when the pitching axis is located at the three-quarter chord point (i.e.  $a = 1/2$ ). Hence, it can be seen that the square bracket quantity represents the downwash at three-quarter chord. Moreover, note that one cannot define a unique angle of attack for unsteady flow, since the flow direction varies along the chordline as a result of the varying downwash. However, it is possible to introduce a

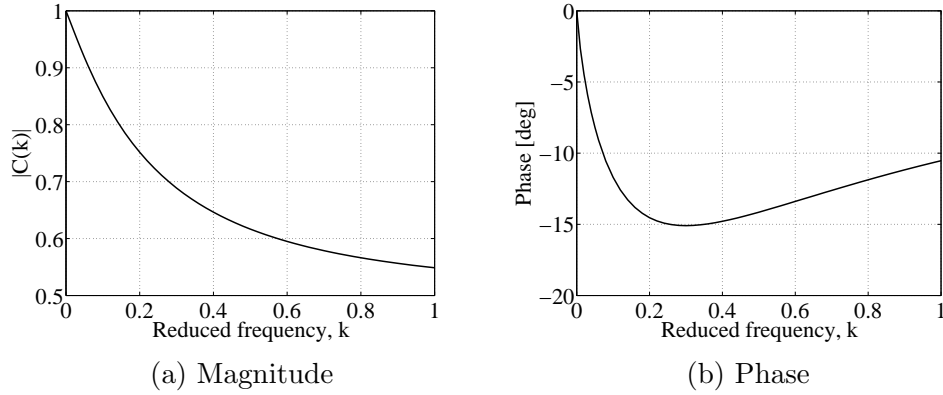


Figure 2.27: Theodorsen lift deficiency function

so-called *effective angle of attack*, as

$$\alpha_{eff} = \left[ \alpha + \frac{\dot{h}}{U} + \left( \frac{1}{2} - a \right) \frac{b}{U} \dot{\alpha} \right] C(k) \quad (2.225)$$

Additionally, the noncirculatory lift is a result of the mass of air being accelerated by motion of the airfoil, perpendicular to its chord. Unlike its circulatory counterpart, the non-circulatory lift does not depend upon vorticity and it can exist even when the free-stream velocity is zero. It is composed of the following two terms [77]:

1. A lift force with center of pressure at the mid-chord, of magnitude equal to the apparent mass of a cylinder of air, of radius equal to the semi-chord  $b$ , multiplied by the vertical acceleration at the mid-chord point:

$$L_{NC}^{(1)} = \rho_{\infty} \pi b^2 \left( \ddot{h} - ab \ddot{\alpha} \right)$$

2. A lift force with center of pressure at the 3/4-chord point, of the nature of a centrifugal force, of amount equal to the apparent mass  $\rho_{\infty} \pi b^2$  times

$U\dot{\alpha}$ :

$$L_{NC}^{(2)} = \rho_{\infty}\pi b^2 U\dot{\alpha}$$

Finally, the noncirculatory moment is a nose-down couple equal to the apparent moment of inertia  $\rho_{\infty}\pi b^2(b^2/8)$  multiplied by the angular acceleration  $\ddot{\alpha}$ :

$$M_a = -\frac{\rho_{\infty}\pi b^4}{8}\ddot{\alpha}$$

Combining the results above, the total lift per unit span is

$$L = L_C + L_{NC}^{(1)} + L_{NC}^{(2)} \quad (2.226)$$

$$= 2\pi\rho_{\infty}Ub \left[ U\alpha + \dot{h} + \left(\frac{1}{2} - a\right) b\dot{\alpha} \right] C(k) + \rho_{\infty}\pi b^2 \left[ U\dot{\alpha} + \ddot{h} - ab\ddot{\alpha} \right] \quad (2.227)$$

And the total moment per unit span about the pitching axis is

$$M = b \left(\frac{1}{2} + a\right) L_C + ab L_{NC}^{(1)} - \left(\frac{1}{2} - a\right) b L_{NC}^{(2)} + M_a \quad (2.228)$$

$$= 2\pi\rho_{\infty}Ub^2 \left(\frac{1}{2} + a\right) \left[ U\alpha + \dot{h} + \left(\frac{1}{2} - a\right) b\dot{\alpha} \right] C(k) \\ + \rho_{\infty}\pi b^3 \left[ a\ddot{h} - \left(\frac{1}{2} - a\right) U\dot{\alpha} - \left(\frac{1}{8} + a^2\right) b\ddot{\alpha} \right] \quad (2.229)$$

These equations were derived for the case of a flat plate undergoing pitching and heaving oscillations in a two-dimensional flow. They can now be adapted to the case of a rotor blade in hover.

### 2.6.1.2 Unsteady aerodynamics theory for a rotor blade in hover

In the case of a rotor blade, it is assumed that the pitching axis coincides with the elastic axis. In addition, the chord  $c$  is used instead of the semi-

chord  $b$ . We also introduce the variable  $x_A$  representing the distance of the aerodynamic center aft of the pitch axis ( $x_A = -b(1/2 + a)$ ).

The 2-D lift coefficient slope of the thin plate (equal to  $2\pi$  from thin airfoil theory) is replaced by the lift coefficient slope of the airfoil  $C_{l\alpha}$ . Note that substituting  $2\pi$  for  $C_{l\alpha}$  affects both the circulatory and noncirculatory lifts and moments, as shown in Ref. [82]. In addition, for a nonsymmetric circular arc airfoil, a lift coefficient and a moment coefficient at zero angle of attack,  $C_{l0}$  and  $C_{m0}$ , must be included.

Additionally, Theodorsen's theory has represented an isolated 2-D airfoil with the wake convected downstream to infinity. However, when rotor blades are modeled, the effect of the returning wake shed by blades in previous revolutions, on the blade in question, must be considered. The two-dimensional model for unsteady aerodynamics of rotor blades, developed by Loewy [36], includes this effect. In Loewy's model, the Theodorsen lift deficiency function  $C(k)$  is replaced by Loewy function  $C'(k)$  to model the influence of the returning shed wake on the unsteady airloads. Loewy function is defined as

$$C'(k, m, h) = \frac{H_1^{(2)}(k) + 2 J_1(k) W(k, m, h)}{H_1^{(2)}(k) + i H_0^{(2)}(k) + 2 [J_1(k) + i J_0(k)] W(k, m, h)} \quad (2.230)$$

where  $m = \omega/\Omega$ , and  $h$  is the vertical separation between vortex sheets below the airfoil. This distance depends on the mean induced velocity  $\bar{\lambda}_i$  and the rotor solidity  $\sigma$  ( $h = 2c\bar{\lambda}_i/\sigma$ ). In addition, the complex valued function  $W$  is

given by

$$W(k, m, h) = \frac{1}{e^{\frac{2kh}{c}} e^{i2\pi m} - 1} \quad (2.231)$$

Plots of the magnitude and phase of Loewy function as a function of the reduced frequency and wake spacing, and for various values of  $m$  can be found in Ref. [82].

Consequently, the total lift and pitching moment about the elastic axis become

$$L = C'(k) \left\{ \frac{1}{2} \rho_\infty U^2 c C_{l0} + \frac{1}{2} \rho_\infty U c C_{l\alpha} \left[ (\dot{h} + U\alpha) + \left(x_A + \frac{c}{2}\right) \dot{\alpha} \right] \right\} + \frac{1}{2} \rho_\infty C_{l\alpha} \frac{c^2}{4} \left[ (\ddot{h} + U\dot{\alpha}) + \left(x_A + \frac{c}{4}\right) \ddot{\alpha} \right] \quad (2.232)$$

$$M = C'(k) \left\{ \frac{1}{2} \rho_\infty U^2 c^2 C_{m0} - \frac{1}{2} \rho_\infty U^2 c C_{l0} x_A - \frac{1}{2} \rho_\infty U c C_{l\alpha} x_A \left[ (\dot{h} + U\alpha) + \left(x_A + \frac{c}{2}\right) \dot{\alpha} \right] \right\} + \frac{1}{2} \rho_\infty C_{l\alpha} \frac{c^2}{4} \left[ - \left(x_A + \frac{c}{4}\right) (\ddot{h} + U\dot{\alpha}) - \frac{c}{4} U \dot{\alpha} - \frac{c^2}{4} \left( \frac{3}{8} + \frac{2x_A}{c} \left( 1 + \frac{2x_A}{c} \right) \right) \ddot{\alpha} \right] \quad (2.233)$$

The quantity  $(\dot{h} + U\alpha)$  in the previous equations represents the airfoil upwash velocity at the elastic axis. It is the opposite of the airfoil downwash velocity, classically used in the rotorcraft community, and denoted by  $U_P$  (see Fig. 2.28).

$$U_P = -(\dot{h} + U\alpha) \quad (2.234)$$

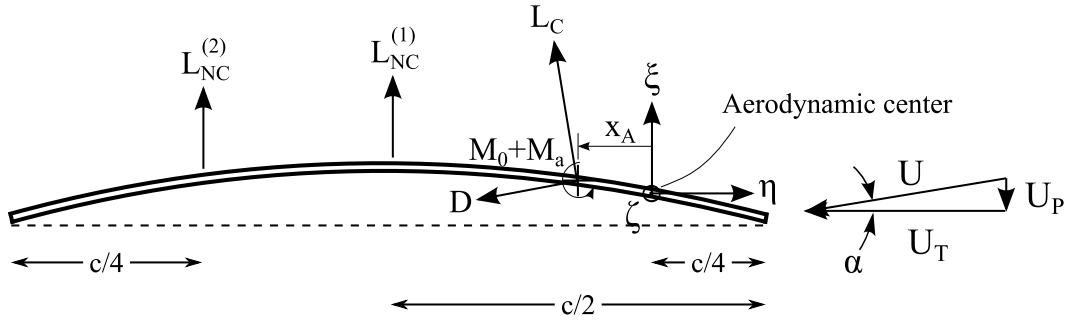


Figure 2.28: Aerodynamic forces on a blade cross-section

In addition, the airfoil velocity parallel to the chord is denoted by  $U_T$ , and  $\mathbf{U}$  is the vector resultant of the sum of  $\mathbf{U}_T$  and  $\mathbf{U}_P$ . Since  $U_P$  is typically much smaller than  $U_T$ , we have

$$U = \sqrt{U_T^2 + U_P^2} \sim U_T \quad (2.235)$$

Note also the instantaneous angle of attack  $\alpha$  in Fig. 2.28, defined as the angle between the airfoil chord and the resultant velocity  $\mathbf{U}$ . Substituting Eq. (2.234) and (2.235) into Eq. (2.232), we can re-write the unsteady lift as

$$L = C'(k) \left\{ \frac{1}{2} \rho_\infty U_T^2 c C_{l0} + \frac{1}{2} \rho_\infty U_T c C_{l\alpha} \left[ -U_P + \left( x_A + \frac{c}{2} \right) \dot{\alpha} \right] \right\} + \frac{1}{2} \rho_\infty C_{l\alpha} \frac{c^2}{4} \left[ -\dot{U}_P + \left( x_A + \frac{c}{4} \right) \ddot{\alpha} \right] \quad (2.236)$$

Finally, the aerodynamic profile drag, acting parallel to  $\mathbf{U}$  is included based on a constant profile drag coefficient  $C_{d0}$ ,

$$D = \frac{1}{2} \rho_\infty U^2 c C_{d0} \quad (2.237)$$

The components of the aerodynamic forces can be projected in the  $\{\zeta, \eta, \xi\}$

coordinate system, giving

$$\left\{ \begin{array}{l} F_\eta = -L_C \sin \alpha - D \cos \alpha \\ F_\xi = L_C \cos \alpha + L_{NC} - D \sin \alpha \end{array} \right. \quad (2.238a)$$

$$\quad (2.238b)$$

where  $\cos \alpha = U_T/U$  and  $\sin \alpha = U_P/U$ . The aerodynamic force along the  $\zeta$ -axis  $F_\zeta$ , due to the radial velocity  $U_R$ , is a profile drag force which is neglected in the present model. Substitution of Eq. (2.232)-(2.237) into Eq. (2.238a) and (2.238b) yields

$$F_\eta = \left\{ -\frac{1}{2} \rho_\infty c C_{l0} U_T U_P + \frac{1}{2} \rho_\infty c C_{l\alpha} \left[ U_P^2 - U_P \left( x_A + \frac{c}{2} \right) \dot{\alpha} \right] \right\} C'(k) - \frac{1}{2} \rho_\infty U_T^2 c C_{d0} \quad (2.239)$$

$$F_\xi = \left\{ \frac{1}{2} \rho_\infty c C_{l0} U_T^2 + \frac{1}{2} \rho_\infty c C_{l\alpha} \left[ -U_P U_T + U_T \left( x_A + \frac{c}{2} \right) \dot{\alpha} \right] \right\} C'(k) + \frac{1}{2} \rho_\infty C_{l\alpha} \frac{c^2}{4} \left[ -\dot{U}_P + \left( x_A + \frac{c}{4} \right) \ddot{\alpha} \right] \quad (2.240)$$

$$M_\zeta = \left\{ \frac{1}{2} \rho_\infty c^2 C_{m0} U_T^2 - \frac{1}{2} \rho_\infty U_T^2 c C_{l0} x_A - \frac{1}{2} \rho_\infty U_T c C_{l\alpha} x_A \left[ -U_P + \left( x_A + \frac{c}{2} \right) \dot{\alpha} \right] \right\} C'(k) + \frac{1}{2} \rho_\infty C_{l\alpha} \frac{c^2}{4} \left[ \left( x_A + \frac{c}{4} \right) \dot{U}_P - \frac{c}{4} U_T \dot{\alpha} - \frac{c^2}{4} \left( \frac{3}{8} + \frac{2x_A}{c} \left( 1 + \frac{2x_A}{c} \right) \right) \ddot{\alpha} \right] \quad (2.241)$$

where  $U_P/U_T$  and  $C_{d0}/C_{l\alpha}$  are neglected compared to unity.

Next,  $U_P$ ,  $U_T$  and  $\alpha$  must be obtained in terms of the rotor blade degrees of freedom  $u$ ,  $v$ ,  $w$  and  $\theta$ . The velocity vector of a point located on the elastic axis of the deformed blade rotating in vacuum was obtained in § 2.5

(see Eq. (2.171), for which  $\eta = \xi = 0$ ). Adding to this expression the induced velocity  $V_i$ , directed along the vertical  $Z$ -axis, we obtain the components of the blade velocity projected in the  $\{X, Y, Z\}$  coordinate system, as

$$\mathbf{U} = (\dot{u} - \Omega v) \mathbf{i}_X + (\dot{v} + \Omega(x + u)) \mathbf{j}_Y + (\dot{w} + V_i) \mathbf{k}_Z \quad (2.242)$$

Using the transformation matrix  $\mathbf{T}$  (defined in Eq. (2.148)), we obtain the air velocity components in the deformed  $\{\zeta, \eta, \xi\}$  coordinate system, as follows

$$\begin{aligned} \begin{Bmatrix} U_R \\ U_T \\ U_P \end{Bmatrix} &= [\mathbf{T}] \begin{Bmatrix} \dot{u} - \Omega v \\ \dot{v} + \Omega(x + u) \\ \dot{w} + V_i \end{Bmatrix} \\ &= \begin{Bmatrix} -\Omega v + \Omega x v' + w' \dot{w} + v' \dot{v} + w' V_i + \dot{u} \\ (\Omega x + \dot{v}) \cos \bar{\theta} + (\dot{w} + V_i) \sin \bar{\theta} + \Omega v v' \cos \bar{\theta} + \Omega v w' \sin \bar{\theta} \\ \quad + \Omega u \cos \bar{\theta} - \Omega x \frac{v'^2}{2} \cos \bar{\theta} \\ (\dot{w} + V_i) \cos \bar{\theta} - (\Omega x + \dot{v}) \sin \bar{\theta} - \Omega v v' \sin \bar{\theta} + \Omega v w' \cos \bar{\theta} \\ \quad - \Omega u \sin \bar{\theta} + \Omega x \frac{v'^2}{2} \sin \bar{\theta} \end{Bmatrix} + \mathcal{O}(\epsilon^3) \end{aligned} \quad (2.243)$$

Note that  $U_T$  and  $U_P$  must be second-order accurate for the virtual work done by the aerodynamic forces to also have second-order accuracy [83]. Hence, the truncated terms in Eq. (2.243) are of order  $\mathcal{O}(\epsilon^3)$ .

Moreover, recall that  $\dot{\alpha}$  is the angular velocity of the blade section about the deformed elastic axis ( $\zeta$ -axis). It can be regarded as composed of two parts:

- One part that arises from rigid-body angular velocity of the rotor hub,

- Another part that arises from the angular velocities associated with the blade deformations.

The first contribution is obtained from

$$\begin{Bmatrix} \dot{\alpha}_\zeta \\ \dot{\alpha}_\eta \\ \dot{\alpha}_\xi \end{Bmatrix}_\Omega = [\mathbf{T}] \begin{Bmatrix} 0 \\ 0 \\ \Omega \end{Bmatrix} = \begin{Bmatrix} w'\Omega + \mathcal{O}(\epsilon^3) \\ \left(1 - \frac{w'^2}{2}\right) \Omega \sin \bar{\theta} + \mathcal{O}(\epsilon^3) \\ \left(1 - \frac{w'^2}{2}\right) \Omega \cos \bar{\theta} + \mathcal{O}(\epsilon^3) \end{Bmatrix} \quad (2.244)$$

The second contribution was derived previously (see Eq. (2.27)), as

$$\begin{Bmatrix} \dot{\alpha}_\zeta \\ \dot{\alpha}_\eta \\ \dot{\alpha}_\xi \end{Bmatrix}_{deform} = \begin{Bmatrix} \dot{\zeta} \sin \bar{\beta} + \dot{\theta} \\ \dot{\zeta} \cos \bar{\beta} \sin \bar{\theta} - \dot{\beta} \cos \bar{\theta} \\ \dot{\zeta} \cos \bar{\beta} \cos \bar{\theta} + \dot{\beta} \sin \bar{\theta} \end{Bmatrix} = \begin{Bmatrix} \dot{v}'w' + \dot{\theta} + \mathcal{O}(\epsilon^3) \\ \dot{v}' \sin \bar{\theta} - \dot{w}' \cos \bar{\theta} + \mathcal{O}(\epsilon^3) \\ \dot{v}' \cos \bar{\theta} + \dot{w}' \sin \bar{\theta} + \mathcal{O}(\epsilon^3) \end{Bmatrix} \quad (2.245)$$

Therefore, to second order, the local angular velocity is

$$\dot{\alpha} = \dot{\alpha}_\zeta = \dot{\theta} + \dot{v}'w' + \Omega w' \quad (2.246)$$

Finally, the aerodynamic loads are responsible for a virtual work which can be written as

$$(\delta W_a)_b = \int_R (a_v \delta v + a_w \delta w + a_\theta \delta \theta) dx + \mathcal{O}(\epsilon^5) \quad (2.247)$$

The generalized forces  $a_v$  and  $a_w$ , and the generalized moment  $a_\theta$  are computed by coordinate system transformation of the expressions given by Eq. (2.239)-  
(2.241)

$$\begin{Bmatrix} a_u \\ a_v \\ a_w \end{Bmatrix} = [\mathbf{T}]^T \begin{Bmatrix} 0 \\ F_\eta \\ F_\xi \end{Bmatrix} \quad (2.248)$$

which gives

$$a_v = F_\eta \left[ \left(1 - \frac{v'^2}{2}\right) \cos \bar{\theta} - v'w' \sin \bar{\theta} \right] - F_\xi \left[ \left(1 - \frac{v'^2}{2}\right) \sin \bar{\theta} - v'w' \cos \bar{\theta} \right] \quad (2.249)$$

$$a_w = F_\eta \left(1 - \frac{w'^2}{2}\right) \sin \bar{\theta} + F_\xi \left(1 - \frac{w'^2}{2}\right) \cos \bar{\theta} \quad (2.250)$$

$$a_\theta = M_\zeta \quad (2.251)$$

The final equations are simplified by retaining the first and second-order terms in the non-dimensionalized virtual works. In particular, note that we make the following assumptions

$$\frac{C_{l0}}{C_{l\alpha}}, \frac{C_{m0}}{C_{l\alpha}} = \mathcal{O}(\epsilon) \quad (2.252)$$

$$\frac{C_{d0}}{C_{l\alpha}} = \mathcal{O}(\epsilon^2) \quad (2.253)$$

in addition to the ordering scheme defined in § 2.4.

Upon simplification, and introducing the dimensionless constants  $\lambda_i = V_i/(\Omega R)$  and  $r = x/R$ , the generalized forces and moments associated with the aerodynamic loads are

$$\begin{aligned} a_v = & -\frac{1}{2}\rho_\infty(\Omega x)^2 c C_{l\alpha} \left[ \left(1 + \frac{\dot{v}}{\Omega x}\right) \left(\frac{\lambda_i}{r} + \frac{\dot{w}}{\Omega x}\right) \sin \bar{\theta} - \left(\frac{\lambda_i}{r} + \frac{\dot{w}}{\Omega x}\right)^2 \cos \bar{\theta} \right] C'(k) \\ & -\frac{1}{2}\rho_\infty(\Omega x) c C_{l\alpha} \left[ \frac{\left(\frac{\lambda_i}{r} + \frac{\dot{w}}{\Omega x}\right) \left(\frac{c}{2} + x_A\right) \dot{\theta} + (\Omega v w' + \Omega x v' w') \sin \bar{\theta}}{\phantom{\left(\frac{\lambda_i}{r} + \frac{\dot{w}}{\Omega x}\right) \left(\frac{c}{2} + x_A\right) \dot{\theta} + (\Omega v w' + \Omega x v' w') \sin \bar{\theta}}} \right] C'(k) \\ & -\frac{1}{2}\rho_\infty(\Omega x)^2 c C_{l0} \left(\frac{\lambda_i}{r} + \frac{\dot{w}}{\Omega x}\right) \cos \bar{\theta} C'(k) \\ & -\frac{c^2}{16}\rho_\infty(\Omega x) C_{l\alpha} \left[ \frac{\left(\frac{\lambda_i}{r} + \frac{\dot{w}}{\Omega x}\right) (1 - \cos 2\bar{\theta})}{\phantom{\left(\frac{\lambda_i}{r} + \frac{\dot{w}}{\Omega x}\right) (1 - \cos 2\bar{\theta})}} + \frac{\left(1 + \frac{\dot{v}}{\Omega x}\right) \sin 2\bar{\theta}}{\phantom{\left(1 + \frac{\dot{v}}{\Omega x}\right) \sin 2\bar{\theta}}} \right] \dot{\theta} \end{aligned}$$

$$\begin{aligned}
& -\frac{c^2}{16}\rho_\infty C_{l\alpha} \left[ \ddot{v}(1 - \cos 2\bar{\theta}) - \ddot{w} \sin 2\bar{\theta} + \left( 2x_A + \frac{c}{2} \right) \ddot{\theta} \sin \bar{\theta} \right] \\
& -\frac{1}{2}\rho_\infty (\Omega x)^2 \frac{c}{4} C_{d0} (3 \cos \bar{\theta} + \cos 3\bar{\theta})
\end{aligned} \tag{2.254}$$

$$\begin{aligned}
a_w = & -\frac{1}{2}\rho_\infty (\Omega x)^2 c C_{l\alpha} \left[ \left( 1 + \frac{\dot{v}}{\Omega x} \right) \left( \frac{\lambda_i}{r} + \frac{\dot{w}}{\Omega x} \right) \cos \bar{\theta} - \left( 1 + \frac{\dot{v}}{\Omega x} \right)^2 \sin \bar{\theta} \right. \\
& \left. + \left( v'^2 + \frac{w'^2}{2} \right) \sin \bar{\theta} \right] C'(k) \\
& + \frac{1}{2}\rho_\infty (\Omega x) c C_{l\alpha} \left[ \left( \frac{c}{2} + x_A \right) \left( 1 + \frac{\dot{v}}{\Omega x} \right) \dot{\theta} + \Omega w' \left( \frac{c}{2} + x_A \right) - \Omega v w' \cos \bar{\theta} \right. \\
& \left. + (2\Omega u + 2\Omega v v') \sin \bar{\theta} \right] C'(k) \\
& + \frac{1}{2}\rho_\infty (\Omega x)^2 c C_{l0} \left[ \left( 1 + \frac{2\dot{v}}{\Omega x} \right) \cos \bar{\theta} + \left( \frac{\lambda_i}{r} + \frac{\dot{w}}{\Omega x} \right) \sin \bar{\theta} \right] C'(k) \\
& + \frac{c^2}{16}\rho_\infty (\Omega x) C_{l\alpha} \left[ \left( 1 + \frac{\dot{v}}{\Omega x} \right) (1 + \cos 2\bar{\theta}) + \left( \frac{\lambda_i}{r} + \frac{\dot{w}}{\Omega x} \right) \sin 2\bar{\theta} \right] \dot{\theta} \\
& - \frac{c^2}{16}\rho_\infty C_{l\alpha} \left[ \ddot{w}(1 + \cos 2\bar{\theta}) - \ddot{v} \sin 2\bar{\theta} - \left( 2x_A + \frac{c}{2} \right) \ddot{\theta} \cos \bar{\theta} \right] \\
& - \frac{1}{2}\rho_\infty (\Omega x)^2 \frac{c}{2} C_{d0} \sin \bar{\theta} (1 + \cos 2\bar{\theta})
\end{aligned} \tag{2.255}$$

$$\begin{aligned}
a_\theta = & \frac{1}{2}\rho_\infty (\Omega x)^2 \frac{c^2}{2} C_{m0} (1 + \cos 2\bar{\theta}) C'(k) \\
& + \frac{1}{2}\rho_\infty (\Omega x)^2 \frac{c}{2} x_A C_{l\alpha} \left[ 2 \left( \frac{\lambda_i}{r} + \frac{\dot{w}}{\Omega x} \right) \cos 2\bar{\theta} - \left( 1 + \frac{2\dot{v}}{\Omega x} \right) \sin 2\bar{\theta} \right] C'(k) \\
& - \frac{1}{2}\rho_\infty (\Omega x) c x_A C_{l\alpha} \left[ \left( \frac{c}{2} + x_A \right) \dot{\theta} \cos \bar{\theta} \right] C'(k) \\
& - \frac{c^2}{16}\rho_\infty (\Omega x) C_{l\alpha} (c + 2x_A) \dot{\theta} \cos \bar{\theta}
\end{aligned}$$

$$-\frac{1}{2}\rho_\infty(\Omega x)^2\frac{c}{2}x_A C_{l0}(1 + \cos 2\bar{\theta})C'(k) \quad (2.256)$$

---



---

Underline	Meaning
_____	Significant terms for large twist angles
-----	Non-vanishing terms for asymmetric airfoil sections about the $\eta$ -axis

---



---

The non-underlined terms in the previous equations are similar to those reported in analyses found in the literature (see Eq. (23) in Ref. [84] for instance). The double-underlined terms arise due to the differences between the ordering schemes in this dissertation and in other studies. In particular, these terms must be retained for arbitrarily large angles of twist. The dash-underlined terms are present due to the non-symmetry of the circular arc airfoil about the  $\eta$ -axis. Finally, note that the nonlinear terms quadratic in  $\dot{v}\dot{\theta}$ ,  $\dot{w}\dot{\theta}$ ,  $\dot{w}^2$  and  $\dot{v}\dot{w}$  are included in the previous equations because they are of same order as the other retained terms, but they do not contribute to a linearized stability analysis.

The virtual work done by the aerodynamic forces can also be linearized about the trim condition, giving rise to mass, damping and stiffness matrix terms. The results of the linearization is given in Appendix D.6.

### 2.6.2 Quasi-steady aerodynamic model

The analysis can be specialized to the case of quasi-steady aerodynamics. This is particularly useful to obtain the steady rotor blade deformations,

also called trim state. In this case, the lift, drag and aerodynamic pitching moment are solely functions of the steady local angle of attack. In addition, the Theodorsen function, when the reduced frequency  $k = 0$ , is equal to unity. The noncirculatory forces and moments vanish. Consequently, the quasi-steady lift and drag forces, and the aerodynamic pitching moments are

$$L_{QS} = \frac{1}{2}\rho_{\infty}U^2cC_l \quad (2.257)$$

$$D_{QS} = \frac{1}{2}\rho_{\infty}U^2cC_d \quad (2.258)$$

$$M_{QS} = \frac{1}{2}\rho_{\infty}U^2c^2C_{m0} - \frac{1}{2}\rho_{\infty}U^2cx_A C_l \quad (2.259)$$

where  $C_l$  and  $C_d$  are computed from table look-up as functions of the angle of attack. The steady-state angle of attack can be obtained by comparison of the quasi-steady lift (Eq. (2.257)) to the unsteady lift (Eq. (2.236)). Hence,

$$\alpha_{QS} = -\frac{U_T}{U_P} \quad (2.260)$$

By retaining the first and second-order terms in the previous expression, we find

$$\alpha_{QS} = \frac{1}{2}\sin 2\bar{\theta} - \frac{\lambda_i}{r}\cos 2\bar{\theta} - \frac{vw'}{x}\cos 2\bar{\theta} + \underbrace{\left[ \frac{vv'}{x} - \frac{v'^2}{2} + \frac{u}{x} - \frac{1}{2}\left(\frac{\lambda_i}{r}\right)^2 \right]}_{\text{discarded}} \sin 2\bar{\theta} + \mathcal{O}(\epsilon^3) \quad (2.261)$$

The underlined terms are usually discarded for analyses assuming small twist angles.

Then, the resultant of the quasi-steady aerodynamic forces along the  $\eta$ -axis

and the  $\xi$ -axis are

$$F_{(\eta \ QS)} = -\frac{1}{2}\rho_\infty U_T^2 c C_d - \frac{1}{2}\rho_\infty U_P U_T c C_l \quad (2.262)$$

$$F_{(\xi \ QS)} = \frac{1}{2}\rho_\infty U_T^2 c C_l - \frac{1}{2}\rho_\infty U_P U_T c C_d \quad (2.263)$$

$$M_{(\zeta \ QS)} = \frac{1}{2}\rho_\infty U_T^2 c (c C_{m0} - x_A C_l) \quad (2.264)$$

Finally, the virtual work done by the aerodynamic forces and moment acting on the blade section can be written as

$$\begin{aligned} (\delta W_a \ QS)_b = & \int_{x_0}^R \left[ \left\{ -\frac{1}{2}\rho_\infty (\Omega x)^2 c C_d \cos \bar{\theta} \right. \right. \\ & \left. \left. - \frac{1}{2}\rho_\infty (\Omega x)^2 (c C_l \cos \bar{\theta} + c C_d \sin \bar{\theta}) \frac{\lambda_i}{r} \right\} \delta v \right. \\ & + \left\{ \frac{1}{2}\rho_\infty (\Omega x)^2 c C_l \cos \bar{\theta} \right. \\ & \left. + \frac{1}{2}\rho_\infty (\Omega x)^2 (c C_l \sin \bar{\theta} - c C_d \cos \bar{\theta}) \frac{\lambda_i}{r} \right\} \delta w \\ & + \left\{ \frac{1}{2}\rho_\infty (\Omega x)^2 (c^2 C_{m0} - c x_A C_l) \cos^2 \bar{\theta} \right. \\ & \left. - \frac{1}{2}\rho_\infty (\Omega x)^2 c x_A C_l \sin 2\bar{\theta} \frac{\lambda_i}{r} \right\} \delta \theta \Big] dx \\ & + \mathcal{O}(\epsilon^5) \end{aligned} \quad (2.265)$$

Finally, the linearization of Eq. (2.265) is obtained by Taylor expansion, and shown in Appendix D.7.

## Chapter 3

### Numerical Models

The full nonlinear equations of motion derived in the previous chapter do not have a closed-form solution. Instead, the solution must be computed numerically. Two numerical approaches are described in this dissertation. First, a numerical model based on the *assumed-modes method* is presented in § 3.1. The use of this method is focused on the computation of the trim solution. The strengths and weaknesses of this approach are discussed. Second, a numerical model relying on the *finite element method* (FEM) is developed in § 3.2. The FEM model is used to compute the trim solution as well as the stability boundaries of the rotor blades.

#### 3.1 Solution by Assumed-Modes Method

One way to solve the steady-state equation of motion given by Eq. (2.3) is to approximate the deformation functions  $u(x)$ ,  $v(x)$ ,  $w(x)$  and  $\theta(x)$  by the

finite series

$$\left\{ \begin{array}{l} u(x) = \sum_{l=1}^L p_l \psi_l^u(x) \\ v(x) = \sum_{m=1}^M q_m \psi_m^v(x) \\ w(x) = \sum_{n=1}^N r_n \psi_n^w(x) \\ \theta(x) = \sum_{p=1}^P s_p \psi_p^\theta(x) \end{array} \right. \quad (3.1)$$

where  $\psi^u, \psi^v, \psi^w, \psi^\theta$  are known basis functions (or mode shapes), and  $p_l, q_m, r_n, s_p$  are unknown generalized coordinates. Taking the variations of Eq. (3.1), we obtain

$$\left\{ \begin{array}{l} \delta u(x) = \sum_{l=1}^L \delta p_l \psi_l^u(x) \\ \delta v(x) = \sum_{m=1}^M \delta q_m \psi_m^v(x) \\ \delta w(x) = \sum_{n=1}^N \delta r_n \psi_n^w(x) \\ \delta \theta(x) = \sum_{p=1}^P \delta s_p \psi_p^\theta(x) \end{array} \right. \quad (3.2)$$

We can replace the deformation variables and the virtual deformation variables in Eq. (2.3) by the finite series shown above. Then, by invoking the arbitrariness of the virtual generalized coordinates, we obtain a system of “ $L + M + N + O$ ” coupled, nonlinear equations of motion. The solution of these equations are the generalized coordinates  $p_l, q_m, r_n$  and  $s_p$ , which are

used to re-construct the continuous functions of deformation, according to Eq. (3.1).

Note that the level of approximation of this approach is dependent upon the nature of the modes shapes and the number of elements in the finite series shown above. The mode shapes are typically simple functions, and must be chosen from the class of admissible functions, which are continuous, differentiable and satisfy the essential boundary conditions of the problem. In the case of the clamped-free blade studied in this dissertation, the essential boundary conditions are

$$u(x_0) = v(x_0) = v'(x_0) = w(x_0) = w'(x_0) = \theta(x_0) = 0 \quad (3.3)$$

Accordingly, the mode shapes are chosen as follows

$$u(x) = \sum_{l=1}^L p_l \left( \frac{x - x_0}{R} \right)^l \quad (3.4)$$

$$v(x) = \sum_{m=2}^M q_m \left( \frac{x - x_0}{R} \right)^m \quad (3.5)$$

$$w(x) = \sum_{n=2}^N r_n \left( \frac{x - x_0}{R} \right)^n \quad (3.6)$$

$$\theta(x) = \sum_{p=1}^P s_p \left( \frac{x - x_0}{R} \right)^p \quad (3.7)$$

The spatial discretization of the equation of motion is coded in the *Matlab*<sup>®</sup> environment. In addition, the solution to the system of nonlinear, coupled equations are obtained iteratively by means of the built-in *Matlab*<sup>®</sup> function *fsolve*, part of the Fortran library *MINPACK* [85]. The orders of

the polynomial series approximating the deformations are selected such that a prescribed level of accuracy of the solution is obtained, with a reasonable cost of computing time.

In conclusion, the strength of the assumed-modes method stems from its simple and concise numerical implementation. The corresponding source code developed for this dissertation contains approximately 1,050 lines of code. However, the increase in number of degrees of freedom leads to a significant increase in computational time. Furthermore, the *fsolve* algorithm fails to converge for problems including the full set of extensional, lead-lag bending, flapwise bending, and torsional degrees of freedom. Therefore, it appears that the assumed-modes method is very well suited, and should be limited, to the computation of preliminary predictions of blade deformation, where a moderate level of accuracy is expected. For instance, this approach was used to solve a simplified version of the equations of motion, including only flap bending and torsional deformations.

Alternatively, a numerical model based on the finite element method can be implemented. This model is presented in the next section.

## **3.2 Solution by Finite Element Method**

A finite element method of solution can be derived directly from the expression of the EHP (see Eq. (2.2)), which can be seen as a weak formulation of the equation of motion. In this approach, the equation is discretized by approximating the deformation variables as finite series of piecewise continuous

finite element basis functions (also called shape functions). Upon discretization of the rotor blade into  $N$  beam elements, the EHP expression can be written in discretized form as

$$\int_{t_1}^{t_2} \left[ \sum_{i=1}^N (\delta T_i - \delta V_i + \delta W_{nc\ i}) \right] dt = 0 \quad (3.8)$$

where  $i$  represents the index of the  $i$ th beam element. In the following sections, some attributes of the finite element model developed in this dissertation are given. The finite beam elements and the spatial discretization of the rotor blades are defined in § 3.2.1. The choice of shape functions is motivated in § 3.2.2. Additionally, the procedure to compute the trimmed solution is described in § 3.2.3. Finally, the computation of the stability boundaries is presented in § 3.2.4.

### 3.2.1 Beam finite elements

Each beam element consists of 14 degrees of freedom (DOF), distributed over three nodes (see Fig. 3.1). The degrees of freedom form an elemental vector of generalized coordinates

$$\mathbf{q}_i = \{u_1 \ u_2 \ u_3 \ v_1 \ v'_1 \ v_3 \ v'_3 \ w_1 \ w'_1 \ w_3 \ w'_3 \ \theta_1 \ \theta_2 \ \theta_3\}^T \quad (3.9)$$

Therefore, the spatial discretization of the rotor blade into  $N$  elements yields  $N_n = 2N + 1$  nodes. Assembly of the elemental vectors of generalized coordinates yields the global displacement vector

$$\mathbf{u} = \left\{ \underbrace{u_1 \ u_2 \ \cdots \ u_{N_n}}_{2N+1 \text{ DOF}} \ \underbrace{v_1 \ v'_1 \ \cdots \ v_{N_n} \ v'_{N_n}}_{2(N+1) \text{ DOF}} \ \underbrace{w_1 \ w'_1 \ \cdots \ w_{N_n} \ w'_{N_n}}_{2(N+1) \text{ DOF}} \ \underbrace{\theta_1 \ \theta_2 \ \cdots \ \theta_{N_n}}_{2N+1 \text{ DOF}} \right\}^T \quad (3.10)$$

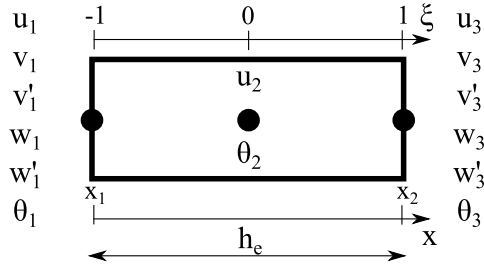


Figure 3.1: Beam finite element

where  $N_n$  is equal to the total number of nodes, and  $N_{DOF} = 2(4N + 3)$  is the total number of DOF. Between the elements, there is continuity of displacement and slope for the lead-lag and flap bending deflections, and continuity of the axial displacement and the elastic pitch angle. Using appropriate shape functions (Hermite cubic polynomials for the bending degrees of freedom, and Lagrange quadratic polynomials for the extension and twist degrees of freedom), we can express the continuous variables of deformation over one element as a function of the generalized coordinates as follows

$$\left\{ \begin{array}{l} u(x, t) = \sum_{i=1}^3 u_i(t)L_i(x) \quad (3.11a) \\ v(x, t) = \sum_{i=1}^2 (v_i(t)H_i^0(x) + w'_i(t)H_i^1(x)) \quad (3.11b) \\ w(x, t) = \sum_{i=1}^2 (w_i(t)H_i^0(x) + w'_i(t)H_i^1(x)) \quad (3.11c) \\ \theta(x, t) = \sum_{i=1}^3 \theta_i(t)L_i(x) \quad (3.11d) \end{array} \right.$$

or in a more compact form

$$\left\{ \begin{array}{l} u(x, t) \\ v(x, t) \\ w(x, t) \\ \theta(x, t) \end{array} \right\} = \begin{bmatrix} \mathbf{L}(x) \\ \mathbf{H}(x) \\ \mathbf{H}(x) \\ \mathbf{L}(x) \end{bmatrix}^T \mathbf{q}_i(t) \quad (3.12)$$

Additionally, we can simplify the computation of deformation by performing the calculations on a master element defined by the interval  $-1 \leq \xi \leq 1$ , so that limits of integration are  $-1$  and  $1$  instead of  $x_1$  and  $x_2$ . Specifically, the transformation from local to global coordinates follows the relation

$$x = x_1 + \frac{1}{2}(x_2 - x_1)(1 + \xi) \quad (3.13)$$

or

$$\xi = \frac{2}{x_2 - x_1} x - \frac{x_2 + x_1}{x_2 - x_1} \quad (3.14)$$

If  $h_e$  is the length of the global element, then

$$h_e = x_2 - x_1 \quad (3.15)$$

### 3.2.2 Shape functions

The order of the shape functions is imposed by the number of degrees of freedom in each element. With four bending DOF in each element, bending deformation can be modeled by a third order polynomial. Hence, the shape functions corresponding to bending deformations are Hermite cubic polynomials. Similarly, the Lagrange shape functions for extension and twist, defined by three DOF, must be quadratic polynomials. The general expressions for the Hermite shape functions are derived hereafter. The elements of derivation to obtain the Lagrange shape functions are similar, thus only the final result is indicated.

To derive the Hermite cubic shape functions, we start by expanding, in the elemental coordinate system, the finite series approximating one of the

two bending variables (Eq. (3.11c) for instance)

$$w(\xi, t) = w_1(t)H_1^0(\xi) + w_2(t)H_2^0(\xi) + w_1'(t)H_1^1(\xi) + w_2'(t)H_2^1(\xi) \quad (3.16)$$

Since  $w(\xi, t)$  must be a third order polynomial, it can be written as

$$w(\xi, t) = a_0(t) + a_1(t)\xi + a_2(t)\xi^2 + a_3(t)\xi^3 \quad (3.17)$$

Hence, at the nodes of the master element, we must have

$$\left\{ \begin{array}{l} w(-1) = w_1 = a_0 - a_1 + a_2 - a_3 \end{array} \right. \quad (3.18a)$$

$$\left\{ \begin{array}{l} w'(-1) = w_1' = \frac{2}{h_e}(a_1 - 2a_2 + 3a_3) \end{array} \right. \quad (3.18b)$$

$$\left\{ \begin{array}{l} w(1) = w_2 = a_0 + a_1 + a_2 + a_3 \end{array} \right. \quad (3.18c)$$

$$\left\{ \begin{array}{l} w'(1) = w_2' = \frac{2}{h_e}(a_1 + 2a_2 + 3a_3) \end{array} \right. \quad (3.18d)$$

While deriving these boundary conditions, note that the change of variable from  $x$  to  $\xi$  leads to a Jacobian which must be taken into account when computing derivatives. In particular,

$$w'(x) = \frac{d}{dx}(w) = \frac{d}{d\xi}(w) \frac{d\xi}{dx} = w'(\xi) \frac{2}{h_e} \quad (3.19)$$

Eq. (3.18a) through (3.18d) can be rewritten in matrix form as

$$\begin{Bmatrix} w_1 \\ w_1' \\ w_2 \\ w_2' \end{Bmatrix} = \begin{bmatrix} 1 & -1 & 1 & -1 \\ 0 & 2/h_e & -4/h_e & 6/h_e \\ 1 & 1 & 1 & 1 \\ 0 & 2/h_e & 4/h_e & 6/h_e \end{bmatrix} \begin{Bmatrix} a_0 \\ a_1 \\ a_2 \\ a_3 \end{Bmatrix} \quad (3.20)$$

After inversion, we obtain

$$\begin{Bmatrix} a_0 \\ a_1 \\ a_2 \\ a_3 \end{Bmatrix} = \begin{bmatrix} 1/2 & h_e/8 & 1/2 & -h_e/8 \\ -3/4 & -h_e/8 & 3/4 & -h_e/8 \\ 0 & -h_e/8 & 0 & h_e/8 \\ 1/4 & h_e/8 & -1/4 & h_e/8 \end{bmatrix} \begin{Bmatrix} w_1 \\ w_1' \\ w_2 \\ w_2' \end{Bmatrix} \quad (3.21)$$

Thus, Eq.(3.16) rewrites

$$w(\xi) = \left(\frac{1}{2} - \frac{3}{4}\xi + \frac{1}{4}\xi^3\right)w_1 + \frac{h_2}{2} \left(\frac{1}{4} - \frac{1}{4}\xi - \frac{1}{4}\xi^2 + \frac{1}{4}\xi^3\right)w_1' \\ + \left(\frac{1}{2} + \frac{3}{4}\xi - \frac{1}{4}\xi^3\right)w_2 + \frac{h_2}{2} \left(-\frac{1}{4} - \frac{1}{4}\xi + \frac{1}{4}\xi^2 + \frac{1}{4}\xi^3\right)w_2' \quad (3.22)$$

From which we can identify the Hermite cubic polynomials as

$$\left\{ \begin{array}{l} H_1^0(\xi) = \frac{1}{4}(2 - 3\xi + \xi^3) \\ H_2^0(\xi) = \frac{1}{4}(1 - \xi - \xi^2 + \xi^3) \frac{h_e}{2} \\ H_1^1(\xi) = \frac{1}{4}(2 + 3\xi - \xi^3) \\ H_2^1(\xi) = \frac{1}{4}(-1 - \xi + \xi^2 + \xi^3) \frac{h_e}{2} \end{array} \right. \quad (3.23)$$

We can similarly derive the Lagrange quadratic shape functions, and find

$$\left\{ \begin{array}{l} L_1(\xi) = \frac{1}{2}(\xi^2 - \xi) \\ L_2(\xi) = 1 - \xi^2 \\ L_3(\xi) = \frac{1}{2}(\xi^2 + \xi) \end{array} \right. \quad (3.24)$$

In the next section, the algorithm developed to compute the trim solution is presented.

### 3.2.3 Computation of the trim solution

The discretized form of the EHP (Eq. (3.8)) leads to a system of  $N_{DOF}$  nonlinear, coupled equations, once arbitrariness of the virtual generalized coordinates has been invoked. Keeping the time-invariant terms only, the resulting

system of equations prescribes the trim solution. In this dissertation, this system of equations is solved using the Newton-Raphson method, along with a line search algorithm, both described below.

### 3.2.3.1 Newton-Raphson method

The Newton-Raphson method in numerical analysis is a method for finding increasingly accurate guesses to the roots of a real-valued function, or vector of functions. It is applied in this dissertation to solve the steady-state equations of motion of a rotor blade.

In the following paragraphs, we denote values calculated at the  $i^{th}$  iteration by the superscript  $( )^i$ . Substituting the global displacement vector  $\mathbf{u}^i$  (defined by Eq. (3.10)) in the system of nonlinear steady-state equations of motion leads to a residue vector  $\mathbf{R}^i$  on the right hand side. Taking the partial derivatives of the residue vector with respect to the displacement vector  $\mathbf{u}^i$ , we obtain the Jacobian matrix

$$\mathbf{K}^i = \frac{\partial \mathbf{R}^i}{\partial \mathbf{u}^i} \quad (3.25)$$

which is the same as the stiffness matrix for the system of equations. In this dissertation, the components of the Jacobian matrix are calculated analytically (see Appendix D) and entered in closed form into the numerical model. This effort leads to improved convergence of the Newton-Raphson algorithm. In addition, the exactness of the components of the Jacobian matrix is verified by comparing them to the results obtained from numerical differentiation of

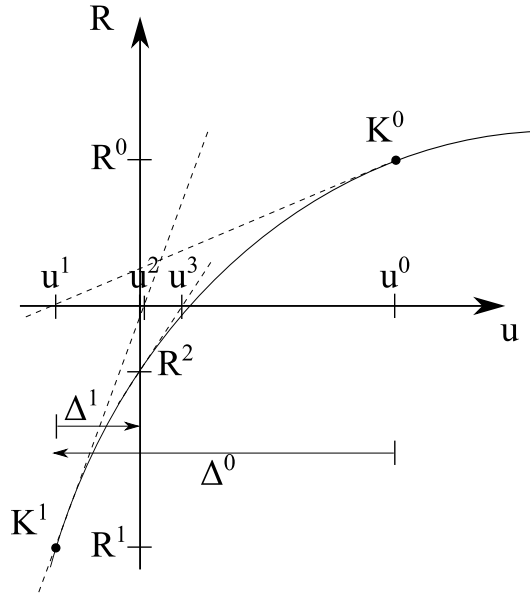


Figure 3.2: Newton-Raphson algorithm for 1-D case

the residue vector. To maximize the accuracy of the numerical differentiation, a complex-step derivative formula is used (see details Appendix E).

The Newton-Raphson method determines the displacement vector for the next iteration as

$$\mathbf{u}^{i+1} = \mathbf{u}^i + \Delta^i \quad (3.26)$$

$$= \mathbf{u}^i - \lambda^i (\mathbf{K}^{-1} \mathbf{R})^i \quad (3.27)$$

where  $\lambda^i$  is a constant calculated using the line search algorithm (described in the next section), used to improve the convergence of the algorithm.

For the one-dimensional case, the Newton-Raphson algorithm can be represented graphically, as shown in Fig. 3.2. First, a guess for the displacement variable  $u$  is made. This guessed value is denoted  $u^0$ . The residue function

is computed for the argument  $u^0$ . If the result  $R^0$  is greater than the error tolerance for the numerical model, then the slope of the residue function at  $u^0$  is calculated, which determines the variable  $u$  for the next iteration, as  $u^1 = u^0 - \frac{R^0}{K^0}$ . The iterative process is repeated until an approximated value for the root of the residue function is obtained.

In addition, the convergence of the Newton-Raphson method can be improved by coupling it with a line search algorithm.

### 3.2.3.2 Line search and backtracking algorithm

While progressing towards the trim solution, the Newton-Raphson algorithm may take steps  $\Delta^i$  yielding large displacements. In particular, the elastic twist angles may take very large values during the iterative process, leading to large effective angles of attack. These non-physical, large angles of attack can prevent the aerodynamic model from converging, particularly because look-up tables for the aerodynamic coefficients are only defined for a bounded range of angles of attack. Consequently, the whole numerical model can fail.

To address this issue, the Newton-Raphson method using a line search with backtracking algorithm [86] is implemented, so that steps never yield excessive displacements. The elements of this algorithm are described below.

The objective of the line search algorithm is to guarantee some progress towards the solution at each iteration. Recall that the Newton step for the set

of equations

$$\mathbf{R}^i = \mathbf{0} \quad (3.28)$$

is

$$\mathbf{u}^{i+1} = \mathbf{u}^i + \Delta\mathbf{u}^i \quad (3.29)$$

where

$$\Delta\mathbf{u}^i = -(\mathbf{K}^{-1}\mathbf{R})^i \quad (3.30)$$

A reasonable strategy to decide whether the Newton step  $\Delta\mathbf{u}^i$  is acceptable is to require that the step decreases the function  $f$ , defined as

$$f = \frac{1}{2} \mathbf{R}^i \cdot \mathbf{R}^i \quad (3.31)$$

Thus, the strategy is as follows: the full Newton step is always tried first, because it yields quadratic convergence once the guess is close enough to the solution. However, if the Newton step does not reduce  $f$ , then the guess is modified by backtracking along the Newton direction until an acceptable step is obtained. Because the Newton direction is a descent direction for  $f$ , it is guaranteed to find an acceptable step by backtracking, as

$$\mathbf{u}^{i+1} = \mathbf{u}^i + \lambda\Delta\mathbf{u}^i \quad (3.32)$$

The parameter  $\lambda$  is determined based on an optimized strategy described in Ref. [86].

### 3.2.3.3 Gaussian quadrature rule

The numerical evaluation of integrals is accomplished by Gaussian quadrature of the form

$$I = \int_{x_1}^{x_2} f(x) dx = \sum_{l=1}^{N_l} f(x_l) w_l \quad (3.33)$$

where  $x_l$  are integration points in the interval  $x_1 \leq x \leq x_2$ ,  $w_l$  are weighting values, and  $N_l$  is the order of the formula. The order of the Gaussian quadrature rule is selected such that the numerical integration formula does not induce any error by itself. In particular, recall that a Gauss quadrature of order  $N_l$  can exactly integrate polynomials of degree  $2N_l - 1$ . Based on the type of shape functions selected in § 3.2.2, the highest degree of polynomial to be integrated in this analysis is equal to six. Consequently, a Gaussian quadrature of 4th order is used in this analysis.

### 3.2.3.4 Computation of the cross-sectional constants

We defined in Chapter 2 of this dissertation a set of constants representing the result of integrals evaluated over the rotor blade cross-section (see § 2.5.7.2 and § 2.5.8.1). The bounds of these integrals are defined relative to the cartesian coordinate system  $\{\zeta, \eta, \xi\}$ . However, it can be seen that for the case of a circular arc cross-section, a transformation to cylindrical coordinates is convenient to compute the integrals.

We introduce a set of geometric parameters (shown in Fig. 3.3) to define the blade cross-section studied in this analysis. The chord, camber and

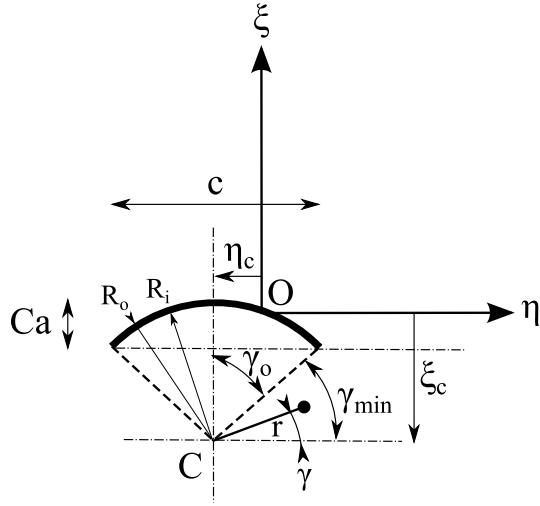


Figure 3.3: Polar coordinate system for calculation of cross-sectional constants

thickness of the blade airfoil are denoted  $c$ ,  $Ca$  and  $t$  respectively. In addition, the center of curvature of the circular arc airfoil, denoted  $C$ , is placed at distances  $\eta_c$  and  $\xi_c$  from the blade elastic axis (i.e. from the origin of the coordinate system  $\{\zeta, \eta, \xi\}$ ). Let us also introduce a cylindrical coordinate system  $\{\zeta, r, \gamma\}$ , centered about  $C$ . The transformation between the coordinate systems  $\{\zeta, \eta, \xi\}$  and  $\{\zeta, r, \gamma\}$  is given by

$$\mathbf{p} : S(\zeta, \eta, \xi) \ni (\zeta, \eta, \xi) \rightarrow \mathbf{p}(\zeta, r, \gamma) \in S(\zeta, r, \gamma)$$

$$\begin{Bmatrix} \zeta \\ \eta \\ \xi \end{Bmatrix} \rightarrow \begin{Bmatrix} \zeta \\ \eta_c + r \cos \gamma \\ \xi_c + r \sin \gamma \end{Bmatrix} \quad (3.34)$$

In addition, the change of coordinates for an area integral is given by

$$\iint_{S(\eta, \xi)} f(\eta, \xi) d\eta d\xi = \iint_{S(r, \gamma)} f(r, \gamma) \left| \frac{\partial \mathbf{p}}{\partial r} \times \frac{\partial \mathbf{p}}{\partial \gamma} \right| dr d\gamma \quad (3.35)$$

Therefore, combining the results of Eq. (3.34) and (3.35), we obtain

$$\iint_{S(\eta,\xi)} f(\eta, \xi) d\eta d\xi = \iint_{S(r,\gamma)} f(r, \gamma) r dr d\gamma \quad (3.36)$$

$$= \int_{\gamma_{min}}^{\pi-\gamma_{min}} \int_{R_i}^{R_o} f(r, \gamma) r dr d\gamma \quad (3.37)$$

where  $\gamma_{min}$  is as defined in Fig. 3.3,  $R_i$  and  $R_o$  are the radii of curvature of the lower and upper surfaces of the blade airfoil respectively. We can relate the boundaries of the integral to the geometric parameters defined earlier ( $c$ ,  $Ca$ ,  $t$ ,  $\eta_c$ ,  $\xi_c$ ) as follows. First, invoking Pythagorean theorem, the radius of curvature of the upper surface of the airfoil is

$$\begin{aligned} R_o^2 &= \left(\frac{c}{2}\right)^2 + (R_o - Ca)^2 \\ \Leftrightarrow R_o &= \frac{Ca}{2} + \frac{c^2}{8Ca} \end{aligned} \quad (3.38)$$

Then, the radius of curvature of the lower surface can be deduced as

$$\begin{aligned} R_i &= R_o - t \\ \Leftrightarrow R_i &= \frac{Ca}{2} + \frac{c^2}{8Ca} - t \end{aligned} \quad (3.39)$$

In addition, the angle  $\gamma_{min}$  is given by

$$\begin{aligned} \gamma_{min} &= \frac{\pi}{2} - \gamma_0 \\ &= \frac{\pi}{2} - \arcsin\left(\frac{c/2}{R_o}\right) \end{aligned} \quad (3.40)$$

Finally, a relationship between  $\eta_c$ ,  $\xi_c$  and the radii of curvature is

$$\left(\frac{R_o + R_i}{2}\right)^2 = \eta_c^2 + \xi_c^2 \quad (3.41)$$

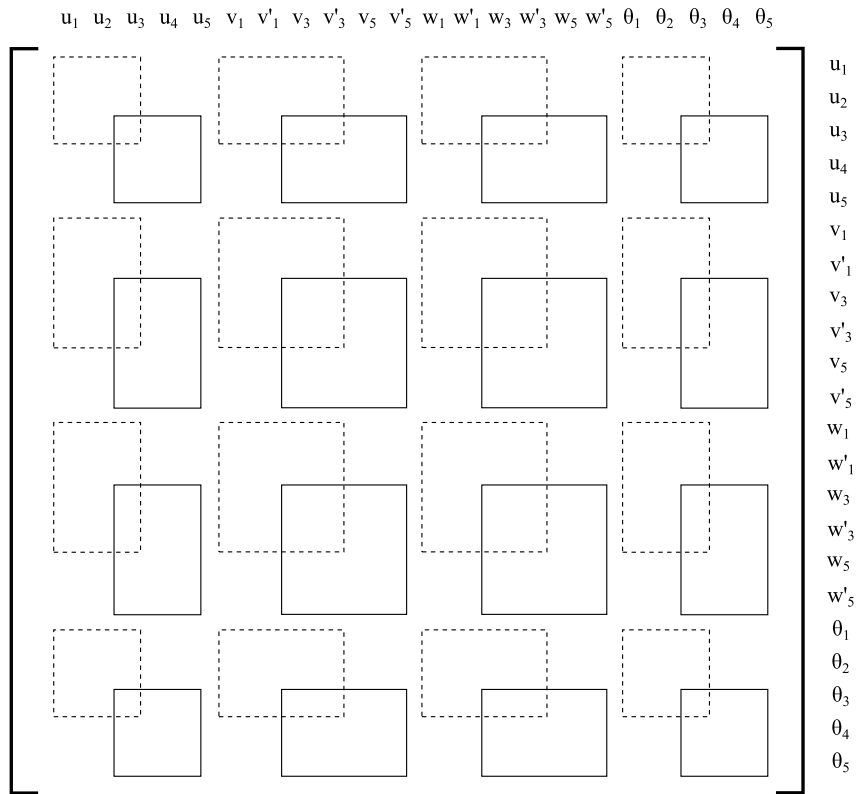


Figure 3.4: Assembly of the global stiffness matrix for  $N = 2$  elements. The dashed-line and solid-line boxes correspond to the local matrices of elements numbered 1 and 2 respectively.

### 3.2.3.5 Assembly of the global stiffness matrix

The components of the stiffness matrix are computed locally for one beam element and assembled into a global matrix. Figure. 3.4 shows the assembly of the global stiffness matrix for two elements, respectively shown by the dashed-line and solid-line boxes. The size of the local stiffness matrices is  $14 \times 14$ . Note that overlapping matrix components sum up.

### 3.2.3.6 Boundary conditions

This section summarizes the various types of boundary conditions encountered in this analysis. Particularly, it presents how discrete stiffness and mass properties can be prescribed, to model the presence of a discrete spring or a tip mass.

**Prescribed displacement** Components of the displacement vector must be prescribed to model the rotor blade clamped root condition, which corresponds to homogeneous Dirichlet boundary conditions. The modeling of Dirichlet boundary condition is classical and a description can be found in Ref. [87]. For instance, a clamp boundary condition can be imposed on the flap degree of freedom at the blade root by modifying the stiffness matrix and the force vector as follows

$$\begin{bmatrix} 1 & 0 & \cdots & \cdots & 0 \\ 0 & 1 & 0 & \cdots & 0 \\ \vdots & 0 & K_{33} & \cdots & K_{3,2N+2} \\ \vdots & \vdots & \vdots & \ddots & \vdots \\ 0 & 0 & K_{2N+2,3} & \cdots & K_{2N+2,2N+2} \end{bmatrix} \begin{Bmatrix} w_1 \\ w'_1 \\ w_3 \\ \vdots \\ w'_{N_n} \end{Bmatrix} = \begin{Bmatrix} 0 \\ 0 \\ F_3^0 - K_{2N+1,1} w_1 - K_{2N+1,2} w'_1 \\ \vdots \\ F_{N_n}^1 - K_{2N+2,1} w_1 - K_{2N+2,2} w'_1 \end{Bmatrix} \quad (3.42)$$

in which we substitute  $w_1 = w'_1 = 0$ .

**Prescribed stiffness** The presence of a torsional spring at the root of the rotor blade implies a modification of the stiffness matrix  $K$ . For instance, if a flapping spring of stiffness  $k_\beta$  is located at the root of the blade, then the stiffness of this spring should be added to the bending stiffness of the blade at

the node where the spring is acting, i.e.

$$\begin{bmatrix} K_{11} & K_{12} & \cdots & K_{1N} \\ K_{21} & K_{22} + k_\beta & \cdots & K_{2N} \\ \vdots & \vdots & \ddots & \vdots \\ K_{N1} & K_{N2} & \cdots & K_{NN} \end{bmatrix} \begin{Bmatrix} w_1 \\ w'_1 \\ \vdots \\ w'_M \end{Bmatrix} = \begin{Bmatrix} F_1^0 \\ F_1^1 \\ \vdots \\ F_M^1 \end{Bmatrix} \quad (3.43)$$

**Prescribed tip mass** The presence of the concentrated tip mass introduces additional kinetic and potential gravitational energies. These energies are modeled by discrete stiffness terms acting on the degrees of freedom of the node located at the tip of the blade. A program is written to create a local stiffness matrix composed of these stiffness terms. This local matrix takes the following form

$$K_m = \begin{bmatrix} 0 & \cdots & \cdots & \cdots & \cdots & 0 & 0 & \cdots & \cdots & 0 & 0 & \cdots & \cdots & 0 \\ & 0 & 0 & \vdots & \vdots & 0 & 0 & \vdots & \vdots & 0 & 0 & \vdots & \vdots & 0 \\ & & K_{3,3} & \vdots & \vdots & K_{3,6} & K_{3,7} & \vdots & \vdots & K_{3,10} & K_{3,11} & \vdots & \vdots & K_{3,14} \\ & & & 0 & \vdots & 0 & 0 & \vdots & \vdots & 0 & 0 & \vdots & \vdots & 0 \\ & & & & 0 & 0 & 0 & \vdots & \vdots & 0 & 0 & \vdots & \vdots & 0 \\ & & & & & K_{6,6} & K_{6,7} & \vdots & \vdots & K_{6,10} & K_{6,11} & \vdots & \vdots & K_{6,14} \\ & & & & & & K_{7,7} & \vdots & \vdots & K_{7,10} & K_{7,11} & \vdots & \vdots & K_{7,14} \\ & & & & & & & 0 & \vdots & 0 & 0 & \vdots & \vdots & 0 \\ & & & & & & & & 0 & 0 & 0 & \vdots & \vdots & 0 \\ & & & & & & & & & K_{10,10} & K_{10,11} & \vdots & \vdots & K_{10,14} \\ & & & & & & & & & & K_{11,11} & \vdots & \vdots & K_{11,14} \\ & & & & & & & & & & & 0 & \vdots & 0 \\ & & & & & & & & & & & & 0 & 0 \\ & & & & & & & & & & & & & K_{14,14} \end{bmatrix} \quad (3.44)$$

Then, the local matrix is assembled to the global stiffness matrix.

Once the boundary conditions are applied, a Gaussian elimination algorithm is used to solve the linear system of equations  $\mathbf{K}^i \Delta \mathbf{u}^i = -\mathbf{R}^i$ . Upon convergence of the Newton-Raphson algorithm, the full set of generalized coordinates describing the steady-state deformations of the flexible rotor blade in hover is obtained. The next objective is to determine the response of the rotor blade to small perturbations of the generalized coordinates about the trim state. The computation of the stability boundaries is presented in the next section.

### 3.2.4 Computation of the stability boundaries

The stability boundaries are obtained by a study of the solutions to the perturbed equations of motion (see derivation in § 2.1)

$$\mathbf{M} \Delta \ddot{\mathbf{q}} + \mathbf{G} \Delta \dot{\mathbf{q}} + \mathbf{K} \Delta \mathbf{q} - (\mathbf{M}^a \Delta \ddot{\mathbf{q}} + \mathbf{C}^a \Delta \dot{\mathbf{q}} + \mathbf{K}^a \Delta \mathbf{q}) = \mathbf{0} \quad (3.45)$$

The solutions of Eq. (3.45) can typically be oscillatory or non-oscillatory, with an exponential increase or decay of the amplitude. They take the general form

$$\Delta \mathbf{q} = \Delta \bar{\mathbf{q}} e^{p \tau} \quad (3.46)$$

where  $p = \delta \pm ik$  are  $N_{DOF}$  complex conjugate roots, and  $\tau$  is defined as the dimensionless time ( $\tau = 2Ut/c$ ). It can be seen that the nature of the solutions depends upon the sign of the real and imaginary parts of  $p$ . The different cases which can be encountered are summarized in Table. 3.1.

Table 3.1: Nature of the free response for various values of  $\delta$  and  $k$

$\delta$	$k$	Type of motion	Stability
$< 0$	$\neq 0$	Decaying oscillations	Stable
$= 0$	$\neq 0$	Pure harmonic oscillations	Limit cycle
$> 0$	$\neq 0$	Diverging oscillations	Unstable
$< 0$	$= 0$	Exponentially decaying motion	Stable
$= 0$	$= 0$	Time invariant	Stable
$> 0$	$= 0$	Exponentially diverging motion	Unstable

In the absence of aerodynamic forces and moments, the solutions to Eq. (3.45) are purely oscillatory (see proof in Appendix F). In the presence of airloads, two types of instability can occur. The first type of instability corresponds to the case where  $\delta > 0$  and  $k = 0$ , and is typically called *divergence*. The second type is characterized by diverging oscillations for  $\delta > 0$  and  $k \neq 0$  and is referred to as *classical flutter*. The onset of divergence or flutter is predicted according to the numerical methods presented in the following sections.

### 3.2.4.1 Determination of divergence

Divergence is a static aeroelastic instability characterized by a monotonic growth of one of the degrees of freedom after perturbation of the trim state. In the case of rotary wing, divergence instability typically affects the pitch degree of freedom. It occurs when an increase in blade pitch produces a change in aerodynamic pitching moment greater than the change in elastic restoring pitching moment. From a mathematical point of view, divergence occurs if the equilibrium position calculated by the trim analysis is statically

unstable, i.e. when

$$|\mathbf{K} - \mathbf{K}^{\mathbf{a}}| < 0 \quad (3.47)$$

### 3.2.4.2 Determination of flutter

Flutter is a dynamic instability that must be predicted by the analysis of the solutions of the perturbed equations of motion.

A non-trivial solution to Eq. (3.45) exists when the flutter determinant  $D(p, k)$  equals zero, i.e

$$D(p, k) = \det \left( p^2 \mathbf{M} + \frac{c}{2U} p \mathbf{G} + \left( \frac{c}{2U} \right)^2 \mathbf{K} - \mathbf{A}(p) \right) = 0 \quad (3.48)$$

where

$$\mathbf{A}(p) = \left[ p^2 \mathbf{M}^{\mathbf{a}} + p \frac{c}{2U} \mathbf{C}^{\mathbf{a}} + \left( \frac{c}{2U} \right)^2 \mathbf{K}^{\mathbf{a}} \right] \quad (3.49)$$

Note that the chain rule applied to the time derivatives gives

$$\frac{\partial}{\partial t} = \frac{\partial}{\partial \tau} \frac{\partial \tau}{\partial t} = \frac{2U}{c} \frac{\partial}{\partial \tau} \quad (3.50)$$

The real and imaginary parts of the roots of the determinant  $D(p, k)$ , which are equal to the eigenvalues of the state space matrix (see Eq. (2.14)), give insights on the stability of the rotor blade.

However, a limitation of the aerodynamic model developed in § 2.6 of this dissertation is that it is only valid for small harmonic motion of the blade airfoil, with oscillations of constant amplitude. Therefore, it applies only when  $p = ik$  or

$$\Delta \mathbf{q} = \Delta \bar{\mathbf{q}} e^{ik\tau} \quad (3.51)$$

Nonetheless, it is typically assumed that for sinusoidal motion with slowly increasing or decreasing amplitude, aerodynamics based on constant amplitude is a good approximation [88]. Such an assumption is made in this dissertation, thus we can rewrite the flutter determinant given in Eq. (3.48) as

$$\left| p^2 \mathbf{M} + p \frac{c}{2U} \mathbf{G} + \left( \frac{c}{2U} \right)^2 \mathbf{K} - \mathbf{A}(ik) \right| = \mathbf{0} \quad (3.52)$$

The computation of the roots of the flutter determinant follows an iterative process, called the  $p$ - $k$  method of flutter analysis [88], describe hereafter:

1. Guess a value for the reduced frequency  $k$ .
2. Calculate  $\mathbf{A}(ik)$ .
3. Solve the characteristic equation (Eq. (3.48)) for  $N_{DOF}$  complex roots  $p$ .
4. For the root representing the mode of interest, compute

$$k_i = |\Im(p_i)| \quad \gamma_i = \Re(p_i)/k_i$$

5. Repeat steps 2-4 until convergence of  $k_i$  is obtained.
6. Repeat steps 1-5 for all the modes of interest.

An efficient numerical scheme, proposed by Hassig [89], was implemented to achieve the whole iterative process. This scheme relies on the *Regula Falsi method* (see graphical representation of this method in Fig. 3.5) and consists of the following steps.

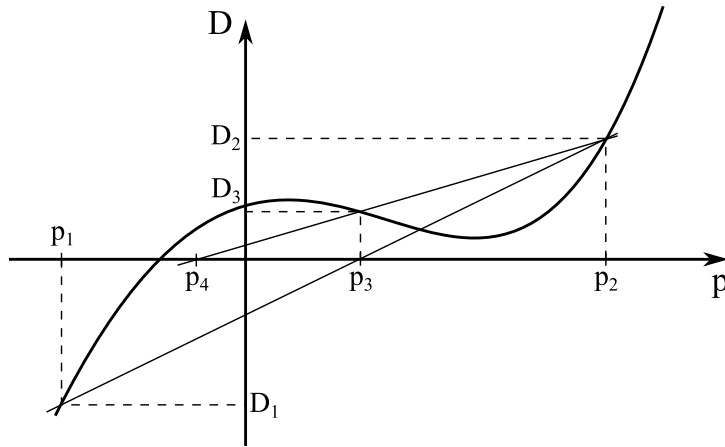


Figure 3.5: Regula Falsi method for  $p \in \mathbb{R}$

1. Estimate the reduced frequency of the mode of interest  $k$ .
2. Set

$$p_1 = -0.01k + ik \quad p_2 = 0 + ik$$

3. Compute the flutter determinants

$$D_1 = D(p_1, k) \quad D_2 = D(p_2, k)$$

4. Compute  $p_3$  according to the recurrence formula

$$p_{i+2} = (p_{i+1}D_i - p_iD_{i+1})/(D_i - D_{i+1})$$

5. Iterate until a specified degree of convergence is attained.
6. Repeat for all the desired modes.

Finally, onset of flutter instability is detected by a negative damping coefficient for one of the eigenmodes.

### 3.3 Algorithm Flow Chart

The finite element model described in the previous section was coded in the *Matlab*<sup>®</sup> environment and named *Vinci*. The entire numerical model comprises approximately 2,750 lines of code. A flow chart describing the model is shown in Fig. 3.6.

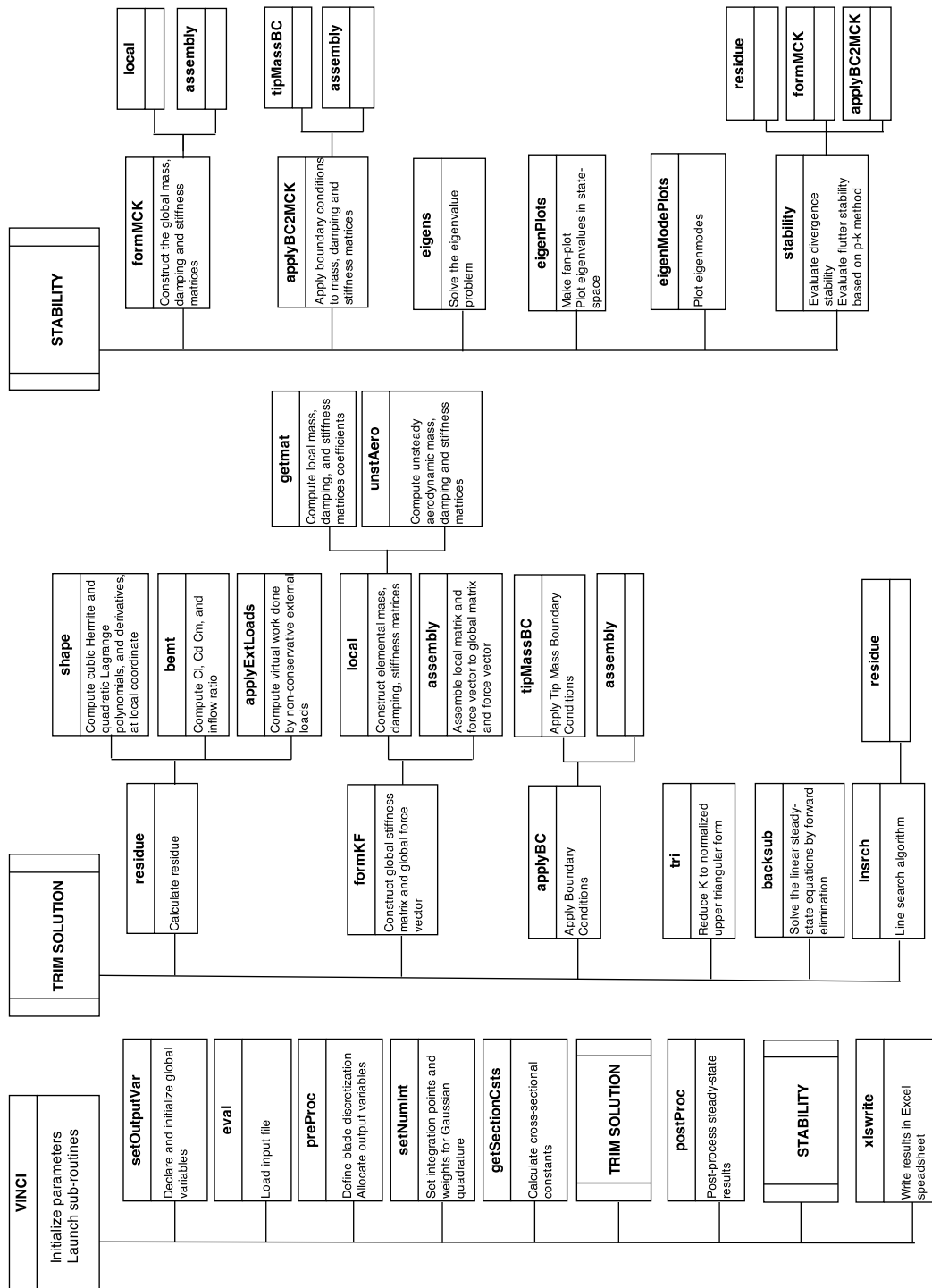


Figure 3.6: Algorithm flow chart

# Chapter 4

## Experimental Procedures

This chapter documents the experimental test campaigns conducted to support the development of an extremely flexible rotor. The design and fabrication of prototype flexible rotor blades, as well as stiff baseline blades are described in § 4.1. In addition, the matrix of tests is summarized in § 4.4. The test bench designed and fabricated for hover testing is presented in § 4.5. The equipment needed to measure rotor blade deformations using the DIC technique is described in § 4.6. In particular, the full experimental procedure allowing the measurement of deformation is detailed.

### 4.1 Rotor Blades Design and Fabrication

Extremely flexible rotor blades and conventional, stiff rotor blades were designed and fabricated in-house. They were incorporated in two-bladed rotor systems and tested in hover.

Two different flexible blade designs were tested. The first design is labeled *flexible blade C*. It comprises a tip body designed to minimize its drag. The second design, labeled *flexible blade BP*, features an alternate orientation of the tip mass designed to passively control the blade tip pitch angle.

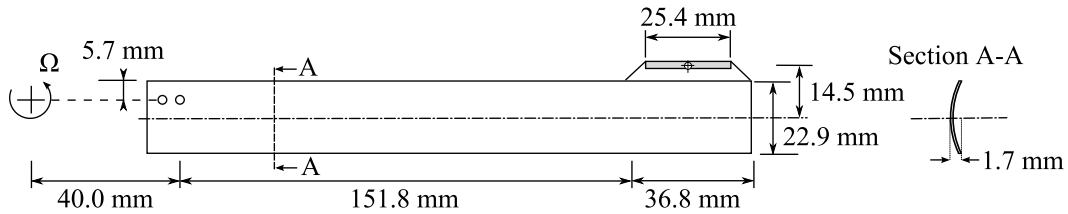


Figure 4.1: Schematic of flexible rotor blade C

Additionally, two sets of conventionally stiff rotor blades were fabricated. The first set of blades has a constant chord and is untwisted. It is referred to as *stiff blade R*. The second set is labeled *stiff blade M* and features blades with a constant chord and a linear twist distribution. The detailed geometry of each blade design is described in the next sections.

#### 4.1.1 Flexible blade C

A planform schematic of the rotor blade C is shown in Fig. 4.1. This blade features a constant chord, untwisted, circular arc airfoil, of camber equal to 7.5% of the blade chord, and thickness to chord ratio of 2.2%. The span of this blade, from the axis of rotation to the tip, equals 228.6 mm (9 inches). The lead-lag hinge is coincident with the blade quarter-chord.

In addition, a 25.4 mm (1 inch) long, 2.4 mm (3/32 inch) diameter tungsten rod is enclosed at the blade tip, near the leading-edge. The longitudinal axis of the tip mass is parallel to the span of the blade, to minimize its drag.

The blade is fabricated out of carbon fiber and aramid fiber, using a wet lay-up process. The resin employed is a polyurethane elastomer (Free-

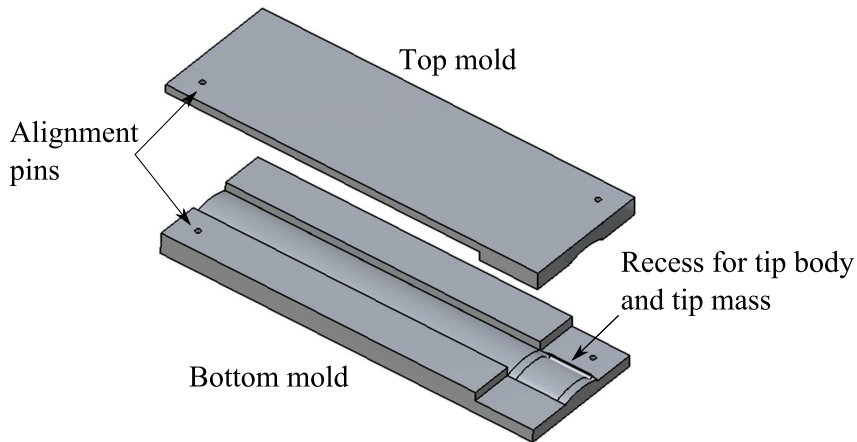


Figure 4.2: Mold for wet lay-up of blades C

man 1035 [90]). One ply of impregnated aramid fibers holds the tip body and is enclosed between two plies of impregnated  $[0^\circ/90^\circ]$  carbon-fiber cloth (CST CF-131 [91]). The resulting laminate is cured at room temperature in a compression mold that has the desired airfoil shape and blade planform. The mold, shown in Fig. 4.2, is made out of ABS and built in a Computer Numerically Controlled (CNC) machine which allows to make shapes with very fine contours. The resulting blade, shown at rest in Fig. 4.5a, is extremely soft both in torsion and in bending. It weighs 5.25 g, the tip mass accounting for 41% of the total mass.

#### 4.1.2 Flexible blade BP

The flexible blade BP is designed with the purpose of passively controlling the pitch angle at the tip of the blade. In particular, the goal is to make use of the propeller moment acting on the tip body to impart pitching

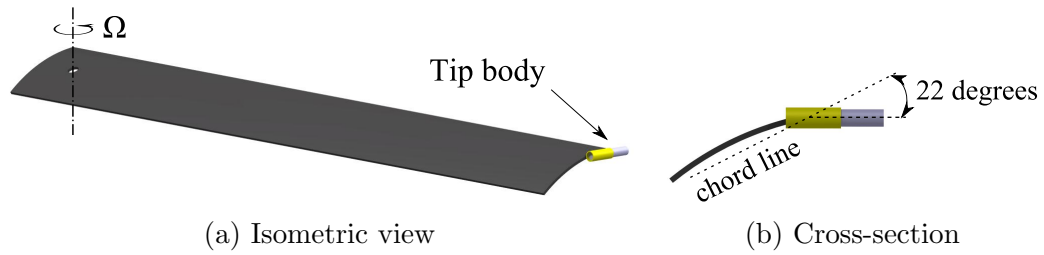


Figure 4.3: Sketch of flexible blade BP

moments. Accordingly, a tip mass consisting of a solid tungsten rod (25.4 mm long, 2.4 mm diameter) is secured perpendicularly to the blade span, at an index angle equal to 22 deg with respect to the blade chord (see Fig. 4.3). While in rotation, the propeller moment acting on the tip body tends to align its principal axis of inertia (i.e. its longitudinal axis) with the plane of rotation, effectively imparting a nose-up pitching moment at the tip of the blade.

The airfoil geometry of blade BP is identical to that of blade C. The fabrication procedure is also similar to that described in the previous section. However, the composite laminate consists of two plies of a  $[+45^\circ/-45^\circ]$  carbon fiber cloth, impregnated with a polyurethane epoxy (Aircraft Spruce Alphapoxy [92]). This combination of ply orientation and material shear modulus is found to be the most favorable to roll the blade into a cylinder with minimal radius of curvature. While the choice of the matrix results in a blade soft in torsion, the angle of the fibers lowers the bending stiffness to accommodate the roll-up of the blade.

A 51  $\mu\text{m}$  thick rectangular brass plate, having the same camber as the blade airfoil, a chord length of 7.6 mm and a length of 15.2 mm is inserted

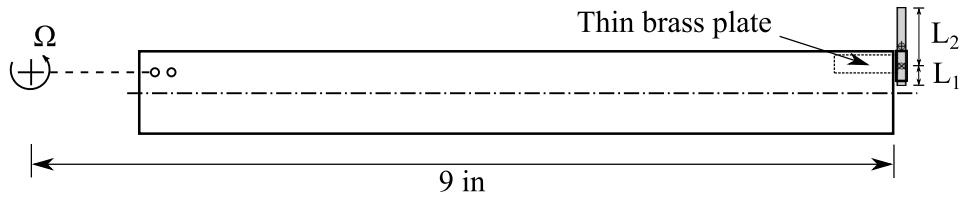


Figure 4.4: Planform of flexible blade BP

at the leading edge of the mid-ply of the composite laminate (see Fig. 4.4). A thin-walled brass cylinder is soldered to the plate, such that it makes an angle of 22 deg with the blade chord. A mold is used to make the assembly process repeatable with accuracy. Then, the tip body is inserted inside the brass tube and its chordwise position is adjusted as desired. For the present prototype, the length  $L_1$  and  $L_2$  are respectively equal to 33% and 78% of the blade chord. The entire tip body assembly is securely attached to the flexible blade by using a high strength epoxy.

The total mass of the flexible blade BP is equal to 4.30 g and the tip mass is equal to 2.05 g. The flexible blades BP are incorporated into a 2-bladed, 457.2 mm (18 inch) diameter rotor and shown at rest in Fig. 4.5b. It can be seen that their bending rigidity is higher than the bending rigidity of the flexible blades C. However, the torsional rigidities of both rotors are of the same order of magnitude.

#### 4.1.3 Stiff blade R

The stiff blade R is designed and fabricated to provide a set of baseline data for comparison with the flexible blade designs. In particular, the geome-

try and mass of the blade R are comparable to that of the flexible blades, so that performance and efficiency metrics can be compared. Accordingly, the stiff blades R are fabricated using two plies of  $[+45^\circ/-45^\circ]$  carbon-fiber cloth, impregnated with a conventional room-temperature cure resin [93], and compressed in a mold. The choice of epoxy guarantees a high bending stiffness while the orientation of the fibers is optimized for maximum torsional rigidity. The resulting 228.6 mm long rotor blades are shown in Fig. 4.5c.

#### 4.1.4 Stiff blade M

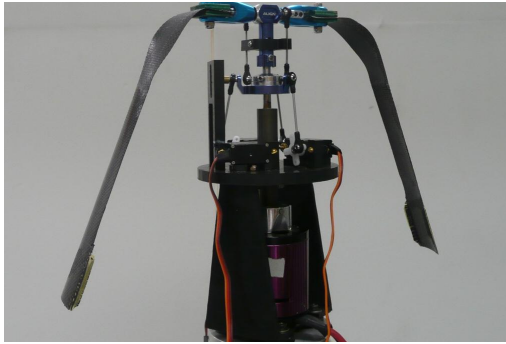
The stiff blade M features a built-in linear twist distribution of  $-0.7^\circ/\text{cm}$ , and is specifically fabricated for the experimental validation of the DIC measurement technique. The blade M has a constant chord of 50 mm and a thin circular arc airfoil. It is fabricated in-house by curing two plies of carbon-fiber prepreg (AS4/3501) in a hot compression mold. The rotor blades M are incorporated into a 418 mm diameter, two-bladed rotor, as shown in Fig. 4.5d.

#### 4.1.5 Blade design matrix

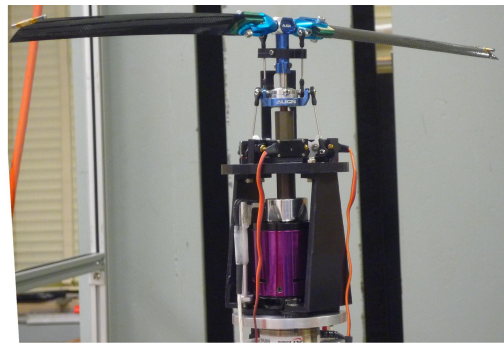
The properties of each rotor presented above are summarized in Table 4.1. In addition, each rotor is shown at rest, mounted on the hover test stand in Fig. 4.5.

Table 4.1: Blade design matrix

	Flexible blade C	Flexible blade BP	Stiff blade R	Stiff blade M
Airfoil	Circular arc	Circular arc	Circular arc	Circular arc
Rotor radius, mm (in)	228.6 (9)	228.6 (9)	228.6 (9)	209.0 (8.228)
Root cutout, mm (in)	40 (1.575)	40 (1.575)	40 (1.575)	51 (2.008)
Chord, mm (in)	22.9 (0.9)	22.9 (0.9)	17.8 (0.7)	50 (1.969)
Twist, deg cm <sup>-1</sup> , (deg in <sup>-1</sup> )	-	-	-	-0.7 (-1.8)
Camber, (% of c)	7.5	7.5	5.5	5.5
Thickness, (% of c)	2.2	1.39	3.6	1.3
Tip body mass, g (oz)	2.03 (0.072)	2.03 (0.072)	-	-
Blade mass, g (oz)	4.35 (0.153)	4.30 (0.152)	4.65 (0.164)	7.48 (0.264)
Blade material	Carbon fiber cloth/ Freeman 1035	Carbon fiber cloth/ Alphapoxy	Carbon fiber cloth/ Pro-Set 125-226	AS4/3501 prepreg



(a) Design C



(b) Design BP



(c) Design R



(d) Design M

Figure 4.5: Extremely flexible rotors and stiff rotors at rest

## 4.2 Blade Material Properties

The flexible blades BP and C are fabricated out of unique custom made composites, whose material characteristics cannot be found in the literature. However the material properties of these composites, specifically the Young's and shear moduli, can be estimated as described below.

First, the total mass  $m_c$ , mass density  $\rho$ , and mass per unit length  $m_0$  of the laminate used to fabricate the blade BP can be measured as

$$\left\{ \begin{array}{l} m_c = 2.3 \text{ g} \\ \rho = 1742 \text{ kg/m}^3 \\ m_0 = 0.013 \text{ kg/m} \end{array} \right. \quad \begin{array}{l} (4.1a) \\ (4.1b) \\ (4.1c) \end{array}$$

In addition, the mass and mass density of the two plies of carbon fiber cloth constituting the composite are

$$\left\{ \begin{array}{l} m_f = 0.855 \text{ g} \\ \rho_f = 1800 \text{ kg/m}^3 \end{array} \right. \quad \begin{array}{l} (4.2a) \\ (4.2b) \end{array}$$

From Eq. (4.1a) and (4.2a), we deduce that the mass of resin used to impregnate the fibers is

$$m_r = 1.445 \text{ g} \quad (4.3)$$

The weight fraction of the fibers and the resin can also be calculated as

$$\left\{ \begin{array}{l} w_f = \frac{m_f}{m_c} = 0.37 \\ w_r = \frac{m_r}{m_c} = 0.63 \end{array} \right. \quad \begin{array}{l} (4.4a) \\ (4.4b) \end{array}$$

Finally, the volume fractions occupied by the fibers and the resin in the com-

Table 4.2: Material properties of carbon fibers and resins

	E (GPa)	G (GPa)
Carbon fiber	240	27
Freeman 1035	0.025	0.0086
Alphapoxy	3.5	1.4

posite laminate are given by

$$\left\{ \begin{array}{l} v_f = \frac{\rho}{\rho_f} w_f = 0.36 \\ v_r = \frac{\rho}{\rho_r} w_r = 0.64 \end{array} \right. \quad \begin{array}{l} (4.5a) \\ (4.5b) \end{array}$$

Note that to obtain the results shown by Eq. (4.5a) and (4.5b), it is assumed that the volume fraction of the void inside the composite laminate ( $v_v$ ) is negligible (typically,  $v_v < 1\%$ ). In addition, noting that the total mass and the volume of the laminate constituting the blade C are almost similar to that of blade BP, we assume that the volume fractions derived above apply to both the blade C and the blade BP.

Using Eq. (4.5a) and (4.5b) as well as the material properties of the carbon fibers and the resins, the material properties of the composites can be calculated.

The Young's moduli and shear moduli of the carbon fibers, the polyurethane elastomer (Freeman 1035) and the Alphapoxy are summarized in Table. 4.2. From the rule of mixture [76], we can calculate the equivalent Young's modulus and shear modulus in the system of principal axes (i.e axes 1 and 2 in Fig. 4.6) of the composite laminate as

$$E_1 = E_2 = E_f v_f + E_r v_r \quad (4.6)$$

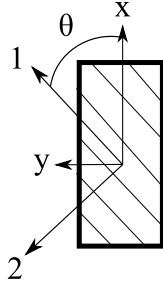


Figure 4.6: Coordinate system of a generally orthotropic material

Table 4.3: Material properties of flexible blades

	$E_x, E_y$ (GPa)	$G_{xy}$ (GPa)
Flexible blade C	0.0512	33.1
Flexible blade BP	7.7	34.1

$$G_{12} = \frac{G_f G_r}{G_f \nu_r + G_r \nu_f} \quad (4.7)$$

Then, the properties of a laminate with fibers oriented  $[+\theta/-\theta]$  are obtained from coordinate transformations [76].

$$\frac{1}{E_x} = \frac{\cos^2 \theta}{E_1} (\cos^2 \theta - \nu_{12} \sin^2 \theta) + \frac{\sin^2 \theta}{E_2} (\sin^2 \theta - \nu_{21} \cos^2 \theta) + \frac{\cos^2 \theta \sin^2 \theta}{G_{12}} \quad (4.8)$$

$$\frac{1}{G_{xy}} = \frac{4 \cos^2 \theta \sin^2 \theta}{E_1} (1 + \nu_{12}) + \frac{4 \cos^2 \theta \sin^2 \theta}{E_2} (1 + \nu_{21}) + \frac{(\cos^2 \theta - \sin^2 \theta)^2}{G_{12}} \quad (4.9)$$

For  $\theta = 45^\circ$ , assuming that  $\nu_{12} = \nu_{21} = 0.25$ , we obtain the material properties shown in Table. 4.3. Note that these material properties constitute estimates of the actual properties of the composites, which will be refined by correlating the predictions of blade deformation to experimental measurements.

### 4.3 Aerodynamic Coefficients

The 2-D aerodynamic coefficients  $C_l$ ,  $C_d$  and  $C_{m0}$  of a circular arc airfoil at low Reynolds number are computed for various angles of attack using the software *ANSYS Fluent*<sup>®</sup>, and compared to experimental data on similar airfoils and for low Reynolds number found in the literature [59, 60]. Note that no experimental data on circular arc airfoils exists at the Reynolds number of interest in this dissertation.

A circular arc airfoil of identical camber and thickness-to-chord ratio as the airfoil of the rotor blades presented in § 4.1 is created in *ANSYS Fluent*<sup>®</sup>. The flow surrounding the airfoil is meshed using 2-D elements, as shown in Fig. 4.7. A constant laminar inflow is modeled and its direction is varied between successive simulations to account for various angles of attack. In addition, the flow near the airfoil profile is assumed to be turbulent, based on a  $k - \epsilon$  turbulence model.

The pressure distribution acting on the upper and lower surfaces of the airfoil are computed by *ANSYS Fluent*<sup>®</sup> using a Reynolds-averaged Navier-Stokes (RANS) equations solver. Integrating the pressure distribution over the surface of the airfoil yields the lift, drag and pitching moment coefficients about the aerodynamic center.

Contours of pressure distribution at angles of attack  $\alpha = 0^\circ$  and  $15^\circ$  are shown in Fig. 4.8. In addition, the variations of lift and drag coefficients as functions of the angle of attack are shown in Fig. 4.9. The good correlation

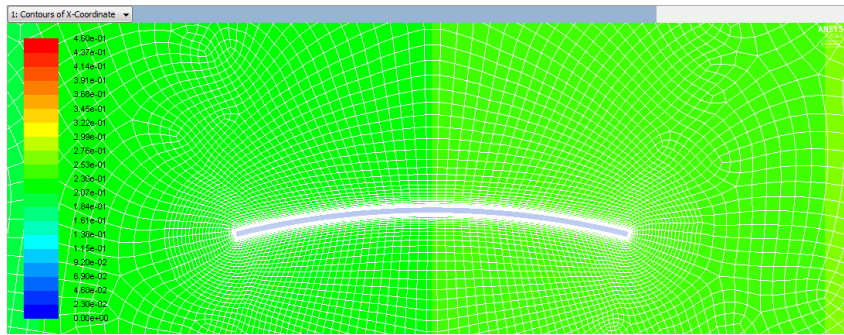
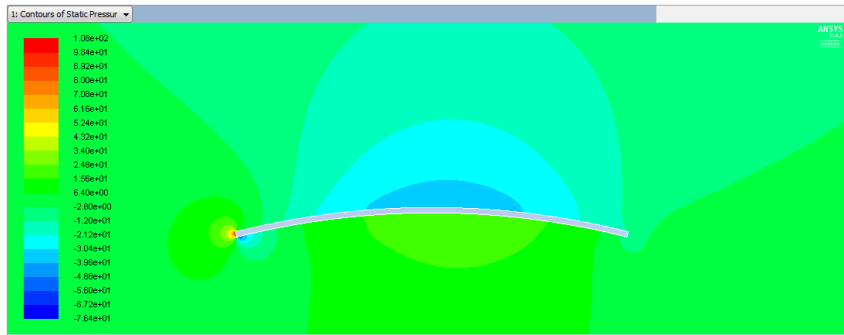
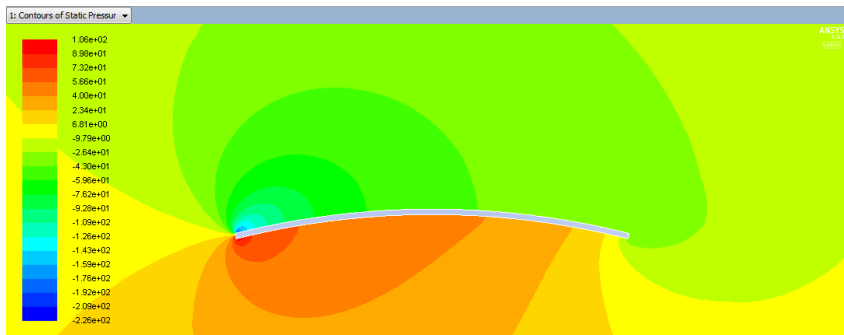


Figure 4.7: 2-D mesh of the flow surrounding a circular arc airfoil

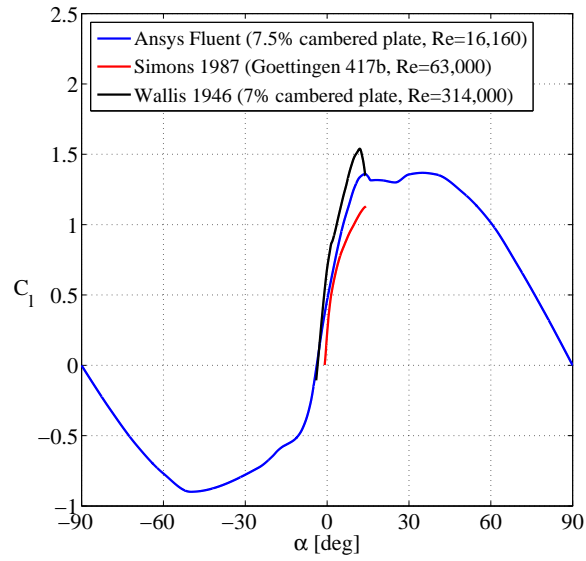


(a)  $\alpha = 0^\circ$

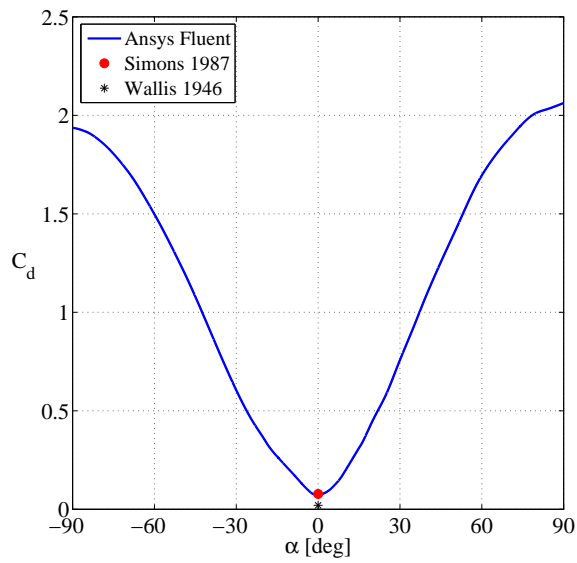


(b)  $\alpha = 15^\circ$

Figure 4.8: Contours of static pressure for various angles of attack ( $Re = 16, 160$ )



(a) Lift coefficient



(b) Drag coefficient

Figure 4.9: Simulated lift and drag coefficients compared to experimental measurements

between the simulated aerodynamic coefficients and similar measurements reported in the literature gives some confidence in the *Ansys Fluent*<sup>®</sup> model. For the analysis presented in this dissertation, the simulated values of  $C_l$  and  $C_d$  are used because they are tabulated for a larger range of angles of attack than the experimental measurements.

Additionally, the pitching moment coefficient at zero angle of attack  $C_{m0}$  of the blade airfoils studied in this analysis is interpolated from the data published in the literature [59, 60], and is chosen equal to -0.15.

#### 4.4 Test Matrix

The performance of the flexible rotor blades C and BP in hover is measured on a test stand designed and built in-house, and compared to the performance of the baseline stiff rotor blades R. The variations of thrust coefficient and figure of merit are computed for each rotor, as a function of the collective pitch angle. The thrust coefficient is a dimensionless representation of the rotor thrust, defined as

$$C_T = \frac{T}{\rho_\infty A V_{tip}^2} \quad (4.10)$$

where  $A$  is the rotor disk area. The figure of merit is a nondimensional measure of hovering thrust efficiency and is defined as the ratio of the *ideal* power required to hover to the *actual* power required. Using results from momentum

theory, it can be written as [41]

$$FM = \frac{\frac{C_T^{3/2}}{\sqrt{2}}}{\frac{\kappa C_T^{3/2}}{\sqrt{2}} + \frac{\sigma C_{d0}}{8}} \quad (4.11)$$

where  $\kappa$  is called an induced power correction factor, which accounts for power losses due to nonuniform inflow, tip losses, wake swirl and finite number of blades. Based on the results from the hover tests, the flexible rotor showing the best figure of merit is chosen for the DIC tests.

The DIC test campaign is conducted in two phases. First, the validation of the DIC measurements in the rotating frame is achieved through the following procedure. The stiff rotor blade M of known geometry is tested and its shape as measured by DIC is compared to the shape of the mold from which it is made. At a constant radial station, DIC measurements of the surface height of the rotor blade are compared to measurements from a laser distance sensor (LDS) mounted in close proximity to the spinning rotor. Note that such an arrangement is not practical for performance measurements because of transient loads introduced by the aerodynamic interference between the LDS and the rotor blade. In addition, the pitch angle at the root of the blade is measured by a laser inclinometer and compared to the pitch angle calculated from DIC measurements.

Once the DIC technique is validated on the stiff rotor blade M, it is used to measure the surface heights of the flexible blades on the 457.2 mm diameter rotor. From these measurements, the spanwise distribution of the

three components of displacement ( $u$ ,  $v$  and  $w$ ) as well as twist of the rotor blade ( $\theta$ ) is computed. The experiment is repeated at several blade pitch angles to generate a detailed set of experimental data for correlation with the aeroelastic analysis.

## 4.5 Test Bench

The rotor blades are tested on a vertical hover test stand with a rotor plane approximately 120 cm (4 ft) from the ground. The stiff blades M are spun on a different rotor hub than the flexible blades and stiff blades R to accommodate their specific root geometry.

### 4.5.1 Hover test stands

For the tests involving the stiff blades M, a 418 mm diameter, one-bladed rotor with counterweight is mounted on a rigid hub (Fig. 4.10), and spun by a brushless in-runner DC motor (Feigao 130) at rotational speeds varying from 300 to 900 RPM. Blade root pitch angles are manually set at values ranging from  $0^\circ$  to  $15^\circ$ . The rotational speed of the rotor is measured using a once-per-revolution (1/rev) optical switch, which consists of a laser beam passing through the rotor disk and aimed at a phototransistor (NTE 3037 [94]). Every time the laser beam is blocked by the rotor blade passage, a voltage pulse is generated. This 1/rev signal is used to trigger other instruments and for phase averaging of the data collected over multiple revolutions.

For the tests involving the flexible rotor blades and the stiff blades

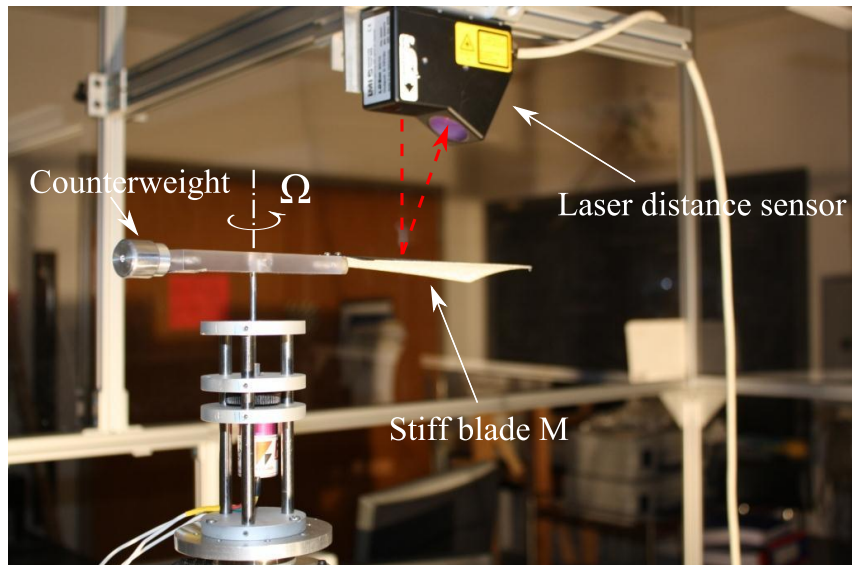


Figure 4.10: Stiff rotor blade M mounted on hover test stand

R, the 457.2 mm diameter rotors are mounted on a two-bladed rigid hub (Fig. 4.11), driven by a brushless out-runner DC motor (Hacker A50 16S). The motor is chosen to have a high torque and low speed constant so that it can directly drive a rotor of diameter up to 600 mm at a tip speed of up to 150 m/s without the need for a gearbox. A swashplate assembly operated by three high-speed digital servos (JR DS285 [95]) allows for precise adjustment of the rotor collective and cyclic pitch angles. The motor and rotor assembly is mounted directly on a six-component strain gage load cell (ATI Mini40E [96]), with a full-scale rating of 60 N (15 lbf) in the thrust direction and 1 N.m (10 lbf-in) in the torque direction. A magnetic pickup provides a 1/rev pulse, which is used to measure the rotational speed as well as to perform synchronous averaging of all the signals. This is also used to trigger a strobe light to illuminate the

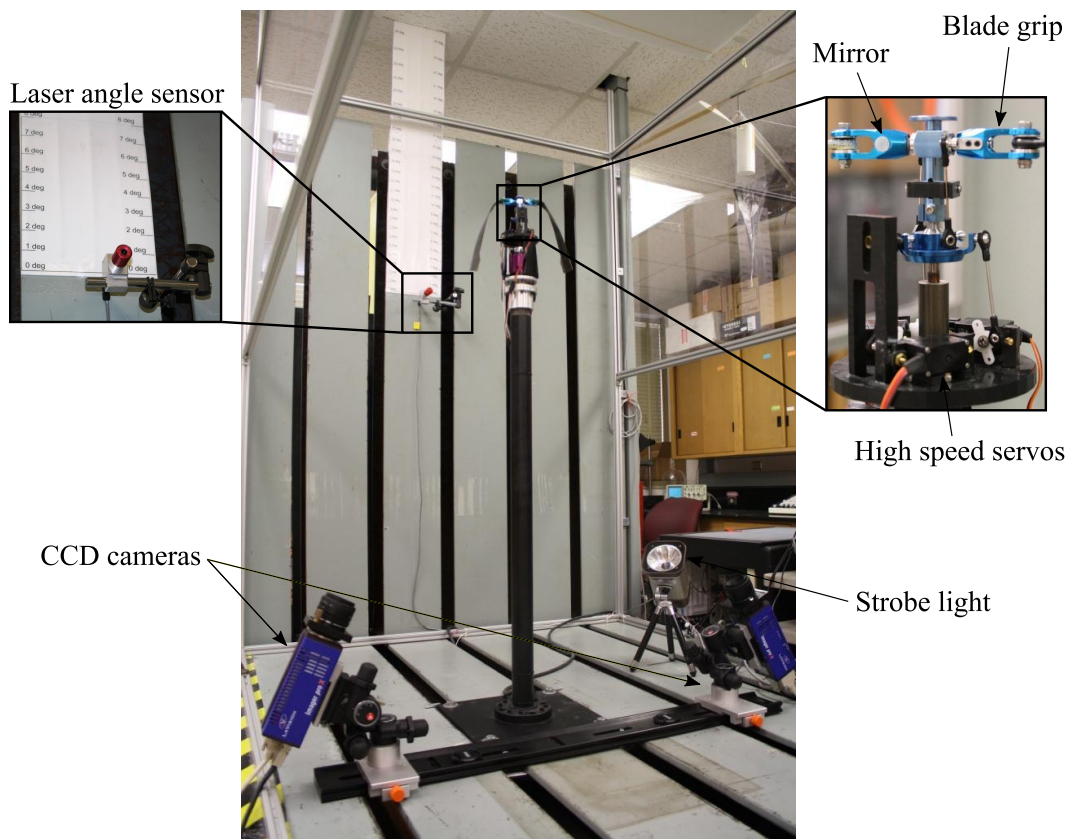


Figure 4.11: Extremely flexible rotor blades C mounted on hover test stand

rotor and enable photography of the blades in-flight. Data are acquired by a National Instruments multifunction data acquisition card (NI-PCI-6052E) with a custom virtual instrument programmed in NI LabView<sup>®</sup> (see images of the front panel in Appendix G). The measured quantities are the rotor forces and moments in the fixed frame, the rotational speed, the motor voltage, and the motor current. A circuit diagram of the data acquisition equipment is shown in Appendix H.

#### 4.5.2 Laser distance sensor

A high-frequency, laser triangulation sensor (LMI LDS 80/10 M) is mounted on a fixture above the rotor plane to measure the blade surface height during rotation. Note that this sensor has a stand-off distance of 80 mm, therefore the sensor is mounted approximately at this distance above the rotor plane (see Fig. 4.10). The laser beam projected by the sensor is reflected from the top surface of the blade to a CCD array through a collection lens. This measurement device is able to sense distances from 0 to 10 mm with a resolution of 0.001 mm, a standard deviation of 0.01 mm and a bandwidth of 10 kHz. The output voltages are recorded by a 50 MHz digital oscilloscope, before being converted into distances based on the calibration constant. Note that this sensor gives a measurement only during the time when the rotor blade passes through the laser beam; during the remainder of the rotor revolution, there is no object in the sensing range of the LDS and the output of the sensor is zero.

### 4.5.3 Laser inclinometer

A laser inclinometer is constructed by attaching a mirror to the blade grips and reflecting a laser beam from it to a calibrated screen (shown in Fig. 4.11). This method is able to give a direct measurement of the rotor blade root pitch during rotation, in the range of  $0^\circ$  to  $23^\circ$  with an accuracy of  $0.2^\circ$ .

## 4.6 Digital Image Correlation Technique

The three-dimensional DIC technique involves preparation of the rotor blade surface, calibration of the camera setup and capturing images of the rotor blades during rotation. In the first step, the DIC setup is calibrated using a target of known geometry so that a mapping function is established between physical dimensions and the camera images. Secondly, images of the spinning rotor blade are captured at different loading conditions and at a specific azimuthal location. After the images are captured, the DIC software uses photogrammetry to create three-dimensional maps of the blade surface. Image correlation algorithms are then used to generate three-dimensional displacement vectors between the image of the deformed blade and a reference image. The DIC software used in this study is LaVision DaVis 7.2 - Strain-Master 3-D. [97]. Finally, post-processing algorithms developed in-house are used to extract the extensional, flap and lead-lag bending as well as torsional deformation from the displacement vectors.

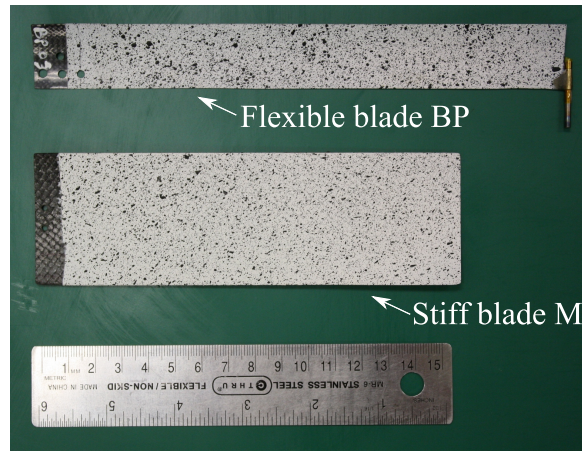


Figure 4.12: High-contrast random pattern on the bottom surface of rotor blades

#### 4.6.1 Blade preparation

The lower surface of the rotor blades is prepared with a high-contrast random dot or speckle pattern (Fig. 4.12) such that points on the surface are easily distinguished. First, the surface is painted with a uniform matte white background. Then, a stiff-bristled brush dipped in matte black paint is used to spray a random pattern of fine black spots on this background. This technique results in the generation of speckles varying in size from 0.15 mm to 1.95 mm, which is appropriate for the resolution of the raw images taken by the cameras (6.75 pixels per millimeter at the distance and magnification of the test setup). In particular, the speckle size is chosen such that it is greater than the dimensions of one pixel, but less than the size of the interrogation window of the cross-correlation algorithm (32- by 32-pixel).

### 4.6.2 Digital cameras

The cameras (Imager ProX 2M) used for these experiments have a 1600x1200 pixel resolution, 29.5Hz operation speed (15 Hz continuous), CCD image sensors, and 16384 (14-bit) gray levels. The exposure time is adjustable within the range of 500ns to 1000ms and the cameras are capable of accepting an auxiliary TTL triggering signal. The cameras are equipped with Nikon 50mm AF NIKKOR f/1.8D lenses; these lenses do not have any zoom, have a minimum focal distance of 450 mm (1.5 ft), and a variable aperture from f1.8 to f22. The cameras are mounted below the rotor disk a fixed distance apart and are oriented such that the image of the rotor blade is aligned with the longer dimension of the CCD sensor, so that the maximum spatial resolution can be achieved. The arrangement of the two cameras with respect to the rotor stand can be seen in Fig. 4.11.

### 4.6.3 Calibration

A calibration procedure is performed to establish a mapping function between real world dimensions and the camera image dimensions. This calibration procedure is crucial, as it defines the position and orientation of the cameras with respect to the test sample as well as a reference coordinate system in which all the output quantities are expressed. In addition, the calibration procedure produces a dewarping function correcting the image distortions due to perspective projections and inherent camera lens distortions. In the present study, a calibration plate is carefully aligned coplanar with the rotor hub plane,

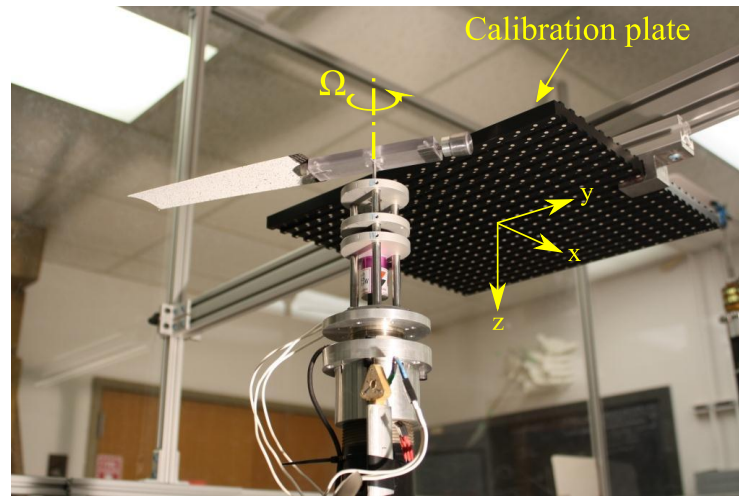


Figure 4.13: Reference system of axes defined during calibration

the  $x$ - and  $y$ - axes being aligned with the radial and tangential directions of the blade respectively (Fig. 4.13). The  $z$ -axis is defined as normal to the calibration plate, parallel to the rotor shaft. The calibration plate has an array of targets imprinted on its surface and in a groove, to give a three-dimensional collection of targets with a precisely known spacing. The dimensions of the plate (310 mm by 310 mm) are such that the target locations encompass the  $x$ - and  $y$ - range of values occupied by the rotor blades during the experiments. Several images of the calibration plate are captured by both cameras. For each set of images, the target locations on the calibration plate are identified and their positions are used to calculate, using a pinhole model, the dewarping function and the mapping function between real world coordinates and camera image coordinates. The resulting calibration is effectively valid everywhere in the volume that is in focus to the camera, i.e. the depth of field.

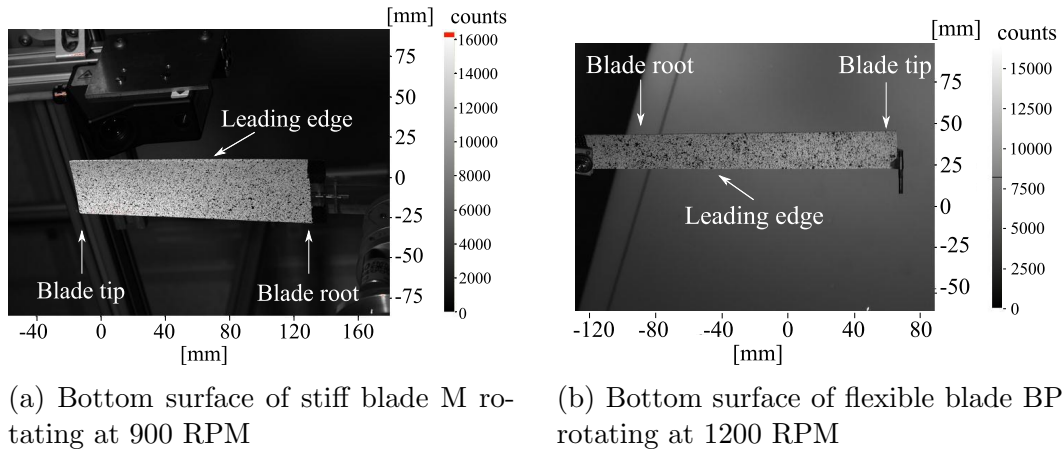


Figure 4.14: Raw images acquired with DIC system

#### 4.6.4 Image acquisition

After the DIC system is calibrated, images of the rotating blades are captured (Fig. 4.14). A 10 Watt Xenon stroboscope, triggered once per revolution by a Hall effect sensor mounted on the rotor shaft, illuminates the blade at a fixed azimuthal position. The duration of the flash ( $10 \mu\text{s}$ ) is short enough for the resulting camera images to appear motionless. To increase the intensity and contrast of the pictures, and therefore produce more accurate correlation computations, the aperture of the cameras is kept open for one second, effectively adding up multiple passes of the blade for each image. This process is repeated at different settings of rotor blade pitch, resulting in a pair of images (one from each camera) at each blade pitch. As the blade pitch increases, the aerodynamic load on the rotor blade increases. The increased lift causes upward bending of the blade, increased drag causes lead-lag bending of the blade (against the direction of rotation) and aerodynamic pitching

moments affect the twist distribution along the blade.

#### 4.6.5 Computation of deformation

Using the raw images, the DIC software calculates a surface height map of the rotor blade and displacement fields. While the surface heights are computed relative to the absolute reference frame defined during calibration, the displacements are obtained with respect to the position of the blade in the undeformed state, as defined by the first image of each data set.

To ensure that the azimuthal position of the blade in the undeformed and deformed states is the same, the undeformed state corresponds to the blade spinning at very low RPM. In addition, the blade root pitch at the undeformed state is set to zero. These two conditions are chosen such that deformations due to centrifugal and aerodynamic forces are negligible. It should be noted that this zero reference also eliminates the contribution of gravitational forces to the computation of blade deformations.

The surface height map generated by the DIC software is directly used to plot the blade shape at a given radial station. In addition, the displacement vectors of points located along the blade elastic axis are extracted from the global displacement fields to plot the blade extension and bending deflections. This way, displacements normal to the rotor disk plane due to the flap bending, and in-plane displacements due to lead-lag bending deflection are decoupled from the displacements produced by the twist of the blade.

Finally, an algorithm is written to compute the spanwise variation of



write

$$\tan \theta_D = \frac{T_{23}}{T_{22}} \quad (4.13)$$

where  $\mathbf{T}$  is the transformation matrix defined in Eq. (2.148). Expanding Eq. (4.13) in terms of the deformation variables and neglecting higher-order terms, we find that

$$\tan \theta_D = \frac{\left(1 - \frac{w'^2}{2} + \mathcal{O}(\epsilon^4)\right) \sin \bar{\theta}}{\left(1 - \frac{v'^2}{2} + \mathcal{O}(\epsilon^4)\right) \cos \bar{\theta} + v'w' \left(1 + \frac{w'^2}{2} + \mathcal{O}(\epsilon^4)\right)} \quad (4.14)$$

Finally,

$$\theta_D = \bar{\theta} + \mathcal{O}(\epsilon^4) \quad (4.15)$$

#### 4.6.6 Spatial resolution

The surface heights are calculated by the DIC software for each pixel of the raw images. For the present study, this leads to a spatial resolution equal to 0.15 mm, or 0.06% of the rotor radius. Local pitch angles, which are computed using the surface heights of leading-edge and trailing-edge, are obtained at the same resolution.

The displacement vectors are calculated for each interrogation window of the DIC algorithm which, in the present study, consists of a square of 32-by 32-pixel with a 50% overlap between two adjacent windows. Consequently, the spatial resolution of the displacement vector field is of 16 pixels (2.37 mm), or 1.04% of the rotor radius.

# Chapter 5

## Results and Discussion

This chapter discusses the results of the experimental testing of rotor blades in hover. In addition, it presents a validation of the numerical model and the experimental technique developed in this dissertation. Finally, it discusses analytical results on blade deformation and stability boundaries obtained by the analysis.

The hover performance of the flexible rotor blades C and BP is measured, and compared to the hover performance of the stiff rotor blades R in § 5.1. The most efficient flexible blade design is selected for the subsequent tests. In addition, the new experimental technique and numerical model are validated. A comprehensive validation of the DIC technique to measure three-dimensional rotor blade displacements is presented in § 5.2. A series of test cases focused on validating the numerical analysis are presented in § 5.3. Then, the full aeroelastic behavior of the selected flexible rotor is investigated in § 5.4. The trim state in hover is predicted using the numerical model and correlated with the measurement of deformation by DIC (§ 5.4.1). Finally, the stability boundaries are predicted using the analysis (§ 5.4.2).

## 5.1 Flexible Rotor Blade Performance in Hover

The hover performance of the flexible rotor blades is assessed relative to the performance of conventional stiff blades of identical geometry by comparing thrust coefficients and figures of merit.

Figure. 5.1 shows the thrust coefficients of the rotor blades C, BP and R spinning at 1500 RPM, as a function of the collective pitch angles. First, it can be seen that both flexible rotors are able to produce the same amount of thrust as the stiff rotor. However, the collective pitch required to obtain a thrust coefficient of 0.01 is equal to  $17^\circ$  in the case of the stiff rotor R, whereas it equals  $22^\circ$  and  $40^\circ$  for the flexible rotor blades BP and C respectively. Due to the low torsional stiffness of the flexible blades C, pitch angles input at the root are not transferred to the tip of the blade. In addition, the propeller moment acting on the tip mass rotates the tip of the blades C to flat pitch. The combination of these two effects results in highly twisted rotor blades, as shown in Fig. 5.2. Because the outboard sections of the blades develop the greatest percentage of thrust, very large collective pitch angles are necessary to generate magnitudes of thrust similar to the untwisted stiff blades R.

In contrast, it can be seen in Fig. 5.3 that a refined design of the tip body, as in blade BP, eliminates the twist induced along the span of the blade. Thus, the slope of the thrust coefficient curve for the flexible blade BP is approximately equal to that of the stiff blade R.

Note also that the forces and moments produced by the flexible rotor

blades C are not measured and the thrust coefficients are not computed for collective pitch angles below  $10^\circ$ , because the rotors are not stable at these angles and angular velocity. However, the slope of the thrust coefficient curve indicates that, if the blades C were stable at low collective pitch, they would generate a negative thrust. This result is attributed to the nose-down torsional moment caused by the weight of the tip mass, resulting in a net negative twist of the rotor blade and a negative angle of attack at the outboard locations.

The figures of merit of each of the rotors tested in hover are shown in Fig. 5.4, as a function of the blade loading. We can observe that the induced twist along the span of the flexible blades C is responsible for a significant loss in hover efficiency, relative to the untwisted flexible rotor BP and stiff rotor R. In addition, it is seen that the flexible blades BP have a maximum figure of merit of 0.5 equal to the maximum figure of merit of the stiff blades R, both at a blade loading of 0.15.

The stability boundaries of the flexible rotor blades are also experimentally investigated. The sharp transition between stable and unstable regimes can be seen by comparing Fig. 5.2 to Fig. 5.6. The photographs are taken using a stroboscopic light synchronized with the rotational speed of the rotor, and using a long exposure, resulting in the blade position being recorded over multiple rotor revolutions. The blurred image indicates that the corresponding regions of the blade are undergoing motion at a frequency non-integer multiple of 1/rev. The stiff blades R are found to be unconditionally stable, whereas both flexible rotors experience unstable regimes characterized by cou-

pled pitch-flap oscillations of bounded magnitude (limit cycle oscillations), as well as oscillations of increasing magnitude (classical pitch-flap flutter). In particular, it appears that flutter instability of the flexible rotors is not only dependent upon the rotational speed of the rotor, but also the collective pitch angle. The flexible blades C spinning at 1500 RPM are found to be unstable for collective pitch angles from 0 to 10 degrees, and then stable up to very large collective pitch angles, approximately 45 degrees. In addition, the flexible blades BP are unstable at any collective and any rotational speed below 1000 RPM, and stable for larger rotational speeds and collective pitch between 0 and 25 degrees.

In conclusion, the hover testing of the flexible and stiff rotors has shown that the performance and efficiency of the blades BP are comparable to that of the stiff blades R. In contrast, the figure of merit of the flexible blades C is poor, due to a large twist induced by the centrifugal forces acting on the tip body. Therefore, the flexible blade design BP appears more favorable in terms of hover efficiency and is selected for the subsequent tests. In addition, it is found that the stability boundaries of both flexible rotors appear to depend on the rotation speed and the collective pitch angle.

## **5.2 Validation of the DIC Technique**

The surface heights of the stiff rotor blade M at a fixed spanwise position (three-quarter span) are measured using the DIC technique and LDS. A comparison between the results of both techniques at three different rota-

tional speeds (500 RPM, 700 RPM and 900 RPM) is shown in Fig. 5.7. These measurements give not only the shape of the blade section but also its mean vertical position.

As the rotational speed increases, the increased lift on the rotor blade causes it to bend upward. Because the blade is relatively stiff, negligible torsional deformation is expected. Based on the measured data, the first observation is that the DIC data is significantly smoother than the LDS data. Nevertheless, it can be seen that the measurements by DIC, plotted as dashed lines, are contained within the dispersion of the LDS data. Consequently, we conclude that both the DIC and LDS experimental techniques give an identical three-dimensional position in space and identical shape of the rotating blade. This good correlation proves that DIC is a reliable technique to measure the components of displacement of a rotating blade.

To confirm the computation of blade pitch angles using DIC measurements, the experimental data are compared to the geometry of the mold used to fabricate the blade M. Fig. 5.8 shows the spanwise variation of pitch for the stiff blade M rotating at 300 RPM, at various root pitch angles. A linear fit is applied to the experimental data and it is found that the slope of the straight lines is equal to  $-0.7$  deg/cm, which corresponds to the actual structural twist of the blade imparted by the mold (as given in Table 4.1). It can also be seen from this graph that the blade experiences negligible elastic twist deformations, since the pitch at each radial station is approximately equal to the sum of the root pitch and the built-in twist.

Table 5.1: Theoretical precision of displacement vectors computed by DIC

Size of the interrogation window	Precision of 2D vectors
$128 \times 128$	0.005 pixel
$64 \times 64$	0.01 pixel
$32 \times 32$	0.025 pixel
$16 \times 16$	0.05 pixel
Size of the interrogation window	Precision of 3D vectors
$128 \times 128$	0.01 pixel
$64 \times 64$	0.025 pixel
$32 \times 32$	0.05 pixel
$16 \times 16$	0.1 pixel

Furthermore, the pitch angle at the root computed from DIC measurements is compared to the angle given by the laser inclinometer in Fig. 5.9. This test is conducted on the flexible rotor blade BP, spinning at 1200 RPM. It is seen that both measurement techniques are in excellent agreement.

Finally, it is important to determine the accuracy of the measurements obtained using DIC to compare the method with alternative experimental techniques. An estimation of the uncertainties in the DIC measurement based on a literature survey is presented in the next paragraph. Then, the calculation of the error from the recorded experimental data is given.

The manual delivered with the La Vision DaVis 7.2 software package [97] gives an estimate of the accuracy of the displacement vectors computed by the DIC algorithm (see Table. 5.1). This estimate is only a function of the size of the interrogation window used by the algorithm and holds for an ideal experimental setup with high quality images, high contrast speckle

pattern and perfect calibration procedure. In the present study, the size of the interrogation window is 32- by 32-pixel and the resolution of the images is 6.75 pixel/mm. The corresponding accuracy of the 3D vectors as indicated by the manual is 0.05 pixel, which translates to an absolute accuracy of 7  $\mu\text{m}$ .

However, there are other sources of error in the computation of displacement vectors than those produced by the DIC algorithm. Several studies have focused on quantifying overall measurement accuracy in a 3-D DIC setup [98, 99]. Classically, the sources of error are divided into two categories. The first one relates to the correlation process, which is linked to the quality of the speckle pattern, the interrogation window size and correlation algorithms such as interpolation of grey scale intensities [100]. The second type of error affects the 3-D reconstruction of the test specimen and is due to uncertainties in the relative position and orientation of the cameras with respect to the calibration plate. Based on this literature survey, for the present setup, the combined error due to all sources of uncertainty is on the order of 0.01 pixels (1.5  $\mu\text{m}$ ) for in-plane displacements, and 0.1 pixels (15  $\mu\text{m}$ ) for out-of-plane displacements.

In addition, the accuracy of the DIC technique can be estimated from the comparison of displacement measurement carried out with the laser distance sensor and the DIC system. It is found that the standard deviation between the LDS data and DIC data (shown in Fig 5.7) is equal to 120  $\mu\text{m}$ . However, the uncertainty in LDS measurements is dominated by electrical noise, which is absent in the DIC measurements. Therefore, we conclude that

the DIC measurements are at least as accurate as the laser distance sensor.

Finally, the repeatability of the DIC experimental procedure is investigated. The DIC technique uses raw images composed of a number of exposures of the rotor blade at a specific azimuthal location. Hence, the uncertainty in the measurements is dominated by the random variations in the rotor blade displacement from one revolution to another due to turbulence. However, it was noticed that these variations are small and do not cause a noticeable blur when the images are superimposed. Another issue with repeatability is when the camera setup is changed and the experiment is repeated. Guidelines for alignment and spacing of the cameras result in very small variations in the setup of cameras between experimental runs and it is noticed that there is no observable difference in the measured results. Therefore we conclude that the error associated with repeatability is below the uncertainty of the DIC technique.

From the above discussion, we conclude that the DIC technique is a reliable approach to measure rotor blade deformation under rotation. Consequently, the DIC technique can be extensively used to generate the full-field displacements of various blade designs.

### **5.3 Validation of the Numerical Analysis**

A series of validation cases are used to perform checks at various stages of the development of the analysis. A reference study by Hopkins and Ormiston [101] has selected typical problems to verify different features of a rotor

blade aeroelastic model. These problems include the verification of the prediction of static deformations, the modeling of boundary conditions, and the computation of the natural frequencies of both static and rotating beams.

### 5.3.1 Static elasticity test cases

The following problems verify the correctness of the uncoupled terms present in the strain energy of a static beam, as well as the modeling of boundary conditions and the procedure to obtain a numerical solution.

#### 5.3.1.1 Euler-Bernoulli cantilever beam under its own weight

This is the simplest case to verify bending of a cantilever beam. A schematic is shown in Fig. 5.10a. The governing equation with boundary conditions is

$$\int_0^R (-EIw'''' - \rho Ag)\delta w dx = 0 \quad (5.1)$$

At  $x = 0$ :

$$\begin{cases} w = 0 \\ w' = 0 \end{cases} \quad (5.2)$$

At  $x = R$ :

$$\begin{cases} EIw'' = 0 \\ EIw''' = 0 \end{cases} \quad (5.3)$$

The analytical solution of this equation is

$$w(x) = -\frac{\rho Agx^2}{24EI} (6R^2 - 4Rx + x^2) \quad (5.4)$$

$$w(R) = -\frac{\rho AgR^4}{8EI} \quad (5.5)$$

Fig. 5.10b shows the analytical vertical deflection of the deformed beam and the deflection predicted by the numerical model using 20 finite elements. An excellent correlation is observed.

### 5.3.1.2 Euler-Bernoulli cantilever beam under distributed torsion

This validation case verifies how the twist of a cantilever beam loaded uniformly by a distributed torsion (see Fig. 5.11a) is predicted. The governing equation, with boundary conditions is

$$\int_0^R (GJ\theta'' + t)\delta\theta dx = 0 \quad (5.6)$$

At  $x = 0$ :

$$\theta = 0 \quad (5.7)$$

At  $x = R$ :

$$GJ\theta' = 0 \quad (5.8)$$

The analytical solution can be found by integrating the governing equation twice and imposing the boundary conditions. The result is

$$\theta(x) = \frac{tx}{2GJ}(2R - x) \quad (5.9)$$

$$\theta(R) = \frac{tR^2}{2GJ} \quad (5.10)$$

The correlation between the analytical solution and the prediction is shown in Fig. 5.11b.

This test case also exhibits the axial foreshortening associated with the trapeze effect. Figure 5.12 shows the predicted negative axial displacement

resulting from the twist of the beam, compared to the analytical displacements derived for the cases of a trapeze and a thin ribbon (defined by Eq. (2.46) and Eq. (2.61) respectively). An excellent correlation can be observed between the displacement predicted by the numerical model and the analytical solution for the foreshortening of a ribbon. In addition, it can be seen that the additional torsional stiffening due to the interaction between neighboring fibers, forcing them to deform as helices, as opposed to the case of a trapeze where the fibers remain straight, results in a 50% decrease of the tip twist.

### 5.3.1.3 Euler-Bernoulli cantilever beam under its own weight with a torsional spring at the root

This test case allows to verify that the boundary condition associated with a torsional spring is correctly imposed in the numerical model. A cantilever Euler-Bernoulli beam, loaded by its own weight and constrained by a torsional spring at the root, as shown in Fig. 5.13a, is considered. The potential energy of the beam is

$$V = \frac{1}{2} \int_0^R EI w''^2 dx + \frac{1}{2} k_\beta w_0'^2 \quad (5.11)$$

Leading to the following governing equation

$$\int_0^R (-EI w'''' - \rho A g) \delta w dx = 0 \quad (5.12)$$

At  $x = 0$ :

$$\begin{cases} w = 0 \\ EI w'' - k_\beta w' = 0 \end{cases} \quad (5.13)$$

At  $x = R$ :

$$\begin{cases} EIw'' = 0 \\ EIw''' = 0 \end{cases} \quad (5.14)$$

The analytical solution is derived by integrating the governing equation four times, and imposing the appropriate boundary conditions. The result is

$$w(x) = \frac{-\rho Ag}{EI} \left( \frac{x^4}{24} - \frac{Rx^3}{6} + \frac{R^2x^2}{4} + \frac{R^2xEI}{2k_\beta} \right) \quad (5.15)$$

The correlation between the analytical bending deflection and the bending predicted by the numerical model is shown in Fig. 5.13b.

#### 5.3.1.4 Euler-Bernoulli cantilever beam subjected to a concentrated shear force

The action of a concentrated load on a cantilever beam is also simulated and compared to the analytical solution. A cantilever beam with a load acting at a distance  $a$  from the root (see Fig. 5.14a) is considered.

The analytical solution for the bending deflection is given by

$$\begin{cases} w(x) = \frac{F_z x^2}{6EI} (3a - x) & 0 \leq x \leq a \\ w(x) = \frac{F_z a^2}{6EI} (3x - a) & a \leq x \leq R \end{cases} \quad (5.16)$$

The agreement between the analytical and numerical solutions is shown in Fig. 5.14b. Notice the refined meshing of the beam in the neighborhood of the point of application of the concentrated force. The beam is discretized such that the point of application of the force coincides with the end node of an element.

### 5.3.1.5 Euler-Bernoulli cantilever beam subjected to a concentrated torque

Finally, the simple case of a cantilever beam subjected to a concentrated torque, as shown in Fig. 5.15a, is also verified.

It can be shown analytically that the angle of twist as a function of the spanwise coordinate is

$$\theta(x) = \frac{M_x x}{GJ} \quad (5.17)$$

Figure 5.15b shows very good agreement between the numerical twist and the analytical solution.

The series of cases simulated and presented above validates the prediction of uncoupled bending and twist deformations. The predictions of nonlinear coupled deformations are validated in the next section. However, closed-form, analytical solutions do not exist for such cases. Therefore, the results obtained by the numerical model are correlated to experimental measurements collected during the *Princeton beam experiment* [102, 103].

### 5.3.2 Princeton beam test case

An experimental study referred to as the Princeton beam experiment [102, 103] has been widely used in the past as a standard of comparison for nonlinear elastic beam deformations and dynamic response. The recorded data presented in this study includes the combined flatwise bending ( $w^*$ ), chordwise bending ( $v^*$ ) and twist ( $\theta$ ) of a homogeneous cantilever beam with tip load, as well as the flatwise and chordwise natural frequencies of the same beam with

a tip mass.

The experimental setup used to measure static deflections is shown in Fig. 5.16. The cantilever beam was fabricated from 7075 type aluminum and had a rectangular cross-section (see beam parameters in Table 5.2). It was inserted into a precision, milling-machine type, indexing chuck which allowed the root pitch to be varied from  $0^\circ$  to  $90^\circ$  with  $15^\circ$  increments. Gravity loads ranging from 1 to 4 pounds (0.454 to 1.814 kg) were applied at the tip of the beam.

Table 5.2: Princeton beam parameters

Material	Aluminum 7075	
Young's modulus, ksi (GPa)	10,428	(71.9)
Shear modulus, ksi (GPa)	3,902	(26.9)
Mass per unit length, lb/ft (kg/m)	0.076	(0.113)
Length, in (m)	20	(0.508)
Width, in (m)	0.5	(0.0127)
Thickness, in (m)	0.125	(0.0032)

### 5.3.2.1 Static deflections

The beam deflections along the vertical and horizontal axes were recorded by projecting reference points of the beam in the deformed position into vertical and horizontal planes. From these measurements, the flatwise and chordwise bending deflections were calculated and plotted. Additionally, twist measurements were made by attaching lightweight rods at selected spanwise

stations, perpendicularly to the beam span, then measuring the tip deflection of these rods and finally using inverse trigonometric functions (arctan or arccos) to compute the angles of twist.

The experimental static measurements are shown in Fig. 5.17 and Fig. 5.18, and compared to the analytical predictions obtained using the analysis developed in this dissertation. Note that only the experimental data corresponding to a tip load of 1 lb is presented. Cases with larger tip loads result in normalized tip bending deflections on the order of 30%, which is beyond the scope of a beam analysis developed for moderate bending deflections. In addition, due to the symmetry of the Princeton beam and the experimental setup, each bending deflection could be measured identically twice by considering the root angle to be  $+\theta$  or  $-\theta$  degrees. Both measurements are reported in Fig. 5.17. In addition, the same angle of twist could be computed in two ways, using the inverse tangent or inverse cosine function. Thus, four experimental measurements of twist are plotted for every root pitch angle.

For the root pitch angle  $\theta_0 = 0^\circ$ , the beam only bends in the chordwise direction, which corresponds to the direction of maximum bending rigidity. At this angle, we can observe in Fig. 5.17b a small offset between the measured and predicted chordwise bending deflections. This difference is attributed to an imperfect clamp condition in the experiment, which has already been reported in another study by Hopkins and Ormiston [101].

As the root pitch increases, the beam experiences a combination of flatwise bending, chordwise bending, and twist deformations. A very good

correlation can be seen in Fig. 5.17a between the flatwise bending deflections predicted by the analysis and measured during the experiment. In addition, the predicted slope of the chordwise bending deflections also matches the experiment.

The predictions of twist are shown in Fig. 5.18 and it can be seen that they fall within the range of uncertainty of the measured data. In addition, it can be noticed that the maximum twist angle measured during the experiment seems to correspond to the case  $\theta_0 = 45^\circ$ , whereas the maximum twist predicted using the analysis corresponds to  $\theta_0 = 60^\circ$ . It is intuitive to affirm that the root pitch angle associated with the largest tip twist will not correspond to  $\theta_0 = 45^\circ$  since the beam cross-section is not a square. In fact, no trend can be observed from the experimental data because of the measurement uncertainties.

### 5.3.2.2 Natural frequencies

The flatwise and chordwise natural frequencies of the Princeton beam were measured as a function of the beam root pitch angle, tip mass and direction of excitation. Weights were rigidly attached to the beam tip and the beam was excited (by hand) along the flatwise and the chordwise directions. Strain gages used as frequency transducers permitted fairly accurate measurement of both the flatwise and chordwise frequencies. Note that since the geometry of the tip mass was not reported, it is modeled in the present analysis as a concentrated mass attached to the centroid of the beam tip cross-section, and

its rotational inertia is neglected.

Figure 5.19 shows the natural frequencies of the Princeton beam, as reported in Ref. [102], as well as the frequencies predicted using the numerical model developed for this dissertation. A good agreement between the experimental data and the analytical predictions is observed.

Additionally, the torsional frequencies in vacuum and with no tip load of the Princeton beam are predicted using the numerical model. However, they cannot be correlated to experimental data, because they were not measured, nor reported in Ref. [102]. Instead, the frequencies obtained using the numerical model are compared to the analytical frequencies calculated using the design parameters of Table 5.2 and the following formula for the torsional frequencies of a beam [44]

$$\omega_{\theta k} = \left(k - \frac{1}{2}\right) \pi \sqrt{\frac{GJ}{m_0 k_m^2 R^2}} \quad (5.18)$$

The first five natural frequencies are given in Table 5.3. A very good correlation between the analytical solution and the numerical prediction can be observed.

### 5.3.3 Dynamics test cases

The following problems verify the exactness as well as the numerical implementation of the kinetic energy terms arising from the rotation of a beam in vacuum, derived in Chapter 2 of this dissertation.

Table 5.3: Torsional frequencies of Princeton beam ( $\theta_0 = 0$  and  $P = 0$  lb)

Mode	Analytical solution [rad.s <sup>-1</sup> ]	Numerical prediction [rad.s <sup>-1</sup> ]
1	9567	9567
2	28701	28701
3	47836	47836
4	66970	66974
5	86104	86119

### 5.3.3.1 Bending frequencies of a rotating beam

Several analytical solutions to the eigenvalue problem of a rotating blade, clamped or hinged at the root, and experiencing a pure flapping motion can be found in the literature.

For instance, Bisplinghoff *et al.* [78] made use of the Galerkin's method along with Duncan polynomials [104] to compute the first three bending frequencies of a hinged-free uniform rotating beam. Bisplinghoff *et al.* [78] defined a dimensionless reference frequency parameter, as

$$K_{ref} = \frac{m_0 \Omega^2 R^4}{EI} \quad (5.19)$$

and the natural frequencies are computed for the case  $K_{ref} = 250$ .

In addition, Wright *et al.* [105] have also calculated and tabulated the frequencies of rotating beams for a variety of situations including root offset and tip mass, and for both hinged and fixed root boundary conditions. The case  $K_{ref} = 100$  was a subset of their tabulated results.

Finally, Harris [106] proposed an analytical test case for finite element

programs, based on a zero offset, hinged, flap only, rotating beam approximation of a UH-60 helicopter rotor blade.

The blade parameters employed by Harris [106] are used for the present verification. Specifically, the blade radius is equal to 28 feet (8.53 m) and the rotational speed is  $\Omega_{nom} = 222$  RPM. The corresponding reference frequency parameter is  $K_{ref} = 600$ . Additional parameters are summarized in Table 5.4.

Table 5.4: Simplified UH-60 blade parameters

Young's modulus [GPa]	212.1
Shear modulus [GPa]	81.575
Poisson's ratio	0.3
Mass per unit length [ $\text{kg}\cdot\text{m}^{-1}$ ]	9.5194
Radius [m]	8.5344
Chord [m]	0.6159
Thickness [m]	0.0161

A comparison of the frequencies obtained using the analysis developed in this dissertation with the analytical results (from Ref. [78, 105, 106]) is presented in Table 5.5. To match the reference frequency parameters ( $K_{ref} = 250$  for Ref. [78], and  $K_{ref} = 100$  for Ref. [105]) using the model blade described in Table 5.4, the analysis is run with reduced rotor angular velocities  $\Omega = 0.6455 \Omega_{nom}$ , and  $\Omega = 0.4082 \Omega_{nom}$  respectively. The comparison of the results shows a maximum error of 0.5% between the analytical solutions and the numerical predictions.

Secondly, the hinged boundary condition is replaced by a clamped

Table 5.5: Bending frequencies of hinged rotating model blade

$K_{ref}$	Mode	Analytical solution [per rev]	Numerical prediction [per rev]
Comparison with Wright <i>et al.</i> [105]			
100	1	1.00000	1
100	2	2.94432	2.94439
100	3	6.52526	6.52554
100	4	12.01429	12.0146
100	5	19.44698	19.4462
Comparison with Bisplinghoff <i>et al.</i> [78]			
250	1	1.00000	1
250	2	2.67730	2.6798
250	3	5.22268	5.1957
Comparison with Harris [106]			
600	1	1.00000	1
600	2	2.55711	2.55711
600	3	4.57999	4.57997
600	4	7.24448	7.24431
600	5	10.57407	10.5733
600	6	14.60953	14.6067
600	7	19.38809	19.3798
600	8	24.93683	24.9164
600	9	31.27599	31.2299
600	10	38.42277	38.3444

boundary condition. The predicted natural frequencies of the rotating model blade are compared to the analytical values tabulated in Ref. [106]. The results are shown in Table 5.6. The maximum error associated with the predicted values is equal to 0.02%.

Thirdly, the accuracy in modeling the blade root cut-out (or root offset) is verified by comparing the natural frequencies predicted for a blade with a root offset ( $x_0 = R/11$ ) to the analytical frequencies derived in Ref. [106] for

Table 5.6: Bending frequencies of clamped rotating model blade

$K_{ref}$	Mode	Analytical solution [per rev]	Numerical prediction [per rev]
100	1	1.12022	1.12013
100	2	3.36392	3.36375
100	3	7.46459	7.46429
100	4	13.48818	13.48724
100	5	21.44768	21.44426

the same blade design. These frequencies are shown in Table 5.7 for the cases of an hinged and a clamped root boundary condition.

Table 5.7: Bending frequencies of rotating blade with root offset

$K_{ref}$	Mode	Analytical solution [per rev]	Numerical prediction [per rev]
Hinged condition at the root			
100	1	1.07215	1.07206
100	2	3.08852	3.08824
Clamped condition at the root			
100	1	1.18578	1.18579
100	2	3.48786	3.48786

Finally, the effect of a tip mass on the rotating bending frequencies is also verified. The frequencies reported in Ref. [106] for the case of a tip mass to blade mass ratio equal to 1 (i.e.  $M_{tip}/(m_0R) = 1$ ) are correlated to the frequencies obtained using the present analysis. The comparison is shown in Table 5.8.

To complete the validation of the numerical model presented in this dissertation, we verify the torsional frequencies predicted for a rotating beam. In

Table 5.8: Bending frequencies of rotating blade with tip mass

$K_{ref}$	Mode	Analytical solution [per rev]	Numerical prediction [per rev]
Hinged condition at the root			
100	1	1.00000	1.00000
100	2	4.02070	3.91507
Clamped condition at the root			
100	1	1.04864	1.04855
100	2	4.34515	4.34480

particular, we compare the frequencies associated with the propeller moment and the trapeze effect, to the analytical frequencies derived in Chapter 2.

### 5.3.3.2 Torsional frequencies of a rotating beam

**Frequency associated with the propeller moment** We consider the case of a uniform beam of length  $R$ , rectangular cross-section, clamped at the root, free at the tip, and rotating at the angular speed  $\Omega$ . In addition, we assume that the structural stiffness of the beam is large such that the trapeze effect can be neglected. Hence, the kinetic energy of the beam is

$$T = \frac{1}{2} \int_R \left[ m_0 \Omega^2 \left( k_{m_\eta}^2 \cos^2 \theta + k_{m_\xi}^2 \sin^2 \theta + x^2 \right) + m_0 k_m^2 \ddot{\theta} \right] dx \quad (5.20)$$

and the strain energy is

$$U = \frac{1}{2} \int_R GJ \theta'^2 dx \quad (5.21)$$

Using the EHP, we obtain the following boundary value problem

$$\begin{cases} m_0 k_m^2 \ddot{\theta} + m_0 \Omega^2 \left( k_{m_\xi}^2 - k_{m_\eta}^2 \right) \theta - GJ \theta'' = 0 & 0 < x < R \\ \theta = 0 & x = 0 \\ \theta' = 0 & x = R \end{cases} \quad (5.22)$$

It can be shown that the analytical (exact) natural frequencies corresponding to this problem are

$$\omega_k^2 = \left(k - \frac{1}{2}\right)^2 \pi^2 \frac{GJ}{m_0 k_m^2 R^2} + \Omega^2 \frac{(k_{m_\xi}^2 - k_{m_\eta}^2)}{k_m^2} \quad (5.23)$$

where  $k \in \mathbb{N}^*$ . The first term on the right hand side of Eq. (5.23) is the square of the structural torsional frequency of the beam, denoted  $\omega_{k0}^2$ . The second term is the frequency associated with the propeller moment. Upon non-dimensionalization, the analytical torsion frequencies of the beam are given by

$$\nu_k = \sqrt{\frac{(k_{m_\xi}^2 - k_{m_\eta}^2)}{k_m^2} + \frac{\omega_{k0}^2}{\Omega^2}} \quad (5.24)$$

The analytical frequencies are computed for the first 5 torsional modes of the beam ( $k = 1, \dots, 5$ ) and compared to the numerical predictions, shown in Table 5.9. A very good correlation can be observed, the maximum error being on the order of 0.02%.

Table 5.9: Torsional frequencies of clamped-free rotating blade

$\Omega$ [RPM]	Mode	Analytical solution [per rev]	Numerical prediction [per rev]
222	1	73.0758	73.0758
222	2	219.2092	219.2097
222	3	365.3462	365.3522
222	4	511.4838	511.5157
222	5	657.6215	657.7326

It is also interesting to simulate the case of a rotating hinged-free beam

in torsion. The corresponding analytical frequencies are

$$\omega_k^2 = k^2 \pi^2 \frac{GJ}{m_0 k_m^2 R^2} + \Omega^2 \frac{(k_{m_\xi}^2 - k_{m_\eta}^2)}{k_m^2} \quad (5.25)$$

where  $k \in \mathbb{N}$ . The comparison with the predicted frequencies is reported in Table 5.10. Note that the first rotating torsional frequency corresponds to the case  $k = 0$  in Eq. (5.25) which is

$$\omega_1 = \Omega \sqrt{\frac{(k_{m_\xi}^2 - k_{m_\eta}^2)}{k_m^2}} \quad (5.26)$$

or in dimensionless form

$$\nu_1 = \sqrt{\frac{(k_{m_\xi}^2 - k_{m_\eta}^2)}{k_m^2}} \quad (5.27)$$

Typically  $k_{m_\eta}^2 \ll k_{m_\xi}^2$ , therefore the first torsional frequency is slightly less than 1/rev.

Table 5.10: Torsional frequencies of hinged-free rotating blade

$\Omega$ [RPM]	Mode	Analytical solution [per rev]	Numerical prediction [per rev]
222	1	0.9993	0.9993
222	2	146.1414	146.1414
222	3	292.2776	292.2796
222	4	438.4150	438.4298
222	5	584.5526	584.6146

**Frequency associated with the trapeze effect** To verify the numerical prediction of the torsional frequency associated with the trapeze effect, a circular cantilever pipe with extensional and torsional degrees of freedom, rotating

in vacuum at constant angular velocity  $\Omega$  is modeled. Since the pipe is axisymmetric, the propeller moment vanishes. In addition, the elastic center at every cross-section is coincident with the area centroid and the mass centroid. Therefore, the kinetic energy and potential energy of the pipe are

$$T = \frac{1}{2} \int_R \left[ m_0 (\Omega^2 x^2 + 2\Omega^2 x u) + m_0 k_m^2 \dot{\theta}^2 \right] dx \quad (5.28)$$

$$V = \frac{1}{2} \int_R \left[ E A u'^2 + E A k_A^2 u' \theta'^2 + E B_1 \frac{\theta'^4}{4} \right] dx \quad (5.29)$$

Additionally, to focus on the trapeze effect, we assume that the pipe is inextensible. Therefore,  $u_e = 0$  and

$$\begin{cases} u = - \int_0^x \frac{k_A^2}{2} \theta'^2 d\chi \\ u' = - \frac{k_A^2}{2} \theta'^2 \end{cases} \quad (5.30)$$

Substituting Eq. (5.30) into Eq. (5.28) and (5.29), we obtain

$$T = \frac{1}{2} \int_R \left[ m_0 \Omega^2 x^2 - 2m_0 \Omega^2 x \int_0^x \frac{k_A^2}{2} \theta'^2 d\chi + m_0 k_m^2 \dot{\theta}^2 \right] dx \quad (5.31)$$

$$V = \frac{1}{2} \int_R \left[ \frac{E}{4} (B_1 - A k_A^4) \theta'^4 \right] dx \quad (5.32)$$

The integral term in Eq (5.31) can be simplified using Fubini's theorem, as

$$\frac{1}{2} \int_R \left[ -2m_0 \Omega^2 x \int_0^x \frac{k_A^2}{2} \theta'^2 d\chi \right] dx = \frac{1}{2} \int_R \left[ -m_0 \Omega^2 \frac{k_A^2}{2} \theta'^2 (R^2 - x^2) \right] dx \quad (5.33)$$

Then, the variations in the kinetic and potential energies are

$$\delta T = \int_R \left[ -m_0 \Omega^2 \frac{k_A^2}{2} (R^2 - x^2) \theta' \delta \theta' + m_0 k_m^2 \dot{\theta} \delta \dot{\theta} \right] dx \quad (5.34)$$

$$\delta V = \int_R \left[ \frac{E}{2} (B_1 - Ak_A^4) \theta'^3 \delta \theta' \right] dx \quad (5.35)$$

It can be seen that the nonlinear term in the variation in the strain energy (Eq. (5.35)) does not contribute to the dynamic analysis of small perturbations about the steady equilibrium position ( $\theta_e = \theta'_e = 0$ ). Ignoring this term, the variation in the Hamiltonian is

$$\delta H = \int_R \left[ -m_0 \Omega^2 \frac{k_A^2}{2} (R^2 - x^2) \theta' \delta \theta' + m_0 k_m^2 \dot{\theta} \delta \dot{\theta} \right] dx \quad (5.36)$$

From which the perturbed equation of motion is

$$\int_t \int_R \left[ -m_0 \Omega^2 \frac{k_A^2}{2} (R^2 - x^2) \Delta \theta' \delta \theta' + m_0 k_m^2 \Delta \dot{\theta} \delta \dot{\theta} \right] dx dt = 0 \quad (5.37)$$

An approximate expression for the natural frequencies associated with this equation of motion can be obtained using the assumed-modes approach. In particular, assuming

$$\theta(x, t) = \boldsymbol{\psi}^T(x) \mathbf{q}(t) = \sum_{i=1}^N \psi_i(x) q_i(t) \quad (5.38)$$

It can be shown that the terms in the mass and stiffness matrices are

$$M_{ij} = \int_R m_0 k_m^2 \psi_i \psi_j dx \quad (5.39)$$

$$K_{ij} = \int_R m_0 k_A^2 \Omega^2 \frac{R^2 - x^2}{2} \psi'_i \psi'_j dx \quad (5.40)$$

Table. 5.11 shows the first five frequencies obtained by the assumed-modes method, with  $\psi_i(x) = (x/R)^i$ , compared to the first five torsional frequencies predicted by the numerical model. An excellent correlation between the results

Table 5.11: Torsional frequencies of cantilever rotating pipe

Mode	Approximated solution [per rev]	Numerical prediction [per rev]
1	0.9999	1.0000
2	2.4491	2.4495
3	3.8720	3.8731
4	5.2897	5.2922
5	6.7052	6.7121

can be observed. In addition, it can be seen in Table. 5.11 that for the case of a rotor blade with no tip mass, the uncoupled torsional frequency associated with the trapeze effect is equal to  $1/\text{rev}$ . For comparison, it was shown in § 2.5.1 that the frequency of a cable rotor with axisymmetric tip body is on the order of  $\sqrt{2}/\text{rev}$  for circular tip body, or  $\sqrt{3}/\text{rev}$  for a cruciform tip body.

Finally, this example demonstrates the accuracy of the numerical solution to the equations derived in Chapter 2.

## 5.4 Aeroelastic Behavior of the Flexible Rotor BP

### 5.4.1 Trim state in hover

The DIC technique and the numerical analysis are used to compute the trim state in hover of the flexible rotor BP, spinning at 1200 RPM and for a range of collective pitch angles. The trim results include:

- The spanwise variations of blade deformation predicted by the analysis and correlated with experimental measurements.
- The variation of rotor thrust as a function of the collective pitch predicted

by the analysis and correlated with measurements.

The spanwise variations of flap bending and torsional deformations measured by DIC are shown in Fig. 5.20 for a range of collective pitch angles from  $10^\circ$  to  $25^\circ$ . Also shown on the same plots are the deformation predicted by the analysis. Recall that the measurements of flap bending deflection are absolute (i.e. relative to the absolute coordinate system defined during calibration) because they are computed by extracting the surface heights of points located on the blade elastic axis. The measured twist distribution is also absolute because it relies on the measurement of surface heights (see Eq. (4.15)). Note that in contrast, the axial and lead-lag bending deflections are based on a reference “undeformed” state of the rotor blade, which corresponds to the blade spinning at very low rotational speed and low collective (as described in § 4.6).

First, by looking at the experimental measurements of flap bending deformation, it appears that the bending deflections contain not only quadratic and cubic content (which are linked to beam elastic deformation), but also a non-negligible linear component. As a matter of fact, cubic polynomials can be fitted to the experimental data and are found to be equal to

$$w_{10}(x) = 403x^3 - 115x^2 + 21x - 1 \quad (5.41)$$

$$w_{14}(x) = 115x^3 + 1x^2 + 19x - 1 \quad (5.42)$$

$$w_{18}(x) = -112x^3 + 70x^2 + 20x - 1 \quad (5.43)$$

$$w_{25}(x) = -499x^3 + 231x^2 + 11x - 1 \quad (5.44)$$

where the subscripts refer to the collective pitch angles. Therefore, the experimental measurement of bending deformation suggests the presence of a local discontinuity in flap bending stiffness at the root of the rotor blade. In fact, a visual inspection of the deformation of the blade airfoil at the root reveals that as the bending deflection increases, the camber of the circular arc cross-section diminishes, up to becoming almost flat for the larger collective pitch angles. To model this discontinuity in flap stiffness, a flapping spring at the root of the blade is added to the analysis. The magnitude of the flapping spring ( $k_\beta$ ) is determined by matching the linear components in the predicted and measured bending deflections and it is found that

$$k_\beta \simeq 1.5 \text{ N.m/rad} \quad (5.45)$$

By comparing the experimental measurements of flap bending to the analytical predictions, some discrepancy can be observed near the blade tip where the tip mass is located. The drag force and the destabilizing aerodynamic pitching moment acting on the tip mass induce both bending and twist deformation, which are not modeled by the present analysis. This refinement is the object of future work.

Furthermore, a very good correlation can be observed in Fig. 5.20b between the experimental measurements of pitch and the analytical predictions. Note that for any tip pitch angle less than the tip mass index angle ( $\theta_{ind} = 22^\circ$ ), the propeller moment acting on the tip mass is nose-up. However, the slope of the twist distribution in Fig 5.20b is negative, due to the

action of the nose-down aerodynamic pitching moment and the nose-down propeller moment acting on the blade airfoil.

Additionally, the axial and lead-lag bending deformations measured by DIC are shown in Fig. 5.21. Note that these deformations are calculated relative to the undeformed reference condition, which is why they are labeled  $\Delta u$  and  $\Delta v$  in Fig. 5.21a and 5.21b. Because the absolute axial and lead-lag deformations cannot be calculated by DIC, a correlation with the numerical predictions is not possible. However, the following qualitative remarks can be made.

It can be seen in Fig. 5.21a that as the blade collective pitch increases, the blade appears to decrease in length, i.e the axial extension is negative and decreases. This effect is due to the kinematic foreshortening associated with bending and twist, described in Chapter 2.

In addition, the increase in lag bending deflection (Fig. 5.21b) is the result of an increase in drag with increasing blade pitch. Due to the choice of orientation of the  $Y$ -axis in § 2.2, the lead-lag bending due to the drag is negative.

The errors associated with the DIC measurements are on the order of  $1.5 \mu\text{m}$  for the axial and lag bending deflections, and  $15 \mu\text{m}$  for the flap bending deflections. The corresponding error bars in Fig. 5.20 and 5.21 are contained within the thickness of the plotted lines.

Finally, the analytical prediction of thrust produced in hover by the rotor blade BP is shown as a function of the collective pitch in Fig. 5.22. A very good correlation between the predictions and the experiment measurements of thrust obtained using a load cell can be observed.

#### 5.4.2 Stability Analysis

In this section, the stability of the response of the rotor blade BP to small perturbations about the trim condition is investigated using the numerical model.

First, a flutter analysis of the blades BP at various collective pitch angles is conducted and the results are compared to the experimental conclusions reported in § 5.1. Then, the effect of a change in chordwise position of the tip mass, or in the rotor diameter, on the stability boundary is investigated.

##### 5.4.2.1 Flutter boundaries of the flexible blades BP

Figure. 5.23 shows the natural frequencies of the first 5 modes of vibration of the blade BP at 5° and 15° collective. The mode shapes are labeled "F" for flap, "L" for lead-lag and "T" for torsion. Due to the non-coincidence of the area centroid, the center of gravity and the elastic center at every section of the blade BP, all the modes of vibration are coupled. However, one degree of freedom may contribute more significantly than others. This can be identified visually by plotting the mode shapes. Figure. 5.25 shows the shape of the first 5 eigenmodes, and it can be seen that:

- the first eigenmode (F/L/T) fully couples the flap, lag and pitch deformations,
- the second eigenmode (T1) and third eigenmode (T2) are predominantly torsional modes,
- the fourth mode (L/T) involves lag-torsion coupling,
- the fifth mode (T3) (not shown in Fig. 5.25) is also predominantly a torsional mode.

For comparison with the frequencies of the flexible blade BP, the frequencies of a Sikorsky UH-60A Black Hawk helicopter blade [107] are shown in Fig. 5.24. It can be seen in Fig. 5.23 that three of the first five eigenmodes of the blade BP are torsional modes. The first torsional frequency ( $T1$ ) is on the order of 3/rev at the nominal hover RPM, and the second torsional frequency ( $T2$ ) is approximately equal to 7/rev. Note that since the pitch control mechanism in this analysis is modeled as infinitely stiff, the whole torsional flexibility comes from the blade itself. In contrast, only one of the first seven eigenmodes of the Black Hawk blade is a torsional mode, which vibrates at approximately 4/rev. In addition, note that some of the torsional flexibility is due to the control pitch link, which is responsible for an equivalent torsional stiffness at the root of the blade of 1090 ft-lb/deg [107]. From these observations, it can be seen that the rotating torsional frequencies of the flexible rotor BP are much lower than that of conventional rotor blades.

In addition, an indication of coalescence between the eigenmodes  $T2$  and  $L/T$  can be seen in Fig 5.23, for blade rotational speeds greater than 1100 RPM and for a collective pitch of  $5^\circ$ . Typically, the coalescence of two eigenmodes is the sign of a flutter instability. A confirmation of the stable or unstable nature of a particular mode is given by the study of damping coefficients.

The damping coefficients associated to each eigenmode are plotted as functions of the rotational speed in Fig 5.26-5.28. Recall that the damping coefficient  $\gamma$  was defined in § 3.2.4 as

$$\gamma = \frac{\Re(p)}{k} \quad (5.46)$$

Therefore, a change in the sign of  $\gamma$ , from negative to positive, indicates the onset of flutter.

From Fig. 5.26 and 5.27b, it can be seen that the  $F/L/T$  mode and the  $T2$  mode are unconditionally stable over the range of rotational speeds simulated (0 - 1400 RPM). However, the  $L/T$  mode is found to become unstable at  $\Omega = 1100 \text{ RPM}$  (see Fig. 5.28a). In this case, the onset of flutter is due to a coalescence between the  $L/T$  mode and the  $T2$  mode. An important observation is that the stability boundary is a function of the rotational speed. This result correlates with experimental observations of the blade BP in hover. It can also be seen in Fig. 5.28a that at  $\Omega = 1250 \text{ RPM}$ , the blade BP is predicted to be stable when  $\theta_0 = 15^\circ$  and unstable when  $\theta_0 = 5^\circ$ . This result agrees with experimental investigations which concluded that the blades

BP were unstable for collective below  $10^\circ$  when spinning at 1200 RPM.

Note also in Fig. 5.27a that the first torsional mode ( $T1$ ) becomes unstable at 1350 RPM and  $5^\circ$  collective. The cause of this instability is not explained yet, and a refined numerical simulation of the damping coefficients for higher rotation speeds is needed.

The aeroelastic model is then used to investigate ways of improving the aeroelastic stability of the flexible blades BP.

#### 5.4.2.2 Influence of the chordwise position of the tip mass on the flutter boundaries

One of the design parameters is the chordwise position of the tip mass (defined by  $\eta_m$  in Fig. 2.24). The analytical study presented in Chapter 2 has shown that the torsional frequency of a ribbon stiffened by a tip mass is maximum when the center of gravity of the tip mass is located on the elastic axis (see Fig. 2.13a). In the configuration fabricated and tested in hover, the flexible blade BP has its tip body mass balanced a distance equal to 34% of the chord forward of the elastic axis. Therefore, a case where the tip mass is moved aft is simulated, and the natural frequencies of the new configuration are compared to that of the original blade. Note that this approach is unconventional since a decrease in the stability margins is classically expected when the blade center of mass is moved aft.

It can be seen in Fig. 5.29 that the change in position of the tip mass predominantly affects the first two torsional modes of the rotor blade (modes

$T1$  and  $T2$ ). However, a decrease of the frequencies is observed, whereas a stiffening was expected considering uncoupled torsion. Nevertheless, by decreasing the frequencies associated with the third mode ( $T2$ ) while keeping those of the fourth mode ( $L/T$ ) relatively constant, coalescence of these two modes is avoided, as can be inferred by looking at the sign of the damping coefficients (Fig. 5.31). Consequently, the center of mass shift of the tip body allows an increase in the range of rotational speeds ensuring stable operation. Note also that at  $\Omega = 1600$  RPM, the analysis indicates a change in the sign of the determinant of the stiffness matrix. This can imply the onset of non-oscillatory diverging blade motion in the case of eigenmodes having positive damping. The stability analysis at rotational speeds higher than the operating hover RPM is out of the scope of this dissertation and is the object of future work.

Finally, note that another way to shift the coupled lag-torsion frequency relative to the second torsional frequency is to modify the lead-lag stiffness discretely at the root of the blade. This can be done by replacing the clamped condition by a lag hinge. The influence of this design modification will be investigated in the future.

#### **5.4.2.3 Effect of a change in rotor diameter on the flutter boundaries**

The effect of a change in rotor diameter on the stability boundaries is also studied. To simulate an expansion of the rotor, its radius is doubled

while all the other geometric parameters are kept constant. In addition, the rotational speed is adjusted such that the blade loading and the rotor thrust remain constant. Therefore, it can be shown that the product  $\Omega^2 R^3$  must remain constant. According to these assumptions, a rotor initially spinning at 1200 RPM before full blade deployment must be spinning at 425 RPM once the rotor diameter is doubled. Figure 5.32a shows the natural frequencies of the extended rotor at  $15^\circ$  collective and for rotational speeds up to 300 RPM. Note that due to the slower rotational speeds, the magnitudes of the natural frequencies of the deployed rotor are well under those corresponding to the original rotor. For clarity, only the frequencies of the deployed rotor are shown. It can be seen that the change in rotor diameter affects predominantly the first torsional mode ( $T1$ ) whose natural frequency increases and becomes closer to that of the second torsional mode ( $T2$ ). While coalescence of the modes  $T2$  and  $L/T$  is avoided, as shown by the sign of the damping coefficients in Fig. 5.32b, a flutter instability is observed at 220 RPM, due to coalescence of the two torsional modes. As a result, it can be seen that the change in rotor diameter has led to shifts of the natural frequencies and new stability boundaries. This indicates that when designing a variable-diameter extremely flexible rotor, the stability boundaries must be investigated for every operating rotor diameter.

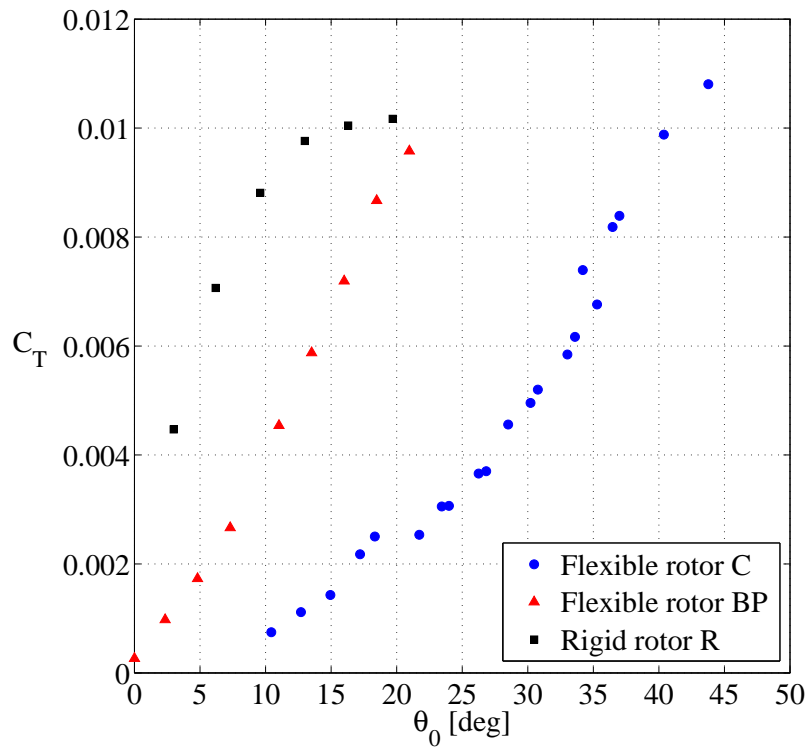


Figure 5.1: Thrust coefficients ( $\Omega = 1500$  RPM)

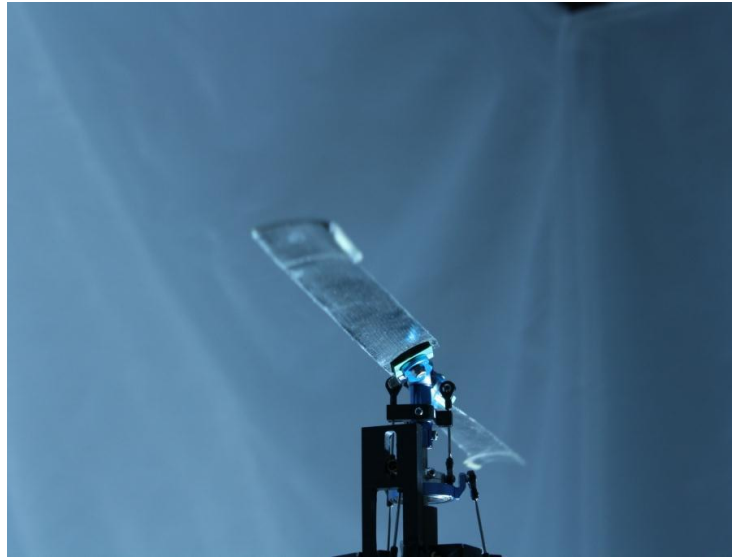


Figure 5.2: High twist induced over the inboard section of flexible blades C ( $\Omega = 1500 \text{ RPM}$ ,  $\theta_0 = 16^\circ$ )

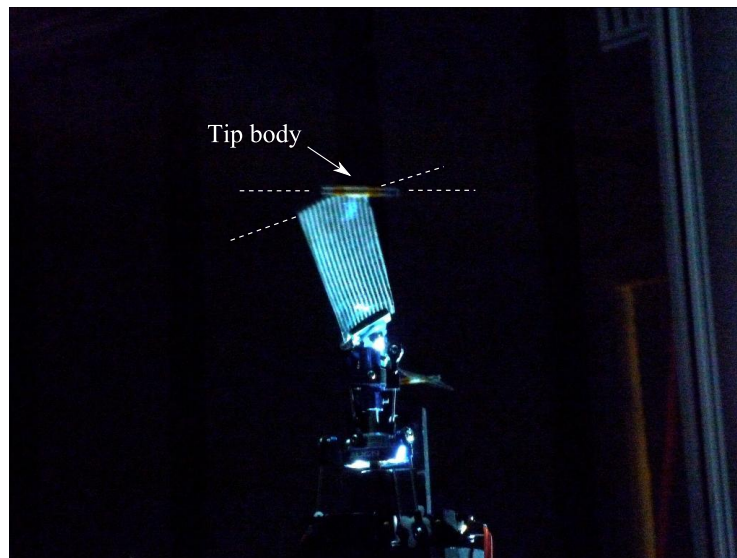


Figure 5.3: Tip pitch angle controlled by use of the propeller moment acting on the tip mass ( $\Omega = 1500 \text{ RPM}$ ,  $\theta_0 = 22^\circ$ )

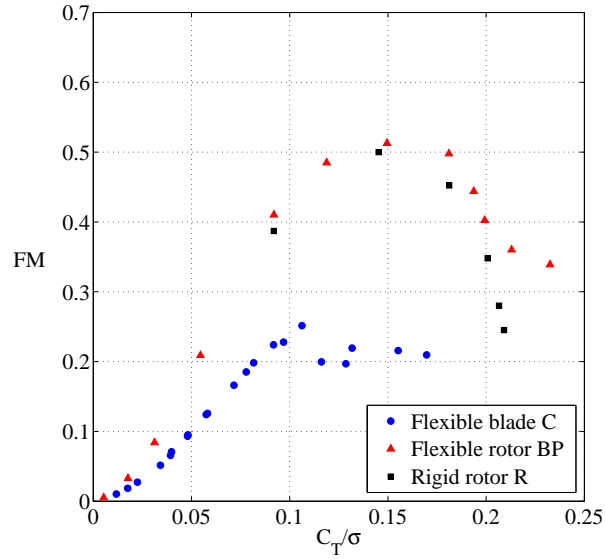


Figure 5.4: Figures of merit ( $\Omega = 1500 \text{ RPM}$ )

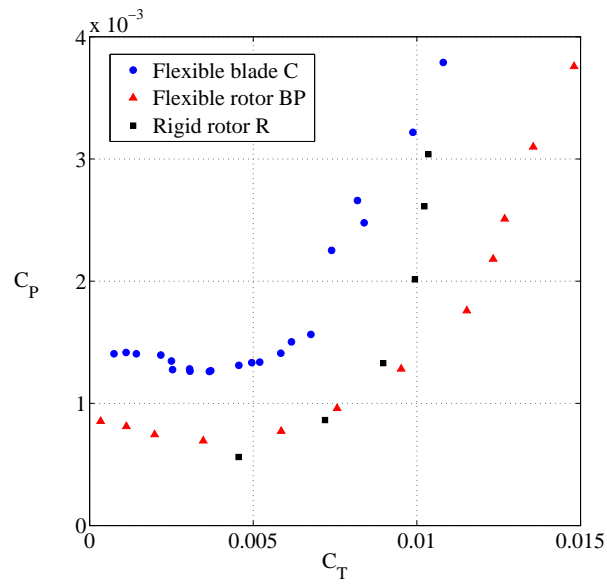


Figure 5.5: Power coefficient vs. thrust coefficient ( $\Omega = 1500 \text{ RPM}$ )

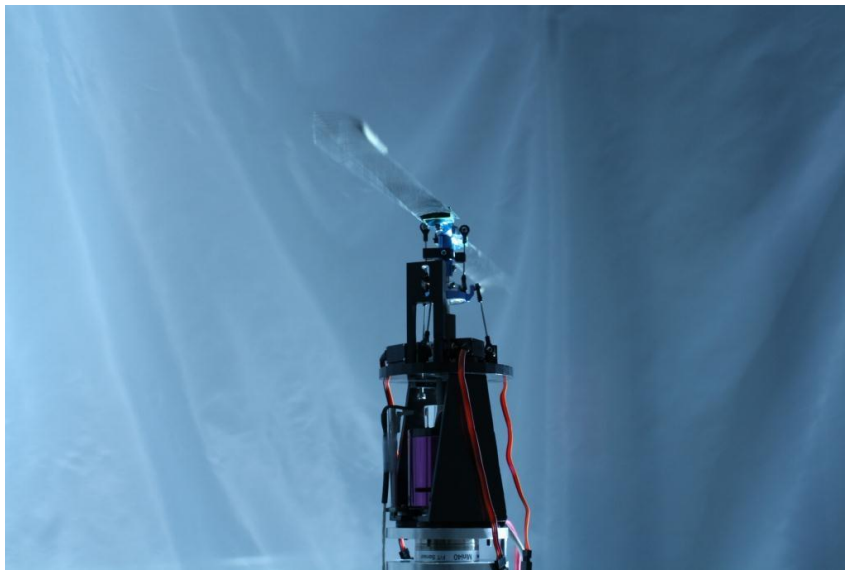


Figure 5.6: Pitch-flap flutter observed on flexible rotor blades C ( $\Omega = 1500$  RPM,  $\theta_0 = 0^\circ$ )

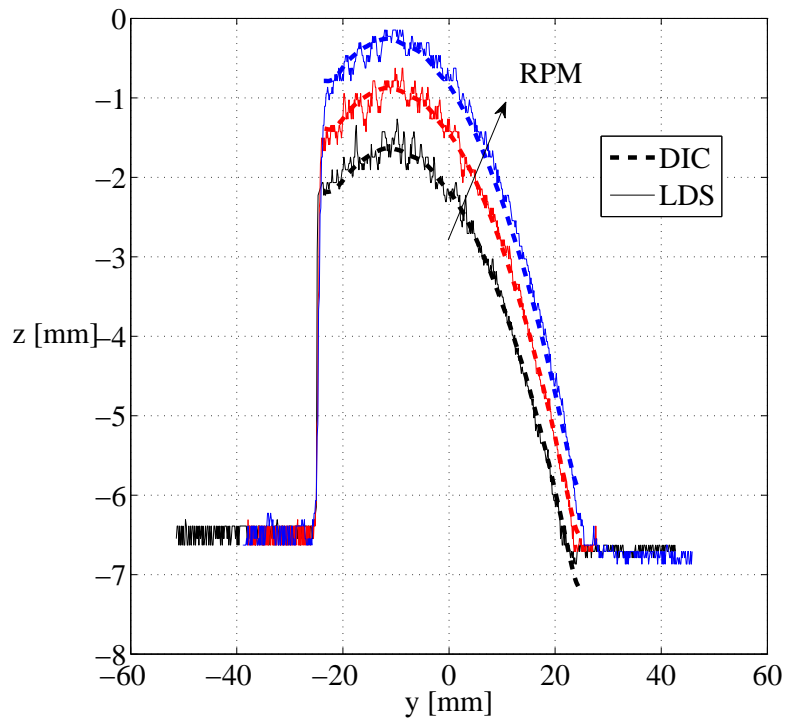


Figure 5.7: Blade section position and shape measured by DIC and LDS at 3/4 span of rigid blade M ( $\theta_0 = 11^\circ$ ,  $\Omega=500, 700, 900$  RPM)

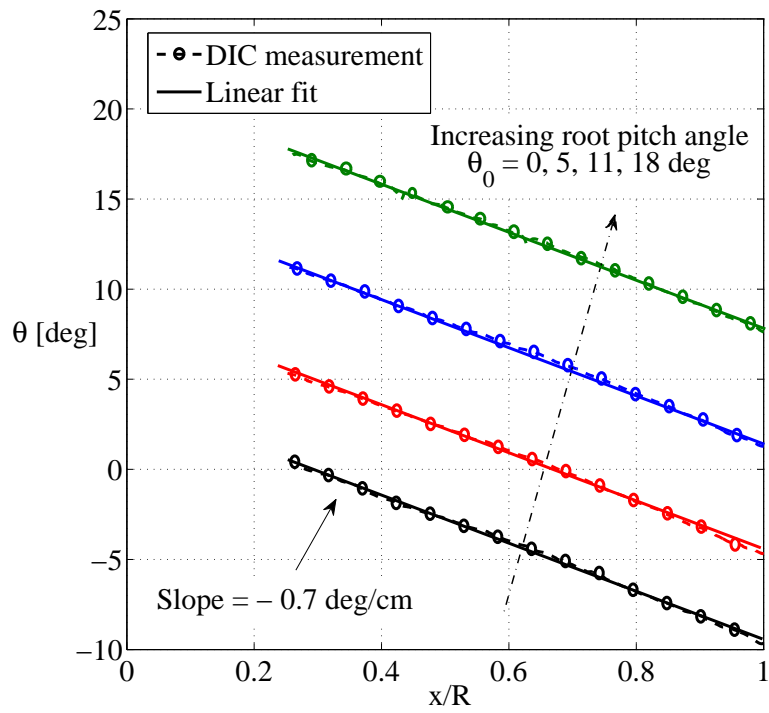


Figure 5.8: Spanwise variation of pitch measured by DIC, compared to design parameters (rigid blade M, washout twist,  $-0.7$  deg/cm), at various root pitch angles ( $\Omega = 300$  RPM)

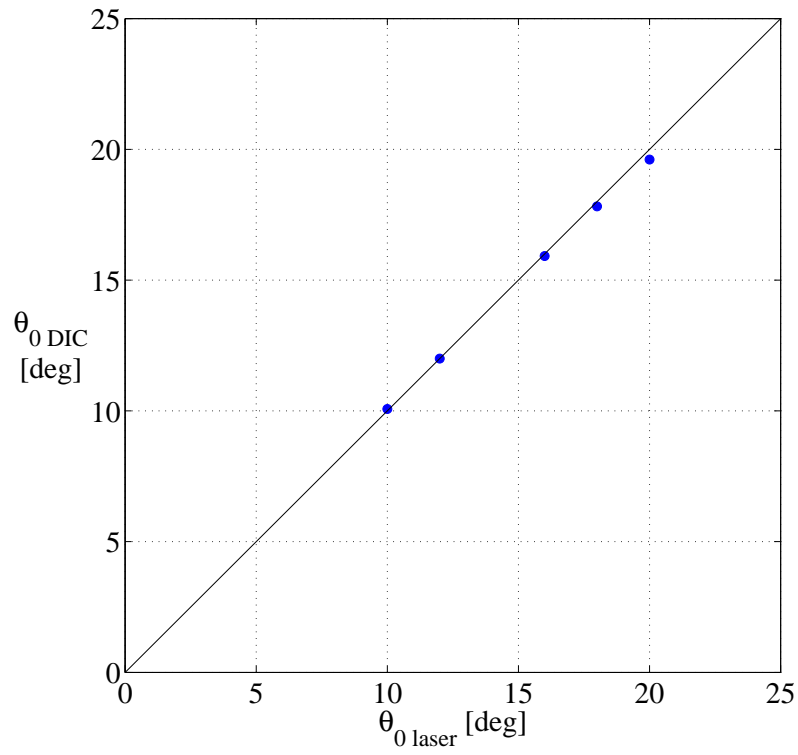
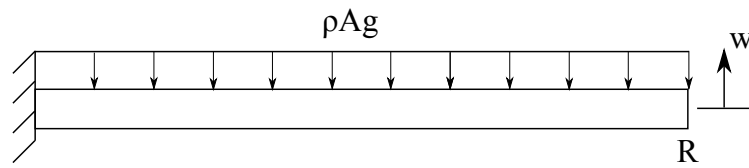
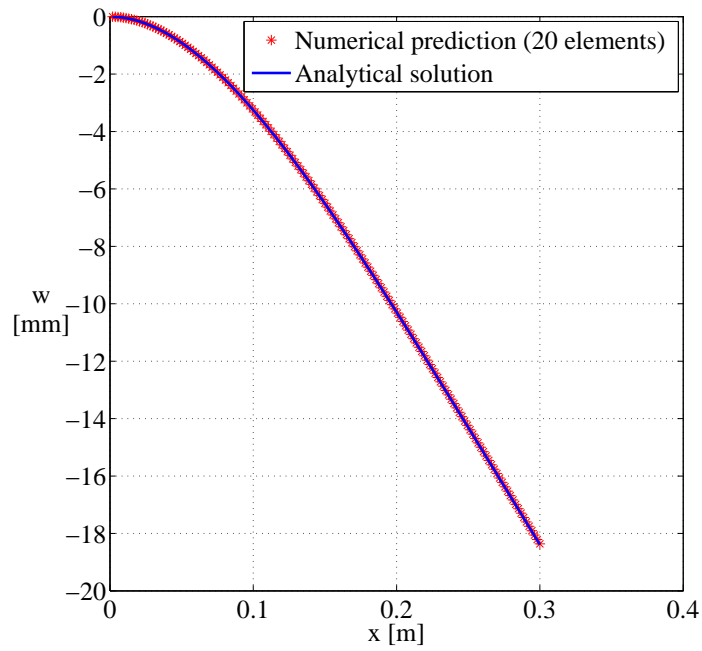


Figure 5.9: Root pitch angle of flexible blade BP measured by DIC, and compared to measurement of root pitch angles by laser inclinometer ( $\Omega = 1200$  RPM)

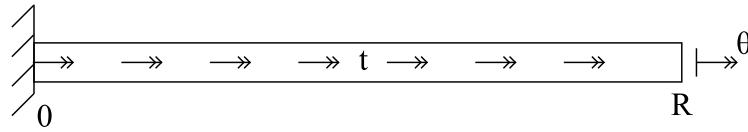


(a) Schematic

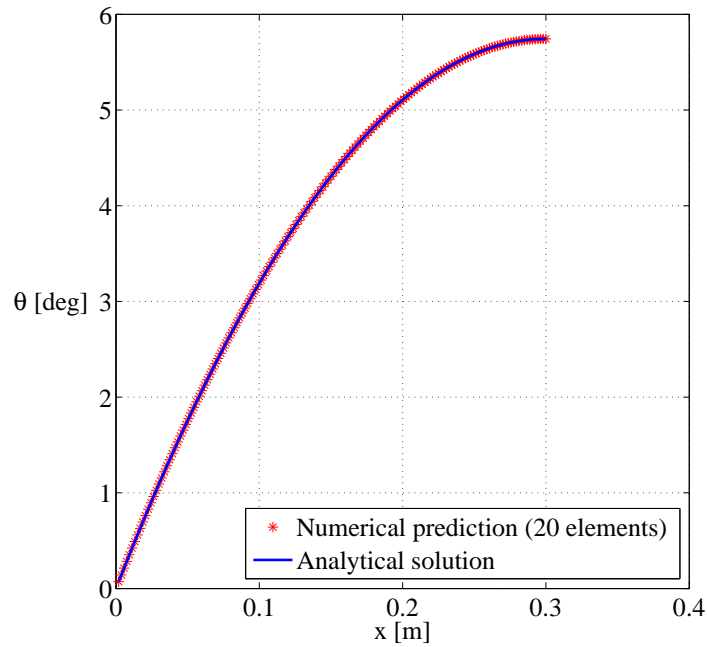


(b) Bending deflection

Figure 5.10: Euler-Bernoulli cantilever beam of rectangular cross-section, loaded by its own weight ( $\rho = 2700 \text{ kg/m}^3$ ,  $EI_\eta = 0.0073 \text{ N.m}^2$ )



(a) Schematic



(b) Twist angle

Figure 5.11: Euler-Bernoulli cantilever beam of rectangular cross-section, loaded by uniformly distributed torsion ( $t = 1 \text{ N.m/m}$ ,  $GJ = 0.4489 \text{ N.m}^2$ )

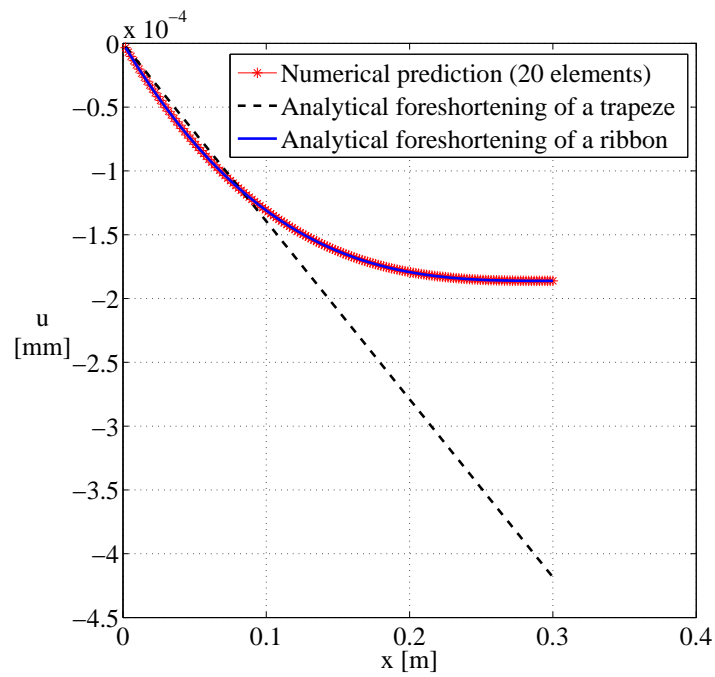
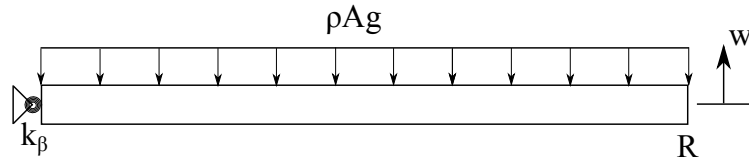
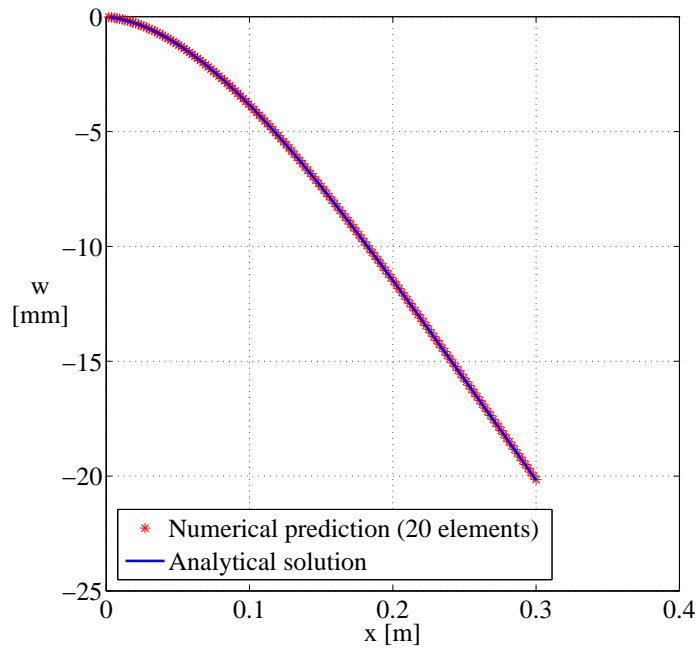


Figure 5.12: Axial foreshortening in beam under distributed torsion ( $t = 1 \text{ N.m/m}$ ,  $GJ = 0.4489 \text{ N.m}^2$ )



(a) Schematic



(b) Bending deflection

Figure 5.13: Euler-Bernoulli beam of rectangular cross-section, with spring at the root, loaded by its own weight ( $\rho = 2700 \text{ kg/m}^3$ ,  $EI_\eta = 0.0073 \text{ N.m}^2$ ,  $k_\beta = 1 \text{ N.m/rad}$ )

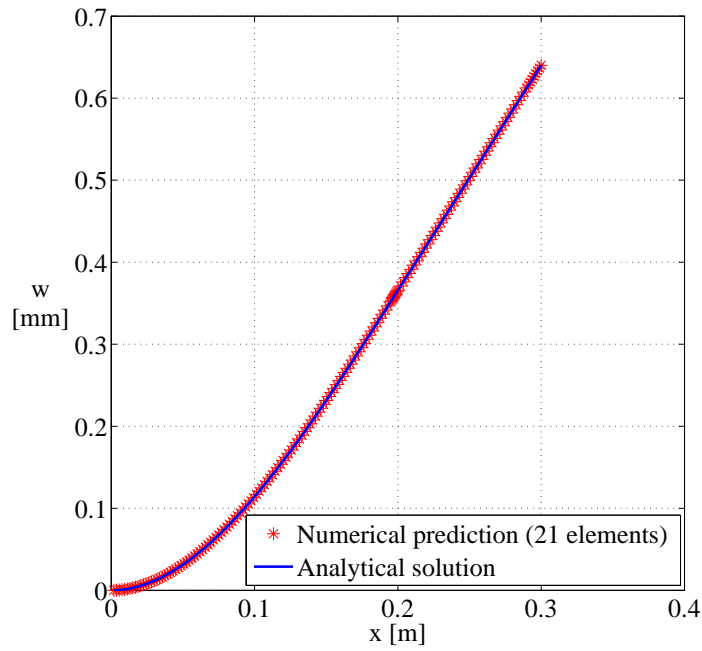
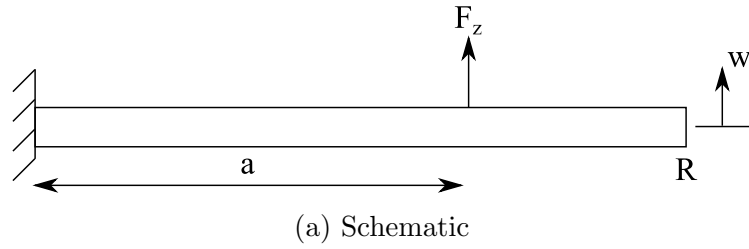
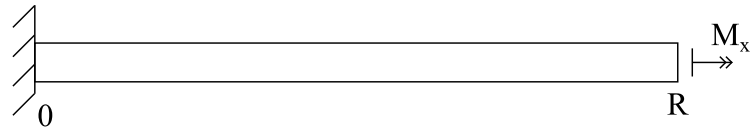
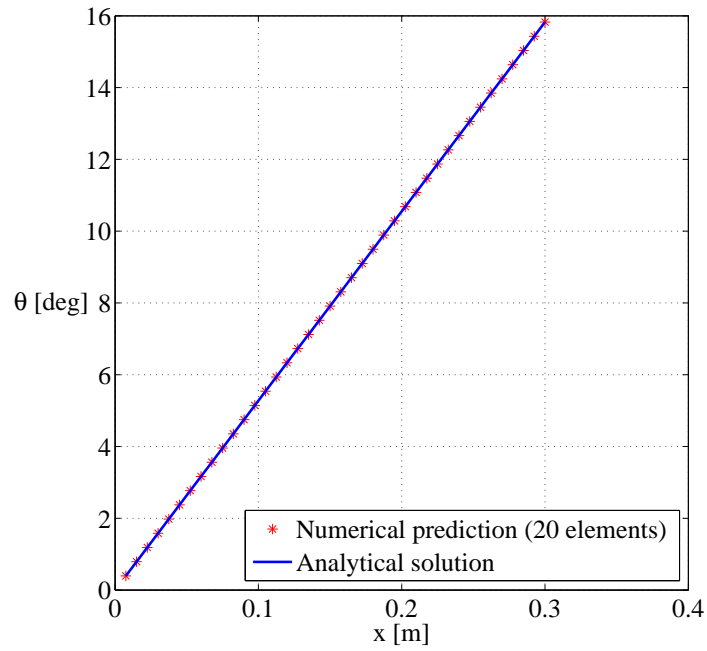


Figure 5.14: Euler-Bernoulli cantilever beam of rectangular cross-section, subjected to a concentrated load ( $a = 2R/3$ ,  $F_z = 1 \text{ mN}$ ,  $EI_\eta = 0.0073 \text{ N.m}^2$ )

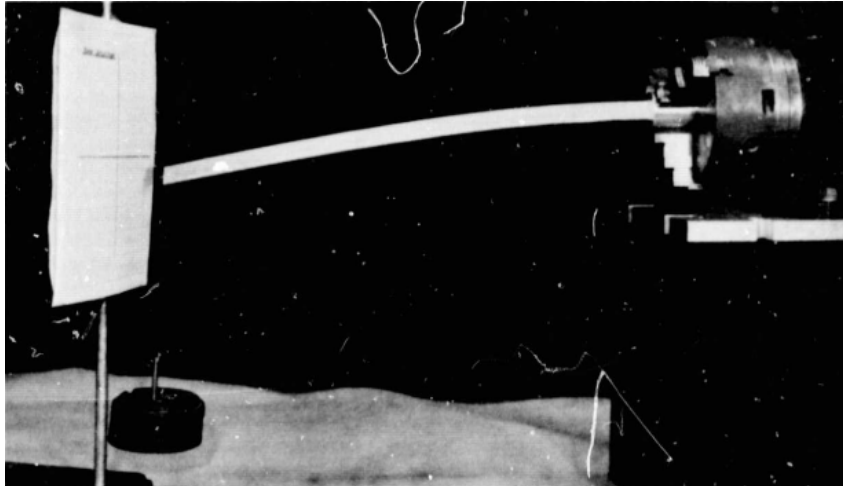


(a) Schematic

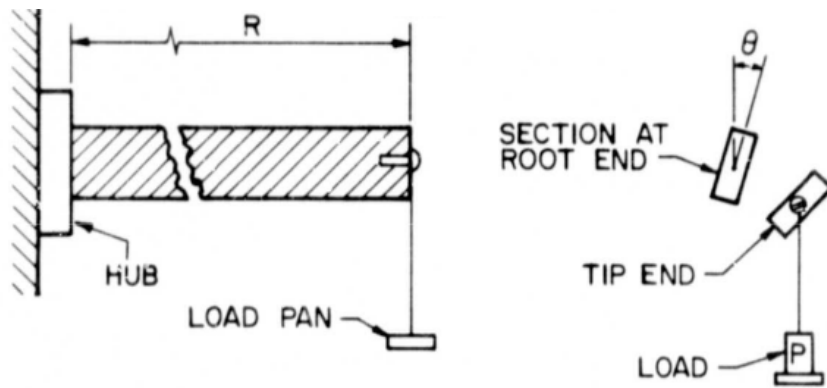


(b) Elastic twist

Figure 5.15: Cantilever beam of rectangular cross-section, subjected to a concentrated torque ( $M_x = 1$  N.m,  $GJ = 1.0860$  N.m<sup>2</sup>)

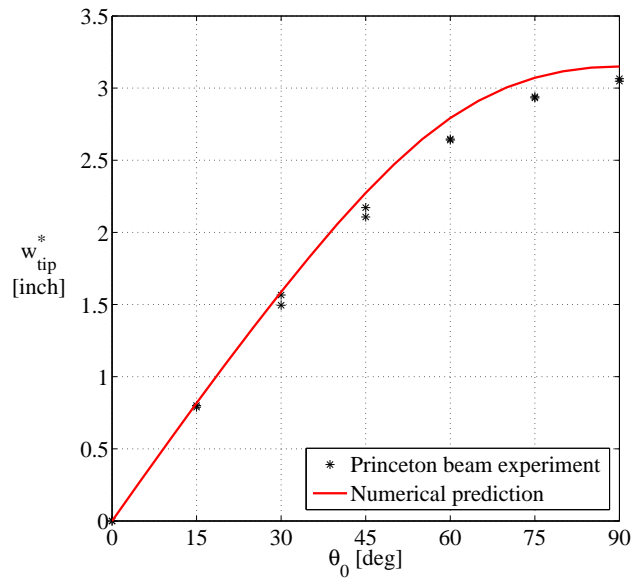


(a) Photograph of apparatus

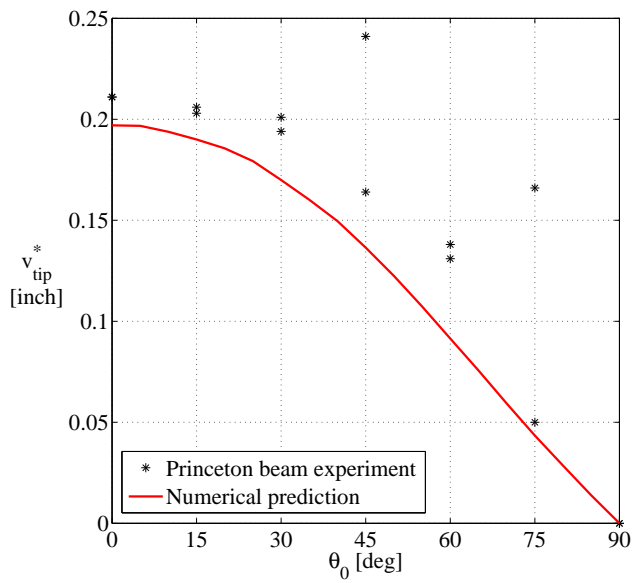


(b) Schematic of experiment

Figure 5.16: Apparatus and experimental set-up for the Princeton beam static deflection experiments, from Dowell & Traybar, 1975



(a) Flatwise bending



(b) Chordwise bending

Figure 5.17: Bending deflections of Princeton beam for tip load  $P = 1$  lb

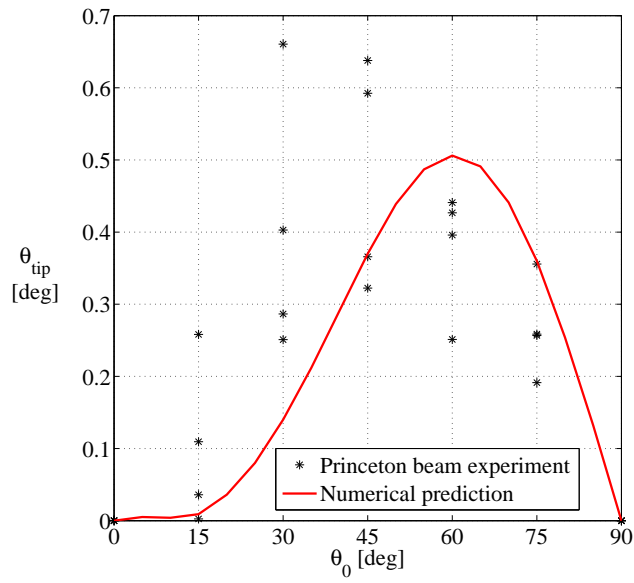
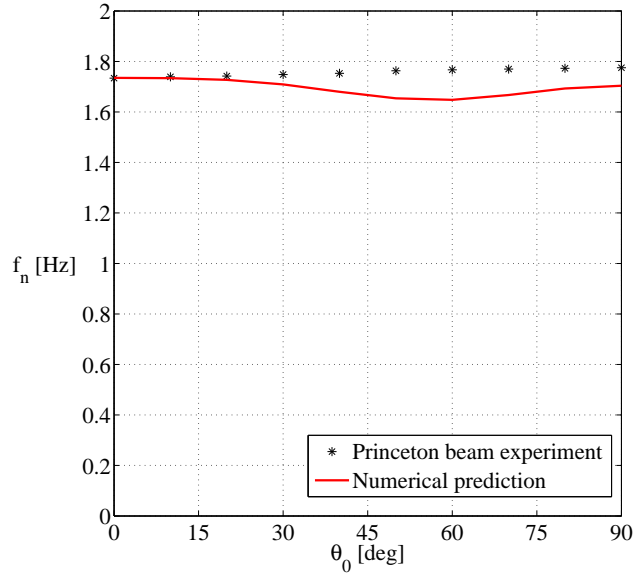
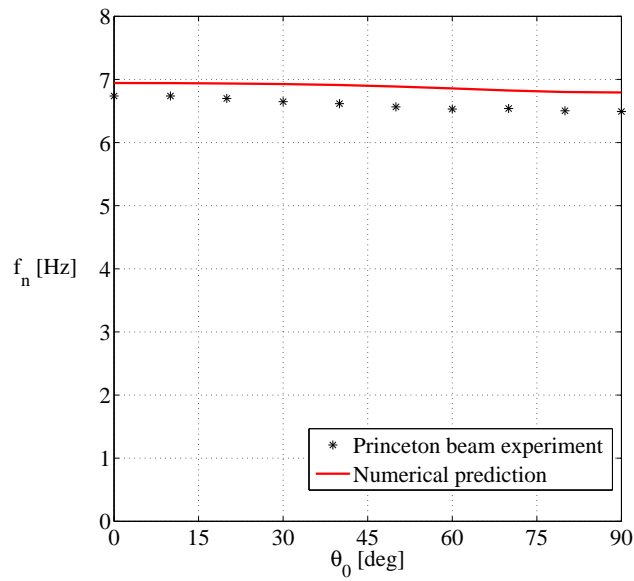


Figure 5.18: Twist of Princeton beam for tip load  $P = 1$  lb

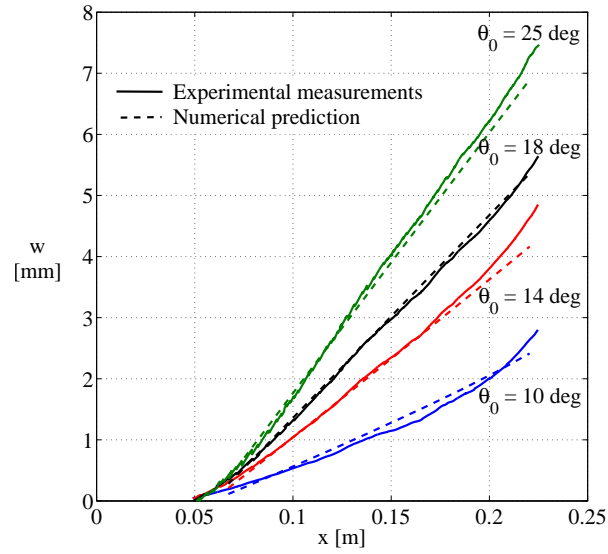


(a) Flatwise frequencies

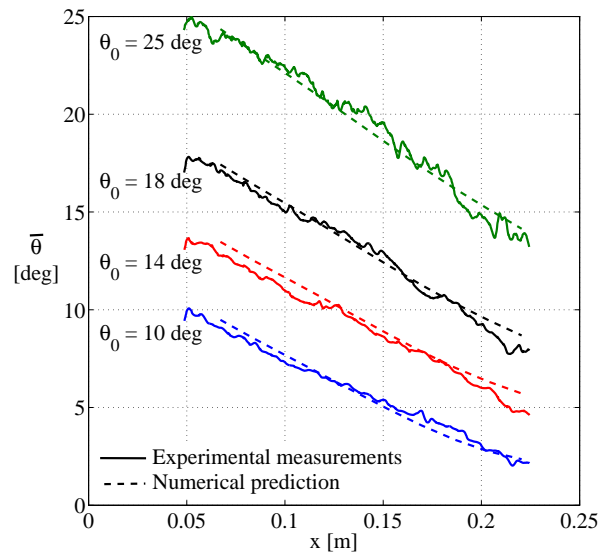


(b) Chordwise frequencies

Figure 5.19: Natural frequencies of Princeton beam for tip load  $P = 1$  lb

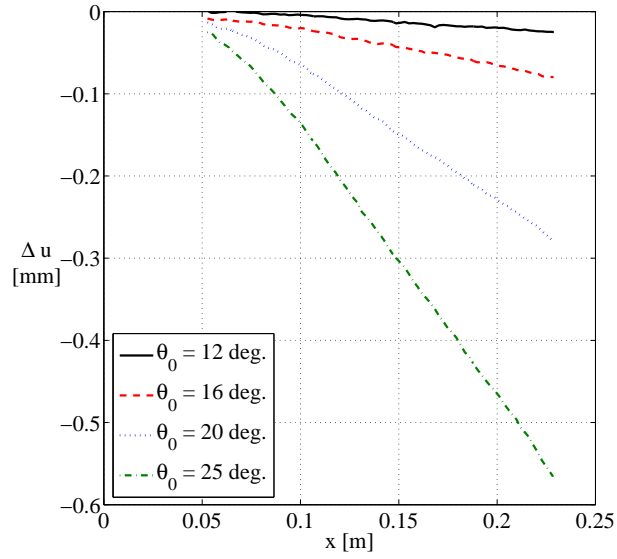


(a) Flap bending

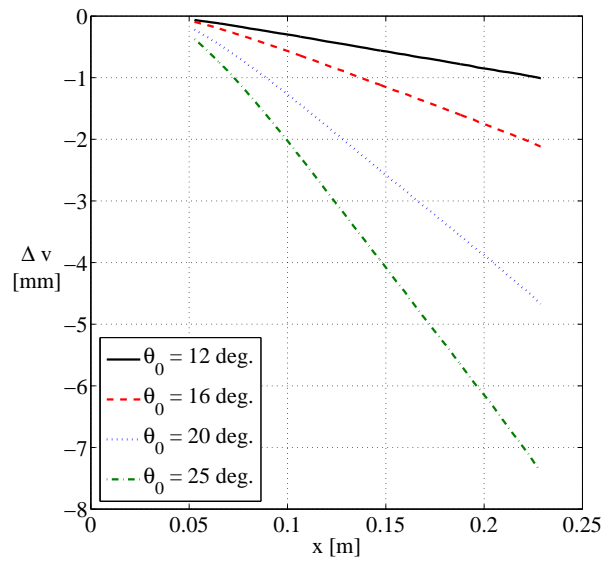


(b) Pitch angle

Figure 5.20: Measured deformation of rotor blade BP compared to numerical predictions ( $\Omega = 1200$  RPM)



(a) Axial displacement



(b) Lead-lag bending

Figure 5.21: Measured axial displacement and lead-lag bending of rotor blade BP ( $\Omega = 1200$  RPM)

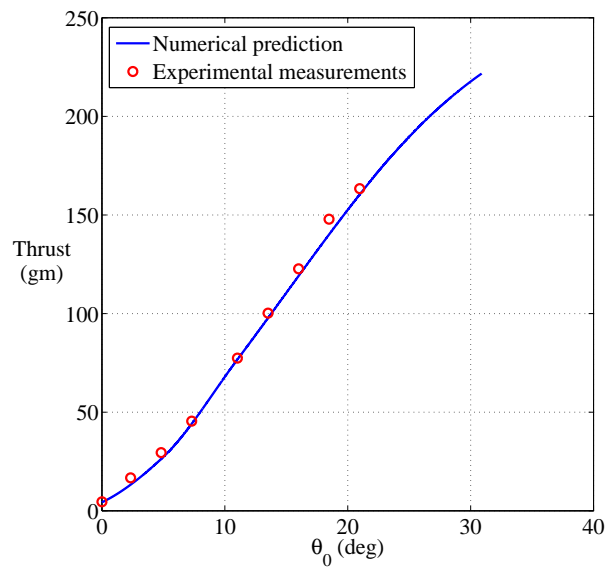


Figure 5.22: Variation of thrust of rotor blade BP as a function of the collective pitch

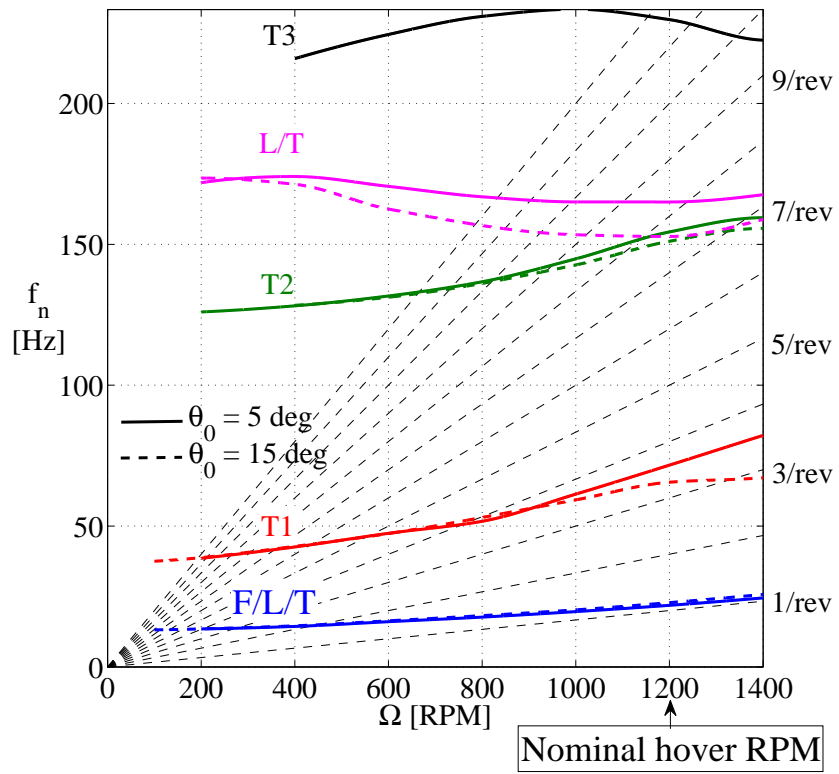


Figure 5.23: Natural frequencies of rotor blade BP

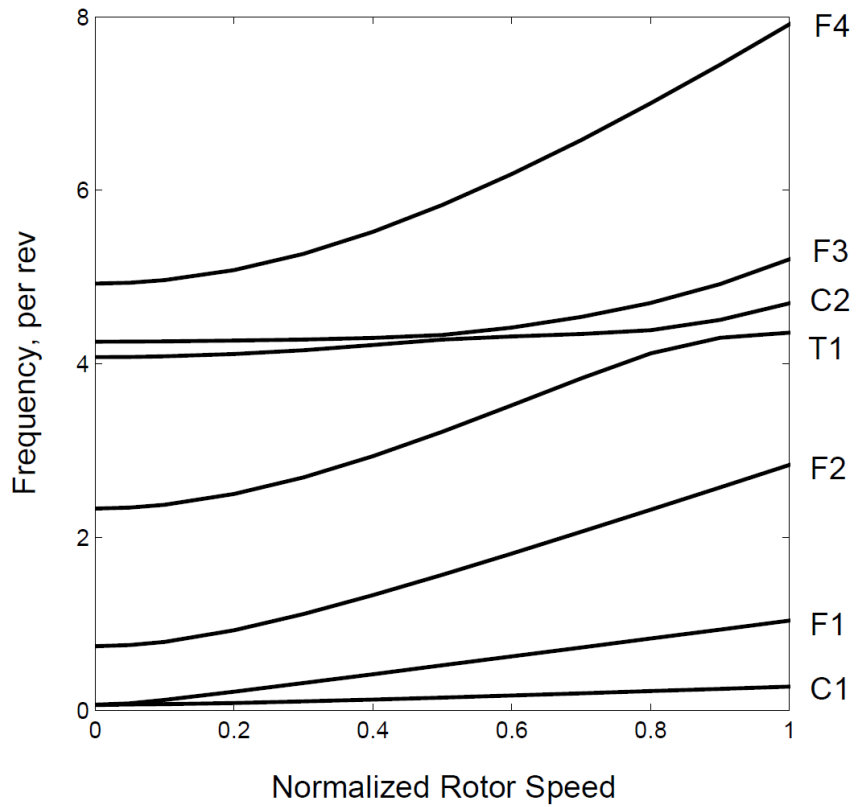


Figure 5.24: Natural frequencies in vacuum of UH-60A rotor blade; F: Flap, C:Lag, T:Torsion; pitch link stiffness 1090 ft-lb/deg, from Datta & Chopra, 2004

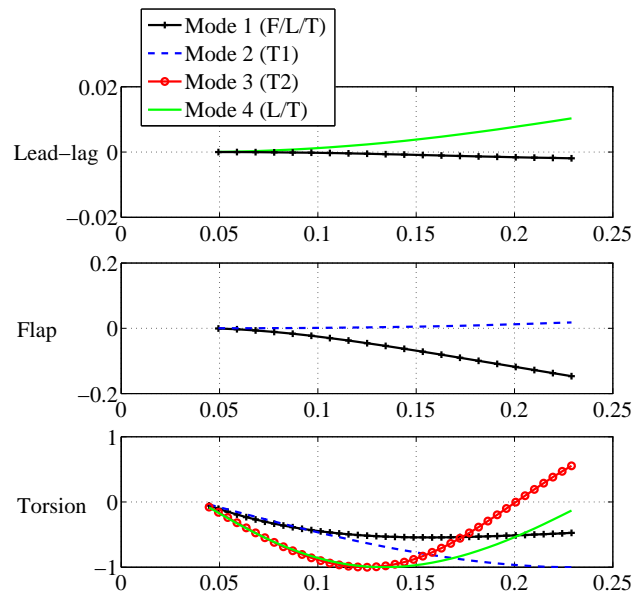


Figure 5.25: Mode shapes ( $\theta_0 = 0^\circ$ ,  $\Omega = 1000$  RPM)

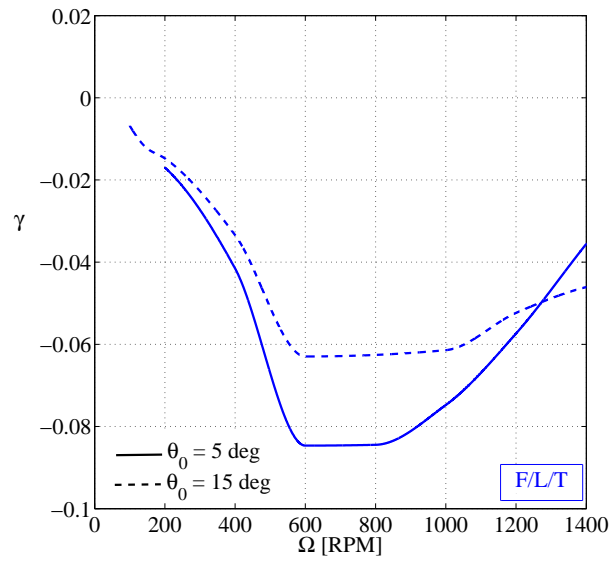
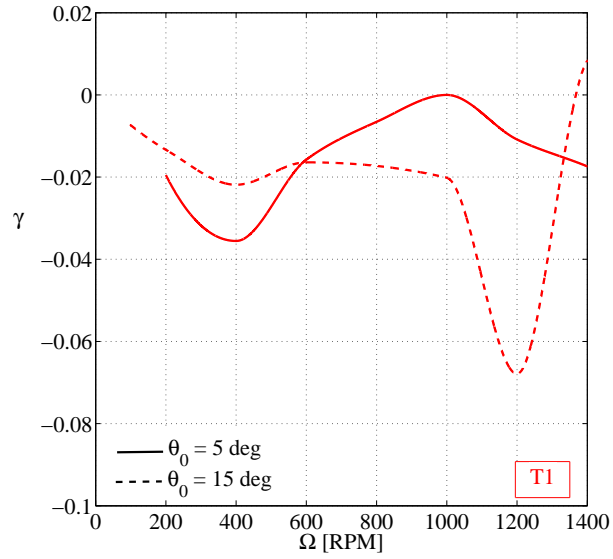
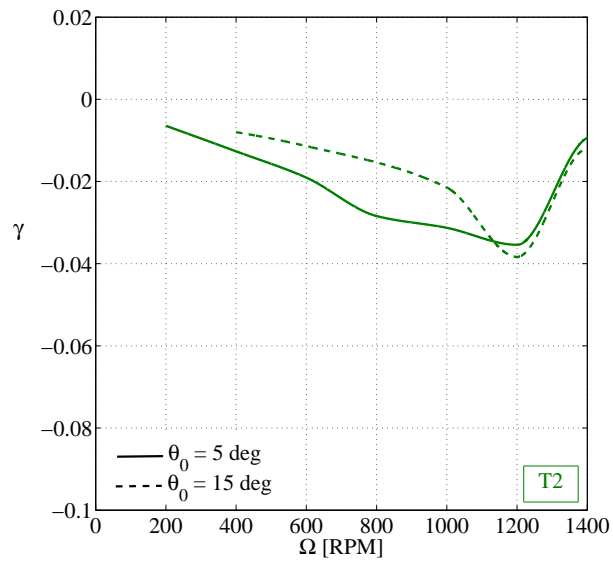


Figure 5.26: Damping coefficient of flap-lag-torsion mode

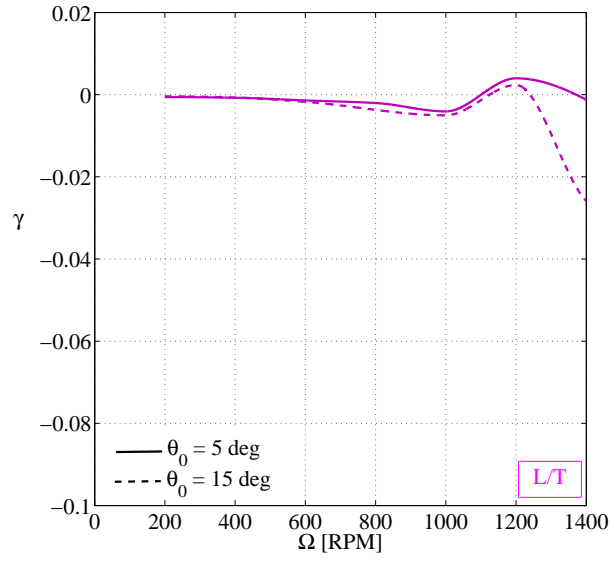


(a) Torsion mode 1

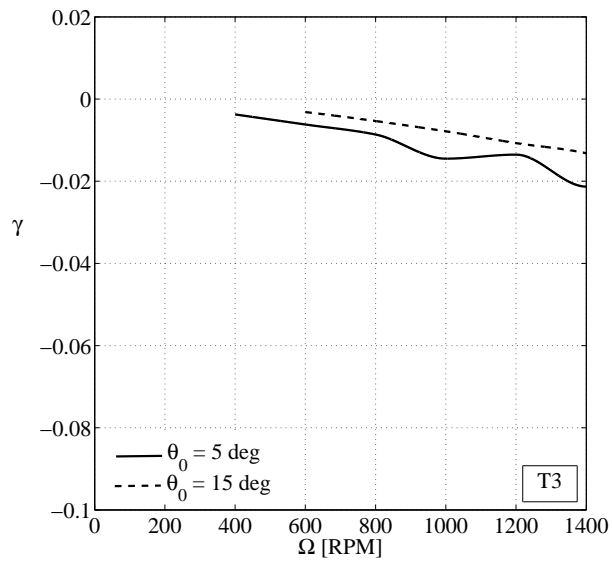


(b) Torsion mode 2

Figure 5.27: Damping coefficient of torsional modes



(a) Lag-torsion mode



(b) Torsion mode 3

Figure 5.28: Damping coefficient of coupled lag-torsion and third torsional mode

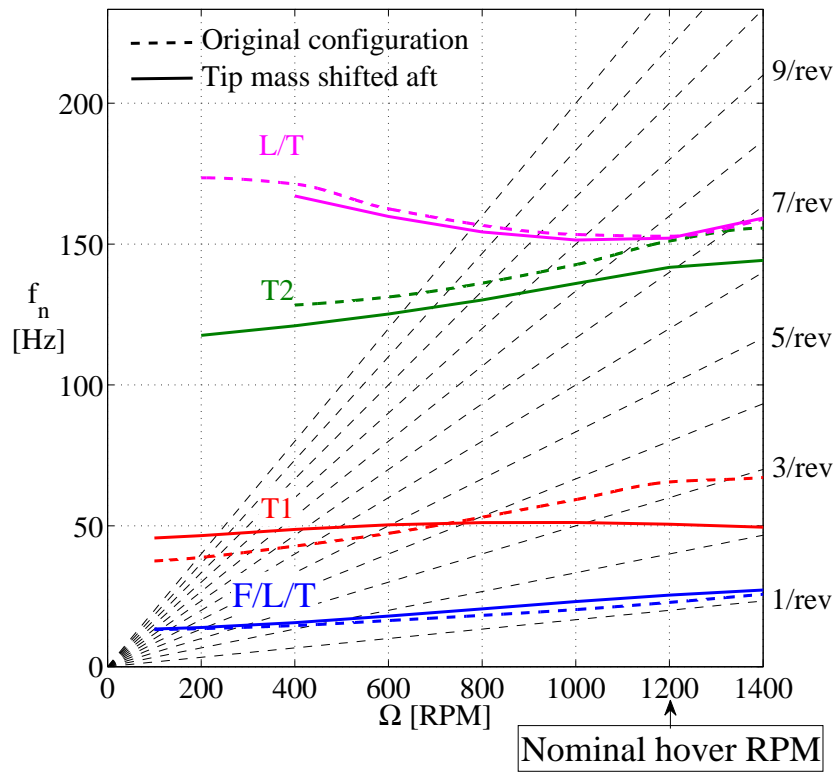
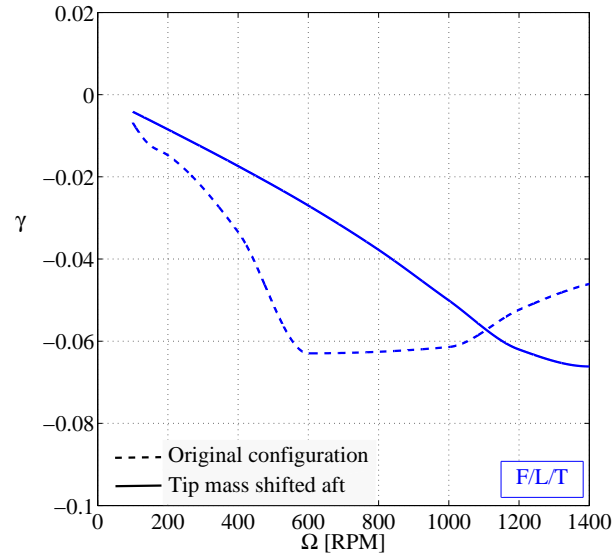
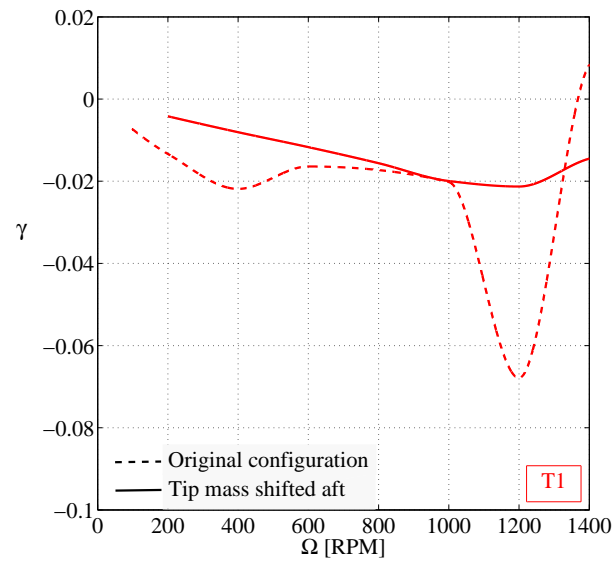


Figure 5.29: Influence of the tip mass chordwise position on the natural frequencies

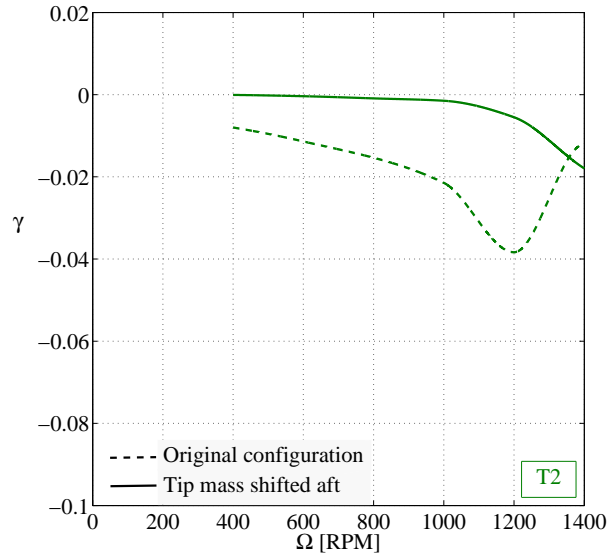


(a) Flap-lag-torsion mode

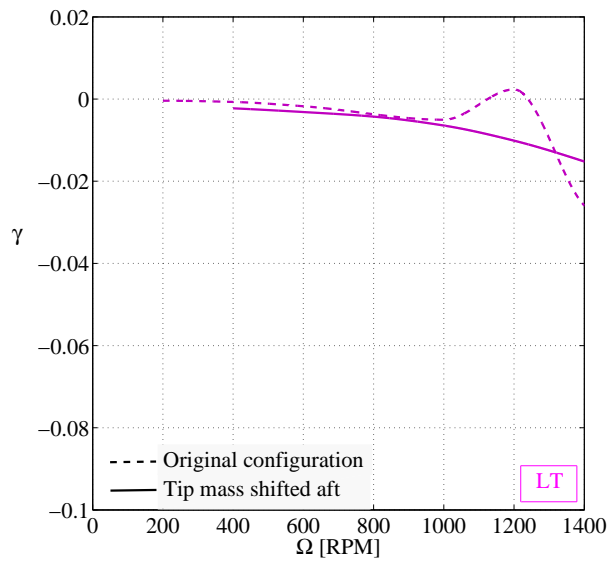


(b) Torsion mode 1

Figure 5.30: Influence of the tip mass chordwise position on the damping of the coupled flap-lag-torsion mode and the first torsional mode

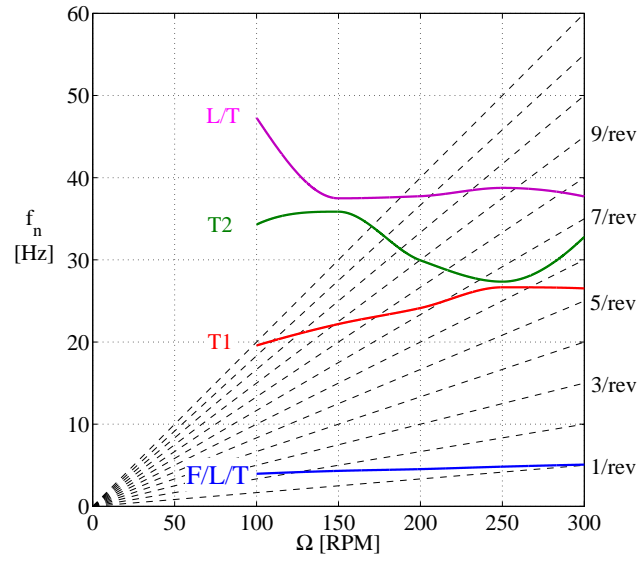


(a) Torsion mode 2

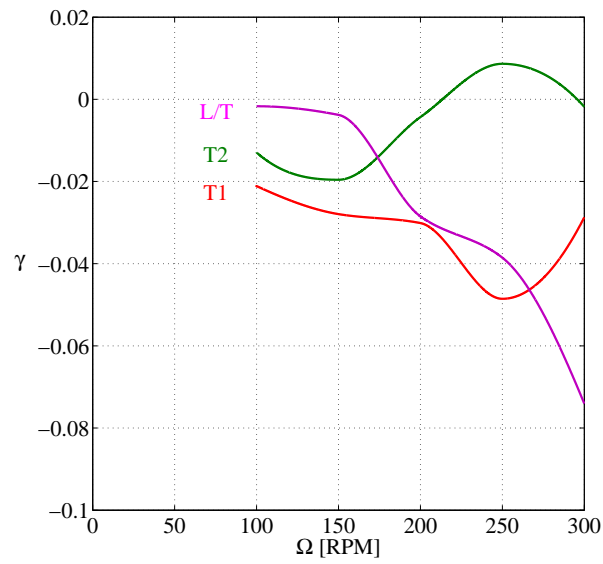


(b) Lag-torsion mode

Figure 5.31: Influence of the tip mass chordwise position on the damping of the second torsional mode and the coupled lag-torsion mode



(a) Natural frequencies



(b) Damping coefficients

Figure 5.32: Influence of the rotor diameter on the stability boundaries

## Chapter 6

### Summary and Future Work

Rotors with extremely flexible composite blades were designed, analyzed, fabricated and tested in hover. The goal was to develop blades so flexible that they could be rolled up and stowed in the rotor hub. The design of the rotor blades was focused toward application on a micro-helicopter. Accordingly, the blades had a circular arc airfoil section with 7.5% camber, untwisted, constant chord planform, and a span consistent with a rotor diameter of 18 inches. A tip mass was used to stiffen and stabilize the flexible rotor in flight.

An aeroelastic analysis tailored to rotor blades with negligible structural stiffness and experiencing large torsional deformation was developed. In particular, the analysis showed that large twist deformation combined with an axial load give rise to an increase in the blade torsional stiffness due to the trapeze effect. The axial displacement, restoring moment and natural frequencies associated with this effect were analytically derived for the case of a cable rotor with tip mass, and a ribbon rotor with tip mass. It was shown that the torsional frequency of a cable rotor with axisymmetric tip mass, spinning in vacuum, is on the order of  $\sqrt{2}/\text{rev}$  or  $\sqrt{3}/\text{rev}$ , depending on the tip mass

geometry.

Using an Hamiltonian dynamics approach, the equations of motion of a rotating blade with axial, flap bending, lead-lag bending and torsional degrees of freedom were derived. The blades were modeled as second-order isotropic Euler-Bernoulli beams. The kinetic energy, potential energy and virtual work done by non-conservative forces were approximated to second-order, based on an ordering scheme consistent with rotor blades having negligible torsional stiffness. In particular, the blade elastic twist was considered to be of the same order of magnitude as the collective pitch angles. Compared to typical analyses based on ordering schemes and derived for conventional stiff rotors, the analysis presented in this dissertation included additional terms related to the presence of large elastic twist angles. The significance of these terms was identified and discussed in detail. Additionally, an aerodynamic model was developed based on strip theory and including unsteady effects according to Theodorsen's theory. The unsteady effect of the returning wake shed by blades in previous revolutions was also modeled, based on Loewy's theory. Two-dimensional aerodynamic coefficients were extracted from lookup tables obtained for circular airfoils operating at low Reynolds number.

The trim state of the rotor blades in hover was obtained by solving the time-invariant equations of motion. The nonlinear, coupled equations were solved using a finite element approach. Nonlinear terms were linearized and incorporated to the stiffness matrix using a Newton-Raphson scheme. The convergence of the Newton-Raphson scheme yielded the spanwise variations

of axial, lead-lag bending, flap bending and torsional deformation of a flexible rotor blade in hover.

The predictions of deformation were correlated to experimental measurements obtained by a non-contacting, optical technique called three-dimensional digital image correlation (3-D DIC). This technique, which combines photogrammetry, stereoscopic principles and image correlation, was used to generate a three-dimensional deformation map of a rotor blade in hover. In particular, it was demonstrated that this technique is applicable to the measurement of deformation of a 46 cm diameter rotor rotating at 1200 RPM, with a spatial resolution of 1.04% of the rotor radius and an accuracy of 15  $\mu\text{m}$ .

Both the analysis and the DIC technique were used to compute the deformation in hover of the extremely flexible blade BP. This blade design features a tip body comprised of a 1-inch long tungsten rod oriented perpendicular to the spanwise direction, inclined at an index angle relative to the blade chord. Experimental hover tests conducted on the blade BP showed that it has a figure of merit equal to that of a stiff rotor of similar planform and airfoil section. Experimental investigations also showed unstable regimes of operation, characterized by limit-cycle, coupled pitch-flap oscillations. These regimes of instability were found to be dependent on the rotational speed and the collective pitch angle.

The predictions of flap bending and twist deformations of the flexible blade BP rotating at 1200 RPM showed good agreement with experimental measurements obtained by stereoscopic DIC. Small discrepancies between the

analytical predictions and the measurements were observed at the blade tip, and attributed to the absence of the modeling of the aerodynamic forces and pitching moment acting on the tip mass.

In addition, the rotor blade stability was investigated analytically by studying the response of the blade to small perturbations, linearized about the trim condition. In particular, onset of flutter instability was determined by the  $p$ - $k$  method of flutter analysis. The flutter analysis was conducted on the rotor blade BP for various collective pitch angles and over a range of rotational speeds. Flutter instability was observed to occur as a result of the coalescence between the second torsional mode and the first coupled lag/torsion mode of oscillation of the rotor blade. It was found that changing the collective pitch or the rotational speed affected the stability boundary. This result agrees with experimental observations. In addition, it was shown that by moving the chordwise position of the tip mass aft, the torsional frequencies of the new blade were uncoupled from the lag/torsion mode and flutter instability was avoided.

Finally, the effect of a change in rotor diameter on the stability boundaries was investigated. Analytical predictions of frequencies and damping coefficients showed that a change in rotor diameter leads to shifts of the natural frequencies and therefore new stability boundaries. This result indicates that when designing a variable-diameter extremely flexible rotor, the stability boundaries must be investigated for every operating rotor diameter.

The future work will address shortcomings which were identified in this

dissertation, as well as additional objectives. A list of the shortcomings is given below:

- The prediction of flap bending deflection at the blade tip showed discrepancies with experimental measurements.
- Limit cycle oscillations observed during hover testing could not be predicted by the numerical model derived in the frequency domain.
- The frequencies and the mode shapes of blade oscillation during unstable regimes were not experimentally measured.
- The transient aeroelastic behavior of the flexible blades during deployment and retraction was not addressed.
- The aeroelastic behavior of the flexible rotor blades in forward flight was not investigated.

Consequently, future plans involve the refined modeling of the aerodynamic forces and moments acting on the tip body, to better match the predicted flap bending deflections with the experimental measurements.

In addition, the stability analysis will be extended to an analysis in the time domain, to investigate the presence of limit cycle oscillations. A formulation based on Wagner's theory to obtain the indicial lift on an airfoil undergoing a transient step change in angle of attack will be derived. The perturbed equations of motion will then be solved by time marching, according to the generalized- $\alpha$  theory.

Future effort will also involve extending the use of the DIC technique to the measurement of unsteady rotor blade deformation and to the computation of rotating natural frequencies and mode shapes. High-speed cameras in conjunction with a laser strobe will be used to capture successive images of the rotor blades in hover.

Finally, the aeroelastic behavior of an extremely flexible rotor in forward flight, as well as during deployment and retraction of the rotor blades will be developed.

## Appendices

## Appendix A

### An alternative derivation of the torsional frequency associated with the trapeze effect

Consider the cable rotor shown in Fig. A.1 composed of four massless inextensible cables stiffened by a cruciform tip body (2 bars of length  $c$  and mass  $M/2$ ). Due to the symmetry of the problem about the  $X$ -axis, the tensile forces in the four cables are identical, and are equal to

$$F_c = \frac{1}{4} M \Omega^2 L \quad (\text{A.1})$$

In the plane of the tip body, the component of  $F_c$  responsible for a restoring torque is

$$F_R = F_c \sin \zeta \quad (\text{A.2})$$

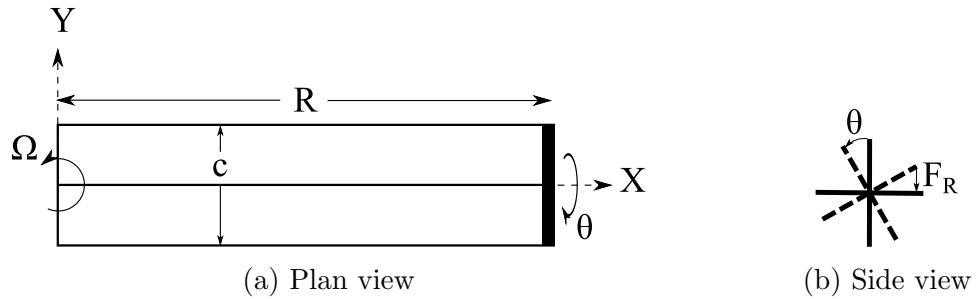


Figure A.1: Cable rotor with cross bars at the tip

where  $\zeta$  is the angle made by the deformed cable relative to the  $X$ -axis. For small twist  $\theta$ , Eq. (A.2) rewrites

$$F_R = F_c \frac{c\theta}{2L} \quad (\text{A.3})$$

In addition, the total restoring torque acting on the tip body is given by

$$M_t = 4 F_R \frac{c}{2} \cos \theta \quad (\text{A.4})$$

Therefore, substituting Eq. (A.1) and (A.3) into Eq. (A.4) and assuming small angles of twist  $\theta$ , we obtain

$$M_t = \frac{M \Omega^2 c^2}{4} \theta \quad (\text{A.5})$$

Then, using Newton's 2nd law, the equation describing the motion of the tip body, of inertia  $I_0 = Mc^2/12$  is

$$\frac{Mc^2}{12} \ddot{\theta} + \frac{M \Omega^2 c^2}{4} \theta = 0 \quad (\text{A.6})$$

And the corresponding dimensionless torsional frequency is  $\nu_\theta = \sqrt{3}/\text{rev}$ .

## Appendix B

### Use of quasi-coordinates in Hamilton's Principle

The classical form of Hamilton's principle given by equation (2.1) is valid when the generalized coordinates are true coordinates. When quasi-coordinates are used, the formulation of Hamilton's principle is generally different, given by [62]

$$\frac{d}{dt} \left\{ \frac{\partial \bar{T}}{\partial \omega} \right\} + [\beta]^T [\gamma] \left\{ \frac{\partial \bar{T}}{\partial \omega} \right\} - [\beta]^T \left\{ \frac{\partial \bar{T}}{\partial q} \right\} = \{N\} \quad (\text{B.1})$$

where  $\bar{T} = \bar{T}(\mathbf{q}, \boldsymbol{\omega})$  is the kinetic energy as a function of the generalized coordinates  $q_k$ , and  $n$  independent linear combinations  $\omega_k$  ( $k = 1 \dots n$ ) of the velocities  $\dot{q}_k$ . In addition,

$$\{\omega\} = [\alpha]^T \{\dot{q}\} \quad (\text{B.2})$$

$$[\gamma] = \left[ \{\omega\}^T [\beta]^T \left\{ \frac{\partial \alpha}{\partial q} \right\} \right] - \left[ \{\omega\}^T [\beta]^T \left[ \frac{\partial \alpha}{\partial q} \right] \right] \quad (\text{B.3})$$

$$\{N\} = [\beta]^T \{Q\} \quad (\text{B.4})$$

But in the specific case where the quasi-coordinates are the variables  $\phi$  and  $u_e$ , as defined by Eq. (2.121) and (2.123), it can be shown that the classical form of Hamilton's principle can be applied. The proof shown below is adapted from [63] and the methodology is as follows. First, we will start from the

standard extended form of Hamilton's principle using the true coordinates. For simplicity, we will consider only the time invariant part of the equation and ignore the virtual work done by non-conservative forces, but the extension of the derivation to time dependent terms is trivial. We will take the variation in the equations, as functions of the true coordinates, and then make the change of variables to the quasi-coordinates. The resulting expression should correspond to the expression obtained by starting the formulation in terms of the quasi-coordinates and then taking the variation.

The classical form of Hamilton's principle, in terms of the true-coordinates  $u, v, w$  and  $\theta$  and their derivatives, retaining time-invariant terms only, is

$$\int_0^L \delta H(u, u', v, v', v'', w, w', w'', \theta, \theta') dx = 0 \quad (\text{B.5})$$

Expanding the variation of  $H$  yields

$$\int_0^L \left( \frac{\partial H}{\partial u} \delta u + \frac{\partial H}{\partial u'} \delta u' + \frac{\partial H}{\partial v} \delta v + \frac{\partial H}{\partial v'} \delta v' + \frac{\partial H}{\partial v''} \delta v'' + \frac{\partial H}{\partial w} \delta w + \frac{\partial H}{\partial w'} \delta w' + \frac{\partial H}{\partial w''} \delta w'' + \frac{\partial H}{\partial \theta} \delta \theta + \frac{\partial H}{\partial \theta'} \delta \theta' \right) dx = 0 \quad (\text{B.6})$$

Next, the following change of variable is made

$$u = u_e - \int_0^x \left( \frac{v'^2}{2} + \frac{w'^2}{2} + \frac{k_A^2}{2} \theta'^2 \right) d\chi \quad (\text{B.7})$$

$$\theta = \phi - \int_0^x v'' w' d\chi \quad (\text{B.8})$$

The derivative of the previous expressions are

$$u' = u'_e - \left( \frac{v'^2}{2} + \frac{w'^2}{2} + \frac{k_A^2}{2} \theta'^2 \right) \quad (\text{B.9})$$

$$\theta' = \phi' - v''w' \quad (\text{B.10})$$

And the variations are

$$\delta u = \delta u_e - \int_0^x (v' \delta v' + w' \delta w' + k_A^2 \theta' \delta \theta') d\chi \quad (\text{B.11})$$

$$\delta u' = \delta u'_e - (v' \delta v' + w' \delta w' + k_A^2 \theta' \delta \theta') \quad (\text{B.12})$$

$$\delta \theta = \delta \phi - \int_0^x (w' \delta v'' + v'' \delta w') d\chi \quad (\text{B.13})$$

$$\delta \theta' = \delta \phi' - (w' \delta v'' + v'' \delta w') \quad (\text{B.14})$$

We define  $\bar{H} = \bar{H}(u_e, u'_e, v, v', v'', w, w', w'', \phi, \phi')$ . From the chain rule, we have

$$\begin{aligned} \frac{\partial H}{\partial u} \delta u &= \frac{\partial \bar{H}}{\partial u_e} \frac{\partial u_e}{\partial u} \delta u + \frac{\partial \bar{H}}{\partial u'_e} \frac{\partial u'_e}{\partial u} \delta u + \frac{\partial \bar{H}}{\partial v} \frac{\partial v}{\partial u} \delta u + \frac{\partial \bar{H}}{\partial v'} \frac{\partial v'}{\partial u} \delta u + \frac{\partial \bar{H}}{\partial v''} \frac{\partial v''}{\partial u} \delta u \\ &+ \frac{\partial \bar{H}}{\partial w} \frac{\partial w}{\partial u} \delta u + \frac{\partial \bar{H}}{\partial w'} \frac{\partial w'}{\partial u} \delta u + \frac{\partial \bar{H}}{\partial w''} \frac{\partial w''}{\partial u} \delta u + \frac{\partial \bar{H}}{\partial \phi} \frac{\partial \phi}{\partial u} \delta u + \frac{\partial \bar{H}}{\partial \phi'} \frac{\partial \phi'}{\partial u} \delta u \end{aligned} \quad (\text{B.15})$$

Using Eq. (B.7)-(B.10), this equation becomes

$$\frac{\partial H}{\partial u} \delta u = \frac{\partial \bar{H}}{\partial u_e} \delta u \quad (\text{B.16})$$

Likewise,

$$\begin{aligned} \frac{\partial H}{\partial u'} \delta u' &= \frac{\partial \bar{H}}{\partial u'_e} \frac{\partial u'_e}{\partial u'} \delta u' \\ &= \frac{\partial \bar{H}}{\partial u'_e} \delta u' \end{aligned} \quad (\text{B.17})$$

$$\begin{aligned} \frac{\partial H}{\partial v'} \delta v' &= \frac{\partial \bar{H}}{\partial u_e} \frac{\partial u_e}{\partial v'} \delta v' + \frac{\partial \bar{H}}{\partial u'_e} \frac{\partial u'_e}{\partial v'} \delta v' + \frac{\partial \bar{H}}{\partial v'} \delta v' \\ &= \frac{\partial \bar{H}}{\partial u_e} \int_0^x v' \delta v' d\chi + \frac{\partial \bar{H}}{\partial u'_e} v' \delta v' + \frac{\partial \bar{H}}{\partial v'} \delta v' \end{aligned} \quad (\text{B.18})$$

$$\begin{aligned}
\frac{\partial H}{\partial v''} \delta v'' &= \frac{\partial \bar{H}}{\partial v''} \delta v'' + \frac{\partial \bar{H}}{\partial \phi} \frac{\partial \phi}{\partial v''} \delta v'' + \frac{\partial \bar{H}}{\partial \phi'} \frac{\partial \phi'}{\partial v''} \delta v'' \\
&= \frac{\partial \bar{H}}{\partial v''} \delta v'' + \frac{\partial \bar{H}}{\partial \phi} \int_0^x w' \delta v'' d\chi + \frac{\partial \bar{H}}{\partial \phi'} w' \delta v''
\end{aligned} \tag{B.19}$$

$$\begin{aligned}
\frac{\partial H}{\partial w'} \delta w' &= \frac{\partial \bar{H}}{\partial u_e} \frac{\partial u_e}{\partial w'} \delta w' + \frac{\partial \bar{H}}{\partial u'_e} \frac{\partial u'_e}{\partial w'} \delta w' + \frac{\partial \bar{H}}{\partial w'} \delta w' + \frac{\partial \bar{H}}{\partial \phi} \frac{\partial \phi}{\partial w'} \delta w' + \frac{\partial \bar{H}}{\partial \phi'} \frac{\partial \phi'}{\partial w'} \delta w' \\
&= \frac{\partial \bar{H}}{\partial u_e} \int_0^x w' \delta w' d\chi + \frac{\partial \bar{H}}{\partial u'_e} w' \delta w' + \frac{\partial \bar{H}}{\partial w'} \delta w' + \frac{\partial \bar{H}}{\partial \phi} \int_0^x v'' \delta w' d\chi \\
&\quad + \frac{\partial \bar{H}}{\partial \phi'} v'' \delta w'
\end{aligned} \tag{B.20}$$

$$\begin{aligned}
\frac{\partial H}{\partial \theta} \delta \theta &= \frac{\partial \bar{H}}{\partial \phi} \frac{\partial \phi}{\partial \theta} \delta \theta \\
&= \frac{\partial \bar{H}}{\partial \phi} \delta \theta
\end{aligned} \tag{B.21}$$

$$\begin{aligned}
\frac{\partial H}{\partial \theta'} \delta \theta' &= \frac{\partial \bar{H}}{\partial u_e} \frac{\partial u_e}{\partial \theta'} \delta \theta' + \frac{\partial \bar{H}}{\partial u'_e} \frac{\partial u'_e}{\partial \theta'} \delta \theta' + \frac{\partial \bar{H}}{\partial \phi'} \frac{\partial \phi'}{\partial \theta'} \delta \theta' \\
&= \frac{\partial \bar{H}}{\partial u_e} \int_0^x k_A^2 \theta' \delta \theta' d\chi + \frac{\partial \bar{H}}{\partial u'_e} k_A^2 \theta' \delta \theta' + \frac{\partial \bar{H}}{\partial \phi'} \delta \theta'
\end{aligned} \tag{B.22}$$

Inserting Eq. (B.11)-(B.14) and Eq. (B.16)-(B.22) into Eq. (B.6), we obtain

$$\begin{aligned}
&\int_0^L \left[ \frac{\partial \bar{H}}{\partial u_e} \left( \delta u_e - \int_0^x \left( \underline{v' \delta v'} + \underline{w' \delta w'} + \underline{k_A^2 \theta' \delta \theta'} \right) d\chi \right) \right. \\
&\quad + \frac{\partial \bar{H}}{\partial u'_e} \left( \delta u'_e - \left( \underline{v' \delta v'} + \underline{w' \delta w'} + \underline{k_A^2 \theta' \delta \theta'} \right) \right) + \frac{\partial \bar{H}}{\partial v} \delta v + \frac{\partial \bar{H}}{\partial u_e} \int_0^x v' \delta v' d\chi \\
&\quad + \frac{\partial \bar{H}}{\partial u'_e} v' \delta v' + \frac{\partial \bar{H}}{\partial v'} \delta v' + \frac{\partial \bar{H}}{\partial v''} \delta v'' + \frac{\partial \bar{H}}{\partial \phi} \int_0^x w' \delta v'' d\chi + \frac{\partial \bar{H}}{\partial \phi'} w' \delta v'' + \frac{\partial \bar{H}}{\partial w} \delta w \\
&\quad \left. + \frac{\partial \bar{H}}{\partial u_e} \int_0^x w' \delta w' d\chi + \frac{\partial \bar{H}}{\partial u'_e} w' \delta w' + \frac{\partial \bar{H}}{\partial w'} \delta w' + \frac{\partial \bar{H}}{\partial \phi} \int_0^x v'' \delta w' d\chi + \frac{\partial \bar{H}}{\partial \phi'} v'' \delta w' \right]
\end{aligned}$$

$$\begin{aligned}
& + \frac{\partial \bar{H}}{\partial w''} \delta w'' + \frac{\partial \bar{H}}{\partial \phi} \left( \delta \phi - \int_0^x (\underline{w' \delta v''} + \underline{v'' \delta w'}) d\chi \right) + \frac{\partial \bar{H}}{\partial u_e} \int_0^x k_A^2 \theta' \delta \theta' d\chi \\
& + \underline{\frac{\partial \bar{H}}{\partial u_e'} k_A^2 \theta' \delta \theta'} + \underline{\frac{\partial \bar{H}}{\partial \phi'} (\delta \phi' - (\underline{w' \delta v''} + \underline{v'' \delta w'}))} \Big] dx = 0 \tag{B.23}
\end{aligned}$$

All the underlined terms cancel out, leaving

$$\begin{aligned}
\int_0^L \left[ \frac{\partial \bar{H}}{\partial u_e} \delta u_e + \frac{\partial \bar{H}}{\partial u_e'} \delta u_e' + \frac{\partial \bar{H}}{\partial v} \delta v + \frac{\partial \bar{H}}{\partial v'} \delta v' + \frac{\partial \bar{H}}{\partial v''} \delta v'' + \frac{\partial \bar{H}}{\partial w} \delta w + \frac{\partial \bar{H}}{\partial w'} \delta w' \right. \\
\left. + \frac{\partial \bar{H}}{\partial w''} \delta w'' + \frac{\partial \bar{H}}{\partial \phi} \delta \phi + \frac{\partial \bar{H}}{\partial \phi'} \delta \phi' \right] dx = 0 \tag{B.24}
\end{aligned}$$

It can be seen that this equation is identically similar to the equation obtained by taking directly the variation of

$$\int_0^L \delta \bar{H}(u_e, u_e', v, v', v'', w, w', w'', \phi, \phi') dx = 0 \tag{B.25}$$

Therefore, the applicability of Lagrange's equations for true coordinates to the set of variables  $(u_e, v, w, \phi)$  is proven.

## Appendix C

### Additional analytical results

This appendix contains intermediate results needed for the derivation of the equations of motion shown in Chapter 2.

- $\mathbf{dr}_1 \cdot \mathbf{dr}_1 - \mathbf{dr}_0 \cdot \mathbf{dr}_0$

$$\begin{aligned}
 & \mathbf{dr}_1 \cdot \mathbf{dr}_1 - \mathbf{dr}_0 \cdot \mathbf{dr}_0 \\
 &= (dx)^2 \left[ 2u' + v'^2 + w'^2 - 2v''(\eta \cos \bar{\theta} - \xi \sin \bar{\theta}) - 2w''(\eta \sin \bar{\theta} + \xi \cos \bar{\theta}) \right. \\
 &\quad \left. + \theta'^2 (\eta \sin \bar{\theta} + \xi \cos \bar{\theta})^2 + \theta'^2 (\eta \cos \bar{\theta} - \xi \sin \bar{\theta})^2 + \mathcal{O}(\epsilon^4) \right] \\
 &+ (dx d\eta) 2 \left[ -u'v' \cos \bar{\theta} - u'w' \sin \bar{\theta} - \frac{v'^3}{2} \cos \bar{\theta} - \frac{w'^3}{2} \sin \bar{\theta} \right. \\
 &\quad \left. - v'^2 w' \sin \bar{\theta} - v''w'\xi - \theta'\xi + \mathcal{O}(\epsilon^4) \right] \\
 &+ (dx d\xi) 2 \left[ u'v' \sin \bar{\theta} - u'w' \cos \bar{\theta} + \frac{v'^3}{2} \sin \bar{\theta} - \frac{w'^3}{2} \cos \bar{\theta} \right. \\
 &\quad \left. - v'^2 w' \cos \bar{\theta} + v''w'\eta + \theta'\eta + \mathcal{O}(\epsilon^4) \right] \\
 &+ \dots \tag{C.1}
 \end{aligned}$$

- $\epsilon_{xx}^2, \epsilon_{x\eta}^2, \epsilon_{x\xi}^2$

$$\begin{aligned}
\epsilon_{xx}^2 = & \left(u' + \frac{v'^2}{2} + \frac{w'^2}{2}\right)^2 + \left(u' + \frac{v'^2}{2} + \frac{w'^2}{2}\right) \theta'^2 (\eta^2 + \xi^2) + \frac{\theta'^4}{4} (\eta^2 + \xi^2)^2 \\
& + (\eta^2 \cos^2 \bar{\theta} + \xi^2 \sin^2 \bar{\theta} - \eta\xi \sin 2\bar{\theta}) v'^2 \\
& + (\eta^2 \sin^2 \bar{\theta} + \xi^2 \cos^2 \bar{\theta} + \eta\xi \sin 2\bar{\theta}) w'^2 \\
& + ((\eta^2 - \xi^2) \sin 2\bar{\theta} + 2\eta\xi \cos 2\bar{\theta}) v'' w'' \\
& - 2u' v'' (\eta \cos \bar{\theta} - \xi \sin \bar{\theta}) - 2u' w'' (\eta \sin \bar{\theta} + \xi \cos \bar{\theta}) \\
& - \theta'^2 v'' (\eta^2 + \xi^2) (\eta \cos \bar{\theta} - \xi \sin \bar{\theta}) - \theta'^2 w'' (\eta^2 + \xi^2) (\eta \sin \bar{\theta} + \xi \cos \bar{\theta}) \\
& - v'^2 w'' (\eta \sin \bar{\theta} + \xi \cos \bar{\theta}) - w'^2 v'' (\eta \cos \bar{\theta} - \xi \sin \bar{\theta}) \\
& - w'^2 w'' (\eta \sin \bar{\theta} + \xi \cos \bar{\theta}) - v'^2 v'' (\eta \cos \bar{\theta} - \xi \sin \bar{\theta}) \\
& + \mathcal{O}(\epsilon^6)
\end{aligned} \tag{C.2}$$

$$\begin{aligned}
\epsilon_{x\eta}^2 = & \theta'^2 \frac{\xi^2}{4} + v'' w' \theta' \frac{\xi^2}{2} + (v'^3 \cos \bar{\theta} + w'^3 \sin \bar{\theta}) \theta' \frac{\xi}{4} \\
& + (u' v' \cos \bar{\theta} + u' w' \sin \bar{\theta} + v'^2 w' \sin \bar{\theta}) \theta' \frac{\xi}{2} \\
& + \mathcal{O}(\epsilon^6)
\end{aligned} \tag{C.3}$$

$$\begin{aligned}
\epsilon_{x\xi}^2 = & \theta'^2 \frac{\eta^2}{4} + v'' w' \theta' \frac{\eta^2}{2} + (v'^3 \sin \bar{\theta} - w'^3 \cos \bar{\theta}) \theta' \frac{\eta}{4} \\
& + (u' v' \sin \bar{\theta} - u' w' \cos \bar{\theta} - v'^2 w' \cos \bar{\theta}) \theta' \frac{\eta}{2} \\
& + \mathcal{O}(\epsilon^6)
\end{aligned} \tag{C.4}$$

- $\delta\epsilon_{xx}, \delta\epsilon_{x\eta}, \delta\epsilon_{x\xi}$

$$\begin{aligned}
\delta\epsilon_{xx} &= \delta u' + v'\delta v' + w'\delta w' - \delta v'' (\eta \cos \bar{\theta} - \xi \sin \bar{\theta}) - \delta w'' (\eta \sin \bar{\theta} + \xi \cos \bar{\theta}) \\
&\quad + \delta\theta (v'' (\eta \sin \bar{\theta} + \xi \cos \bar{\theta}) - w'' (\eta \cos \bar{\theta} - \xi \sin \bar{\theta})) + \delta\theta' (\eta^2 + \xi^2) \theta' \\
&\quad + \mathcal{O}(\epsilon^4)
\end{aligned} \tag{C.5}$$

$$\begin{aligned}
\delta\epsilon_{x\eta} &= \delta u' \left( -\frac{1}{2}(v' \cos \bar{\theta} + w' \sin \bar{\theta}) \right) + \delta v' \left( -\frac{u'}{2} \cos \bar{\theta} - \frac{3}{4}v'^2 \cos \bar{\theta} - v'w' \sin \bar{\theta} \right) \\
&\quad + \delta v'' \left( -w' \frac{\xi}{2} \right) + \delta w' \left( -v'' \frac{\xi}{2} - \frac{u'}{2} \sin \bar{\theta} - \frac{3}{4}w'^2 \sin \bar{\theta} - \frac{v'^2}{2} \sin \bar{\theta} \right) \\
&\quad + \delta\theta \left( \frac{u'}{2}(v' \sin \bar{\theta} - w' \cos \bar{\theta}) + \frac{v'^3}{4} \sin \bar{\theta} - \frac{w'^3}{4} \cos \bar{\theta} - \frac{v'^2 w'}{2} \cos \bar{\theta} \right) \\
&\quad + \delta\theta' \left( -\frac{\xi}{2} \right) + \mathcal{O}(\epsilon^4)
\end{aligned} \tag{C.6}$$

$$\begin{aligned}
\delta\epsilon_{x\xi} &= \delta u' \left( \frac{1}{2}(v' \sin \bar{\theta} - w' \cos \bar{\theta}) \right) + \delta v' \left( \frac{u'}{2} \sin \bar{\theta} + \frac{3}{4}v'^2 \sin \bar{\theta} - v'w' \cos \bar{\theta} \right) \\
&\quad + \delta v'' \left( w' \frac{\eta}{2} \right) + \delta w' \left( v'' \frac{\eta}{2} - \frac{u'}{2} \cos \bar{\theta} - \frac{3}{4}w'^2 \cos \bar{\theta} - \frac{v'^2}{2} \cos \bar{\theta} \right) \\
&\quad + \delta\theta \left( \frac{u'}{2}(v' \cos \bar{\theta} + w' \sin \bar{\theta}) + \frac{v'^3}{4} \cos \bar{\theta} + \frac{w'^3}{4} \sin \bar{\theta} + \frac{v'^2 w'}{2} \sin \bar{\theta} \right) \\
&\quad + \delta\theta' \left( -\frac{\xi}{2} \right) + \mathcal{O}(\epsilon^4)
\end{aligned} \tag{C.7}$$

- $\frac{d\mathbf{r}_1}{dt} \cdot \frac{d\mathbf{r}_1}{dt}$

$$\frac{d\mathbf{r}_1}{dt} \cdot \frac{d\mathbf{r}_1}{dt} = \dot{x}_1^2 + \dot{y}_1^2 + \dot{z}_1^2 + \Omega^2 (x_1^2 + y_1^2) - 2\Omega \dot{x}_1 y_1 + 2\Omega x_1 \dot{y}_1$$

$$\begin{aligned}
&= \dot{v}^2 + \dot{\theta}^2(\eta \sin \bar{\theta} + \xi \cos \bar{\theta})^2 - 2\dot{v}\dot{\theta}(\eta \sin \bar{\theta} + \xi \cos \bar{\theta}) + \dot{w}^2 \\
&\quad + \dot{\theta}^2(\eta \cos \bar{\theta} - \xi \sin \bar{\theta})^2 + 2\dot{w}\dot{\theta}(\eta \cos \bar{\theta} - \xi \sin \bar{\theta}) \\
&\quad + \Omega^2 \left[ x^2 + 2xu - 2xw'(\eta \sin \bar{\theta} + \xi \cos \bar{\theta}) - 2xv'(\eta \cos \bar{\theta} - \xi \sin \bar{\theta}) + v^2 \right. \\
&\quad \left. + (\eta \cos \bar{\theta} - \xi \sin \bar{\theta})^2 + 2v(\eta \cos \bar{\theta} - \xi \sin \bar{\theta}) \right] \\
&\quad - 2\Omega \left[ \dot{u}v - v\dot{w}'(\eta \sin \bar{\theta} + \xi \cos \bar{\theta}) - vw'\dot{\theta}(\eta \cos \bar{\theta} - \xi \sin \bar{\theta}) \right. \\
&\quad \left. - v\dot{v}'(\eta \cos \bar{\theta} - \xi \sin \bar{\theta}) + vv'\dot{\theta}(\eta \sin \bar{\theta} + \xi \cos \bar{\theta}) + \dot{u}(\eta \cos \bar{\theta} - \xi \sin \bar{\theta}) \right. \\
&\quad \left. - \dot{w}'(\eta \sin \bar{\theta} + \xi \cos \bar{\theta})(\eta \cos \bar{\theta} - \xi \sin \bar{\theta}) - w'\dot{\theta}(\eta \cos \bar{\theta} - \xi \sin \bar{\theta})^2 \right. \\
&\quad \left. - \dot{v}'(\eta \cos \bar{\theta} - \xi \sin \bar{\theta})^2 + v'\dot{\theta}(\eta \sin \bar{\theta} + \xi \cos \bar{\theta})(\eta \cos \bar{\theta} - \xi \sin \bar{\theta}) \right] \\
&\quad + 2\Omega \left[ x\dot{v} - x \left( 1 - \frac{v^2}{2} \right) \dot{\theta}(\eta \sin \bar{\theta} + \xi \cos \bar{\theta}) - xv'\dot{v}'(\eta \cos \bar{\theta} - \xi \sin \bar{\theta}) \right. \\
&\quad \left. - xv'\dot{w}'(\eta \sin \bar{\theta} + \xi \cos \bar{\theta}) - xv'\dot{w}'(\eta \sin \bar{\theta} + \xi \cos \bar{\theta}) \right. \\
&\quad \left. - xv'w'\dot{\theta}(\eta \cos \bar{\theta} - \xi \sin \bar{\theta}) + uv - u\dot{\theta}(\eta \sin \bar{\theta} + \xi \cos \bar{\theta}) \right. \\
&\quad \left. - w'\dot{v}(\eta \sin \bar{\theta} + \xi \cos \bar{\theta}) + w'\dot{\theta}(\eta \sin \bar{\theta} + \xi \cos \bar{\theta})^2 \right. \\
&\quad \left. - v'\dot{v}(\eta \cos \bar{\theta} - \xi \sin \bar{\theta}) + v'\dot{\theta}(\eta \cos \bar{\theta} - \xi \sin \bar{\theta})(\eta \sin \bar{\theta} + \xi \cos \bar{\theta}) \right] \\
&\quad + \mathcal{O}(\epsilon^4) \tag{C.8}
\end{aligned}$$

- $\ddot{x}_1, \ddot{y}_1, \ddot{z}_1$

$$\begin{aligned}
\ddot{x}_1 &= \ddot{u} - \ddot{w}'(\eta \sin \bar{\theta} + \xi \cos \bar{\theta}) - 2\dot{w}'\dot{\theta}(\eta \cos \bar{\theta} - \xi \sin \bar{\theta}) \\
&\quad - w'\ddot{\theta}(\eta \cos \bar{\theta} - \xi \sin \bar{\theta}) + w'\dot{\theta}^2(\eta \sin \bar{\theta} + \xi \cos \bar{\theta}) \\
&\quad - \ddot{v}'(\eta \cos \bar{\theta} - \xi \sin \bar{\theta}) + 2\dot{v}'\dot{\theta}(\eta \sin \bar{\theta} + \xi \cos \bar{\theta}) \\
&\quad + v'\ddot{\theta}(\eta \sin \bar{\theta} + \xi \cos \bar{\theta}) + v'\dot{\theta}^2(\eta \cos \bar{\theta} - \xi \sin \bar{\theta}) \tag{C.9}
\end{aligned}$$

$$\begin{aligned}
\ddot{y}_1 = & \ddot{v} - \left(1 - \frac{v'^2}{2}\right) \ddot{\theta} (\eta \sin \bar{\theta} + \xi \cos \bar{\theta}) + v' \dot{v}' \dot{\theta} (\eta \sin \bar{\theta} + \xi \cos \bar{\theta}) \\
& - \left(1 - \frac{v'^2}{2}\right) \dot{\theta}^2 (\eta \cos \bar{\theta} - \xi \sin \bar{\theta}) - \dot{v}'^2 (\eta \cos \bar{\theta} - \xi \sin \bar{\theta}) \\
& - v' \ddot{v}' (\eta \cos \bar{\theta} - \xi \sin \bar{\theta}) + v' \dot{v}' \dot{\theta} (\eta \sin \bar{\theta} + \xi \cos \bar{\theta}) \\
& - \ddot{v}' w' (\eta \sin \bar{\theta} + \xi \cos \bar{\theta}) - 2 \dot{v}' \dot{w}' (\eta \sin \bar{\theta} + \xi \cos \bar{\theta}) \\
& - 2 \dot{v}' w' \dot{\theta} (\eta \cos \bar{\theta} - \xi \sin \bar{\theta}) - v' \ddot{w}' (\eta \sin \bar{\theta} + \xi \cos \bar{\theta}) \\
& - 2 v' \dot{w}' \dot{\theta} (\eta \cos \bar{\theta} - \xi \sin \bar{\theta}) - v' w' \ddot{\theta} (\eta \cos \bar{\theta} - \xi \sin \bar{\theta}) \\
& + v' w' \dot{\theta}^2 (\eta \sin \bar{\theta} + \xi \cos \bar{\theta}) \tag{C.10}
\end{aligned}$$

$$\begin{aligned}
\ddot{z}_1 = & \ddot{w} + \left(1 - \frac{w'^2}{2}\right) \ddot{\theta} (\eta \cos \bar{\theta} - \xi \sin \bar{\theta}) - w' \dot{w}' \dot{\theta} (\eta \cos \bar{\theta} - \xi \sin \bar{\theta}) \\
& - \dot{w}'^2 (\eta \sin \bar{\theta} + \xi \cos \bar{\theta}) - \left(1 - \frac{w'^2}{2}\right) \dot{\theta}^2 (\eta \sin \bar{\theta} + \xi \cos \bar{\theta}) \\
& - w' \ddot{w}' (\eta \sin \bar{\theta} + \xi \cos \bar{\theta}) - w' \dot{w}' \dot{\theta} (\eta \cos \bar{\theta} - \xi \sin \bar{\theta}) \tag{C.11}
\end{aligned}$$

- $\delta x_1, \delta y_1, \delta z_1$

$$\begin{aligned}
\delta x_1 = & \delta u - (\eta \sin \bar{\theta} + \xi \cos \bar{\theta}) \delta w' - w' (\eta \cos \bar{\theta} - \xi \sin \bar{\theta}) \delta \theta \\
& - (\eta \cos \bar{\theta} - \xi \sin \bar{\theta}) \delta v' + v' (\eta \sin \bar{\theta} + \xi \cos \bar{\theta}) \delta \theta \tag{C.12}
\end{aligned}$$

$$\begin{aligned}
\delta y_1 = & \delta v - \left(1 - \frac{v'^2}{2}\right) (\eta \sin \bar{\theta} + \xi \cos \bar{\theta}) \delta \theta - v' (\eta \cos \bar{\theta} - \xi \sin \bar{\theta}) \delta v' \\
& - w' (\eta \sin \bar{\theta} + \xi \cos \bar{\theta}) \delta v' - v' (\eta \sin \bar{\theta} + \xi \cos \bar{\theta}) \delta w' \\
& - v' w' (\eta \cos \bar{\theta} - \xi \sin \bar{\theta}) \delta \theta \tag{C.13}
\end{aligned}$$

$$\delta z_1 = \delta w + \left(1 - \frac{w'^2}{2}\right) (\eta \cos \bar{\theta} - \xi \sin \bar{\theta}) \delta \theta - w' (\eta \sin \bar{\theta} + \xi \cos \bar{\theta}) \delta w' \quad (\text{C.14})$$

- $\int_{t_1}^{t_2} (\delta T)_b dt$

$$\begin{aligned} & \int_{t_1}^{t_2} (\delta T)_b dt = \\ & \int_{t_1}^{t_2} \int_R \int \int_A \rho \left\{ \left[ 2\Omega \left( \dot{v} - \dot{\theta}(\eta \sin \bar{\theta} + \xi \cos \bar{\theta}) \right) + \Omega^2 x \right] \right. \\ & \quad \left[ \delta u - (\eta \sin \bar{\theta} + \xi \cos \bar{\theta}) \delta w' \right. \\ & \quad \quad - w' (\eta \cos \bar{\theta} - \xi \sin \bar{\theta}) \delta \theta - (\eta \cos \bar{\theta} - \xi \sin \bar{\theta}) \delta v' \\ & \quad \quad \left. \left. + v' (\eta \sin \bar{\theta} + \xi \cos \bar{\theta}) \delta \theta \right] \right. \\ & \quad + \left[ \Omega^2 \left( v + (\eta \cos \bar{\theta} - \xi \sin \bar{\theta}) \right) - \ddot{v} + \ddot{\theta} (\eta \sin \bar{\theta} + \xi \cos \bar{\theta}) \right. \\ & \quad \quad + \dot{\theta}^2 (\eta \cos \bar{\theta} - \xi \sin \bar{\theta}) \\ & \quad \quad - 2\Omega \left( \dot{u} - \dot{w}' (\eta \sin \bar{\theta} + \xi \cos \bar{\theta}) - w' \dot{\theta} (\eta \cos \bar{\theta} - \xi \sin \bar{\theta}) \right. \\ & \quad \quad \left. \left. - \dot{v}' (\eta \cos \bar{\theta} - \xi \sin \bar{\theta}) + v' \dot{\theta} (\eta \sin \bar{\theta} + \xi \cos \bar{\theta}) \right) \right] \\ & \quad \left[ \delta v - (\eta \sin \bar{\theta} + \xi \cos \bar{\theta}) \delta \theta \right] \\ & \quad + \left[ -\ddot{w} - \ddot{\theta} (\eta \cos \bar{\theta} - \xi \sin \bar{\theta}) + \dot{\theta}^2 (\eta \sin \bar{\theta} + \xi \cos \bar{\theta}) \right] \\ & \quad \left[ \delta w + (\eta \cos \bar{\theta} - \xi \sin \bar{\theta}) \delta \theta \right] \\ & \quad \left. + \mathcal{O}(\epsilon^4) \right\} d\eta d\xi dx dt \quad (\text{C.15}) \end{aligned}$$

- $\delta x_{1m}, \delta y_{1m}, \delta z_{1m}$

$$\begin{aligned}
\delta x_{1m} = & \delta u_m \\
& - \left\{ \eta_m \sin \bar{\theta}_m + \xi_m \cos \bar{\theta}_m + \lambda \sin (\bar{\theta}_m - \theta_{ind}) \right\} \delta w'_m \\
& - \left\{ \eta_m \cos \bar{\theta}_m - \xi_m \sin \bar{\theta}_m + \lambda \cos (\bar{\theta}_m - \theta_{ind}) \right\} \delta v'_m \\
& - \left\{ w'_m [\eta_m \cos \bar{\theta}_m - \xi_m \sin \bar{\theta}_m + \lambda \cos (\bar{\theta}_m - \theta_{ind})] \right. \\
& \quad \left. - v'_m [\eta_m \sin \bar{\theta}_m + \xi_m \cos \bar{\theta}_m + \lambda \sin (\bar{\theta}_m - \theta_{ind})] \right\} \delta \theta_m
\end{aligned} \tag{C.16}$$

$$\begin{aligned}
\delta y_{1m} = & \delta v \\
& - \left\{ v'_m [\eta_m \cos \bar{\theta}_m - \xi_m \sin \bar{\theta}_m + \lambda \cos (\bar{\theta}_m - \theta_{ind})] \right. \\
& \quad \left. + w'_m [\eta_m \sin \bar{\theta}_m + \xi_m \cos \bar{\theta}_m + \lambda \sin (\bar{\theta}_m - \theta_{ind})] \right\} \delta v'_m \\
& - \left\{ v'_m [\eta_m \sin \bar{\theta}_m + \xi_m \cos \bar{\theta}_m + \lambda \sin (\bar{\theta}_m - \theta_{ind})] \right\} \delta w'_m \\
& - \left\{ \left( 1 - \frac{v_m'^2}{2} \right) [\eta_m \sin \bar{\theta}_m + \xi_m \cos \bar{\theta}_m + \lambda \sin (\bar{\theta}_m - \theta_{ind})] \right. \\
& \quad \left. + v'_m w'_m [\eta_m \cos \bar{\theta}_m - \xi_m \sin \bar{\theta}_m + \lambda \cos (\bar{\theta}_m - \theta_{ind})] \right\} \delta \theta_m
\end{aligned} \tag{C.17}$$

$$\begin{aligned}
\delta z_{1m} = & \delta w_m \\
& - \left\{ w'_m [\eta_m \sin \bar{\theta}_m + \xi_m \cos \bar{\theta}_m + \lambda \sin (\bar{\theta}_m - \theta_{ind})] \right\} \delta w'_m
\end{aligned}$$

$$+ \left\{ \left( 1 - \frac{w_m'^2}{2} \right) \left[ \eta_m \cos \bar{\theta}_m - \xi_m \sin \bar{\theta}_m + \lambda \cos (\bar{\theta}_m - \theta_{ind}) \right] \right\} \delta \theta_m$$

(C.18)

## Appendix D

### First-order Taylor approximation of energy expressions

#### D.1 Linearized strain energy

A first-order Taylor series expansion of the variations of strain energy (see Eq. (2.158)) is given by

$$\begin{aligned}
 (\delta U)_{b\,Lin} &= (\delta U)_{b0} \\
 &+ \int_R \left\{ \left[ U_{01}\Delta u' + U_{02}\Delta v' + U_{03}\Delta v'' + U_{04}\Delta w' + U_{05}\Delta w'' + U_{06}\Delta\theta + U_{07}\Delta\theta' \right] \delta u' \right. \\
 &\quad + \left[ U_{08}\Delta u' + U_{09}\Delta v' + U_{10}\Delta v'' + U_{11}\Delta w' + U_{12}\Delta w'' + U_{13}\Delta\theta + U_{14}\Delta\theta' \right] \delta v' \\
 &\quad + \left[ U_{15}\Delta u' + U_{16}\Delta v' + U_{17}\Delta v'' + U_{18}\Delta w' + U_{19}\Delta w'' + U_{20}\Delta\theta + U_{21}\Delta\theta' \right] \delta v'' \\
 &\quad + \left[ U_{22}\Delta u' + U_{23}\Delta v' + U_{24}\Delta v'' + U_{25}\Delta w' + U_{26}\Delta w'' + U_{27}\Delta\theta + U_{28}\Delta\theta' \right] \delta w' \\
 &\quad + \left[ U_{29}\Delta u' + U_{30}\Delta v' + U_{31}\Delta v'' + U_{32}\Delta w' + U_{33}\Delta w'' + U_{34}\Delta\theta + U_{35}\Delta\theta' \right] \delta w'' \\
 &\quad + \left[ U_{36}\Delta u' + U_{37}\Delta v' + U_{38}\Delta v'' + U_{39}\Delta w' + U_{40}\Delta w'' + U_{41}\Delta\theta + U_{42}\Delta\theta' \right] \delta\theta \\
 &\quad \left. + \left[ U_{43}\Delta u' + U_{44}\Delta v' + U_{45}\Delta v'' + U_{46}\Delta w' + U_{47}\Delta w'' + U_{48}\Delta\theta + U_{49}\Delta\theta' \right] \delta\theta' \right\} dx
 \end{aligned} \tag{D.1}$$

Note that due to the positive definiteness of the strain energy operator, the Jacobian matrix is symmetric. Hence, the lower triangular part of the Jacobian

matrix is equal to the upper triangular part, i.e.

$$\begin{aligned}
U_{02} = U_{08} \quad U_{03} = U_{15} \quad U_{04} = U_{22} \quad U_{05} = U_{29} \quad U_{06} = U_{36} \quad U_{07} = U_{43} \\
U_{10} = U_{16} \quad U_{11} = U_{23} \quad U_{12} = U_{30} \quad U_{13} = U_{37} \quad U_{14} = U_{44} \\
U_{18} = U_{24} \quad U_{19} = U_{31} \quad U_{20} = U_{38} \quad U_{21} = U_{45} \\
U_{26} = U_{32} \quad U_{27} = U_{39} \quad U_{28} = U_{46} \\
U_{34} = U_{40} \quad U_{35} = U_{47} \\
U_{42} = U_{48}
\end{aligned}$$

The coefficients of the upper triangular part and the diagonal of the Jacobian matrix are given by

$$U_{01} = EA$$

$$U_{02} = EA v_0' + GA \theta_0' (e_\eta \sin \bar{\theta}_0 + e_\xi \cos \bar{\theta}_0)$$

$$U_{03} = -EA (e_\eta \cos \bar{\theta}_0 - e_\xi \sin \bar{\theta}_0)$$

$$U_{04} = EA w_0' - GA \theta_0' (e_\eta \cos \bar{\theta}_0 - e_\xi \sin \bar{\theta}_0)$$

$$U_{05} = -EA (e_\eta \sin \bar{\theta}_0 + e_\xi \cos \bar{\theta}_0)$$

$$U_{06} = (EA v_0'' + GA \theta_0' w_0') (e_\eta \sin \bar{\theta}_0 + e_\xi \cos \bar{\theta}_0)$$

$$- (EA w_0'' - GA \theta_0' v_0') (e_\eta \cos \bar{\theta}_0 - e_\xi \sin \bar{\theta}_0)$$

$$U_{07} = EA k_A^2 \theta_0' - GA w_0' (e_\eta \cos \bar{\theta}_0 - e_\xi \sin \bar{\theta}_0) + GA v_0' (e_\eta \sin \bar{\theta}_0 + e_\xi \cos \bar{\theta}_0)$$

$$U_{09} = EA v_0'^2 + EA \left( u_0' + \frac{v_0'^2}{2} + \frac{w_0'^2}{2} \right) + EA \frac{k_A^2}{2} \theta_0'^2$$

$$- (EA v_0'' + 2GA w_0' \theta_0') (e_\eta \cos \bar{\theta}_0 - e_\xi \sin \bar{\theta}_0)$$

$$- (EA w_0'' - 3GA v_0' \theta_0') (e_\eta \sin \bar{\theta}_0 + e_\xi \cos \bar{\theta}_0)$$

$$\begin{aligned}
U_{10} &= -EA v'_0 (e_\eta \cos \bar{\theta}_0 - e_\xi \sin \bar{\theta}_0) \\
U_{11} &= EA w'_0 v'_0 - 2GA v'_0 \theta'_0 (e_\eta \cos \bar{\theta}_0 - e_\xi \sin \bar{\theta}_0) \\
U_{12} &= -EA v'_0 (e_\eta \sin \bar{\theta}_0 + e_\xi \cos \bar{\theta}_0) \\
U_{13} &= (EA v'_0 v''_0 + 2GA v'_0 w'_0 \theta'_0) (e_\eta \sin \bar{\theta}_0 + e_\xi \cos \bar{\theta}_0) \\
&\quad - (EA v'_0 w''_0 - GA u'_0 \theta'_0 - \frac{3}{2} GA v_0'^2 \theta_0') (e_\eta \cos \bar{\theta}_0 - e_\xi \sin \bar{\theta}_0) \\
U_{14} &= EA k_A^2 v'_0 \theta'_0 - 2GA v' w' (e_\eta \cos \bar{\theta}_0 - e_\xi \sin \bar{\theta}_0) \\
&\quad + GA \left( u'_0 + \frac{3}{2} v_0'^2 \right) (e_\eta \sin \bar{\theta}_0 + e_\xi \cos \bar{\theta}_0) \\
U_{17} &= EI_\xi \cos^2 \bar{\theta}_0 + EI_\eta \sin^2 \bar{\theta}_0 - EI_{\eta\xi} \sin 2\bar{\theta}_0 \\
U_{18} &= -EA w'_0 (e_\eta \cos \bar{\theta}_0 - e_\xi \sin \bar{\theta}_0) + GJ \theta'_0 \\
U_{19} &= \frac{1}{2} [(EI_\xi - EI_\eta) \sin 2\bar{\theta}_0 + 2EI_{\eta\xi} \cos 2\bar{\theta}_0] \\
U_{20} &= [-EI_\xi \sin 2\bar{\theta}_0 + EI_\eta \sin 2\bar{\theta}_0 - 2EI_{\eta\xi} \cos 2\bar{\theta}_0] v''_0 \\
&\quad + [(EI_\xi - EI_\eta) \cos 2\bar{\theta}_0 - 2EI_{\eta\xi} \sin 2\bar{\theta}_0] w''_0 \\
&\quad + \frac{EB_2}{2} \theta_0'^2 \sin \bar{\theta}_0 + \frac{EB_3}{2} \theta_0'^2 \cos \bar{\theta}_0 \\
&\quad + EA \left( u'_0 + \frac{v_0'^2}{2} + \frac{w_0'^2}{2} \right) (e_\eta \sin \bar{\theta}_0 + e_\xi \cos \bar{\theta}_0) \\
U_{21} &= -EB_2 \theta'_0 \cos \bar{\theta}_0 + EB_3 \theta'_0 \sin \bar{\theta}_0 + GJ w'_0 \\
U_{25} &= EA w_0'^2 + EA \left( u'_0 + \frac{v_0'^2}{2} + \frac{w_0'^2}{2} \right) + EA \frac{k_A^2}{2} \theta_0'^2 \\
&\quad - (EA v_0'' + 3GA w_0' \theta_0') (e_\eta \cos \bar{\theta}_0 - e_\xi \sin \bar{\theta}_0) - EA w_0'' (e_\eta \sin \bar{\theta}_0 + e_\xi \cos \bar{\theta}_0) \\
U_{26} &= -EA w'_0 (e_\eta \sin \bar{\theta}_0 + e_\xi \cos \bar{\theta}_0) \\
U_{27} &= (EA w'_0 v''_0 + GA u'_0 \theta'_0 + GA v_0'^2 \theta_0' + \frac{3}{2} GA w_0'^2 \theta_0') (e_\eta \sin \bar{\theta}_0 + e_\xi \cos \bar{\theta}_0) \\
&\quad - EA w_0' w''_0 (e_\eta \cos \bar{\theta}_0 - e_\xi \sin \bar{\theta}_0)
\end{aligned}$$

$$\begin{aligned}
U_{28} &= E A k_A^2 w'_0 \theta'_0 - (G A u'_0 + G A v'^2 + \frac{3}{2} G A w'^2) (e_\eta \cos \bar{\theta}_0 - e_\xi \sin \bar{\theta}_0) + G J v''_0 \\
U_{33} &= [E I_\xi \sin^2 \bar{\theta}_0 + E I_\eta \cos^2 \bar{\theta}_0 + E I_{\eta\xi} \sin 2\bar{\theta}_0] \\
U_{34} &= [E I_\xi \sin 2\bar{\theta}_0 - E I_\eta \sin 2\bar{\theta}_0 + 2 E I_{\eta\xi} \cos 2\bar{\theta}_0] w''_0 \\
&\quad + [(E I_\xi - E I_\eta) \cos 2\bar{\theta}_0 - 2 E I_{\eta\xi} \sin 2\bar{\theta}_0] v''_0 \\
&\quad - \frac{E B_2}{2} \theta_0'^2 \cos \bar{\theta}_0 + \frac{E B_3}{2} \theta_0'^2 \sin \bar{\theta}_0 \\
&\quad - E A \left( u'_0 + \frac{v_0'^2}{2} + \frac{w_0'^2}{2} \right) (e_\eta \cos \bar{\theta}_0 - e_\xi \sin \bar{\theta}_0) \\
U_{35} &= -E B_2 \theta'_0 \sin \bar{\theta}_0 - E B_3 \theta'_0 \cos \bar{\theta}_0 \\
U_{41} &= [(E I_\xi - E I_\eta) \cos 2\bar{\theta}_0 - 2 E I_{\eta\xi} \sin 2\bar{\theta}_0] w''_0^2 \\
&\quad - [(E I_\xi - E I_\eta) \cos 2\bar{\theta}_0 - 2 E I_{\eta\xi} \sin 2\bar{\theta}_0] v''_0^2 \\
&\quad - 2 [(E I_\xi - E I_\eta) \sin 2\bar{\theta}_0 + 2 E I_{\eta\xi} \cos 2\bar{\theta}_0] v''_0 w''_0 \\
&\quad + \left( \frac{E B_2}{2} \sin \bar{\theta}_0 + \frac{E B_3}{2} \cos \bar{\theta}_0 \right) w''_0 \theta_0'^2 \\
&\quad + \left( \frac{E B_2}{2} \cos \bar{\theta}_0 - \frac{E B_3}{2} \sin \bar{\theta}_0 \right) v''_0 \theta_0'^2 \\
&\quad + \left[ E A \left( u'_0 + \frac{v_0'^2}{2} + \frac{w_0'^2}{2} \right) v''_0 + G A u'_0 w'_0 \theta'_0 \right. \\
&\quad \quad \left. + G A v_0'^2 w'_0 \theta'_0 + G A \frac{w_0'^3 \theta'_0}{2} \right] (e_\eta \cos \bar{\theta}_0 - e_\xi \sin \bar{\theta}_0) \\
&\quad - \left[ -E A \left( u'_0 + \frac{v_0'^2}{2} + \frac{w_0'^2}{2} \right) w''_0 \right. \\
&\quad \quad \left. + G A u'_0 v'_0 \theta'_0 + G A \frac{v_0'^3 \theta'_0}{2} \right] (e_\eta \sin \bar{\theta}_0 + e_\xi \cos \bar{\theta}_0) \\
U_{42} &= - (E B_2 \cos \bar{\theta}_0 - E B_3 \sin \bar{\theta}_0) w''_0 \theta'_0 + (E B_2 \sin \bar{\theta}_0 + E B_3 \cos \bar{\theta}_0) v''_0 \theta'_0 \\
&\quad + \left( G A u'_0 w'_0 + G A v_0'^2 w'_0 + G A \frac{w_0'^3}{2} \right) (e_\eta \sin \bar{\theta}_0 + e_\xi \cos \bar{\theta}_0) \\
&\quad + \left( G A u'_0 v'_0 + G A \frac{v_0'^3}{2} \right) (e_\eta \cos \bar{\theta}_0 - e_\xi \sin \bar{\theta}_0)
\end{aligned}$$

$$\begin{aligned}
U_{49} = & E A k_A^2 \left( u_0' + \frac{v_0'^2}{2} + \frac{w_0'^2}{2} \right) + \left( \frac{3}{2} E B_1 \right) \theta_0'^2 \\
& - (E B_2 \sin \bar{\theta}_0 + E B_3 \cos \bar{\theta}_0) w_0'' - (E B_2 \cos \bar{\theta}_0 - E B_3 \sin \bar{\theta}_0) v_0'' + G J
\end{aligned}$$

## D.2 Linearized kinetic energy

A first-order Taylor expansion of Eq. (2.177) gives

$$\begin{aligned}
(\delta T)_{b Lin} = & (\delta T)_{b0} \\
& + \int_R \left\{ \left[ M_{01} \Delta \ddot{u} + M_{02} \Delta \ddot{v}' + M_{03} \Delta \ddot{w}' + M_{04} \Delta \ddot{\theta} \right] \delta u \right. \\
& + \left[ M_{05} \Delta \ddot{v} + M_{06} \Delta \ddot{\theta} \right] \delta v \\
& + \left[ M_{07} \Delta \ddot{u} \right] \delta v' + \left[ M_{08} \Delta \ddot{w} + M_{09} \Delta \ddot{\theta} \right] \delta w + \left[ M_{10} \Delta \ddot{u} \right] \delta w' \\
& \left. + \left[ M_{11} \Delta \ddot{u} + M_{12} \Delta \ddot{v} + M_{13} \Delta \ddot{w} + M_{14} \Delta \ddot{\theta} \right] \delta \theta \right\} dx \\
& + \int_R \left\{ \left[ G_{01} \Delta \dot{v} + G_{02} \Delta \dot{\theta} \right] \delta u \right. \\
& + \left[ G_{03} \Delta \dot{u} + G_{04} \Delta \dot{v}' + G_{05} \Delta \dot{w}' + G_{06} \Delta \dot{\theta} \right] \delta v \\
& + \left[ G_{07} \Delta \dot{v} + G_{08} \Delta \dot{\theta} \right] \delta v' + \left[ G_{09} \Delta \dot{v} + G_{10} \Delta \dot{\theta} \right] \delta w' \\
& \left. + \left[ G_{11} \Delta \dot{u} + G_{12} \Delta \dot{v} + G_{13} \Delta \dot{v}' + G_{14} \Delta \dot{w}' \right] \delta \theta \right\} dx \\
& + \int_R \left\{ \left[ K_{01} \Delta v + K_{02} \Delta \theta \right] \delta v + \left[ K_{03} \Delta \theta \right] \delta v' \right. \\
& + \left[ K_{04} \Delta \theta \right] \delta w' \\
& \left. + \left[ K_{05} \Delta v + K_{06} \Delta v' + K_{07} \Delta w' + K_{08} \Delta \theta \right] \delta \theta \right\} dx \quad (D.2)
\end{aligned}$$

where

$$M_{01} = -m_0$$

$$M_{02} = m_0(d_\eta \cos \bar{\theta}_0 - d_\xi \sin \bar{\theta}_0)$$

$$M_{03} = m_0(d_\eta \sin \bar{\theta}_0 + d_\xi \cos \bar{\theta}_0)$$

$$M_{04} = m_0 w'_0(d_\eta \cos \bar{\theta}_0 - d_\xi \sin \bar{\theta}_0) - m_0 v'_0(d_\eta \sin \bar{\theta}_0 + d_\xi \cos \bar{\theta}_0)$$

$$M_{05} = -m_0$$

$$M_{06} = m_0(d_\eta \sin \bar{\theta}_0 + d_\xi \cos \bar{\theta}_0)$$

$$M_{07} = m_0(d_\eta \cos \bar{\theta}_0 - d_\xi \sin \bar{\theta}_0)$$

$$M_{08} = -m_0$$

$$M_{09} = -m_0(d_\eta \cos \bar{\theta}_0 - d_\xi \sin \bar{\theta}_0)$$

$$M_{10} = m_0(d_\eta \sin \bar{\theta}_0 + d_\xi \cos \bar{\theta}_0)$$

$$M_{11} = m_0 w'_0(d_\eta \cos \bar{\theta}_0 - d_\xi \sin \bar{\theta}_0) - m_0 v'_0(d_\eta \sin \bar{\theta}_0 + d_\xi \cos \bar{\theta}_0)$$

$$M_{12} = m_0(d_\eta \sin \bar{\theta}_0 + d_\xi \cos \bar{\theta}_0)$$

$$M_{13} = -m_0(d_\eta \cos \bar{\theta}_0 - d_\xi \sin \bar{\theta}_0)$$

$$M_{14} = -m_0 k_m^2$$

$$G_{01} = 2m_0 \Omega$$

$$G_{02} = -2m_0 \Omega(d_\eta \sin \bar{\theta}_0 + d_\xi \cos \bar{\theta}_0)$$

$$G_{03} = -2m_0 \Omega$$

$$G_{04} = 2m_0 \Omega(d_\eta \cos \bar{\theta}_0 - d_\xi \sin \bar{\theta}_0)$$

$$G_{05} = 2m_0 \Omega(d_\eta \sin \bar{\theta}_0 + d_\xi \cos \bar{\theta}_0)$$

$$G_{06} = -2m_0\Omega v'_0(d_\eta \sin \bar{\theta}_0 + d_\xi \cos \bar{\theta}_0) + 2m_0\Omega w'_0(d_\eta \cos \bar{\theta}_0 - d_\xi \sin \bar{\theta}_0)$$

$$G_{07} = -2m_0\Omega(d_\eta \cos \bar{\theta}_0 - d_\xi \sin \bar{\theta}_0)$$

$$G_{08} = m_0\Omega(k_{m_\xi}^2 - k_{m_\eta}^2) \sin 2\bar{\theta}_0 + 2m_0\Omega k_{m_\eta\xi}^2 \cos 2\bar{\theta}_0$$

$$G_{09} = -2m_0\Omega(d_\eta \sin \bar{\theta}_0 + d_\xi \cos \bar{\theta}_0)$$

$$G_{10} = 2m_0\Omega(k_{m_\xi}^2 \sin^2 \bar{\theta}_0 + k_{m_\eta}^2 \cos^2 \bar{\theta}_0) + 2m_0\Omega k_{m_\eta\xi}^2 \sin 2\bar{\theta}_0$$

$$G_{11} = 2m_0\Omega(d_\eta \sin \bar{\theta}_0 + d_\xi \cos \bar{\theta}_0)$$

$$G_{12} = -2m_0\Omega w'_0(d_\eta \cos \bar{\theta}_0 - d_\xi \sin \bar{\theta}_0) + 2m_0\Omega v'_0(d_\eta \sin \bar{\theta}_0 + d_\xi \cos \bar{\theta}_0)$$

$$G_{13} = -m_0\Omega(k_{m_\xi}^2 - k_{m_\eta}^2) \sin 2\bar{\theta}_0 - 2m_0\Omega k_{m_\eta\xi}^2 \cos 2\bar{\theta}_0$$

$$G_{14} = -2m_0\Omega(k_{m_\xi}^2 \sin^2 \bar{\theta}_0 + k_{m_\eta}^2 \cos^2 \bar{\theta}_0) - 2m_0\Omega k_{m_\eta\xi}^2 \sin 2\bar{\theta}_0$$

$$K_{01} = m_0\Omega^2$$

$$K_{02} = -m_0\Omega^2(d_\eta \sin \bar{\theta}_0 + d_\xi \cos \bar{\theta}_0)$$

$$K_{03} = m_0\Omega^2 x(d_\eta \sin \bar{\theta}_0 + d_\xi \cos \bar{\theta}_0)$$

$$K_{04} = -m_0\Omega^2 x(d_\eta \cos \bar{\theta}_0 - d_\xi \sin \bar{\theta}_0)$$

$$K_{05} = -m_0\Omega^2(d_\eta \sin \bar{\theta}_0 + d_\xi \cos \bar{\theta}_0)$$

$$K_{06} = m_0\Omega^2 x(d_\eta \sin \bar{\theta}_0 + d_\xi \cos \bar{\theta}_0)$$

$$K_{07} = -m_0\Omega^2 x(d_\eta \cos \bar{\theta}_0 - d_\xi \sin \bar{\theta}_0)$$

$$K_{08} = m_0\Omega^2 x w'_0(d_\eta \sin \bar{\theta}_0 + d_\xi \cos \bar{\theta}_0) + m_0\Omega^2 x v'_0(d_\eta \cos \bar{\theta}_0 - d_\xi \sin \bar{\theta}_0)$$

$$- m_0\Omega^2(k_{m_\xi}^2 - k_{m_\eta}^2) \cos 2\bar{\theta}_0 + 2m_0\Omega^2 k_{m_\eta\xi}^2 \sin 2\bar{\theta}_0$$

$$- m_0\Omega^2 v_0(d_\eta \cos \bar{\theta}_0 - d_\xi \sin \bar{\theta}_0)$$

### D.3 Linearized gravitational potential energy

Upon linearization by first-order Taylor expansion, Eq. (2.189) becomes

$$(\delta V_g)_{bLin} = (\delta V_g)_{b0} + \int_R \left\{ \left[ V_{g01} \Delta w' + V_{g02} \Delta \theta \right] \delta w' + \left[ V_{g03} \Delta w' + V_{g04} \Delta \theta \right] \delta \theta \right\} dx \quad (\text{D.3})$$

where

$$\begin{aligned} V_{g01} &= -m_0 g (d_\eta \sin \bar{\theta}_0 + d_\xi \cos \bar{\theta}_0) \\ V_{g02} &= -m_0 g w'_0 (d_\eta \cos \bar{\theta}_0 - d_\xi \sin \bar{\theta}_0) \\ V_{g03} &= -m_0 g w'_0 (d_\eta \cos \bar{\theta}_0 - d_\xi \sin \bar{\theta}_0) \\ V_{g04} &= -m_0 g \left( 1 - \frac{w_0'^2}{2} \right) (d_\eta \sin \bar{\theta}_0 + d_\xi \cos \bar{\theta}_0) \end{aligned}$$

### D.4 Linearized tip mass kinetic energy

$$\begin{aligned} (\delta T)_m &= (\delta T)_{m0} + \left[ M_{m01} \Delta \ddot{u}_m + M_{m02} \Delta \ddot{v}'_m + M_{m03} \Delta \ddot{w}'_m + M_{m04} \Delta \ddot{\theta}_m \right] \delta u_m \\ &\quad + \left[ M_{m05} \Delta \ddot{v}_m + M_{m06} \Delta \ddot{\theta}_m \right] \delta v_m + \left[ M_{m07} \Delta \ddot{u}_m \right] \delta v'_m \\ &\quad + \left[ M_{m08} \Delta \ddot{w}_m + M_{m09} \Delta \ddot{\theta}_m \right] \delta w_m + \left[ M_{m10} \Delta \ddot{u}_m \right] \delta w'_m \\ &\quad + \left[ M_{m11} \Delta \ddot{u}_m + M_{m12} \Delta \ddot{v}_m + M_{m13} \Delta \ddot{w}_m + M_{m14} \Delta \ddot{\theta}_m \right] \delta \theta_m \\ &\quad + \left[ C_{m01} \Delta \dot{v}_m + C_{m02} \Delta \dot{\theta}_m \right] \delta u_m \\ &\quad + \left[ C_{m03} \Delta \dot{u}_m + C_{m04} \Delta \dot{v}'_m + C_{m05} \Delta \dot{w}'_m + C_{m06} \Delta \dot{\theta}_m \right] \delta v_m \\ &\quad + \left[ C_{m07} \Delta \dot{v}_m + C_{m08} \Delta \dot{\theta}_m \right] \delta v'_m + \left[ C_{m09} \Delta \dot{u}_m + C_{m10} \Delta \dot{\theta}_m \right] \delta w'_m \end{aligned}$$

$$\begin{aligned}
& + \left[ C_{m11} \Delta \dot{v}_m + C_{m12} \Delta \dot{v}'_m + C_{m13} \Delta \dot{v}_m + C_{m14} \Delta \dot{v}'_m \right] \delta \theta_m \\
& + \left[ K_{m01} \Delta v_m + K_{m02} \Delta \theta_m \right] \delta v_m + \left[ K_{m03} \Delta \theta_m \right] \delta v'_m + \left[ K_{m04} \Delta \theta_m \right] \delta w'_m \\
& + \left[ K_{m05} \Delta v_m + K_{m06} \Delta v'_m + K_{m07} \Delta w'_m + K_{m08} \Delta \theta_m \right] \delta \theta_m
\end{aligned} \tag{D.4}$$

where

$$M_{m01} = -m_m$$

$$M_{m02} = m_m (T_2)_0$$

$$M_{m03} = m_m (T_1)_0$$

$$M_{m04} = m_m w'_0 (T_2)_0 - m_m v'_0 (T_1)_0$$

$$M_{m05} = -m_m$$

$$M_{m06} = m_m (T_1)_0$$

$$M_{m07} = m_m (T_2)_0$$

$$M_{m08} = -m_m$$

$$M_{m09} = -m_m (T_2)_0$$

$$M_{m10} = m_m (T_1)_0$$

$$M_{m11} = m_m w'_0 (T_2)_0 - m_m v'_0 (T_1)_0$$

$$M_{m12} = m_m (T_1)_0$$

$$M_{m13} = -m_m (T_2)_0$$

$$M_{m14} = -m_m (T_3 + T_4)_0$$

$$C_{m01} = 2m_m\Omega$$

$$C_{m02} = -2m_m\Omega (T_1)_0$$

$$C_{m03} = -2m_m\Omega$$

$$C_{m04} = 2m_m\Omega (T_2)_0$$

$$C_{m05} = 2m_m\Omega (T_1)_0$$

$$C_{m06} = -2m_m\Omega v'_{m0} (T_1)_0 + 2m_m\Omega w'_{m0} (T_2)_0$$

$$C_{m07} = -2m_m\Omega (T_2)_0$$

$$C_{m08} = 2m_m\Omega (T_5)_0$$

$$C_{m09} = -2m_m\Omega (T_1)_0$$

$$C_{m10} = 2m_m\Omega (T_3)_0$$

$$C_{m11} = 2m_m\Omega (T_1)_0$$

$$C_{m12} = 2m_m\Omega v'_{m0} (T_1)_0 - 2m_m\Omega w'_{m0} (T_2)_0$$

$$C_{m13} = -2m_m\Omega (T_5)_0$$

$$C_{m14} = -2m_m\Omega (T_3)_0$$

$$K_{m01} = m_m\Omega^2$$

$$K_{m02} = m_m\Omega^2 \left( \frac{\partial T_2}{\partial \theta} \right)_0$$

$$K_{m03} = -m_m\Omega^2 x_m \left( \frac{\partial T_2}{\partial \theta} \right)_0$$

$$K_{m04} = -m_m\Omega^2 x_m \left( \frac{\partial T_1}{\partial \theta} \right)_0$$

$$K_{m05} = -m_m\Omega^2 (T_1)_0$$

$$K_{m06} = m_m \Omega^2 x_m (T_1)_0$$

$$K_{m07} = -m_m \Omega^2 x_m (T_2)_0$$

$$K_{m08} = m_m \Omega^2 (x_m v'_{m0} - v_{m0}) \left( \frac{\partial T_1}{\partial \theta} \right)_0 - m_m \Omega^2 x_m w'_{m0} \left( \frac{\partial T_2}{\partial \theta} \right)_0 - m_m \Omega^2 \left( \frac{\partial T_5}{\partial \theta} \right)_0$$

## D.5 Linearized tip mass gravitational potential energy

$$\begin{aligned} (\delta V_g)_{mLin} &= (\delta V_g)_{m0} + V_{gm01} \Delta w'_m \delta w'_m \\ &\quad + V_{gm02} \Delta \theta_m \delta w'_m + V_{gm03} \Delta w'_m \delta \theta_m + V_{gm04} \Delta \theta_m \delta \theta_m \end{aligned} \quad (D.5)$$

where

$$V_{gm01} = -m_m g (T_1)_0$$

$$V_{gm02} = -m_m g w'_{m0} \left( \frac{\partial T_1}{\partial \theta_m} \right)_0$$

$$V_{gm03} = -m_m g w'_{m0} (T_2)_0$$

$$V_{gm04} = m_m g \left( 1 - \frac{w'^2_{m0}}{2} \right) \left( \frac{\partial T_2}{\partial \theta_m} \right)_0$$

## D.6 Linearized virtual work done by unsteady aerodynamic loads

$$\begin{aligned} (\delta W_a)_{bLin} &= (\delta W_a)_{b0} \\ &\quad + \int_R \left[ M_{a01} \Delta \ddot{v} + M_{a02} \Delta \ddot{w} + M_{a03} \Delta \ddot{\theta} \right] \delta v \\ &\quad + \left[ M_{a04} \Delta \ddot{v} + M_{a05} \Delta \ddot{w} + M_{a06} \Delta \ddot{\theta} \right] \delta w \end{aligned}$$

$$\begin{aligned}
& + \int_R \left[ C_{a01} \Delta \dot{v} + C_{a02} \Delta \dot{w} + C_{a03} \Delta \dot{\theta} \right] \delta v \\
& \quad + \left[ C_{a04} \Delta \dot{v} + C_{a05} \Delta \dot{w} + C_{a06} \Delta \dot{\theta} \right] \delta w \\
& \quad + \left[ C_{a07} \Delta \dot{v} + C_{a08} \Delta \dot{w} + C_{a09} \Delta \dot{\theta} \right] \delta \theta \\
& + \int_R \left[ K_{a01} \Delta v + K_{a02} \Delta v' + K_{a03} \Delta w' + K_{a04} \Delta \theta \right] \delta v \\
& \quad + \left[ K_{a05} \Delta u + K_{a06} \Delta v + K_{a07} \Delta v' + K_{a08} \Delta w' + K_{a09} \Delta \theta \right] \delta w \\
& \quad + K_{a10} \Delta \theta \delta \theta \tag{D.6}
\end{aligned}$$

where

$$M_{a01} = -\frac{c^2}{16} \rho_\infty C_{l\alpha} (1 - \cos 2\bar{\theta}_0)$$

$$M_{a02} = \frac{c^2}{16} \rho_\infty C_{l\alpha} \sin 2\bar{\theta}_0$$

$$M_{a03} = -\frac{c^2}{16} \rho_\infty C_{l\alpha} \left( 2x_A + \frac{c}{2} \right) \sin \bar{\theta}_0$$

$$M_{a04} = \frac{c^2}{16} \rho_\infty C_{l\alpha} \sin 2\bar{\theta}_0$$

$$M_{a05} = -\frac{c^2}{16} \rho_\infty C_{l\alpha} (1 + \cos 2\bar{\theta}_0)$$

$$M_{a06} = \frac{c^2}{16} \rho_\infty C_{l\alpha} \left( 2x_A + \frac{c}{2} \right) \cos \bar{\theta}_0$$

$$C_{a01} = -\frac{1}{2} \rho_\infty (\Omega x) c C_{l\alpha} \left( \frac{\lambda_i}{r} \right) \sin \bar{\theta}_0 C'(k)$$

$$C_{a02} = -\frac{1}{2} \rho_\infty (\Omega x) c C_{l\alpha} \left[ \sin \bar{\theta}_0 - 2 \frac{\lambda_i}{r} \cos \bar{\theta}_0 \right] C'(k) - \frac{1}{2} \rho_\infty (\Omega x) c C_{l0} \cos \bar{\theta}_0 C'(k)$$

$$\begin{aligned}
C_{a03} = & -\frac{1}{2} \rho_\infty (\Omega x) c C_{l\alpha} \left[ \frac{\lambda_i}{r} \left( \frac{c}{2} + x_A \right) \right] C'(k) \\
& - \frac{c^2}{16} \rho_\infty (\Omega x) C_{l\alpha} \left[ \frac{\lambda_i}{r} (1 - \cos 2\bar{\theta}_0) + \sin 2\bar{\theta}_0 \right]
\end{aligned}$$

$$\begin{aligned}
C_{a04} &= -\frac{1}{2}\rho_\infty(\Omega x)cC_{l\alpha} \left[ \frac{\lambda_i}{r} \cos \bar{\theta}_0 - 2 \sin \bar{\theta}_0 \right] C'(k) \\
&\quad + \frac{1}{2}\rho_\infty(\Omega x)cC_{l0} [2 \cos \bar{\theta}_0] C'(k) \\
C_{a05} &= -\frac{1}{2}\rho_\infty(\Omega x)cC_{l\alpha} \cos \bar{\theta}_0 C'(k) + \frac{1}{2}\rho_\infty(\Omega x)cC_{l0} \sin \bar{\theta}_0 C'(k) \\
C_{a06} &= \frac{1}{2}\rho_\infty(\Omega x)cC_{l\alpha} \left( \frac{c}{2} + x_A \right) C'(k) \\
&\quad + \frac{c^2}{16}\rho_\infty(\Omega x)C_{l\alpha} \left( 1 + \cos 2\bar{\theta}_0 + \frac{\lambda_i}{r} \sin 2\bar{\theta}_0 \right) \\
C_{a07} &= -\frac{1}{2}\rho_\infty(\Omega x)cx_A C_{l\alpha} \sin 2\bar{\theta}_0 C'(k) \\
C_{a08} &= \frac{1}{2}\rho_\infty(\Omega x)cx_A C_{l\alpha} \cos 2\bar{\theta}_0 C'(k) \\
C_{a09} &= -\frac{1}{2}\rho_\infty(\Omega x)cx_A C_{l\alpha} \left( \frac{c}{2} + x_A \right) \cos \bar{\theta}_0 C'(k) \\
&\quad - \frac{c^2}{16}\rho_\infty(\Omega x)C_{l\alpha}(c + 2x_A) \cos \bar{\theta}_0
\end{aligned}$$

$$\begin{aligned}
K_{a01} &= -\frac{1}{2}\rho_\infty(\Omega x)cC_{l\alpha}\Omega w'_0 \sin \bar{\theta}_0 C'(k) \\
K_{a02} &= -\frac{1}{2}\rho_\infty(\Omega x)^2 cC_{l\alpha} w'_0 \sin \bar{\theta}_0 C'(k) \\
K_{a03} &= -\frac{1}{2}\rho_\infty(\Omega x)cC_{l\alpha} (\Omega v_0 + \Omega x v'_0) \sin \bar{\theta}_0 C'(k) \\
K_{a04} &= -\frac{1}{2}\rho_\infty(\Omega x)^2 cC_{l\alpha} \left[ \frac{\lambda_i}{r} \cos \bar{\theta}_0 + \left( \frac{\lambda_i}{r} \right)^2 \sin \bar{\theta}_0 \right] C'(k) \\
&\quad - \frac{1}{2}\rho_\infty(\Omega x)cC_{l\alpha} (\Omega v_0 w'_0 + \Omega x v'_0 w'_0) \cos \bar{\theta}_0 C'(k) \\
&\quad + \frac{1}{2}\rho_\infty(\Omega x)^2 cC_{l0} \left( \frac{\lambda_i}{r} \right) \sin \bar{\theta}_0 C'(k) + \frac{1}{2}\rho_\infty(\Omega x)^2 \frac{3c}{4} C_{d0} (\sin \bar{\theta}_0 + \sin 3\bar{\theta}_0) \\
K_{a05} &= \frac{1}{2}\rho_\infty(\Omega x)cC_{l\alpha} (2\Omega) \sin \bar{\theta}_0 C'(k) \\
K_{a06} &= \frac{1}{2}\rho_\infty(\Omega x)cC_{l\alpha} [-\Omega w'_0 \cos \bar{\theta}_0 + 2\Omega v'_0 \sin \bar{\theta}_0] C'(k)
\end{aligned}$$

$$\begin{aligned}
K_{a07} &= -\frac{1}{2}\rho_\infty(\Omega x)^2 c C_{l\alpha} (2v'_0) \sin \bar{\theta}_0 C'(k) + \frac{1}{2}\rho_\infty(\Omega x) c C_{l\alpha} (2\Omega v_0) \sin \bar{\theta}_0 C'(k) \\
K_{a08} &= -\frac{1}{2}\rho_\infty(\Omega x)^2 c C_{l\alpha} w'_0 \sin \bar{\theta}_0 C'(k) \\
&\quad + \frac{1}{2}\rho_\infty(\Omega x) c C_{l\alpha} \left[ \Omega \left( \frac{c}{2} + x_A \right) - \Omega v_0 \cos \bar{\theta}_0 \right] C'(k) \\
K_{a09} &= -\frac{1}{2}\rho_\infty(\Omega x)^2 c C_{l\alpha} \left[ -\frac{\lambda_i}{r} \sin \bar{\theta}_0 - 2 \cos \bar{\theta}_0 + \left( v_0'^2 + \frac{w_0'^2}{2} \right) \cos \bar{\theta}_0 \right] C'(k) \\
&\quad + \frac{1}{2}\rho_\infty(\Omega x) c C_{l\alpha} \left[ \Omega v_0 w'_0 \sin \bar{\theta}_0 + (2\Omega u_0 + 2\Omega v_0 v'_0) \cos \bar{\theta}_0 \right] C'(k) \\
&\quad + \frac{1}{2}\rho_\infty(\Omega x)^2 c C_{l0} \left[ -\sin \bar{\theta}_0 + \frac{\lambda_i}{r} \cos \bar{\theta}_0 \right] C'(k) \\
&\quad - \frac{1}{2}\rho_\infty(\Omega x)^2 \frac{c}{4} C_{d0} (3 \cos 3\bar{\theta}_0 + \cos \bar{\theta}_0) \\
K_{a10} &= -\frac{1}{2}\rho_\infty(\Omega x)^2 c^2 C_{m0} \sin 2\bar{\theta}_0 C'(k) \\
&\quad - \frac{1}{2}\rho_\infty(\Omega x)^2 c x_A C_{l\alpha} \left[ 2 \frac{\lambda_i}{r} \sin 2\bar{\theta}_0 + \cos 2\bar{\theta}_0 \right] C'(k) \\
&\quad + \frac{1}{2}\rho_\infty(\Omega x)^2 c x_A C_{l0} \sin 2\bar{\theta}_0 C'(k)
\end{aligned}$$

## D.7 Linearized virtual work done by steady aerodynamic loads

$$\begin{aligned}
(\delta W_{a \ QS})_b &= (\delta W_{a \ QS})_{b0} \\
&\quad + \int_{x_0}^R K_{(a01 \ QS)} \Delta\theta \delta v + K_{(a02 \ QS)} \Delta\theta \delta w + K_{(a03 \ QS)} \Delta\theta \delta\theta \quad (D.7)
\end{aligned}$$

where

$$\begin{aligned}
K_{(a01 \ QS)} &= -\frac{1}{2} \rho_\infty (\Omega x)^2 \left[ c \left( \frac{\partial C_d}{\partial \theta} \right)_0 \cos \bar{\theta}_0 - c(C_d)_0 \sin \bar{\theta}_0 \right] \\
&\quad - \frac{1}{2} \rho_\infty (\Omega x)^2 \frac{\lambda_i}{r} \left[ c \left( \frac{\partial C_l}{\partial \theta} \right)_0 \cos \bar{\theta}_0 - c(C_l)_0 \sin \bar{\theta}_0 \right]
\end{aligned}$$

$$\begin{aligned}
& +c \left( \frac{\partial C_d}{\partial \theta} \right)_0 \sin \bar{\theta}_0 + c(C_d)_0 \cos \bar{\theta}_0 \Big] \\
K_{(a02 \ QS)} = & \frac{1}{2} \rho_\infty (\Omega x)^2 \left[ c \left( \frac{\partial C_l}{\partial \theta} \right)_0 \cos \bar{\theta}_0 - c(C_l)_0 \sin \bar{\theta}_0 \right] \\
& + \frac{1}{2} \rho_\infty (\Omega x)^2 \frac{\lambda_i}{r} \left[ c \left( \frac{\partial C_l}{\partial \theta} \right)_0 \sin \bar{\theta}_0 + c(C_l)_0 \cos \bar{\theta}_0 \right. \\
& \left. - c \left( \frac{\partial C_d}{\partial \theta} \right)_0 \cos \bar{\theta}_0 + c(C_d)_0 \sin \bar{\theta}_0 \right] \\
K_{(a03 \ QS)} = & -\frac{1}{2} \rho_\infty (\Omega x)^2 c x_A \left( \frac{\partial C_l}{\partial \theta} \right)_0 \cos^2 \bar{\theta}_0 \\
& - \frac{1}{2} \rho_\infty (\Omega x)^2 (c^2 C_{m0} - c x_A (C_l)_0) \sin 2\bar{\theta}_0 \\
& - \frac{1}{2} \rho_\infty (\Omega x)^2 \frac{\lambda_i}{r} c x_A \left( \frac{\partial C_l}{\partial \theta} \right)_0 \sin 2\bar{\theta}_0 \\
& - \rho_\infty (\Omega x)^2 \frac{\lambda_i}{r} c x_A (C_l)_0 \cos 2\bar{\theta}_0
\end{aligned}$$

Note that in theory, the aerodynamic coefficients depend upon all the variables shown in Eq. (2.261). Hence, gradients with respect to each of these quantities should be computed. However, it is reasonable to neglect the influence on  $C_l$ ,  $C_d$  and  $C_{m0}$  of a change in the second-order terms present in Eq. (2.261), relative to the action due to a change in  $\theta$ . Likewise, if we assume that the inflow ratio does not change under small perturbation of the degrees of freedom, then the partial derivatives shown in the previous equation are

$$\left( \frac{\partial C_l}{\partial \theta} \right)_0 = (C_{l\alpha})_0 \quad \text{and} \quad \left( \frac{\partial C_d}{\partial \theta} \right)_0 = (C_{d\alpha})_0 \quad (\text{D.8})$$

## Appendix E

### Numerical computation of the Jacobian matrix using the complex-step derivative approximation

In this dissertation, the components of the Jacobian matrix are derived analytically and then implemented in closed form into the numerical model. However, it is possible that errors are introduced, for instance when the components of the matrix are typed in the computer program. To verify the exactitude of the Jacobian matrix, an algorithm is implemented to compute the components of the matrix numerically.

Recall that the components of the Jacobian matrix are given by

$$J_{ij} = \frac{\partial R_i}{\partial u_j} \tag{E.1}$$

where  $R_i = R_i(u_1, \dots, u_N)$  is the  $i$ th component of the residue vector-valued function, and  $u_j$  is the  $j$ th component of the vector of generalized coordinates. One method to numerically approximate the derivative of the residue function is to use the central difference formula, defined by

$$\frac{\partial R_i}{\partial u_j} = \frac{R_i(u_1, \dots, u_j + \Delta u, \dots, u_N) - R_i(u_1, \dots, u_j - \Delta u, \dots, u_N)}{2 \Delta u} + \mathcal{O}(\Delta u^2) \tag{E.2}$$

The order of magnitude of the terms truncated in this approximation is equal to  $\Delta u^2$ . Therefore, choosing  $\Delta u$  as small as possible minimizes the truncation error. However, it can also be seen in Eq. (E.2) that an excessively small  $\Delta u$  leads to a subtracting cancellation error in the numerator.

A solution to circumvent the issue described above is to use the complex-step differentiation method. This approximate method of differentiation was originally formulated by Lyness and Moler [108] and relies on the following derivation.

First, let us expand  $R_i(\mathbf{u})$  in a Taylor series, as follows

$$R_i(u_1, \dots, u_j + i\Delta u, \dots, u_N) = R_i(u_1, \dots, u_j, \dots, u_N) + i\Delta u \frac{\partial R_i}{\partial u_j} - \Delta u^2 \frac{1}{2!} \frac{\partial^2 R_i}{\partial u_j^2} - i\Delta u^3 \frac{1}{3!} \frac{\partial^3 R_i}{\partial u_j^3} + \dots \quad (\text{E.3})$$

Taking the imaginary parts of both sides of Eq. (E.3) yields

$$\Im[R_i(u_1, \dots, u_j + i\Delta u, \dots, u_N)] = \Delta u \frac{\partial R_i}{\partial u_j} - \Delta u^3 \frac{1}{3!} \frac{\partial^3 R_i}{\partial u_j^3} + \dots \quad (\text{E.4})$$

Dividing both sides by  $\Delta u$ , we obtain

$$\frac{\partial R_i}{\partial u_j} = \Im[R_i(u_1, \dots, u_j + i\Delta u, \dots, u_N)] + \mathcal{O}(\Delta u^2) \quad (\text{E.5})$$

It can be noticed that the magnitude of the truncation error in the previous expression is on the order of  $\Delta u^2$ . In addition, Eq. (E.5) is not subjected to cancellation errors. Therefore, the most accurate approximation of the derivative  $\partial R_i / \partial u_j$  is obtained for the smallest  $\Delta u$  available. In practice,  $\Delta u$  is set equal to the machine precision.

## Appendix F

### Response of a mass-spring system subject to gyroscopic effects

The objective of this appendix is to show that the solution to a mass-spring system subject to gyroscopic forces or moments is purely oscillatory, with no negative or positive damping of the response.

Assume that the motion of the system can be described by the following equations

$$\begin{bmatrix} 1 & 0 \\ 0 & 1 \end{bmatrix} \begin{Bmatrix} \ddot{x}_1 \\ \ddot{x}_2 \end{Bmatrix} + \begin{bmatrix} 0 & \alpha \\ -\alpha & 0 \end{bmatrix} \begin{Bmatrix} \dot{x}_1 \\ \dot{x}_2 \end{Bmatrix} + \begin{bmatrix} \omega_1^2 & 0 \\ 0 & \omega_2^2 \end{bmatrix} \begin{Bmatrix} x_1 \\ x_2 \end{Bmatrix} = \begin{Bmatrix} F_1 \\ F_2 \end{Bmatrix} \quad (\text{F.1})$$

In particular, the mass and stiffness matrices are written in diagonal form, as they would upon normal modes decomposition. Note also that the gyroscopic matrix remains skew-symmetric with the use of normal modes.

The state-space matrix associated with this system is

$$A = \begin{bmatrix} 0 & 0 & 1 & 0 \\ 0 & 0 & 0 & 1 \\ -\omega_1^2 & 0 & 0 & \alpha \\ 0 & -\omega_2^2 & -\alpha & 0 \end{bmatrix} \quad (\text{F.2})$$

The characteristic polynomial of this matrix is

$$|\mathbf{A} - \lambda\mathbf{I}| = \lambda^4 + (\omega_1^2 + \omega_2^2 + \alpha^2)\lambda^2 + \omega_1^2\omega_2^2 \quad (\text{F.3})$$

whose discriminant is

$$\begin{aligned}\Delta &= (\omega_1^2 + \omega_2^2 + \alpha^2)^2 - 4\omega_1^2\omega_2^2 \\ &= ((\omega_1 - \omega_2)^2 + \alpha^2) ((\omega_1 + \omega_2)^2 + \alpha^2)\end{aligned}\tag{F.4}$$

It can be seen that this discriminant is always positive. Therefore, the eigenvalues of the state-space matrix  $\mathbf{A}$  are purely imaginary complex conjugates, equal to

$$\lambda_{1,2,3,4} = \pm i \sqrt{\frac{(\omega_1^2 + \omega_2^2 + \alpha^2) \pm \sqrt{(\omega_1^2 + \omega_2^2 + \alpha^2)^2 - 4\omega_1^2\omega_2^2}}{2}}\tag{F.5}$$

# Appendix G

## Front panel of custom NI LabView virtual instrument

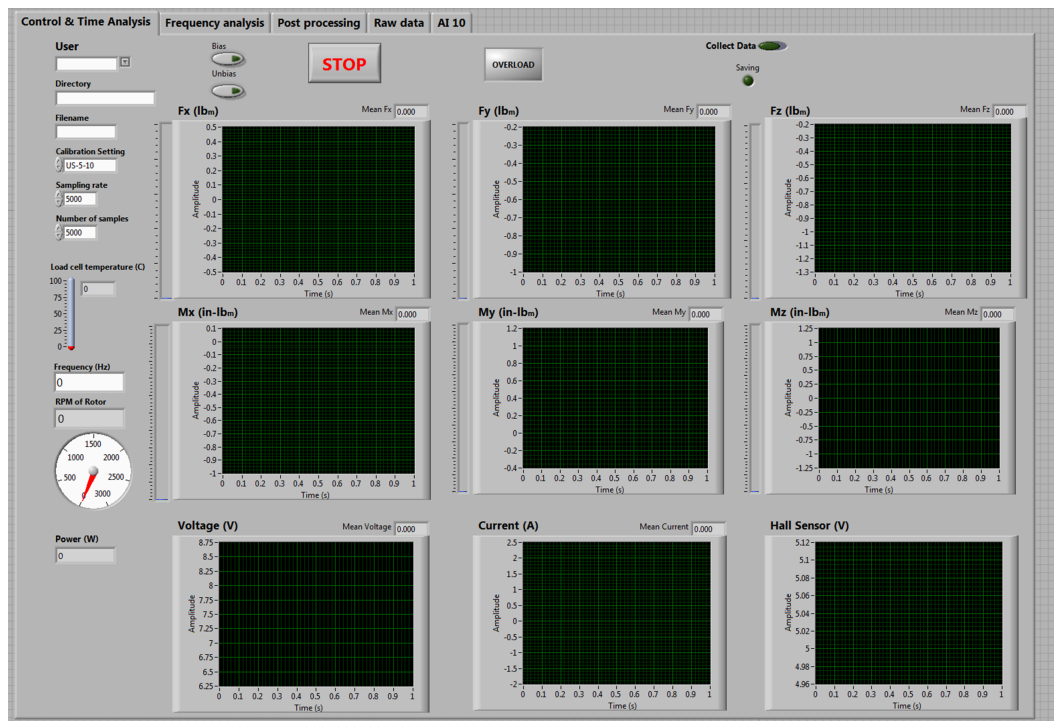


Figure G.1: Control & Time Analysis

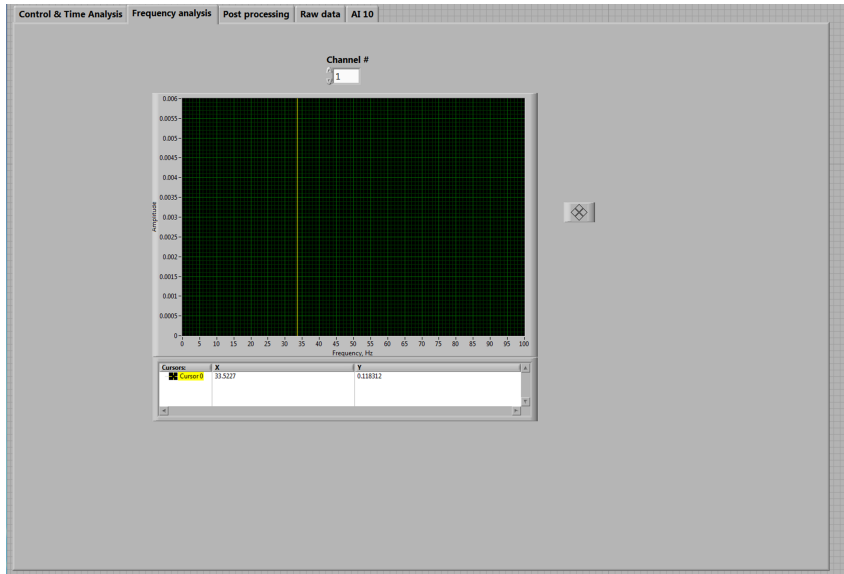


Figure G.2: Frequency Analysis

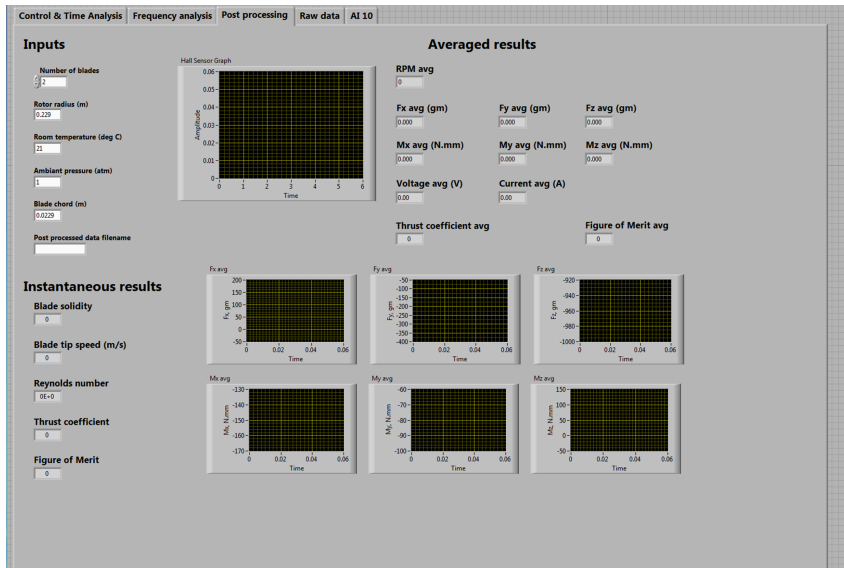


Figure G.3: Post Processing

# Appendix H

## Circuit diagram of DAQ and transducers

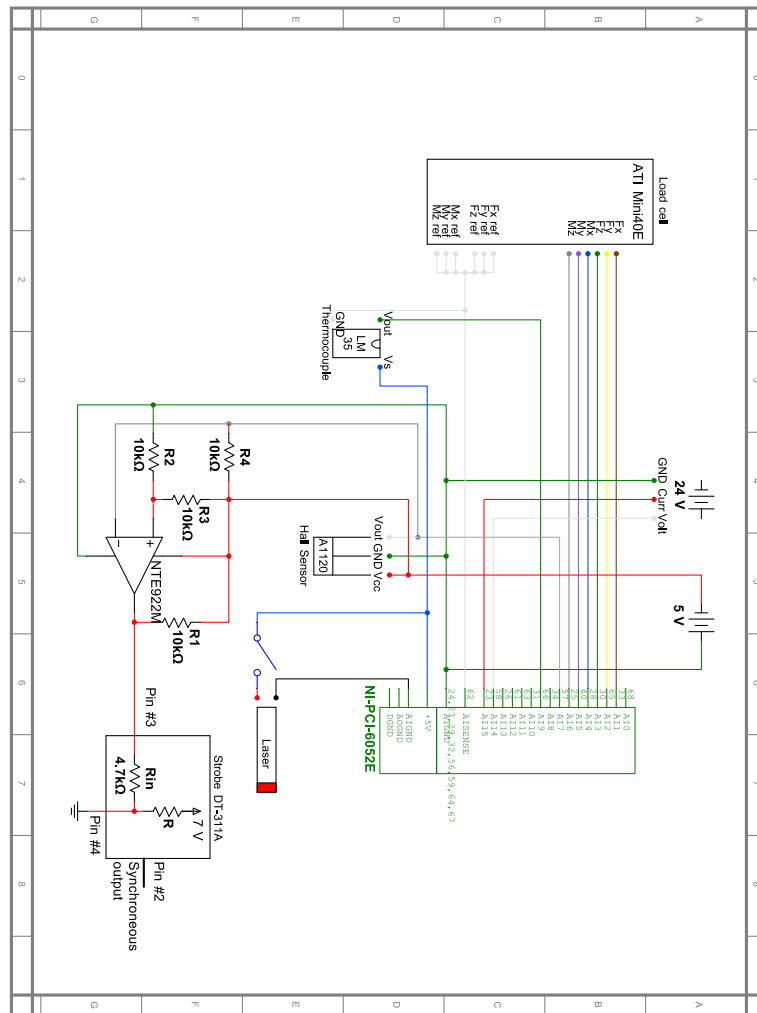


Figure H.1: Circuit diagram of DAQ equipment and transducers

## Bibliography

- [1] D. J. Pines and F. Bohorquez. Challenges facing future micro-air vehicle development. *Journal of Aircraft*, 43(2):290–305, April 2006. doi:[10.2514/1.4922](https://doi.org/10.2514/1.4922).
- [2] W. R. Davis, Jr., B. B. Kosicki, D. M. Boroson, and D. F. Kostishack. Micro air vehicles for optical surveillance. *The Lincoln Laboratory Journal*, 9(2):197–214, 1996.
- [3] I. Chopra. Hovering micro air vehicles: Challenges and opportunities. *Proceedings of the International Forum on Rotorcraft Multidisciplinary Technology, Seoul, South Korea*, October 2007.
- [4] F. Bohorquez, P. Samuel, J. Sirohi, D. Pines, L. Rudd, and R. Perel. Design, analysis and hover performance of a rotary wing micro air vehicle. *Journal of the American Helicopter Society*, 48(2):80–90, April 2003. doi:[10.4050/JAHS.48.80](https://doi.org/10.4050/JAHS.48.80).
- [5] T. Theodorsen and E. F. Andrews. Sustaining rotor for aircraft, September 1939. US Patent 2,172,333.
- [6] T. C. Ryan and P. F. Girard. Flexible blade retractable rotor aircraft, January 1972. US Patent 3,637,168.

- [7] L. Feldman. Flexible sail rotor devices, January 1972. US Patent 3,633,850.
- [8] B. L. Fuller. Rollable airfoil, December 1984. US Patent 4,485,991.
- [9] R. L. Goldman. Some observations on the dynamic behavior of extremely flexible rotor blades. *Proceedings of the 28th Annual Meeting of the IAS, Paper 60-44, Institute of the Aeronautical Sciences, New York, 25-27 January, 1960.*
- [10] R. R. Pruyn and T. G. Swales. Development of rotor blades with extreme chordwise and spanwise flexibility. *American Helicopter Society 20th Annual National Forum Proceedings, Washington D. C., 13-15 May, pages 102–108, 1964.*
- [11] M. M. Winston. An investigation of extremely flexible lifting rotors. Technical Note NASA TN D-4465, Langley Research Center, National Aeronautics and Space Administration, Langley Station, VA, April 1968.
- [12] M. M. Winston. A hovering investigation of an extremely flexible lifting rotor. Technical Note NASA TN D-4820, Langley Research Center, National Aeronautics and Space Administration, Langley Station, VA, October 1968.
- [13] S. B. Spangler and J. N. Nielsen. Theoretical and experimental investigation of sail rotors. *Proceedings of the AIAA 10th Aerospace Sciences Meeting, San Diego, CA, 17-19 January, 1972.* doi:[10.2514/6.1972-66](https://doi.org/10.2514/6.1972-66).

- [14] B. R. Hein and I. Chopra. Hover performance of a micro air vehicle: Rotors at low Reynolds number. *Journal of the American Helicopter Society*, 52(3):254–262, July 2007. doi:[10.4050/JAHS.52.254](https://doi.org/10.4050/JAHS.52.254).
- [15] W. Johnson. Milestones in rotorcraft aeromechanics Alexander A. Nikolsky honorary lecture. *Journal of the American Helicopter Society*, 56(3):1–24, July 2011. doi:[10.4050/JAHS.56.031001](https://doi.org/10.4050/JAHS.56.031001).
- [16] D. H. Hodges. *Nonlinear Composite Beam Theory*, volume 213 of *Progress in Astronautics and Aeronautics*. American Institute of Aeronautics and Astronautics, Inc., Reston, VA, 2006.
- [17] R. T. Yntema. Simplified procedures and charts for the rapid estimation of bending frequencies of rotating beams. Technical Note NACA TN 3459, Langley Aeronautical Laboratory, National Advisory Committee for Aeronautics, Langley Field, Va, June 1955.
- [18] R. M. Wood and W. G. A. Perring. Stresses and strains in airscrews with particular reference to twist. *Reports & Memoranda of the British A.R.C.*, 1274, 1929.
- [19] A. Mendelson. Effect of centrifugal force on flutter of uniform cantilever beam at subsonic speeds with application to compressor and turbine blades. Technical Note NACA TN 1893, National Advisory Committee for Aeronautics, 1949.

- [20] J. C. Houbolt and G. W. Brooks. Differential equations of motion for combined flapwise bending, chordwise bending, and torsion of twisted nonuniform rotor blades. Technical Note 3905, Langley Aeronautical Laboratory, National Advisory Committee for Aeronautics, Langley Field, VA, February 1957.
- [21] D. H. Hodges and E. H. Dowell. Nonlinear equations of motion for the elastic bending and torsion of twisted nonuniform rotor blades. Technical Note NASA TN D-7818, Ames Research Center and U.S. Army Air Mobility R&D Laboratory, Moffett Field, CA, December 1974.
- [22] K. R. V. Kaza and R. G. Kvaternik. Nonlinear aeroelastic equations for combined flapwise bending, chordwise bending, torsion and extension of twisted nonuniform rotor blades in forward flight. Technical Memorandum NASA TM 74059, Langley Research Center, National Aeronautics and Space Administration, Hampton, VA, August 1977.
- [23] A. Rosen and P. P. Friedmann. Nonlinear equations of equilibrium for elastic helicopter or wind turbine blades undergoing moderate deformation. Contractor Report NASA CR 159478, Lewis Research Center, National Aeronautics and Space Administration, Cleveland, OH, December 1978.
- [24] D. H. Hodges. Nonlinear dynamic analysis of pretwisted beams undergoing small strain and large rotations. Technical Paper NASA TP 2470, National Aeronautics and Space Administration, May 1985.

- [25] C. Hong and I. Chopra. Aeroelastic stability analysis of a composite bearingless rotor blade. *Journal of the American Helicopter Society*, 31(4):29–35, October 1986. doi:[10.4050/JAHS.31.29](https://doi.org/10.4050/JAHS.31.29).
- [26] D. H. Hodges. Geometrically exact, intrinsic theory for dynamics of curved and twisted anisotropic beams. *AIAA Journal*, 41(6):1131–1137, June 2003. doi:[10.2514/2.2054](https://doi.org/10.2514/2.2054).
- [27] O. A. Bauchau and N. K. Kang. A multibody formulation for helicopter structural dynamic analysis. *Journal of the American Helicopter Society*, 38(2):3–14, April 1993. doi:[10.4050/JAHS.38.3](https://doi.org/10.4050/JAHS.38.3).
- [28] W. J. M. Rankine. On the mechanical principles of the action of propellers. *Transactions of the Institute of Naval Architects*, 6:13–39, 1865.
- [29] W. Froude. On the elementary relation between pitch, slip, and propulsion efficiency. *Transactions of the Institute of Naval Architects*, 19:47–57, 1878.
- [30] H. Glauert. *Aerodynamic Theory*. Springer Berlin Heidelberg, 1935. doi:[10.1007/978-3-642-91487-4\\_3](https://doi.org/10.1007/978-3-642-91487-4_3).
- [31] S. Drzewiecki. *Theorie Generale de l'Helice*. Gauthier-Villars et Cie, Paris, 1920.
- [32] F. B. Gustafson and A. Gessow. Effect of rotor-tip speed on helicopter hovering performance and maximum forward speed. Wartime Report

ARR L6A16, National Advisory Committee for Aeronautics, Langley Field, VA, March 1946.

- [33] A. Betz. Schraubenpropeller mit geringstem energieverlust. *Nachrichten von der Gesellschaft der Wissenschaften zu Göttingen*, pages 193–217, 1919.
- [34] H. Wagner. Über die entstehung des dynamischen auftriebes von tragflügeln. *Zeitschrift für Angewandte Mathematik und Mechanik*, 5(1):17–35, February 1925. doi:[10.1002/zamm.19250050103](https://doi.org/10.1002/zamm.19250050103).
- [35] T. Theodorsen. General theory of aerodynamic instability and the mechanism of flutter. Technical Report NACA TR 496, National Advisory Committee for Aeronautics, 1935.
- [36] R. G. Loewy. A two-dimensional approximation to the unsteady aerodynamics of rotary wings. *Journal of the Aeronautical Sciences*, 24(2):81–92, February 1957. doi:[10.2514/8.3777](https://doi.org/10.2514/8.3777).
- [37] A. J. Landgrebe. The wake geometry of a hovering rotor and its influence on rotor performance. *Journal of the American Helicopter Society*, 17(4):3–15, October 1972. doi:[10.4050/JAHS.17.3](https://doi.org/10.4050/JAHS.17.3).
- [38] M. P. Scully. *Computation of helicopter rotor wake geometry and its influence on rotor harmonic airloads*. Thesis, Massachusetts Institute of Technology, 1975.

- [39] A. Bagai and J. G. Leishman. Free-wake analysis of tandem, tilt-rotor and coaxial rotor configurations. *Journal of the American Helicopter Society*, 41(3):196–207, July 1996. doi:[10.4050/JAHS.41.196](https://doi.org/10.4050/JAHS.41.196).
- [40] A. Datta, M. Nixon, and I. Chopra. Review of rotor loads prediction with the emergence of rotorcraft CFD. *Journal of the American Helicopter Society*, 52(4):287–317, October 2007. doi:[10.4050/JAHS.52.287](https://doi.org/10.4050/JAHS.52.287).
- [41] J. G. Leishman. *Principles of Helicopter Aerodynamics*. Cambridge University Press, New York, NY, 2nd edition, 2006.
- [42] J. N. Nielsen. Theory of flexible aerodynamic surfaces. *Journal of Applied Mechanics*, 85(3):435–442, September 1963. doi:[10.1115/1.3636575](https://doi.org/10.1115/1.3636575).
- [43] W. G. Roeseler. The effect of ribbon rotor geometry on blade response and stability. Master’s thesis, Massachusetts Institute of Technology, May 1966.
- [44] W. Johnson. *Helicopter Theory*. Dover Publications Inc., New York, NY, 1994.
- [45] J. Sicard and J. Sirohi. Experimental study of an extremely flexible rotor for microhelicopters. *Journal of Aircraft*, 49(5):1306–1314, September–October 2012. doi:[10.2514/1.C031643](https://doi.org/10.2514/1.C031643).
- [46] D. Matuska, A. Dale, and P. Lorber. Wind tunnel test of a variable-diameter tiltrotor (VDTR) model. Contractor Report NASA CR 177629,

National Aeronautics and Space Administration, Ames Research Center, Moffett Field, CA, January 1994.

- [47] S. Brender, H. Mark, and F. Aguilera. The attributes of a variable-diameter rotor system applied to civil tiltrotor aircraft. Contractor Report CR 203092, NASA Ames Research Center, Moffett Field, CA, 1997.
- [48] J. M. Wang, C. T. Jones, and M. W. Nixon. A variable diameter short haul civil tiltrotor. *American Helicopter Society 55th Annual Forum Proceedings, Montreal, Canada, 25-27 May, 1999.*
- [49] G. Bowen-Davies and I. Chopra. Aeromechanics of a variable-radius rotor. *American Helicopter Society 68th Annual Forum Proceedings, Fort Worth, TX, 1-3 May, 2012.*
- [50] G. Bir, I. Chopra, and K. Nguyen. Development of UMARC (University of Maryland Advanced Rotorcraft Code). *American Helicopter Society 46th Annual Forum Proceedings, Washington, D.C., 21-23 May, 1990.*
- [51] T. Schmidt, J. Tyson, and K. Galanulis. Full-field dynamic displacement and strain measurement using advanced 3D image correlation photogrammetry: Part I. *Experimental Techniques*, 27(3):47–50, May 2003. doi:[10.1111/j.1747-1567.2003.tb00115.x](https://doi.org/10.1111/j.1747-1567.2003.tb00115.x).
- [52] G. A. Fleming and S. A. Gorton. Measurement of rotorcraft blade deformation using projection moiré interferometry. *Shock and Vibration*,

7(3):149–166, 2000.

- [53] G. A. Fleming, H. L. Soto, and B. W. South. Projection moiré interferometry for rotorcraft applications: Deformation measurements of active twist rotor blades. *American Helicopter Society 58th Annual Forum Proceedings, Montreal, Canada, 11-13 June, 2002.*
- [54] M. Sekula. The development and hover test application of a projection moiré interferometry blade displacement measurement system. *American Helicopter Society 68th Annual Forum Proceedings, Fort Worth, TX, 1-3 May, 2012.*
- [55] L. E. Olson, A. I. Abrego, D. A. Barrows, and A. W. Burner. Blade deflection measurements of a full-scale UH-60A rotor system. *American Helicopter Society Aeromechanics Specialists's Conference Proceedings, San Francisco, CA, 20-22 January, 2010.*
- [56] A. I. Abrego, L. E. Olson, E. A. Romander, D. A. Barrows, and A. W. Burner. Blade displacement measurement technique applied to a full-scale rotor test. *American Helicopter Society 68th Annual Forum Proceedings, Fort Worth, TX, 1-3 May, 2012.*
- [57] J. Sirohi and M. S. Lawson. Measurement of helicopter rotor blade deformation using digital image correlation. *Optical Engineering*, 51(4), April 2012. doi:[10.1117/1.OE.51.4.043603](https://doi.org/10.1117/1.OE.51.4.043603).

- [58] Z. L. Kahn-Jetter and T. C. Chu. Three-dimensional displacement measurements using digital image correlation and photogrammic analysis. *Experimental Mechanics*, 30(1):10–16, March 1990. doi:[10.1007/BF02322695](https://doi.org/10.1007/BF02322695).
- [59] M. Simons. *Model Aircraft Aerodynamics*. Trans-Atlantic Publications, Inc., Philadelphia, PA, 1999.
- [60] R. A. Wallis. Wind tunnel tests on a series of circular arc airfoils. *ARL Aero Note 74*, 1946.
- [61] E. Reissner. On one-dimensional large-displacement finite-strain beam theory. *Studies in Applied Mathematics*, 52(2):87–96, June 1973.
- [62] L. Meirovitch. *Methods of Analytical Dynamics*. Dover Publications, Inc., Mineola, NY, May 2010.
- [63] D. H. Hodges, R. A. Ormiston, and D. A. Peters. On the nonlinear deformation geometry of Euler-Bernoulli beams. Technical Paper NASA TP 1566, National Aeronautics and Space Administration, Moffett Field, CA, April 1980.
- [64] V. V. Novozhilov. *Foundations of the Nonlinear Theory of Elasticity*. Graylock Press, Rochester, N.Y., 1953.
- [65] A. E. H. Love. *A Treatise on the Mathematical Theory of Elasticity*. Cambridge University Press Warehouse, Cambridge, U.K., 2nd edition, 1906.

- [66] A. Campbell. On vibration galvanometer with unifilar torsional control. *Proceedings of the Physical Society of London*, 25:203–205, 1911. doi:[10.1088/1478-7814/25/1/320](https://doi.org/10.1088/1478-7814/25/1/320).
- [67] H. Pealing. On an anomalous variation of the rigidity of phosphor bronze. *Philosophical Magazine Series 6*, 25(147):418–427, March 1913. doi: [10.1080/14786440308634177](https://doi.org/10.1080/14786440308634177).
- [68] J. C. Buckley. The bifilar property of twisted strips. *Philosophical Magazine Series 6*, 28(168):778–787, 1914. doi:[10.1080/14786441208635264](https://doi.org/10.1080/14786441208635264).
- [69] W. C. Young, R. G. Budynas, and A. M. Sadegh. *Roark's Formulas for Stress and Strain*. McGraw-Hill, 8th edition, 2012.
- [70] S. P. Timoshenko. *Strength of Materials, Part II, Advanced Theory and Problems*. Van Nostrand Reinhold Company, Inc., NY, 1976.
- [71] M. A. Biot. Non-linear theory of elasticity and the linearized case for a body under initial stress. *Philosophical Magazine Series 7*, 27(183):468–489, 1939. doi:[10.1080/14786443908562246](https://doi.org/10.1080/14786443908562246).
- [72] M. A. Biot. Increase of torsional stiffness of a prismatical bar due to axial tension. *Journal of Applied Physics*, 10(12):860–864, December 1939. doi:[10.1063/1.1707272](https://doi.org/10.1063/1.1707272).
- [73] V. Z. Vlasov. *Thin-Walled Elastic Beams*. National Science Foundation and Department of Commerce, Washington, D.C., 1961.

- [74] H. Wagner. Torsion and buckling of open sections. Technical Memorandums NACA TM 807, National Advisory Committee for Aeronautics, October 1936.
- [75] S. P. Timoshenko and J. N. Goodier. *Theory of Elasticity*. Engineering Mechanics Series. McGraw-Hill, 3rd edition, 1970.
- [76] I. M. Daniel and O. Ishai. *Engineering Mechanics of Composite Materials*. Oxford University Press, New York, NY, 2nd edition, 2006.
- [77] Y. C. Fung. *An Introduction to the Theory of Aeroelasticity*. John Wiley and Sons, Inc., New York, 1955.
- [78] R. L. Bisplinghoff, H. Ashley, and R. L. Halfman. *Aeroelasticity*. Dover Publications, Inc, Mineola, NY, 1996.
- [79] P. Kuhn. Remarks on the elastic axis of shell wings. Technical Note NACA TN 562, Langley Memorial Aeronautical Laboratory, National Advisory Committee for Aeronautics, Langley Field, VA, February 1936.
- [80] K. R. V. Kaza and R. G. Kvaternik. Nonlinear flap-lag-axial equations of a rotating beam. *AIAA Journal*, 15(6):871–874, June 1977. doi:[10.2514/3.7376](https://doi.org/10.2514/3.7376).
- [81] T. Theodorsen and I. E. Garrick. Nonstationary flow about a wing-aileron-tab combination including aerodynamic balance. Technical Report NACA TR 736, National Advisory Committee for Aeronautics, January 1942.

- [82] W. Johnson. *Rotorcraft Aeromechanics*. Cambridge University Press, New York, NY, 2013.
- [83] D. A. Peters and R. A. Ormiston. The effects of second order blade bending on the angle of attack of hingeless rotor blades. *Journal of the American Helicopter Society*, 18(4):45–48, October 1973. doi:[10.4050/JAHS.18.45](https://doi.org/10.4050/JAHS.18.45).
- [84] D. H. Hodges and R. A. Ormiston. Stability of elastic bending and torsion of uniform cantilever rotor blades in hover with variable structural coupling. Technical Note NASA TN D-8192, Ames Research Center and U.S. Army Air Mobility R&D Laboratory, Moffett Field, CA, April 1976.
- [85] J. J. Moré, B. S. Garbow, and Hillstrom K. E. User guide for minpack 1. Technical Report ANL-80-74, Argonne National Laboratory, 1980.
- [86] B.P. Flannery, W.H. Press, S.A. Teukolsky, and W. Vetterling. *Numerical Recipes in C*. Press Syndicate of the University of Cambridge, New York, 1992.
- [87] E. B. Becker, G. F. Carey, and J. T. Oden. *Finite Elements: An Introduction*, volume 1. Prentice-Hall, Englewood Cliffs, NJ, 1981.
- [88] D. H. Hodges and G. A. Pierce. *Introduction to the Structural Dynamics and Aeroelasticity*. Cambridge University Press, New York, NY, 2002.

- [89] H. J. Hassig. An approximate true damping solution of the flutter equation by determinant iteration. *Journal of Aircraft*, 8(11):885–889, November 1971. doi:[10.2514/3.44311](https://doi.org/10.2514/3.44311).
- [90] Freeman 1035 flexible polyurethane elastomer. Technical Data Sheet. Available: <http://www.freemansupply.com/datasheets/Freeman/FMSC1035.pdf> [Accessed: May 17, 2014].
- [91] Light weight carbon fiber fabric CF131, 1k tow, 0.007" thick, 2.9 oz/yd<sup>2</sup>, 19x19 thread count, 0/90° plain weave. The Composite Store. Available: [http://www.cstsales.com/carbon\\_fabric.html](http://www.cstsales.com/carbon_fabric.html) [Accessed: May 17, 2014].
- [92] Alphapoxy. Aircraft Spruce. Available: <http://www.aircraftspruce.com/catalog/cmpages/alphapoxy.php> [Accessed: May 17, 2014].
- [93] Pro-Set laminating epoxy 125-226. Technical Data Sheet. Available: [http://www.prosetepoxy.com/PDF/LAM-125\\_LAM-226.pdf](http://www.prosetepoxy.com/PDF/LAM-125_LAM-226.pdf) [Accessed: May 17, 2014].
- [94] NTE3037 silicon NPN phototransistor detector. Technical Data Sheet. Available: <http://www.nteinc.com/specs/3000to3099/pdf/nte3037.pdf> [Accessed: May 17, 2014].
- [95] JR DS285 - digital hi-speed sub-micro servo. Technical Data Sheet. Available: <http://www.servodatabase.com/servo/jr/ds285> [Accessed: May 17, 2014].

- [96] ATI Mini40-E transducer. Technical Data Sheet. Available: [http://www.atia.com/products/ft/ft\\_models.aspx?id=Mini40](http://www.atia.com/products/ft/ft_models.aspx?id=Mini40) [Accessed: May 17, 2014].
- [97] La Vision. *DaVis StrainMaster 3-D, Software Package Ver. 7.2*. La Vision, Göttingen, Germany, January 2010.
- [98] T. Siebert, T. Becker, K. Spilthof, I. Neumann, and R. Krupka. High-speed digital image correlation: error estimations and applications. *Optical Engineering*, 46(5), May 2007. doi:[10.1117/1.2741217](https://doi.org/10.1117/1.2741217).
- [99] Jr. Sharpe and William N. *Springer Handbook of Experimental Solid Mechanics*. Springer Science LLC, New-York, NY, 2008. pp. 581-585.
- [100] W. Schreier, H., R. Braasch, J., and A. Sutton, M. Systematic errors in digital image correlation caused by intensity interpolation. *Optical Engineering*, 39(11):2915–2921, November 2000. doi:[10.1117/1.1314593](https://doi.org/10.1117/1.1314593).
- [101] A. S. Hopkins and R. A. Ormiston. An examination of selected problems in rotor blade structural mechanics and dynamics. *Journal of the American Helicopter Society*, 51(1):104–119, January 2006. doi:[10.4050/1.3092882](https://doi.org/10.4050/1.3092882).
- [102] E. H. Dowell and J. J. Traybar. An experimental study of the nonlinear stiffness of a rotor blade undergoing flap, lag and twist deformations. Contractor Report NASA CR 137968, Princeton University, Princeton, NJ, January 1975.

- [103] E. H. Dowell and J. J. Traybar. Addendum to an experimental study of the nonlinear stiffness of a rotor blade undergoing flap, lag and twist deformations. Contractor Report NASA CR 137969, Princeton University, Princeton, NJ, December 1975.
- [104] W. J. Duncan. Mechanical admittances and their applications to oscillation problems. Reports and Memoranda 2000, British Aeronautical Research Council, 1947.
- [105] A. D. Wright, C. E. Smith, R. W. Thresher, and J. L. C. Wang. Vibration modes of centrifugally stiffened beams. *Journal of Applied Mechanics*, 49(1):197–202, March 1982. doi:[10.1115/1.3161966](https://doi.org/10.1115/1.3161966).
- [106] F. D. Harris. The rotor blade flap bending problem - an analytical test case. *Journal of the American Helicopter Society*, 37(4):64–67, October 1992. doi:[10.4050/JAHS.37.64](https://doi.org/10.4050/JAHS.37.64).
- [107] A. Datta and I. Chopra. Validation and understanding of UH-60A vibratory loads in steady level flight. *Journal of the American Helicopter Society*, 49(3):271–287, July 2004. doi:[10.4050/JAHS.49.271](https://doi.org/10.4050/JAHS.49.271).
- [108] J. N. Lyness and C. B. Moler. Numerical differentiation of analytic functions. *SIAM Journal on Numerical Analysis*, 4(2):202–210, June 1967.

## Vita

Jérôme Sicard was born in Marseille, France on 29 July 1985, the son of Dr. Emile Sicard and Colette Sicard. He received the Bachelor of Science degree in Aerospace Engineering in December, 2008 from the Institut Supérieur de l'Aéronautique et de l'Espace (ISAE, Toulouse, France). During his undergraduate studies, Jérôme studied for 2 semesters at the University of Wisconsin at Madison as an exchange student. Upon graduation from ISAE, he was employed as a structural engineer at Altran. There, he was involved in the mechanical dimensioning and environmental test validation of satellite antennas structures. In September 2009, he entered the Graduate School at the University of Texas at Austin. He received the degree of Master of Science in Aerospace Engineering in May, 2011.

Permanent address: 54 avenue de Russie  
03700 Bellerive sur Allier  
France

This dissertation was typeset by the author.